Self-Assembly of Sb and Bi Nanostructures on Graphite

A thesis submitted in partial fulfilment
of the requirements for the Degree of

Doctor of Philosophy in Physics
in the
University of Canterbury

by

Shelley A. Scott

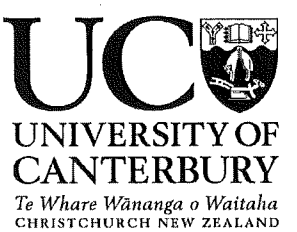

Department of Physics and Astronomy
University of Canterbury
2005

Abstract

Spontaneous pattern formation in the natural world provides a constant source of wonder. Remarkable similarities exist between the patterns observed in the likes of snowflake growth, electrodeposition, and bacterial colonies. The driving force which creates similar patterns from these seemingly different processes is a non-equilibrium growth environment, which results from a diffusion field at the structures' boundary.

Thin film growth from the vapor phase is an interesting and technologically important non-equilibrium system. Particles deposited on atomically flat and weakly interacting substrates diffuse over substantial distances, nucleating islands via collisions with other adatoms and with defects. The final island morphologies are governed by an interplay between kinetics and thermodynamics. Compact structures are thermodynamically favored, but the kinetics of particle diffusion to the growth front often results in dendritic and irregular shapes. Manipulating this balance between kinetics and thermodynamics can allow the self-assembly of nanoscale structures with tailored morphologies.

This study uses scanning electron microscopy, atomic force microscopy, and electron backscatter diffraction to investigate the morphology and structure of antimony and bismuth aggregates on highly oriented pyrolitic graphite (HOPG) substrates. In particular the islands are characterized with varying experimental growth conditions.

For the case of the Sb/HOPG system, altering the deposition flux and the deposited dose results in a transition from compact to branched structures, consistent with other studies. However, the correlation of island heights with varying growth environments has not been performed previously, and in the present case, reveals a transition to flatter structures when the deposition rate is increased. Also, the heights of the branches are found to be strongly dependent on their length.

Island aggregation in the Bi/HOPG system was the primary focus of this work, and on the graphite terraces, revealed the formation of elongated 6-point star shaped islands, with a well defined stripe morphology. Increasing the flux resulted in a transition to more branched and disordered morphologies. Decoration of graphite step edges in a low flux environment, produced ordered arrays of nano-rods at the step edges.

Both the step edge and terrace nucleated Bi aggregates were aligned with the high symmetry directions of the graphite substrate with Bi$\{01\bar{1}2\}$ planes parallel to the plane of the substrate. With increasing deposited dose, a continuous film forms, which undergoes a crystallographic orientation transition to the Bi$\{0001\}$ orientation.

Contents

Chapter 1

Introduction

The development of new materials with novel electronic properties is one of the most active research areas in the physical sciences. In particular, there is immense interest in the the fabrication of nanoscale structures on surfaces. The most obvious reason for this pursuit is the industrial demand for miniaturization of electronic devices, in order to benefit from increased device speed and data density on a chip. However, as the size of these structures decreases, quantum confinement effects become important and the materials' electronic properties begin to differ from those of the bulk material [1]. In particular, the effective band gap of a material often increases as the size is reduced, and it is possible to imagine tailoring the electronic properties of nanostructures by controlling their size [2].

The enormous importance of the practical applications of nanotechnology, has spurred the need for a detailed understanding of the fabrication and behavior of nanostructures. A vast amount of both theoretical and experimental work is devoted to this field, which is still in its infancy. However, with the promise shown so far, nanotechnology is likely to be one of the key technologies of this century and beyond.

Interest in small scale structures is by no means recent. Medieval artisans unknowingly utilized the optical properties of nanoparticles when they introduced metals into their stained glasses. Gold nanoparticles produced rich ruby red colored glass. More recent applications have included: sensor technology (using molecular detection based on conductance quantization of nanowires [3]), new catalytic properties owing to the large surface area to volume ratio of nanoclusters [4], and of course miniaturization of electronic devices by developing new nanostructured materials [5], [6].

Fabrication Techniques: Top Down versus Bottom Up

Most current methods of fabricating nanostructures on surfaces are based on lithographic and etching techniques [7]. This method is known as the top down approach, owing to the fact that a film is organized into nanoscale structures by removing material through a masking and etching process. Current processing technologies are rapidly approaching fundamental size limits, and structures

become exponentially more expensive to manufacture as the size is reduced. However, there is an alternative. When making structures on the nanoscale, it makes sense to think in terms of using particles like atoms and molecules as tiny building blocks - a technique called the bottom up approach. The appeal of this method lies in the idea that nanosize building blocks could self-assemble on surfaces, eliminating the need for laborious masking and etching processes [8], [9], [10].

The top down approach is well established, relatively easy to control, and commercially viable for device fabrication. The problem lies in pushing forward minimum size barriers. Conversely, the bottom up approach is less well understood, and more difficult to control. However, the minimum size of self-assembled structures is limited only by the size of the building blocks, which opens up the possibility of creating a diverse range of new devices and materials that harness the unique properties of structures with reduced dimensions.

Thin Film Growth: Antimony and Bismuth on Graphite Substrates

The growth of thin films from the vapor phase provides a much studied route to nanoscale self-assembly [11], [12]. Atoms are deposited onto carefully controlled substrates, and allowed to diffuse on the surface. Nanoscale structures are then formed by the aggregation of mobile atoms.

The morphology of these diffusion formed islands results from an intricate balance between kinetics and thermodynamics. There exists a thermodynamic tendency to minimize the surface and interface free energies leading to compact shapes. However, the kinetics of particle diffusion at the island boundary often drives the system towards dendritic and irregular shapes [12]. This balance, and consequently island morphologies, can be altered by manipulating experimental parameters [9, chap 3]. The evolution of structures as diverse as compact polygons [13] and fingered dendrites [14] have been the subject of many investigations, due to wide spread interest in the self-assembly of nanoscale surface objects with well defined morphologies.

Highly ordered pyrolitic graphite (HOPG) has been extensively used as a substrate for investigating diffusion mediated island growth processes [15], [16]. Its appeal lies in its atomically smooth and weakly interacting nature [17], which allow for high adatom mobilities and abrupt adsorbate/substrate interfaces [18]. This thesis concerns the growth and characterization of antimony and bismuth nanostructures on HOPG substrates.

Antimony islands bear a conspicuous similarity to other patterns observed in nature, and their structure is strongly dependent on the experimental environment of the deposition process. Previous studies of the Sb/HOPG system [19], [14], [20] have involved systematic investigations of the 2D island morphology as a function of experimental conditions. We expand these investigations to include a 3D analysis, via height profiling of the structures. The bulk crystal structure of

antimony is very similar to that of bismuth, however no systematic investigation of the island morphology and structure of Bi films on sufficiently clean HOPG surfaces has been performed previously.

Bismuth is a group V semi-metal with a carrier density five orders of magnitude lower than in most metals, and a Fermi-wavelength in the order of tens of nanometers. These unusual electronic properties provide for an attractive case study for quantum transport and finite size effects [21]. Desirable properties such as superconductivity [22], increased magnetoresistance [23], and enhanced thermoelectric efficiency [24], have been observed in bismuth nanostructures, leading to extensive interest in their fabrication.

Outline of the Following Chapters

This thesis is organized as follows: Chapter 2 describes the principles of thin film growth from the vapor phase. The modes of film growth are outlined with a focus on energetic considerations. The kinetics of particle diffusion is also discussed. Here, emphasis is placed on deposition, diffusion, nucleation, and aggregation, which are simultaneous processes. Models to describe the aggregation process are reviewed, concluding with a brief review of the behavior of metals adsorbed on HOPG substrates.

Chapter 3 focuses on the experimental procedures used to deposit antimony and bismuth vapor on graphite substrates. The design, construction, and operation of a new ultra high vacuum system that was developed for this project is described. This includes an overview of system preparation and pumping, substrate preparation, and vapor beam generation. The bulk structures of graphite, bismuth, and antimony are also described.

Chapter 4 gives an overview of the film imaging techniques of atomic force microscopy and scanning electron microscopy. Electron backscatter diffraction (the technique used for determination of crystallographic structure) is also described. This Chapter also outlines image processing procedures which were utilized to enable calculation of island area, density, and perimeter.

Chapter 5 discusses the results for antimony deposition. The evolution of film morphology with varying growth conditions is investigated with scanning electron microscopy. The island heights are then characterized as a function of experimental conditions, with atomic force microscopy. The evolution of the film in the high coverage (deposited dose) limit is briefly addressed.

Chapter 6 is the main results and analysis chapter, and represents the primary focus of this project. The island morphologies are described in terms of growth and kinetic influences. This includes characterization of the island areas, density, heights, and general shapes. The evolution of the film in the regime of high surface coverage is also discussed in detail. The morphology is described and the crystallographic orientation determined. The orientation of the bismuth

islands is also determined, and related to the morphology in order to describe the pattern formation. Nucleation of bismuth along the natural step edges in the graphite substrate is investigated as a function of varying deposition conditions. The crystallographic orientation of the step edge aggregates is also correlated with their morphology. The stability of the islands in ambient conditions is addressed, as is the effect on the morphology of deposition on defect contaminated substrates.

In Chapter 7 the conclusions of the previous Chapters are reviewed, including a summary of the future and outlook for studies of island growth on surfaces.

Chapter 2

Mechanisms of Nucleation and Growth

The growth of nanoscale structures by atomic deposition and subsequent diffusion on surfaces, relies on a series of delicate and interdependent processes. This Chapter explores these processes and how they translate to the final morphology of diffusion formed surface islands.

Section 2.1 discusses the energetic considerations relevant in determining the growth mode of thin films. Next, the kinetics of diffusion is explored. This includes a discussion of particle deposition in Section 2.2.1, and subsequent diffusion on substrates in Section 2.2.2. The nucleation of islands is covered in Section 2.2.3, including the effects of adjusting the deposition parameters. Section 2.2.4 explores the aggregation of islands, with particular emphasis placed on the non-equilibrium growth environment which results in the vast array of experimentally observed morphologies. In this Section, growth models such as diffusion limited aggregation are described, and the process of edge diffusion is outlined, including discussions of island morphologies observed in various adsorbate/substrate systems. Section 2.3 overviews island growth for various metals on graphite substrates, including a review of Sb/HOPG and Bi/HOPG. The final Section summarizes the Chapter.

2.1 Growth Modes

The morphology of thin films can be considered within the context of thermodynamics, as was first summarized by Bauer [25]. If a system is close to equilibrium the film structure is determined by the balance of the surface (free) energies of the substrate γ_S, the deposited film γ_F, and the interface between them γ_I. There are three principle modes by which thin film growth can proceed, as illustrated in Figure 2.1. In the Volmer-Weber mode [26], small islands nucleate on the substrate surface, and grow to form larger 3D structures. In this mode the adatoms have a stronger bond to each other than to the substrate. This can be expressed in terms of surface energies as $\gamma_F > \gamma_S + \gamma_I$, and is common for submonolayer coverages of metal adsorbates on inert substrates such as HOPG [19] and mica [27].

The Frank-van de Merwe mode [28] is characteristic of adatoms that experi-

ence a stronger bond to the substrate than to each other. Complete condensation of the first monolayer on the substrate is required before growth can proceed to the next layer, which is less tightly bound than the first. This layer-by-layer growth is only obtained if the binding energy decreases monotonically towards the bulk crystal value for the particular adatom species. In terms of free energies, $\gamma_F < \gamma_S + \gamma_I$. Examples of this growth mode include some metal adsorbates on metal substrates [29], [30], and rare gases on HOPG [31].

The final growth mode is the Stranski-Krastanov mode [32], which incorporates both layer and island growth. Initially the growth follows the Frank-van der Merwe mode, and one, or possibly a few, monolayers form on the surface. Subsequent layer growth become unfavorable and island growth prevails. There are many possibilities for this break down of layer growth. Essentially any mechanism which disrupts the monotonic decrease in binding of the layer mode can be responsible. One common cause is strain due to lattice mismatch. As the number of layers increase the interface energy γ_I also increases. When the condition $\gamma_F > \gamma_S + \gamma_I$ is reached, the growth mode switches to to the Volmer-Weber mode, and island formation is activated. A striking example of a regular array of Au islands grown on a Pt(111) substrate by such strain induced processes is presented by Brune [33]. This mode is also common in metal/semiconductor systems [34].

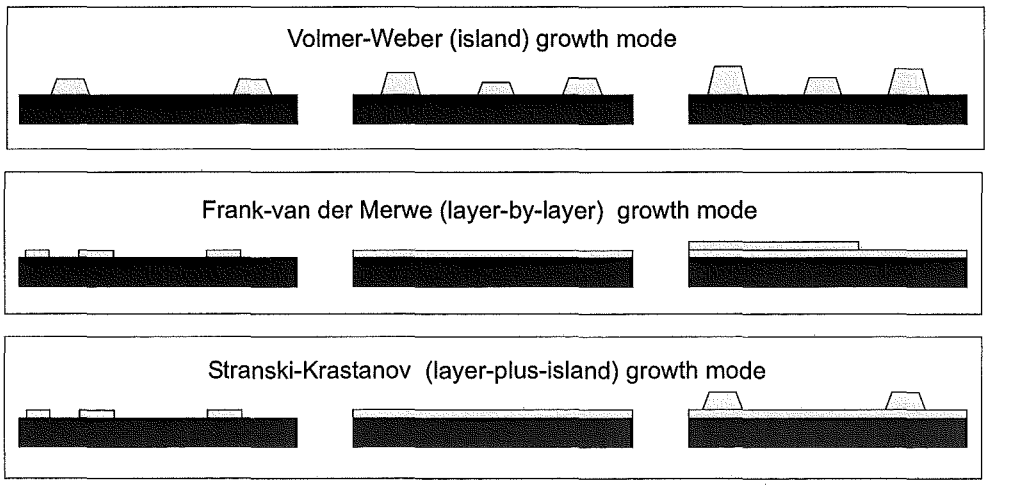

Figure 2.1: The three modes of crystal growth.

2.2 Atomistic Growth Processes

The thermodynamic description of film growth in the previous Section assumed that the system was close to equilibrium. However, this is generally not the case during vapor deposition, since the kinetics of particle diffusion (and subsequent

dynamic processes) must also be considered. Excellent reviews and introductions to atomic-scale growth mechanisms are presented for example by Zhang and Lagally [12], and Brune [8, chap 3], amongst others.

This Section begins with a description of the deposition of particles on the substrate surface and their subsequent diffusion. Island nucleation is discussed in Section 2.2.3, with emphasis placed on the effects of altering the experimental conditions. Section 2.2.4 considers island aggregation. Here, the competing thermodynamic and kinetic effects are addressed with regard to the island morphology.

2.2.1 Deposition

The first stage of thin film growth is deposition. Atoms are deposited on the substrate with flux F, which defines the rate of impingement to the surface and is usually expressed in [Å/s].[1] The deposited dose of material is defined as the coverage and is usually expressed in units of mono-layers (ML), where 1 ML is arbitrarily defined as the average inter-atomic distance in a bulk sample of the material. The energy of the atomic vapor is generally assumed to be low enough that no damage to the substrate occurs upon deposition, otherwise the elementary growth processes will be impeded by defect sites [36].

The flux has an enormous influence over the morphology of the islands. It controls the balance between thermodynamics and kinetics, so will be a dominant factor in determining the degree of departure of the system from equilibrium. Altering the flux can shift the delicate balance of all subsequent elementary growth processes, as will be discussed in Section 2.2.4. Note that the substrate temperature is also a critical parameter, however only room temperature studies are presented in this thesis.

Figure 2.2 illustrates the elementary processes active on a substrate (assumed to be defect free for simplicity) during deposition. Adatoms impact the substrate at a random surface position. Some adatoms may evaporate from the surface, some may bond sufficiently that they become immobile, and the remainder begin to migrate along the surface. Diffusing adatoms encounter and may bond with other wandering adatoms, this process is called nucleation, and results in island formation. Diffusion of adatoms to the island boundaries cause the island to grow in size, and aggregation becomes active. There are now two processes competing to capture the deposited atoms: the nucleation of new islands, and the growth of existing islands.

[1] It is also worth mentioning that many studies have been performed with the deposition of preformed clusters, which subsequently diffuse and aggregate into islands, via similar processes as atomic deposition. A comprehensive review is given by Jensen [35].

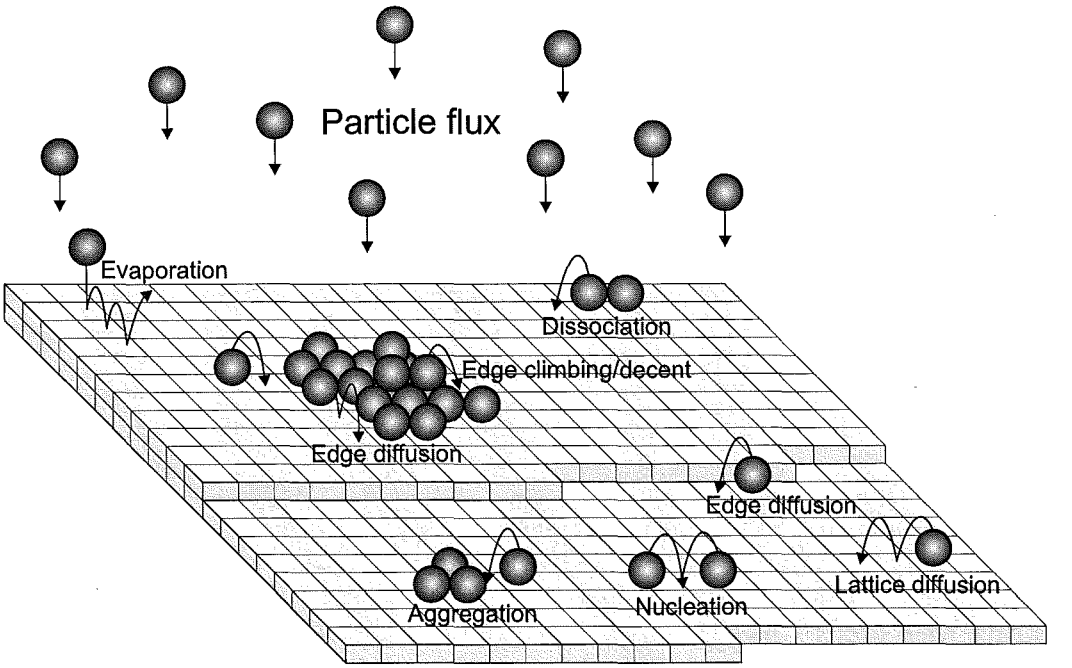

Figure 2.2: Diffusion processes on a substrate during thin film growth from the vapor phase. Particles are deposited on the substrate, and then begin the process of lattice diffusion. An adatom's diffusion comes to an end when it either evaporates from the surface, collides with another migrating adatom to nucleate an island, or finds an existing island and contributes aggregation.

2.2.2 Diffusion

At an atomic level no substrate is perfectly uniform, due to the ordering of surface atoms (the atomic lattice [1, p 8]). The discrete lattice atoms produce a series of peaks and troughs in potential energy that act as sinks for trapping adatoms. An atom incident on the substrate will occupy a specific site corresponding to a potential energy minimum. Figure 2.3 illustrates the barrier for lattice diffusion experienced by an adatom attempting to migrate from site 1 to site 3 (Figure 2.3(a)). Figures 2.3(b) and (c) show a potential energy schematic for motion perpendicular, and parallel (respectively) to the substrate.

Diffusion is activated when an adatom has sufficient thermal energy to overcome the difference in potential energy minima of site 1 and site 2, denoted as E_d. The diffusion process is hence comprised of a series of thermally activated jumps, mostly between adjacent lattice sites. The thermal energy is provided by the phonon field, which is essentially the vibrational energy of the lattice. If the diffusing atom remains at its new site after a jump for a time longer than the periods of the vibrational modes associated with with the jump, it will lose its energy to the phonon field and hence thermally equilibrate with the surface. The adatom then loses all memory of the direction from which it traveled, consequently

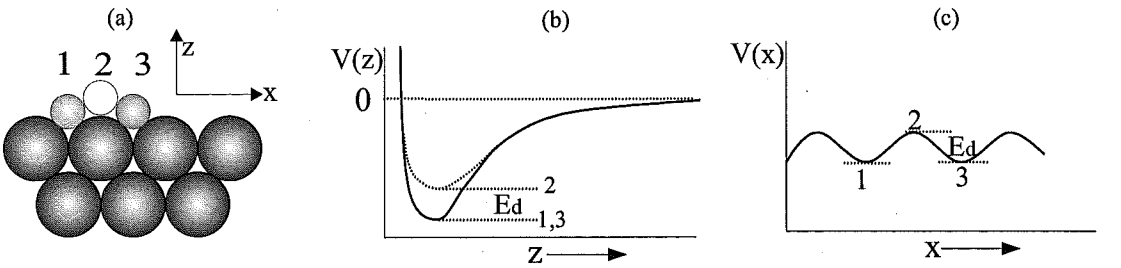

Figure 2.3: (a) Illustration of an adatom hopping between two adjacent lattice sites (labeled 1 and 3). The Z axis is perpendicular to the substrate surface, the X axis is oriented parallel to the substrate. The large spheres represent substrate atoms, and adatoms are depicted by small spheres. (b) Potential energy schematic for motion parallel to the substrate, E_d represents the energy difference between sites 1 and 2 (or 3 and 2). (c) Potential energy schematic for motion perpendicular to the substrate, E_d is again indicated.

the next jump is equally likely to occur in all directions. This type of motion is Brownian in nature [37, chap IV], and results in random 2D walks with no directional preference.

A diffusion coefficient provides a way of quantifying the adatom migration speed, which is in turn dependent on the potential energy barrier described in Figure 2.3. Two definitions for a diffusion coefficient exist [36]. The first describes the collective motion of an ensemble of interacting particles, and is commonly referred to as the chemical (or Fick's) diffusion coefficient. For such an ensemble of particles, it is assumed that the constitutive equation

$$\mathbf{J} = -D\nabla_{\mathrm{r}}\rho \tag{2.1}$$

holds. $\mathbf{J}$ is a diffusion current density and denotes the number of particles per second per unit line length diffusing past a reference line, D is the diffusion coefficient, and ρ is the density of adatoms. Equation 2.1 can be combined with the continuity equation

$$div.\mathbf{J} = -\frac{\partial\rho}{\partial t} \tag{2.2}$$

to obtain

$$\frac{\partial\rho}{\partial t} = D\nabla^2\rho \tag{2.3}$$

assuming D is isotropic (if this is not the case, Equation 2.3 can be written as a matrix equation) and independent of concentration. Equation 2.3 is commonly called Fick's second law.

The second definition applies to the motion of an individual particle, and is known as the tracer diffusion coefficient. For this case, the diffusion coefficient is proportional to the mean square displacement of a single atom executing a random walk, per unit time.

We know from statistical thermodynamics [38] that for an individual particle participating in a random 1D walk

$$\langle \Delta x(t) \rangle \equiv \langle x(t) - x(0) \rangle = 0 \tag{2.4}$$

and

$$\langle |\Delta x|^2 \rangle = a^2 N(t) \tag{2.5}$$

where $N(t)$ is the number of jumps taken in time t and a is the jump length. Extending this to 2D, and assuming jumps in the x and y direction are are independent of each other, we obtain

$$\begin{aligned} \langle (\Delta r)^2 \rangle \equiv \langle |r(t) - r(0)|^2 \rangle &= a_x^2 N_x(t) + a_y^2 N_y(t) && (2.6) \\ &= a^2 N_{tot}(t) && (2.7) \end{aligned}$$

if $a_x = a_y$. $N_{tot}(t)$ can be redefined in terms of an effective atomic jump frequency, ν_{eff} (which is related to the atomic vibration, and is typically of order 10^{12} Hz), giving

$$\langle (\Delta r)^2 \rangle = a^2 \nu_{\text{eff}} t \tag{2.8}$$

The tracer diffusion coefficient, D is now defined by

$$\langle (\Delta r)^2 \rangle = 4Dt \tag{2.9}$$

where the factor of 4 is associated with 2D motion, for 1D motion this factor is 2. Combining Equations 2.9 and 2.8 gives

$$D = \frac{1}{4} a^2 \nu_{\text{eff}} \tag{2.10}$$

An Arrhenius form is assumed for the effective jump frequency, which can be defined in terms of a jump attempt frequency, ν (derived from transition state theory [36]), and the activation energy for lattice diffusion E_d, to yield

$$\nu_{\text{eff}} = \nu \exp\left(\frac{-E_d}{k_B T}\right) \tag{2.11}$$

The tracer diffusion coefficient then becomes

$$D = D_0 \exp\left(\frac{-E_d}{k_B T}\right) \tag{2.12}$$

with

$$D_0 = \frac{1}{4} a^2 \nu \tag{2.13}$$

The diffusing adatom concentration on a substrate is low enough for most experimental growth rates that the interaction range for atoms diffusing on a substrate is small in comparison to the mean inter-particle distances [39], [40]. It is therefore a valid approximation to use the tracer diffusion coefficient to describe diffusion behavior for most systems in the sub-monolayer regime, and it is the tracer coefficient that we have in mind when referring to the diffusion coefficient in the remainder of this thesis.

2.2.3 Nucleation

The formation of stable islands is an accumulative process that is initiated by the nucleation of two diffusing adatoms. This dimer then serves as a diffusion trap for other adatoms. The lateral bond energy, E_b of these two atoms is a dominant force in determining if the dimer is stable. If either atom possesses an energy, E_s greater than the sum of the diffusion energy and the lateral bond energy, dissociation will be the dominant process (illustrated in Figure 2.2), and the island is termed unstable. Islands above a critical size will grow by aggregation, since as the number of lateral bonds increase, growth becomes more probable than decay. The critical island size, i (in units of numbers of adatoms) is defined here as the size of an island which requires only the addition of one more adatom to become stable. A stable island is therefore denoted by $i+1$, and j expresses every other island size, stable or otherwise.

The Critical Island Size

The critical island size has its conceptual foundation in the framework of thermodynamics [41]. The large surface to volume ratio of small clusters results in a positive free energy ΔG, which is strongly dependent on cluster size [42]. This is illustrated qualitatively in Figure 2.4. A rigorous mathematical treatment can be found in Kern [43].

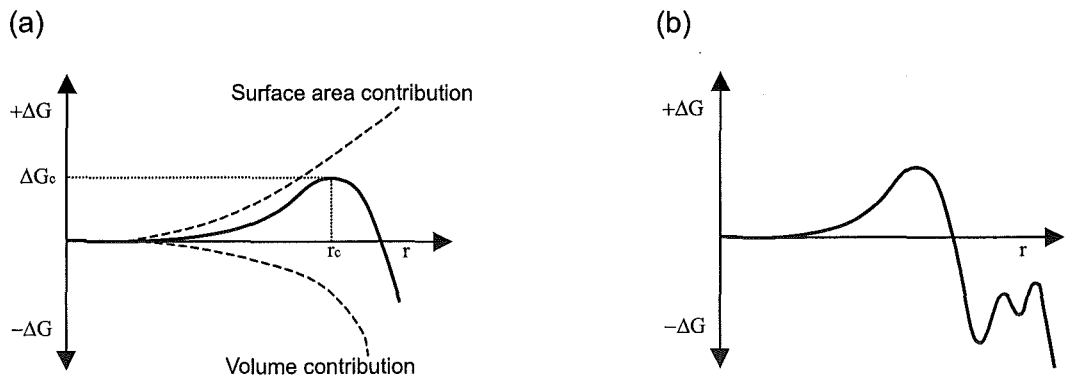

Figure 2.4: Schematic of an island's free energy change, ΔG as a function of island radius, r. (a) Curve showing contributions to the free energy from the surface area (positive) and volume (negative) of the island. r_c and ΔG_c denote the critical island size (radius) and free energy respectively. (b) Plot depicting the oscillation in free energy as a function of island size.

The free energy of formation of the cluster increases until it reaches some maximum value at the critical island radius, r_c corresponding to an island size of $j = i$. The form of the curve depicted in Figure 2.4(a) reflects a contribution to the enthalpy of formation, ΔH from two competing terms. As the cluster grows,

the number of atomic bonds increase, resulting in a negative (favorable) term contributing to ΔH. The magnitude of this term scales with the volume (or area in the 2D regime) of the cluster. The surface area (or perimeter in the 2D case) also increases as the cluster grows, contributing a positive (unfavorable) term to ΔH. Initially the surface area of the the cluster is large in relation to its volume, and the positive term dominates, resulting in an unstable cluster that rapidly decays. When the cluster reaches the critical radius, it has the maximum surface energy to volume energy ratio, and is therefore at the most unstable size.

As the cluster continues to grow the volume term related to the inter-particle bonding increases and rapidly dominates the free energy. Clusters of size $j > i$ have a tendency for growth rather than decay. It should be noted that even stable islands may experience some dissociation, however this occurs on a time scale that is much less than the rate of adatom arrival, and growth dominates. Figure 2.4(b) shows that the free energy curve features local free energy minima, which correspond to the most stable cluster sizes. This thermodynamic description of the critical island size is a simplified account based on a continuum-type picture. A more thorough description, and references to other discussions of the critical island size can be found in Chang and Thiel [42, p 285].

We now consider the mechanisms of nucleation and growth of clusters above the critical size, and how they contribute to the films morphology. The critical island size will vary for different adatom-substrate combinations, and is dependent on many factors, including substrate temperature and adatom-substrate bonding [44]. In the following discussion however, we assume that the critical island size is given by $i = 1$, i.e. the critical island size is a monomer, therefore adatom dimers will be stable. In addition we impose the restriction that all stable islands are immobile. This gives a simplified view of nucleation and growth, but is nonetheless useful for the purposes of gaining an insight into the fundamental processes.

Evolution of Island Density With Coverage

We can consider three principle regimes of nucleation and growth, which are depicted by the three shaded areas in Figure 2.5(a). In the first regime, diffusing adatoms collide with one another and nucleate islands comprised of immobile adatom dimers, resulting in a rapid increase in the nuclei density. As deposition proceeds the number of diffusing adatoms becomes comparable to the number of nucleated dimers. At this stage of film growth, an adatom is just as likely to encounter an existing nucleus as it is to meet another adatom, and the growth of existing islands begins to dominate over the formation of new nuclei. Eventually most migrating adatoms will be captured by existing islands, and the island density reaches saturation, N_s. The competition for adatoms from nucleation and growth is now completely dominated by growth (second regime). As the

coverage is increased further, the islands will grow large enough that they coalesce with neighboring islands, and the island density begins to decrease as the film percolates (third regime).

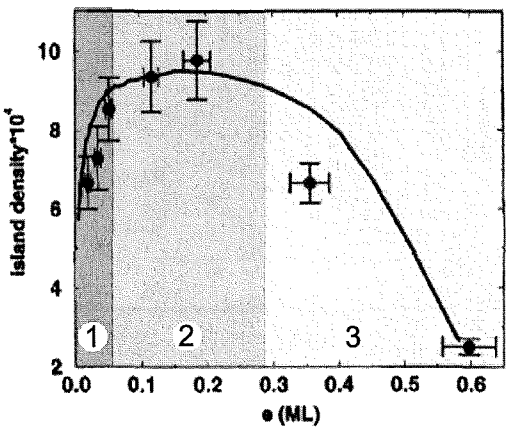

Figure 2.5: Plot of the evolution of island density as a function of coverage [35]. The three regimes of nucleation (depicted by the shaded regions) have been superimposed over the plot. Note that this plot shows results for Sb_{2300} cluster diffusion and nucleation, it was chosen because it clearly (and simply) demonstrates all three regimes in a single plot, however similar results for atomic diffusion can be found in Donohoe and Robins [45] and Brune [46].

Evolution of Island Density With Flux

Adjusting the deposition rate shifts the balance between the competing processes of diffusion and nucleation. Increasing the flux increases the likelihood that a wandering adatom will encounter another of its kind, rather than an existing island, resulting in a higher density of smaller aggregates. Conversely, lower fluxes result in a lower density of larger islands, since a migrating adatom is more likely to encounter an existing island than to nucleate a new one. This is shown schematically in Figure 2.6(a). An example of the flux scaling of N_s is depicted in Figure 2.6(b), where it is clear that higher fluxes increase the island density.

Mean field nucleation theory [48] relates N_s to the diffusion coefficient and the flux by

$$N_s \propto \left(\frac{D}{F}\right)^{-\chi} \tag{2.14}$$

Experimentally, the scaling exponent is given by the slope of the log-log graph of N_s as a function of flux. The value obtained for χ reveals information pertaining to the types of processes that are occurring on the substrate. For example, island growth simply from diffusion and nucleation with $i = 1$, yields a value of $\chi \sim 0.3$, where as $\chi \sim 0.7$ if evaporation is appreciable [35]. This will be discussed further in Chapter 6, when the flux scaling of the saturated island density is investigated in the Bi/HOPG system.

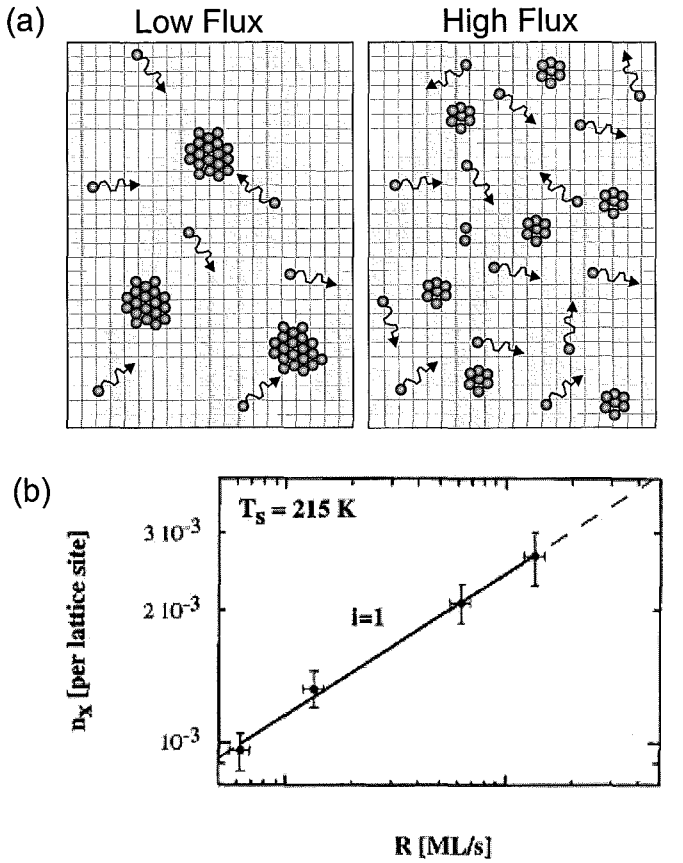

Figure 2.6: (a) Schematic illustration of the effect of flux on the island density, the left image shows the low flux case, the right image depicts the high flux regime. (b) Flux scaling of the saturated island density (Cu/Ni(100) [47]).

Plots of the flux dependence of N_s also provide a useful check that nucleation is not occurring predominantly on defect sites. If defect nucleation dominates, N_s will be independent of flux, and the natural diffusion and nucleation behavior of the adsorbate cannot be studied.

Evolution of Island Density With Temperature

Although all the experiments in Chapters 5 and 6 are performed at room temperature, an outline on the effect of system temperature is given here for completeness.

Elevated temperatures allow adatoms to more easily overcome the energy barrier for lattice diffusion, increasing the diffusion speed (and the diffusion coefficient). Consequently, a migrating adatom is more likely to encounter an existing island before another adatom is deposited in its vicinity, providing an opportunity for nucleation of a new island. The result is a lower overall density of stable islands, which also tend to be larger. Conversely, lower temperatures produce a higher density of smaller stable islands.

Plots of the temperature scaling of the island density allow determination

of the energy barrier for lattice diffusion. Figure 2.7 shows an example of such a graph for the Ag/Pt(111) system [49]. In this system (and temperature window), $\chi = 1/3$. Combining Equations 2.12, 2.13 and 2.14, and substituting in $\chi = 1/3$, yields $N_s \propto (F\nu_0)^{1/3}\exp(E_d/3kT)$. Therefore, the diffusion barrier for Ag adatoms on a Pt(111) substrate can be obtained from slope of the graph, and is found to have the value $E_d = 157 \pm 10$ meV [49].

Note that at sufficiently low temperatures, the temperature scaling of the island density will deviate from the linear form shown in Figure 2.7. In the low temperature limit, adatoms diffuse too slowly to meet each other and monomers are frozen on surface ($i = 0$), N_s then becomes independent of temperature [47].

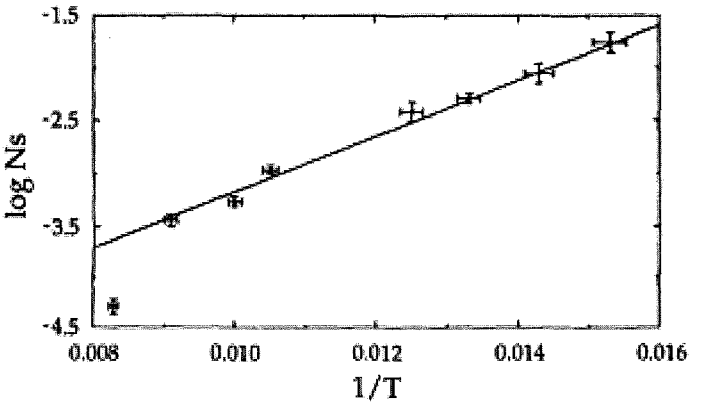

Figure 2.7: Temperature scaling of the saturated island density (Ag/Pt(111) [49]).

2.2.4 Aggregation

We now consider the growth of stable nuclei into islands, and in particular the processes governing pattern formation in diffusion mediated island growth. The enormous variety of structures observed in thin film growth implies that there are many different mechanisms involved in their formation. This Section aims to expand on the elementary growth processes, and review the historic development of models to describe island growth.

Non-equilibrium Phenomena and Morphogenesis

In an equilibrium environment, there is an expectation for the formation of compact structures on the substrate [48], [50], consistent with the thermodynamic condition of minimization of surface energy [51]. For crystalline materials, the free energy of a surface depends strongly on its crystallographic orientation [52]. Consequently, the equilibrium form is often characterized by compact polygonal shapes.

The continuous diffusion of adatoms to an island's growth front tends to

drive the system away from this minimization of free energy, and the state that prevails is not necessarily the most stable, but is kinetically determined. The consequence is the formation of crystals that are often more faceted than their equilibrium form, or even irregular and dendritic structures [53] (and refs. therein). Each type of structure is a signature of a complex balance between kinetics and thermodynamics, and represents an intricate array of inter-atomic processes. A classic and well studied example of non-equilibrium crystal growth is the Au/HOPG system [16], [54], [55], [56], [57]. Dendritic growth usually prevails, even though the equilibrium form of Au crystals on graphite is known to be that of a truncated sphere with limited facets [58].

The non-equilibrium structures observed in thin film growth often represent striking examples of spontaneous pattern formation (Morphogenesis). They also bare resemblance to other patterns observed in nature [59]. Figure 2.8 shows four examples of spontaneous pattern formation in other non-equilibrium systems (bacterial growth, electrochemical deposition, snowflake growth, and viscous fingering), where the similarity between the forms is obvious. Extensive investigations of the common processes linking non-equilibrium growth in different systems has been performed over the the last two decades, most notably by Ben-Jacob and co-workers (see for example refs.[60], [61], [62], [63]). The key feature is a competition between a stabilizing and a destabilizing influence over the growth process [64], which will be described further in Chapter 5, where we discuss results for Sb/HOPG.

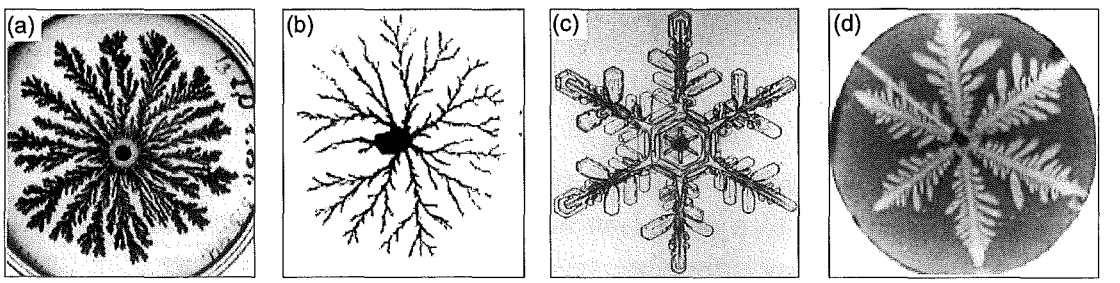

Figure 2.8: Spontaneous pattern formation. (a) The growth of bacterial colonies [65], (b) electrochemical deposition [61], (c) snowflakes [66], (d) viscous fingering in hydrodynamics [62].

Diffusion-Limited Aggregation

Many of the models used today to describe pattern formation in island growth originate from the early work of Witten and Sander [67], who interpreted and modified Eden's biological model of diffusion limited growth [68]. Eden's model has a single particle placed at the center of a square grid. Subsequent particles are individually attached at random positions on the perimeter of the structure formed in the previous step. This model has no provision for diffusion of particles,

and every perimeter position is equally likely to grow at each step. Consequently the Eden structures tend to be compact and circular, as depicted in Figure 2.9(a).

Witten and Sander recognized the potential for utilizing this random deposition model to explain fractal geometries observed in natural processes such as dust and soot formation [69], and structures formed at surfaces during thin film growth. Their motivation was due, in part to the observation that coagulated aerosols are aggregates characterized by a wispy appearance, and that diffusion of particles to the surface is often the rate limiting step in aggregation. Forrest and Witten's earlier work on smoke-particle aggregates [70] revealed that such aggregates were of a size that far exceeded the extent of their forces, and that the particle density had long range correlations. This long range density correlation, $\rho(r)$ was reminiscent of other systems, such as the second order phase transition of a fluid near its liquid-gas critical point, which obeys a characteristic power law of the form

$$\langle \rho(r)\rho(0)\rangle - \langle \rho(0)\rangle^2 \propto r^{-A} \tag{2.15}$$

over a large range of r. The exponent A is referred to as anomalous, since it is not simply a fraction arising from dimensional considerations. It also tends to be unaffected by variation of the systems parameters (universality).

Witten and Sander's growth model is called diffusion limited aggregation (DLA). It is of central importance to note that this model is away from equilibrium and is defined kinetically, in the sense that the aggregates do not conform to shape restrictions imposed by the thermodynamic demand of minimum free energy.

A schematic of a DLA simulation is illustrated in Figure 2.9(b). Eden's seed particle is retained, however the particles are now dropped at random positions on a square lattice. They are prohibited from landing directly on the aggregate, so that adatoms perform random walks across the surface to reach the structures perimeter (growth front). The first atom is dropped and allowed to diffuse until it is either stopped by the seed particle, where it irreversibly sticks, or wanders off the boundary of the lattice. Another particle is then randomly deposited and the process repeats.

The aggregates' morphology is typically modeled with Kinetic Monte-Carlo (KMC) simulations, which use an algorithm to calculate the evolution a complex system for a large (but necessarily finite) number of simultaneous random processes. Essentially the motion of individual adatoms and their interaction with aggregating islands are simulated, enabling the final morphology to be observed. Simulations of DLA revealed the formation of ramified fractal structures (Figure 2.9(c)) that were dilation symmetric[2] [71], like the smoke aggregates. This

[2]If a structure is viewed with a resolution coarser than the size of the aggregating particles and is found to have no natural length scale, then it is said to be scale invariant or dilation symmetric.

ramified appearance is a direct consequence of the random nature of Brownian motion. The exposed branches grow more rapidly than the interior, since they act as shields, capturing the majority of adatoms before they can migrate to the structures interior.

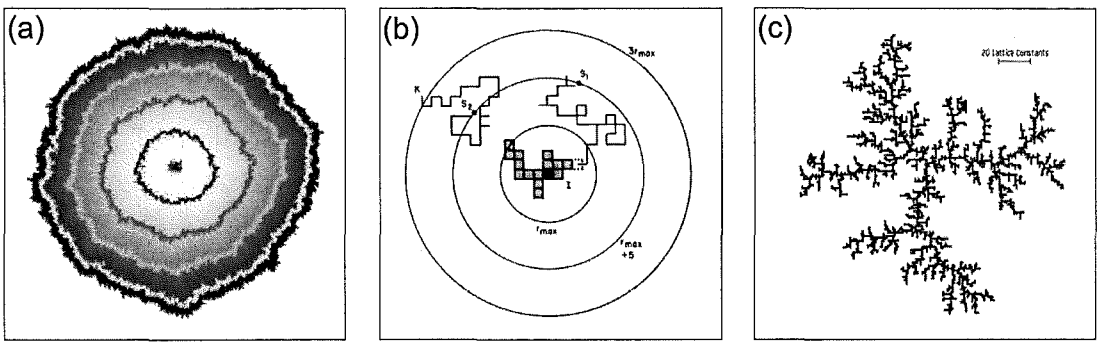

Figure 2.9: Growth Models. (a) Eden's biological growth model [72], the circular contours depict the aggregate morphology at various time scales of deposition. (b) Schematic of of the DLA model [73]. A seed particle is placed at centre of a grid (black dot in image centre). Adatoms are then placed at random positions on the surface (sites S_1 and S_2) and allowed to diffuse with Brownian motion (depicted by the multi-directional traces attached to S_1 and S_2). Their diffusion ends when they either wander off the lattice (particle S_2), or hit the seed particle and contribute to island growth (particle S_1). (c) An example of an aggregate formed with a DLA simulation [71].

The model aggregates generated by DLA also have density-density correlations conforming to a power-law relationship of the form

$$N^{-1}\sum_{r'}\langle\rho(\vec{r'})\rho(\vec{r'}+\vec{r})\rangle \propto r^{-A} \tag{2.16}$$

Equation 2.16 holds over distances ranging from a few lattice sites to almost the size of the cluster. The density $\rho(\vec{r})$ at position $\vec{r}$ is defined to be 1 for an occupied site, and 0 for an unoccupied site, and N represents the number of atoms in the cluster. The exponent A is related to a factor called the fractal (or Hausdorff) dimension f_D, by $A = d - f_D$ where d is the euclidean space dimensionality of the structure. The fractal dimension describes the extent of ramification of an aggregate. The area of an aggregate increases as $area \propto r^{f_D}$, so a filled-in circle would have a trivial dimension of 2. For 2D growth Witten and Sander found that $f_D = 1.7$, so that the projected surface area of an aggregate increases as $area \propto r^{1.7}$.

Inherent to the DLA model is the irreversible sticking of atoms to the aggregate. If this is applied in the strictest sense, diffusion along the edges of the aggregate is completely prohibited, which accounts for the coarse branch like arms of the structure. The mechanisms responsible for this ramified growth can be understood in terms of the Langer and Müller-Krumbhar model of dendritic crystal growth [74]. In this model an instability in a simple system generates complex, yet highly ordered new systems. They consider crystal growth where

a solid phase grows in the direction of an axis of symmetry into a uniformly super-saturated or super-cooled liquid. The rate controlling process here is either chemical or thermal diffusion. The migrating 2-phase boundary develops instabilities associated with random fluctuations in the diffusion field. This produces troughs and peaks which grow in amplitude as the boundary advances, resulting in the formation of side branches. Langer and Müller-Krumbhaar discovered that a smooth interface, like a phase boundary, is unstable against these perturbations at all length scales, and that its growth depends on fluctuations in the diffusion field.[3]

The DLA model is essentially the discrete counterpart to dendritic crystal growth [71], in the limit where these fluctuations are dominant. Deformations in the advancing aggregate boundary capture a larger number of diffusing adatoms than any straight edge sections. If these atoms can not be transported away from the deformity sufficiently fast, then branch growth will prevail. This is of course the case for DLA, where edge diffusion is frozen and adatoms permanently attach at the position where they impinge on the island perimeter. These new branches eventually become susceptible to the same instabilities, due to exposure of the tips to an increasing portion of the diffusion field, producing more branches. This continual ramification leads to the self similarity of the DLA structures, and a fractal dimension of 1.7, which is independent of the adatom species.

Island Edge Diffusion

In real systems it is usually the case that atoms are able to diffuse around the perimeter of an island (edge diffusion), or may not stick on first contact with the aggregate. This situation becomes particularly important at elevated temperatures, and results in shape relaxation for structures that were formed in a predominantly kinetic regime. The degree of edge diffusion will play an important role in determining whether compact morphologies (the thermodynamic tendency) or ramified structures (the kinetic influence) prevail.

The rate of edge diffusion around the perimeter of an aggregate is usually anisotropic. This is because the energy barrier for mobility is dependent on the number of bonds that must be broken and the number of bonds that would be conserved in an adatoms site to site transit [76]. The rate of diffusion along the edge of the island can be expressed as

$$D_{edge} = Dexp\left(\frac{-mE_b - nE_n}{k_B T}\right) \tag{2.17}$$

where:

m is the number of bonds that will be broken by the transit

[3] This is also discussed in the absence of crystal anisotropy, in a 1963 paper by Mullins and Sekerka [75].

E_b is the bond energy (positive for bond forming, negative for bond breaking)

n is the number of unbroken bonds during the move

E_n is the barrier energy per bond

D is the diffusion coefficient (from Equation 2.12) for diffusion across the substrate

Figure 2.10 illustrates the diffusion rates for various edge environments. An adatom will tend to migrate to a site that maximizes its number of nearest neighbor bonds, resulting in shape relaxation. However, the diffusion asymmetry imposed by the ordering of the island periphery atoms often hinders this process. An adatom at site 6 will have an equal probability of relaxing to 7 or 5, however if an atom occupied site 9, diffusion to site 8 would be the preferred direction. Also note the low probability of diffusion for an adatom attempting to migrate around a kink site (site 8 to 9).

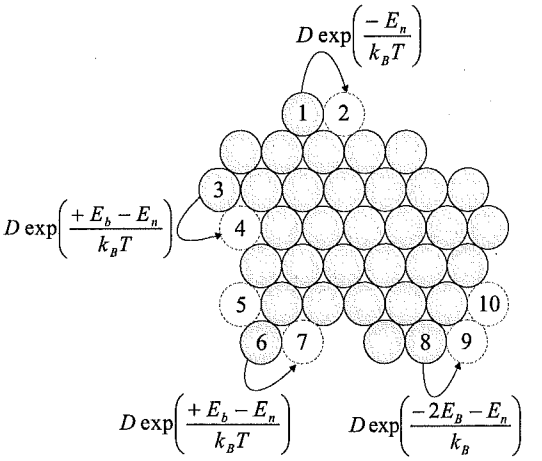

Figure 2.10: Island edge diffusion.

Various workers have explored the results of allowing a non-unity sticking probability. Meakin [73] was one of the earliest in his 1983 paper. He noted that in real systems there was a possibility that diffusing particles may be repelled from the island at short distances, or may not stick on contact. Curiously, Meakin found that altering the sticking probability from 1 to 0.1 had little effect on fractal growth, with no modification to the exponent A in Equation 2.16, and so the fractal dimension retained the value of 1.7. It was noted however, that smaller sticking probabilities lead to a thickening of the branch arms of the classical DLA aggregates from KMC simulations.

Hwang *et al* [77] found experimentally, that for Au on Ru(0001), highly dendritic structures form at room temperature. Thickening of the branches

became pronounced upon annealing, indicating non-unity, or coordination dependent, sticking probabilities. From a dimensional analysis study, they found that $f_D = 1.72 \pm 0.07$, in accordance with Meakin's predictions. For this reason, a system with a limited degree of edge diffusion, but still exhibiting the classical DLA fractal dimension, is generally categorized within the DLA model.

Qualitatively, as well as quantitatively, there is a vast difference between limited, and rapid edge diffusion. Limited edge diffusion may still produce ramified aggregates. Conversely, rapid edge diffusion may result in structures that reside within the equilibrium realm, particularly when the adatoms possess sufficient energy to easily overcome all the different types of edge diffusion barriers [78]. Bales and Chrzan performed KMC simulations of island growth from an analysis of numerical solutions to rate equations [79]. Atoms that deposit on top of an aggregate are incorporated into the inner sections of the island. They also note that the activation barrier for detachment of an atom from an island is generally much higher than the barrier for diffusion along an island edge (purely from a bond counting point of view). Their results are presented in Figure 2.11. The flux and coverage is held constant, while the systems temperature is varied. It is obvious that for rapid edge diffusion, the system no longer resembles the classical DLA structures. The island morphology is now governed by competition between edge diffusion, and the destabilizing influence of the random diffusion field.

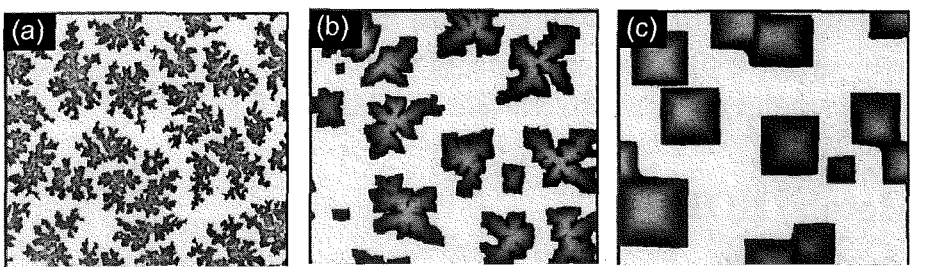

Figure 2.11: Regimes of edge diffusion, E_D denotes the barrier to edge diffusion [79]. (a) $T = \frac{E_D}{16}$, edge diffusion is partially frozen. (b) $T = \frac{E_D}{14}$, appreciable edge diffusion. (c) $T = \frac{E_D}{10}$, rapid edge diffusion.

An increase in the temperature of a system allows edge atoms to more easily overcome diffusion barriers, resulting in enhanced edge diffusion and shape relaxation. Reducing the deposition flux has an analogous effect. In this case, more time is available for adatoms to overcome the diffusion barriers before the next particles arrive from the diffusion field and pin them in place, again leading to more compact shapes. A KMC simulation of island growth demonstrating these two effects is shown in Figure 2.12.

The effect of edge diffusion on island morphologies has been extensively explored in experimental systems (see for example Au/Pt(111) [81] and Pt/Pt(111) [82]), with KMC simulations (see for example Zhong *et al* [78] and Liu *et al* [83]), and using a combination of experimental and KMC simulation analysis (see for

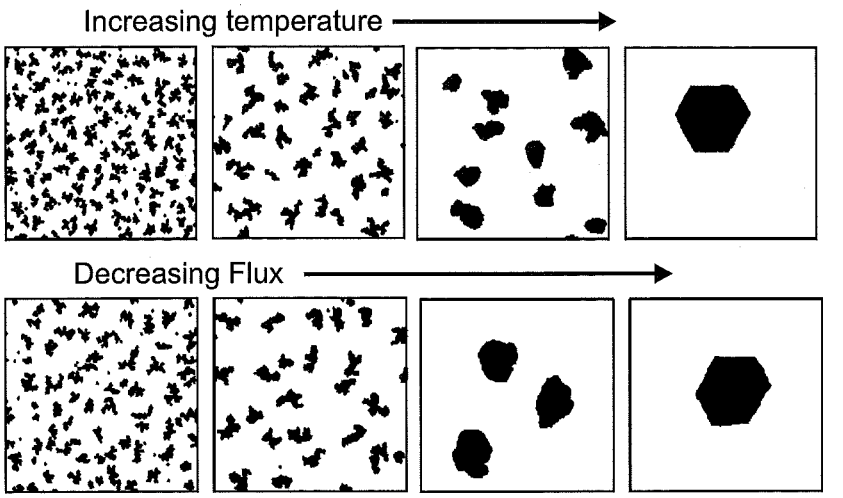

Figure 2.12: KMC simulations of the effect of temperature and flux on island morphologies, reproduced from ref.[80]. The top panel shows the effect of increasing the systems temperature, the bottom panel demonstrates the analogous effect of reducing the deposition flux.

example Ag/Pt(111) [84]). In all these cases ramified structures are found in low temperature regimes, where the kinetics of diffusion is the driving force, and compact islands for higher temperatures, where local atomic rearrangements within the island allow for relaxation to compact polygonal shapes.

The discussion in this Section has been limited to growth of 2D islands, because the results of the present work are mainly 2D. Islands may also grow vertically by upwards diffusion of atoms, or by the direct impingement of atoms. These effects are discussed where relevant in Chapters 5 and 6.

2.3 Metals/HOPG

We now depart from a general description and review of island growth and mechanisms for pattern formation in various systems, and focus on a review of metals aggregated on HOPG substrates. This is by no means an exhaustive account, but is rather designed to give a feel for the types of structures that are often observed on HOPG. Comparisons of the Sb/HOPG and Bi/HOPG morphologies, with other systems will be discussed in more detail in Chapters 5 and 6.

We begin with an overview of Sb_4 diffusion and aggregation on HOPG. Particular emphasis is placed on the work by Kaiser and Stegemann (and co-workers) ([19], [20], [14]), since this will be compared in detail to our film morphologies in Chapter 5.

2.3.1 Sb/Graphite

In 2002 Kaiser *et al* [19] reported on self-organized growth in the Sb/HOPG system, where it was found that several examples of pattern formation existed within the same system, as reproduced in Figure 2.13. Small compact (almost spherical)

particles were observed at low coverage (Figure 2.13(a)), which undergo a transition to fingered morphologies with increasing island size (Figure 2.13(b)), and eventually small faceted crystallites in the high coverage limit (Figure 2.13(c)). Dendritic, and even needle-like morphologies were observed at low deposition rates (Figure 2.13(d)).

The compact particles were reported to be amorphous and the fingered islands are crystalline with different orientations within individual islands. Certainly it is clear that the Sb/HOPG system presents an interesting case of spontaneous pattern formation on the nanoscale, with the morphologies able to be tuned with deposition parameters. In a review-type paper, Kaiser and Stegemann [20] again report on these morphologies, including a transmission electron microscope image of the fingered morphologies, which clearly shows bending contours associated with a strained crystal structure.

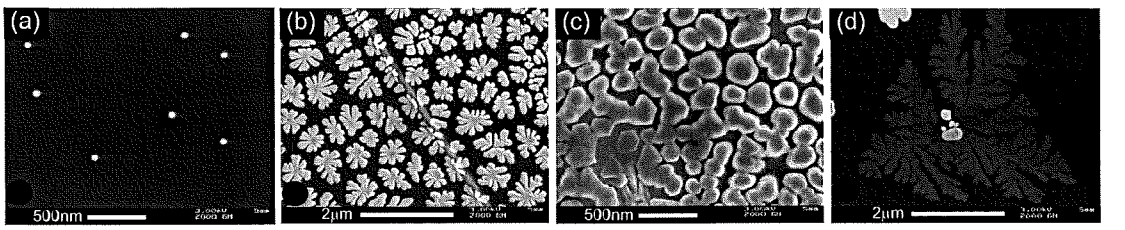

Figure 2.13: Spontaneous pattern formation in the Sb/HOPG system [19]. (a) Small almost spherical particles. (b) Fingered morphologies. (c) Small faceted crystals. (d) Dendritic structures. (note scale changes).

A comprehensive study of pattern formation in the Sb/HOPG system was reported by Stegemann *et al* [14] in 2004, expanding on the above results. Of particular note is the flux dependence of the island morphologies, as reproduced in Figure 2.14, showing a clear transition from fingered to very branched structures with increasing flux. This is consistent with increasing flux producing more ramified growth, discussed in the previous Section.

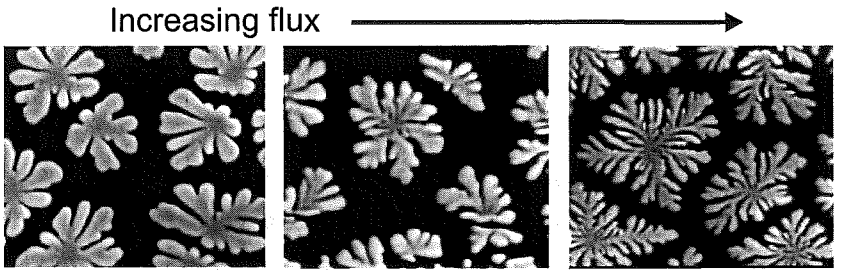

Figure 2.14: Flux dependence of the Sb island morphologies on graphite, reproduced from Stegemann *et al* [14].

Diffusion and aggregation of preformed Sb clusters on HOPG has also been studied by several groups (see for example refs.[85], [86], [15]). In those cases,

varying the cluster size introduces another controllable feature which alters the island morphology. Similar morphologies to those of the aggregates obtained with Sb_4 (the vapor phase of antimony) diffusion are observed. However, more ramified structures are formed with increasing the size of the deposited clusters.

2.3.2 Bi/Graphite

Room temperature growth of bismuth on graphite has been studied previously with atomic force microscopy [87]. Small elongated structures were observed to grow along the high symmetry directions of the substrate at a deposited coverage of 0.2 nm, as shown in Figure 2.15(a). Increasing the coverage to 80.3 nm resulted in almost complete coverage of the substrate with striped features, as shown in Figure 2.15. The angles of intersection of the stripe-like structures were most frequently observed at 60° and 120°, and occasional orientations of 30°, 90°, and 150°.

The authors note a high density of islands on the surface, and attribute this feature to nucleation on defect sites. They also present an argument for a growth mode with the bismuth basal plane parallel to graphite basal plane, which is assumed for all the observed structures. A comprehensive study of the morphology with varying experimental parameters was not performed, due to problems with the AFM tip causing damage to the structures.

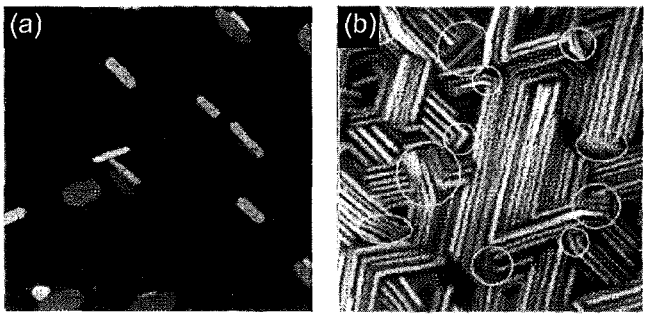

Figure 2.15: AFM images of bismuth on graphite [87], scan sizes are both 1 μm. (a) Coverage $\sim$ 0.6 ML. (b) Coverage $\sim$ 240 ML.

2.3.3 Au/Graphite

Studies of the morphology of gold islands on graphite have been performed almost continuously for the last 30 years (see for example refs. [55], [57], [56], [88], [17]). In 1975 a series of three papers [54], [89], [90] were published by Darby and Wayman, which reported on dendritic growth and the evolution of morphologies with varying experimental parameters. Figure 2.16(a) shows an example in which increasing system temperature leads to a compacting of the dendritic morphologies, and eventually compact polygonal shapes. Diffraction studies revealed that many of the dendrites were single crystal, and aligned with the high symmetry

directions of the (hexagonal) substrate. Figure 2.16(b) shows an example of the symmetry manifested in the dendrite shapes. The left image shows a 3-branch island, with the branches at 120° separations. The right image shows six branches separated by 60°.

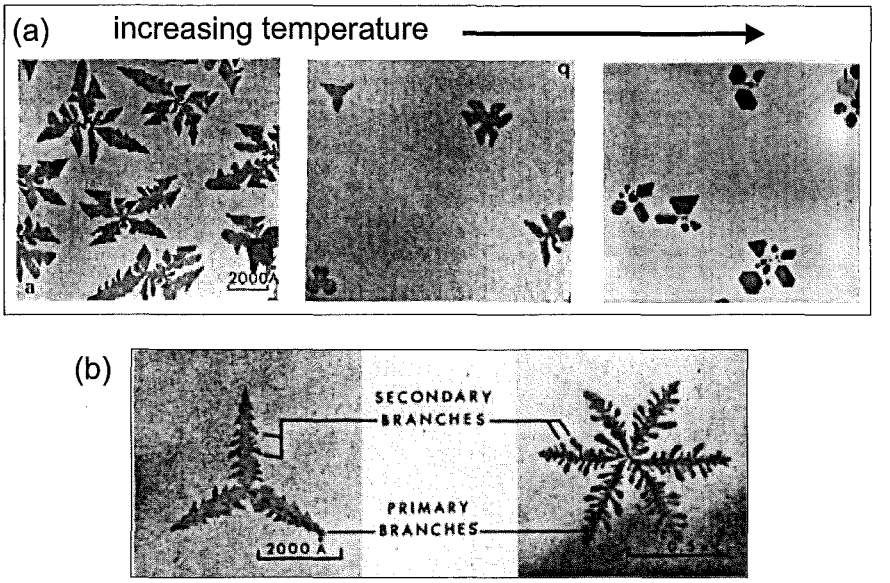

Figure 2.16: (a) Evolution of gold island morphologies with increasing system temperature [90]. (b) Symmetry in the gold dendrites [54].

More recently, *in situ* investigations of dendritic gold growth on HOPG were performed with transmission electron microscopy by Anton and Schneidereit [16]. This study focused on the kinetics of nucleation and growth with real time imaging, contributing to a greater understanding of the fundamental growth mechanisms. In particular, growth kinetics of individual aggregates were compared to a diffusion model, which gave a mean diffusion length of 400nm before adatom desorption, and an upper limit on the lattice diffusion barrier of 0.24 eV. A partner paper was published two years later which looked at the growth kinetics in an elevated temperature regime [91].

2.3.4 Ag/Graphite

Diffusion and growth of silver on graphite showed that natural step edges which form during the substrate cleaving process could be used to trap diffusing adatoms, forming quasi-one-dimensional chains of Ag nanoclusters, as shown in Figure 2.17. By altering the particle flux, nucleation occurred either entirely by defect trapping at the step edges (low flux) or with a combination of terrace and step edge decoration. Further examples of step decoration will be discussed in Chapter 6, where an investigation of the morphology of bismuth aggregates nucleated along step edges is presented.

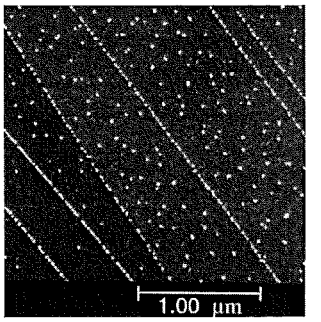

Figure 2.17: Silver on graphite [92].

2.3.5 Other Examples

Numerous other studies of island nucleation and growth on graphite substrates exist in the literature. Examples include Pd [93], Ni [94], Cu [17], Pt [95], Co [96], Cr [97], and Al [98]. A comprehensive account of the growth of transition metals on graphite is also given in ref.[99]. It should be clear by now that graphite is a popular choice of substrate for studying the fundamental growth processes in island formation.

2.4 Summary

The growth of surface islands during thin film deposition from the vapor phase is an inherently non-equilibrium process. A thermodynamic tendency to minimize the free energy of the system favors compact morphologies. However, the kinetics of particle diffusion to the structures' growth front often leads to dendritic and irregular island shapes. Deposition, diffusion, nucleation, and aggregation are simultaneous processes, the interaction of which determines the final morphology.

The non-equilibrium growth environment gives rise to some remarkable examples of spontaneous pattern formation on the nanoscale. Shapes as diverse as polygons, fingered islands, and dendrites have all been observed in thin film growth. Most models of island aggregation originate from the work of Witten and Sander who developed the concept of diffusion limited aggregation. In this model adatoms diffuse to the perimeter of an aggregate and stick irreversibly on contact. However, in most practical system, edge diffusion is also required to explain the experimentally observed morphologies. Morphology investigations of many adsorbate/substrate combinations have led to a greater understanding of diffusion mediated island growth.

Chapter 3

Experimental Description

This Chapter begins with a description of the bulk structure of graphite, antimony, and bismuth. The remainder of the Chapter is devoted to a discussion of the ultra high vacuum (UHV) system that was constructed for this project. Section 3.2.1 gives an overview of the procedure used for obtaining deposited samples. Next the chamber construction is discussed, followed by a discussion of the residual gas atmosphere and system baking. Section 3.2.4 explains the preparation of graphite substrates. The generation of a vapor beam via the system's crucible is described in detail in Section 3.2.5. The final Section summarizes the chapter.

3.1 Materials

This Section reviews the bulk crystallographic structure of HOPG, which is used for the substrate material, and bismuth and antimony, which are the two evaporant materials used in this project.

3.1.1 HOPG

The layered hexagonal structure of the graphite crystal is illustrated in Figure 3.1(a). The C–C bond distance within the layers is 1.42 Å. The layers themselves are separated by a distance of 3.40 Å, and held together by weak van der Waals forces. The layers are stacked in such a way that the stacking sequence repeats after 2 layers, as shown in Figure 3.1(b). When the graphite substrate is cleaved, it is the longer interlayer bonds which are broken, producing very flat and inert surfaces parallel to the basal plane.

3.1.2 Bismuth and Antimony

Bismuth and antimony both have a rhombohedral crystal structure (A7, space group $R3\overline{m}$), with cell constants

$$\begin{aligned} &\text{Sb:} \quad a_r = 4.51 \text{ Å}, \quad \alpha_r = 57°7' \\ &\text{Bi:} \quad a_r = 4.75 \text{ Å}, \quad \alpha_r = 57°14' \end{aligned}$$

and two atoms per unit cell, one at the origin and the other at position $2u, 2u, 2u$, where u has the values

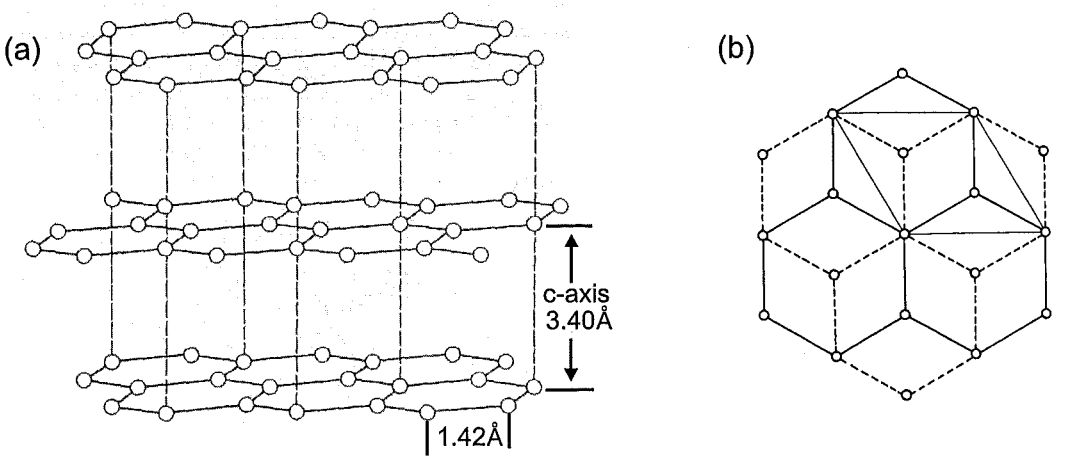

Figure 3.1: (a) The hexagonal layer structure of graphite (reproduced from The Crystal Structure of Solids [100]), broken lines link atoms of successive sheets which are in the same vertical columns. (b) The graphite structure viewed in projection down the c-axis (reproduced from The Structures of the Elements [101]). The solid lines link the top sheet, the dashed lines link the middle sheet of (a).

$$\text{Sb: } u = 0.233 \quad \text{Bi: } u = 0.237$$

The structure is comprised of puckered layers of atoms, with each atom forming three pyramidal nearest neighbor covalent bonds within a layer. The next-nearest neighbors lie in the adjacent layer with weaker bonding.

The rhombohedral geometry can be conveniently described within a hexagonal basis with the lattice constants

$$\begin{aligned} \text{Sb:} \quad & a_h = 4.31 \text{ Å}, \quad c_h = 11.27 \text{ Å} \\ \text{Bi:} \quad & a_h = 4.54 \text{ Å}, \quad c_h = 11.86 \text{ Å} \end{aligned}$$

Figure 3.2 shows two versions of the hexagonal representation. Figure 3.2(a) shows a single rhombohedral cell inscribed within a hexagonal co-ordinate system. The diagonal of the rhombohedral cell (trigonal axis) is perpendicular to the (111) plane [1] which corresponds to the (0001) plane in the hexagonal system (shaded in the Figure). Figure 3.2(b) includes the atoms from neighboring rhombohedral cells within the hexagonal basis, with the covalent intralayer bonds indicated by dashed lines.

An excellent description of hexagonal co-ordinate systems is given in Wood [102]. We present a summary of the main aspects here. Crystallographic planes in the hexagonal system are generally defined by the four Miller index notation $(hkil)$. The third index, i is the negative sum of the first two indices, and is

[1] As a reminder, the convention for the use of brackets in crystallographic notation is as follows: (hkl) = specific plane, $\{hkl\}$ = family of equivalent planes, $[hkl]$ = specific direction, $\langle hkl \rangle$ = family of equivalent directions.

often dropped, leaving a three index notation (hkl).[2] The angle, ϕ between two crystallographic planes defined by $(h_1k_1l_1)$ and $(h_2k_2l_2)$ in the hexagonal system, is given by

$$cos\phi = \frac{h_1h_2 + k_1k_2 + \frac{1}{2}(h_1k_2 + h_2k_1) + \frac{3}{4}\frac{a^2}{c^2}l_1l_2}{\left[\left(h_1^2 + k_1^2 + h_1k_1 + \frac{3}{4}\frac{a^2}{c^2}l_1^2\right)\left(h_2^2 + k_2^2 + h_2k_2 + \frac{3}{4}\frac{a^2}{c^2}l_2^2\right)\right]^{1/2}} \tag{3.1}$$

where a and c are the lattice constants given above.

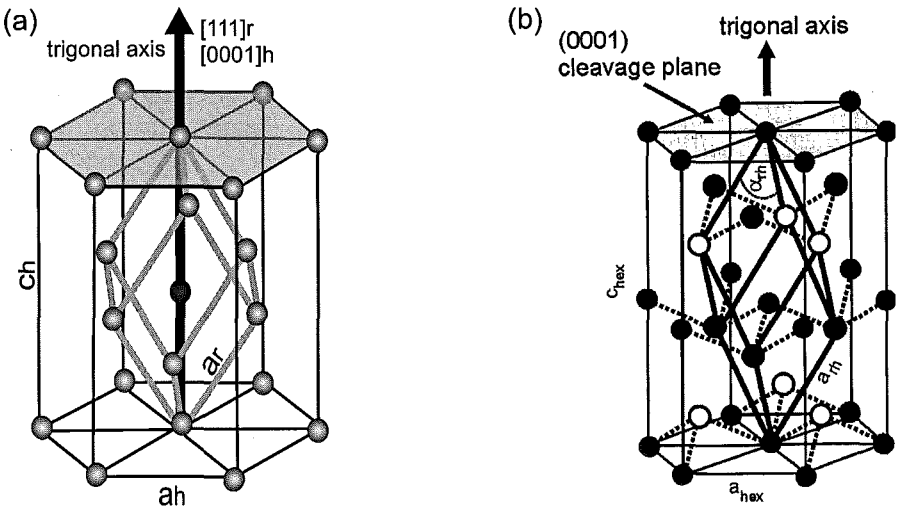

Figure 3.2: Rhombohedral and hexagonal co-ordinate systems. (a) A single rhombohedral cell (with a 2 atom basis, second atom shaded dark) is inscribed within a hexagonal system. (b) Atoms from neighboring rhombohedral cells that lie within the hexagonal basis are included, dashed lines indicate covalently bonded atoms (reproduced from ref.[103]).

The geometry can also be described within a third, pseudo-cubic, co-ordinate system (Figure 3.3), which is a slightly distorted cubic lattice. A simple cubic lattice can be constructed by stacking body centered rhombohedral unit cells with an apex angle of 60° (see for example Fig.1 in ref.[104]). In this case there are two atoms per unit cell, one at the origin and the other at position $\frac{1}{2}$, $\frac{1}{2}$,$\frac{1}{2}$ (the body center) of each cell. The pseudo-cubic structure of Bi and Sb is obtained by sharpening the rhombohedral apex angle to α_r and pushing the second basis atom along the diagonal towards its partner, until it reaches the position $2u, 2u, 2u$.

In Figure 3.3(a), the shorter intralayer bonds are indicated with solid lines, and the longer interlayer bonds are represented with dashed lines. Note that in Figure 3.2(b) (reproduced from Stegemann *et al* [103]), it was the intralayer bonds that were depicted with dashed lines. We adopt the convention of Jona [105] and

[2]Note that this three index labeling system is not equivalent to the three index rhombohedral labeling. Formulas for conversion between the Miller indices of the rhombohedral and hexagonal systems can be found in ref.[102].

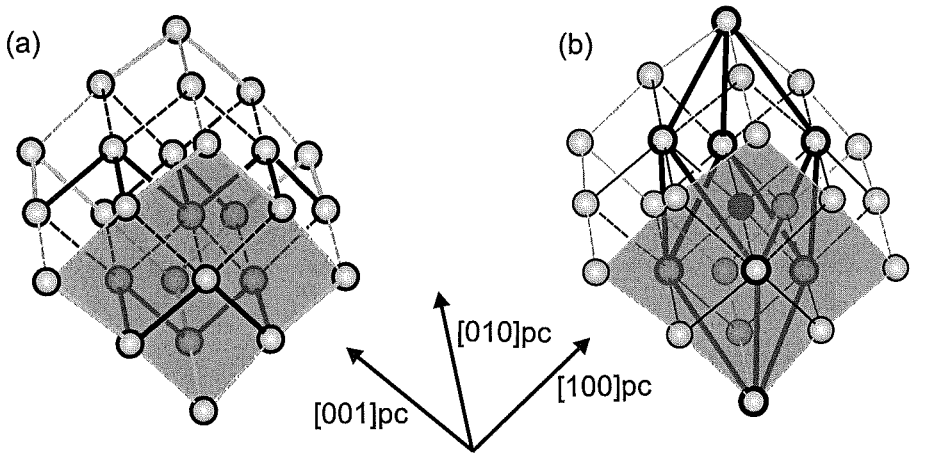

Figure 3.3: The pseudo-cubic co-ordinate system. (a) The solid and dashed lines represent covalent and interlayer bonds respectively. (b) The rhombohedral unit cell inscribed within the pseudo-cubic indexing system. A $(100)_{pc}$ plane is shaded to aid in diagram clarity.

Agergaard [106], and indicate the intralayer bonds with solid lines. Figure 3.3(b) shows the rhombohedral cell (heavy solid lines) inscribed within the pseudo-cubic structure. In both illustrations, a $(100)_{pc}$ plane is shaded to aid in clarity of the geometry.

The three coordinate systems are used extensively in the literature, and a conversion table for the Miller indices can be found in Jona [105]. The indices for the crystallographic orientations that will be discussed in Chapter 6 are given below. We use exclusively the four index hexagonal notation.

Pseudo-cubic	Rhombohedral	Hexagonal
{111}	{111}	{0001}
{100}	{110}	$\{01\bar{1}2\}$

Table 3.1: Conversion between pseudo-cubic, rhombohedral, and hexagonal indices.

3.2 The Ultra High Vacuum System

The study of atomic diffusion processes on surfaces requires the preparation of samples under ultra high vacuum conditions to ensure minimum surface contamination and enable high adatom mobilities. A UHV deposition system with a base pressure of order 10^{-10} torr was designed and constructed for this project. This Section describes the experimental procedures used to deposit particles on surfaces under UHV. Chamber construction is discussed first (including pumping mechanisms), followed by the residual gas atmosphere. Each deposition step is then described in detail, including graphite preparation, and vapor deposition.

3.2.1 Overview of Apparatus and Deposition Steps

A schematic and a photograph of the UHV deposition apparatus are shown in Figure 3.4, with labels for various components which will be referred to in the text. The apparatus is comprised of a three stage pumping system, with the final pressure achieved via ion pumping. The main internal components of the system are: a sample oven for thermal cleaning, a crucible for thermal evaporation of metals, a deposition rate monitor (DRM) for measuring the vapor flux, and a sample translation arm for moving the samples to various regions of the chamber under UHV. The deposition steps are summarized below.

- Graphite is cleaved in air to remove adsorbed contaminants, and immediately loaded into the chamber through the loading port.

- The system to the right of gate valve 1 (gate valve 1 is initially closed) containing the samples is rough pumped to 10^{-4} torr, then isolated from the roughing system. Gate valve 1 is subsequently opened, exposing the entire system to ion pumping. The ultimate base pressure is approximately 5×10^{-10} torr in the sample region. The samples are then wound to the far left of the system (position shown in Figure 3.4) via the bellows translation wheel .

- The samples are heated under UHV in the sample oven, to a temperature of $\sim 420°C$ for approximately 15 hours. This procedure removes surface contaminants, particularly adsorbed water.

- Bismuth or antimony are thermally evaporated with a resistance heated crucible. The vapor passes through a series of baffles to produce a collimated beam.

- The DRM and samples are wound over the atomic beam via the bellows translation wheel, with the DRM recording the flux prior to sample deposition at room temperature.

- On completion of deposition, the samples are wound out of the path of the atomic beam, where they remain for 1 hour under vacuum.

- The samples are wound back to the loading port and gate valve 1 is closed to isolate the left hand side of the system (which always remains under vacuum). The right hand side of the system is nitrogen vented, and the samples removed under ambient conditions for *ex situ* analysis.

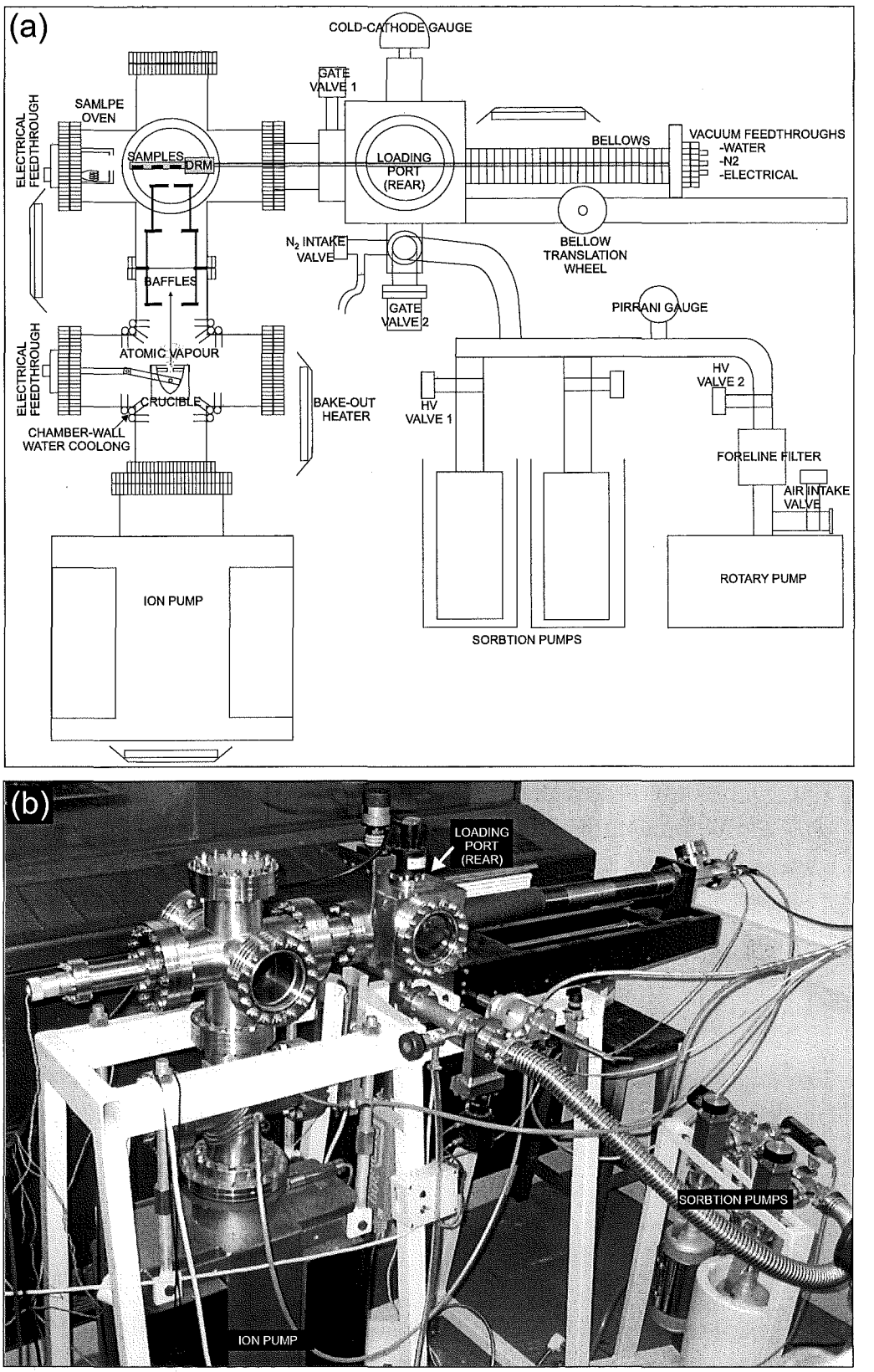

Figure 3.4: Apparatus for UHV vapor deposition: (a) Schematic representation, (b) photograph.

3.2.2 Chamber Construction

The construction of a UHV chamber requires careful consideration of the types of materials that will be exposed to the vacuum environment. The configuration of internal components is also important, to ensure that problems such as stray atomic vapor and back streaming of ions is minimized. We begin with a discussion of the practical aspects of constructing a UHV deposition system, and then proceed with an explanation of each of the deposition processes outlined above.

At atmospheric pressure, surfaces are bombarded with molecules. Even a freshly cleaned surface becomes quickly saturated with adsorbed molecules, particularly water. After a chamber's pressure is reduced via pumping, the density of molecules is reduced and a clean surface may remain uncontaminated for long periods of time. At pressures below a medium vacuum of about 10 mtorr, gases evolving from the surfaces of materials (outgassing) contribute more molecules per second to the pump than do the gasses in the entire volume of the chamber.

Two of the most important factors in determining the ultimate pumping pressure are the materials used for the construction of the chamber and its internal fixtures, and the procedures used for cleaning them. Construction materials with low outgassing rates and low vapor pressures are required. The system is constructed from a combination of grade 304 and 316 stainless steels. All removable seals that are exposed to the UHV environment are composed of knife-edge flanges with copper gaskets. The composition of the internal fixtures will be discussed as they arise in the following Sections.

The cleaning procedure for large components such as the 4 and 6 way crosses involved wiping with low residue AR grade acetone and lint-free tissues. Smaller components were treated with an ultra-sonic clean in AR acetone, followed by a rinse in methanol, and a final rinse in isopropyl alcohol (IPA) to remove any remaining residue. This 3-step procedure is particularly important for materials that may have been exposed to oil residue.

To achieve UHV pressure, the system utilizes a 3-stage pumping mechanism. The first step is rough pumping with an 8 L/s rotary vane pump to 10^{-3} torr. A 2-stage liquid nitrogen cooled sorption pump then further reduces the pressure to 10^{-4} torr. Finally, a 500 L/s galaxy ion pump achieves the ultimate base pressure of approximately 5×10^{-10} torr.

Rotary Pumping

Rotary vane pumping works by drawing air into a chamber, where it is compressed by the rotor and vane, and expelled to the atmosphere via a discharge valve. The downfall of rotary pumping is that the vanes and other surfaces are oil sealed, which can result in back-streaming of oil into the vacuum chamber. However this can be drastically reduced, or even eliminated, by the installation of a foreline filter between the pump and the rest of the system.

Mechanical pumps are an inexpensive solution to roughing the system before other pumps are engaged to achieve UHV pressures. However, in addition to potential back-streaming problems, mechanical pumps are not efficient at removing water vapor, since water is recycled through the oil on each rotation of the pump rotor.

Sorption Pumping

Sorption pumping uses molecular sieve (high surface area material), cooled by liquid nitrogen to trap molecules, and is very efficient at removing water vapor. Once the molecular sieve is saturated it must be baked and rough pumped to remove the adsorbed molecules. Typically 10-20 system runs can be performed between bake-outs.

Ion Pumping

An ion pump operates by capturing gas molecules and binding them to a surface. It uses an electrical, ionizing discharge (the Penning discharge). A combination of magnetic and electric fields maintains and confines the discharge within the type of structure illustrated in Figure 3.5.

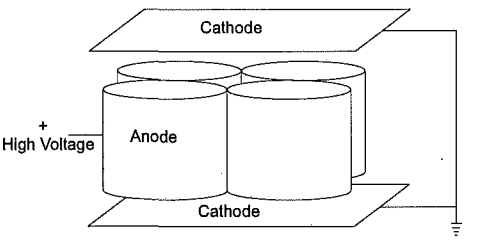

Figure 3.5: Ion pump configuration.

An array of cylindrical anode cells is arranged between two parallel titanium cathodes. A large positive voltage is applied to the anode, and a large magnetic field is applied parallel to the axis of the anode cells, causing a cloud of spiraling electrons to be captured inside the cells. These electrons collide with residual gas molecules, forming positive ions. Since the ions are heavier, and of opposite charge to the electrons, they are accelerated towards the cathodes. Their energy is released when they are buried into the titanium cathode plates, hence removing them from the residual atmosphere.

3.2.3 Residual Gas Atmosphere

A vacuum environment is neither void nor inert. It generally comprises a mixture of several different gases, in varying ratios. For deposition experiments, the composition of the residual atmosphere is important, since some gases (such as

back-streamed pump oils) can irreversibly contaminate the graphite surfaces. For this reason, a residual gas analyzer (RGA) is an invaluable diagnostic tool. An RGA-200 from Stanford Research Systems was mounted to the system via the port behind the samples in Figure 3.4 (concealed from view). This location was chosen because it is close to the position of sample deposition and is out of direct contact with the vapor beam.

The RGA is a mass spectrometer that analyzes the composition of residual gas by ionizing some of the gas molecules. These ions are then separated according to their masses and the ion current is measured for each mass. RGA's do not measure the molecular mass directly, but rather the mass to charge ratio (=M/Q) of the ions, in units of the electron charge. The ion current is interpreted by an electronics control unit, and expressed graphically in terms of a pressure for each atomic mass unit (AMU).

When a molecule is ionized, it is common for fragments of several mass-to-charge ratios to form. For example, when nitrogen is ionized by electron bombardment, the dominant peak is at mass 28, corresponding to N_2. A smaller peak will also be present at mass 14, corresponding to N. Such peaks define a unique fragment (or cracking) pattern for each molecule. However, in real systems the interpretation of the RGA spectra is often complicated by the coincidence of some molecules' primary peaks. For example, carbon monoxide and nitrogen both have their dominant peaks at mass 28. Table 3.2 gives the main fragment patterns for some common vacuum gases [107]. For a clean ion pumped system at UHV pressure, hydrogen will to be the dominant gas load. Hydrogen is pumped by burial and subsequent diffusion into the cathodes of the ion pump, however it can come out of solution and be re-emitted into the system.

AMU	H_2	CO_2	N_2	O_2	CO	H_2O
1	2.7	-	-	-	-	-
2	100	-	-	-	-	-
12	-	6.3	-	-	3.5	-
14	-	-	9	-	1.4	-
16	-	16	-	14	1.4	3.1
17	-	-	-	-	-	3.1
18	-	-	-	-	-	100
28	-	15	100	-	100	-
32	-	-	-	100	-	-
44	-	100	-	-	-	-

Table 3.2: A summary of some common vacuum gas fragment patterns [107].

Figure 3.6(a) shows a recording of the residual gas spectra for the chamber, under background pumping conditions (no sample or crucible heating). The peak

at 2 AMU indicates the expected abundance of hydrogen. H_2O is represented at by the dominant peak at 18 AMU, and by the smaller side peak at 17 AMU. The peak at 44 AMU is a signature of CO_2. Identification of the peak at 28 AMU is more problematic, since both N_2 and CO have their primaries at this value. The coincidence of these primary peaks, coupled with the small magnitude of the 28 AMU peak, makes identification of the origin of this peak from the spectra impossible, since the secondary fragments would appear at about the level of the background noise. We can however, utilize our knowledge of the systems history. Nitrogen is vented to let the system up to atmospheric pressure. The chamber is then opened to air while the samples are removed. There is nothing however to suggest that carbon monoxide would be present in sufficient quantities to account for a major fraction of the 28 AMU peak. We therefore conclude that this peak is dominated by N_2, but cannot rule out the possibility of trace levels of CO in the system. The most important feature of this spectra is the absence of any notable contaminant peaks, such as back-streamed pump fluid or cleaning residue. There is an expected abundance of hydrogen and small amounts of atmospheric gases. The absence of an O_2 peak at 32 AMU also indicates that there is no air leak.

Figure 3.6(b) shows a RGA spectrum for the system during crucible heating. The main background gases from Figure 3.6(a) remain. The increase in the primary CO_2 peak is mirrored by an increase in the secondary fragments at 12 and 16 AMU. The enlargement of the 28 AMU peak could be the result of CO outgassing from the filament, however this is difficult to to confirm due to the masking of the CO secondary at 16 AMU by the H_2O secondary at the same value. The emergence of peaks at 39, 41, and 78 AMU, are signatures of low level contaminants (the concentrations are not significant enough to allow reliable identification). This is not surprising, since we can expect some outgassing as the crucible, its contents, and surroundings are warming. In essence, the spectra of Figure 3.6(b) indicates that the system is clean during crucible heating and hence deposition.

Baking the System

The rate of desorption of molecules from the systems surface is a function of the molecular binding energy, the number of adsorbed monolayers and the temperature of the surface. A moderate system bake can drastically reduce the time required to pump a system to a given pressure. In general, the higher the bake temperature, the lower the achievable base pressure. However the maximum operating temperature of the ion pump during baking imposes a maximum bake temperature of 150°C.

The system is baked by stepping up the temperature to 140°C on a control unit for the four bake out heaters positioned around the system, ensuring that the pressure never exceeds 5×10^{-4} torr. Thermocouples positioned near the heaters

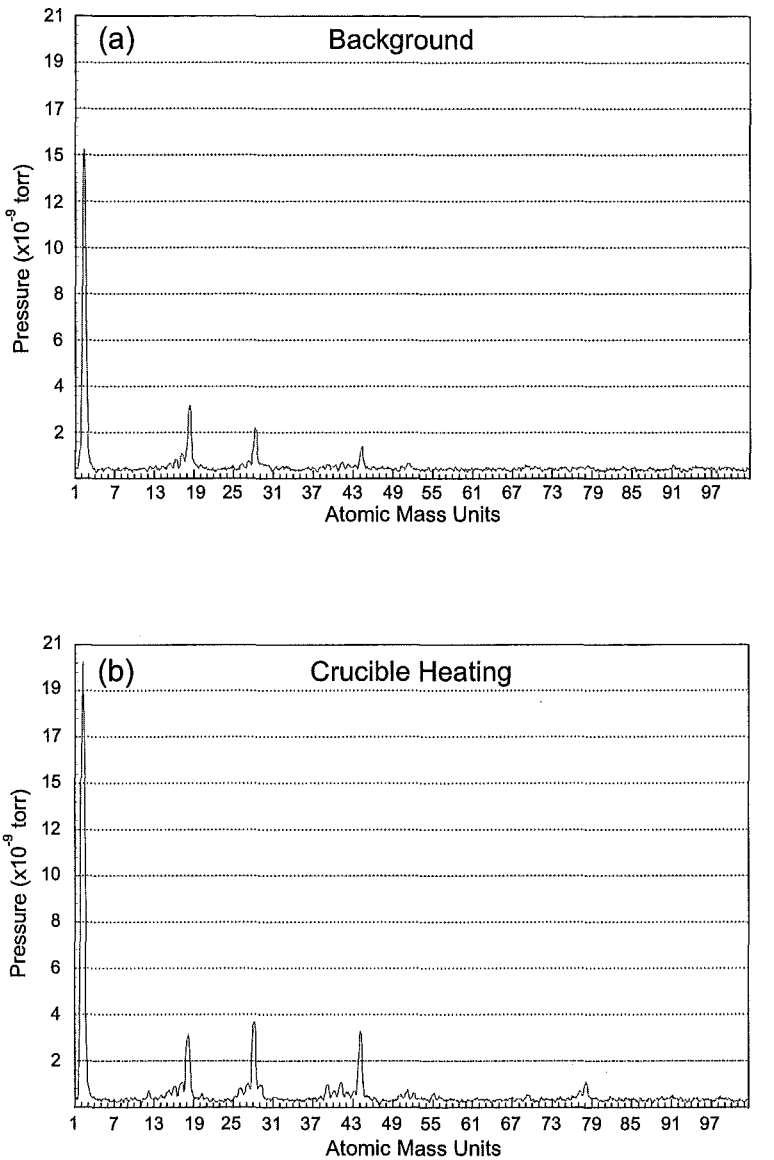

Figure 3.6: Residual gas spectra for the system during (a) background pumping, and (b) and with crucible heating.

determine the temperature of the chamber walls. Typically, 5 hours is required to reach full temperature. To minimize hot-spots and heat loss to the room, thermal insulation was provided by a cover constructed from aluminum foil backed with woven fiber glass (fabric from Pegler Beacon, Christchurch, NZ), and the glass view ports were additionally protected with aluminum foil. Overnight baking at full temperature was required to sufficiently outgas the system. A comparison of the systems pressure recorded at various time scales for both the baked and unbaked systems is given in Table 3.3.

Pumping Time	Pressure (torr) **Unbaked System**	Pressure (torr) **Baked System**
1 hour	5×10^{-7}	-
15 hours	1×10^{-7}	8×10^{-9}
1 week	2×10^{-8}	8×10^{-10}

Table 3.3: A comparison of typical chamber pressures for the unbaked and baked system.

The mechanisms by which gas adsorbs to a surface can be divided into two general categories; physiosorption and chemisorption. Physiosorbed gas particles are bound to the surface by the weak van der Waals force, and are readily removed at room temperature by the standard pumping procedures described above. Chemisorbed molecules however, have much higher adsorption energies (typically greater than 40 MJ/(kg-mol)), and are released slowly from the system's surface under normal pumping conditions. This type of gas release is responsible for most of the out-gassing in vacuum systems, but can be substantially reduced by baking.

Figure 3.7(a) shows the residual gas spectrum for an unbaked system after pumping for 1 hour, and shows a dominant water peak. Figure 3.7(b) shows the spectra after 15 hours pumping, demonstrating a significant reduction in all gas species and a decrease of the the relative concentration of water in the gas load. Water is weakly bonded to itself (energy of 41 MJ/(kg-mol)) and is rapidly removed by room temperature pumping. However water is chemisorbed to metal with an energy of approximately 92 MJ/(kg-mol), making it difficult to further remove at room temperature. Figure 3.7(c) presents the spectra for the baked system which has been pumped for 15 hours. A comparison of (b) and (c) shows a substantial decrease of the water peak at 18 AMU from the unbaked to the baked system, demonstrating that a moderate bake at 140°C removes the majority of residual water. Note however the comparable magnitude of the hydrogen peak at 2 AMU for both the unbaked and baked systems. Hydrogen is the most problematic gas load in the clean baked UHV system. It is strongly chemisorbed at an energy of 160 MJ/(kg-mol), and could not be removed at the baking temperature used on this system.

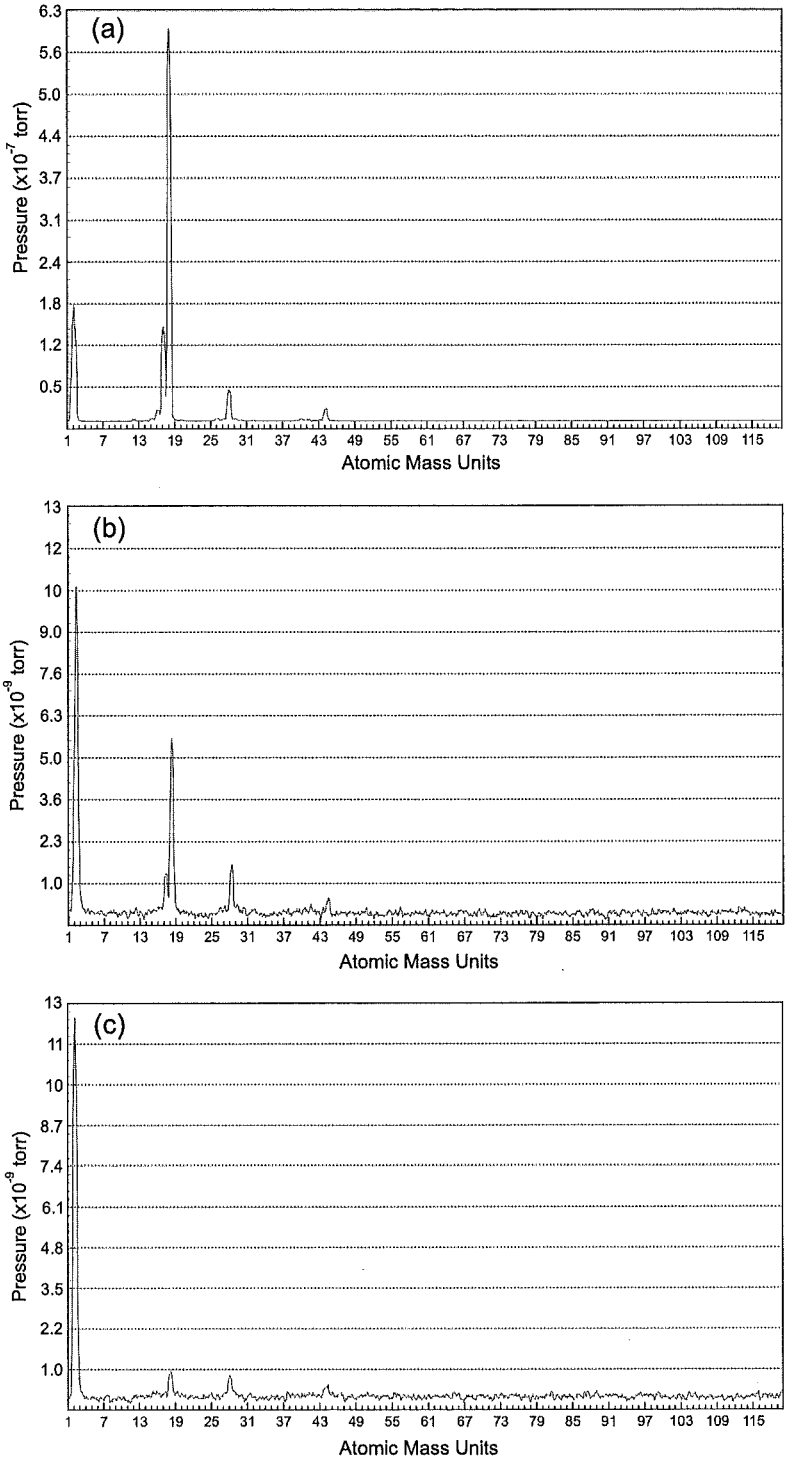

Figure 3.7: Residual gas spectra for: (a) The unbaked system after 1 hour of ion pumping, (b) the unbaked system after 15 hours of ion pumping (note the different pressure scale), (c) the baked system after 15 hours of ion pumping. Note that the discrepancy between the pressure shown on the plot's axes and the overall pressures quoted in Table 3.3 is the result of pressure readings from two different gauge types. In this thesis we always quote the cold cathode gauge (used in Table 3.3) for consistency (the RGA is a temporary chamber attachment), unless otherwise stated.

The system was not baked prior to each deposition run, but only if the entire system had been exposed to atmosphere (for example to clean, or install new components). The left side of the system in Figure 3.4 remains under ion pumping at all times, requiring only brief nitrogen venting of the right side of the system for sample loading. Additionally, the sample cleaning oven heats the chamber walls during overnight thermal treatment of the graphite samples, which contributes to sufficiently low pressures being obtained before deposition. Typically, the system pressure did not exceed 10^{-8} torr during deposition. Early experiments also verified that film quality was not enhanced by reducing the pressure further.

3.2.4 Graphite Preparation

HOPG is available in 3 grades. We used grade ZYH (low grade) for antimony, since this is the grade used in the previous studies by Kaiser *et al* [19]. The moderate grade ZYB was used for bismuth, since a more comprehensive study of aggregation was performed, in which large defect free terraces were desirable (as described below). Both grades were obtained from SPI supplies. HOPG from different suppliers is thought to be sufficiently uniform that no origin-dependent behavioral differences should be observable [108]. This was confirmed by a trial run of HOPG from Advanced Ceramics, under identical experimental conditions as a run with SPI HOPG, no differences were observed.

All grades are of comparable purity, and impurity levels are of the order 10 ppm ash or better. Grade ZYH has a grain size of around 30 nm (compared to ~0.5 mm for ZYB), so we could expect a distortion of the regular hexagonal lattice at about 30 nm intervals where the boundaries of two grains of different orientations meet. Usually this interface is comprised of a series of defects surrounded by an almost completely undeformed hexagonal lattice [109]. While surface defects are of paramount importance here, there is considerable evidence that these grain boundaries have little effect as defect traps for diffusing adatoms[3]. It is likely that a slight distortion of the hexagonal lattice is a minor defect in comparison to adsorbed contaminants.

A comprehensive study of the optimum preparation of clean graphite surfaces is presented by Metois *et al* [108]. Most significantly, they find that cleaving in air, followed by immediate transfer to the UHV system for heating under vacuum at $\sim$ 420°C, yields surfaces of comparable cleanliness to UHV cleaving and heating. They do note however, that additional substrate contamination is observed if the chamber is baked after the samples have been loaded.

The weakness of the interlayer bonding of HOPG makes cleaving straight forward. However the layers do not cleave uniformly, resulting in the formation

[3]Many workers use grade ZYH [19], with their micrographs showing inter-island spacing which far exceeds the predicted distance between grain boundaries.

of step edges between the terraces on a freshly cleaved sample. Generally lower grades produce more step edges and so smaller terrace regions. The steps vary in height from 3.40 Åfor a single step (the distance between 2 atomic carbon layers) up to a thickness that is visible by eye. The following steps are performed to prepare the samples for deposition.

- Adhesive tape is pressed on to 4 mm × 4 mm graphite samples and then pulled off. The tape takes with it a thin flake of graphite (Figure 3.8(a)). This process is repeated if the entire top layer is not cleanly removed.
- The samples are then immediately loaded into the sample holder and inserted into the chamber through the loading port, and pumped to UHV.
- The samples are heated overnight, at a temperature of $\sim 420°C$.

Figure 3.8(b) shows the sample holder configuration, which holds three samples. The holder is made from oxygen-free high conductivity copper to maximize thermal conductivity from the lamp to the sample holder and subsequently to the graphite. The use of oxygen free copper is necessitated by the tendency of copper oxide (which normally forms at elevated temperatures) to react with hydrogen, producing water vapor. In this configuration the three samples can be heated and then sequentially deposited. The sample holder is screwed to a thermally insulating boron nitride spacer, which is attached to the DRM. A tantalum heat shield is fixed to the spacer to protect the DRM from radiant heating by the oven.

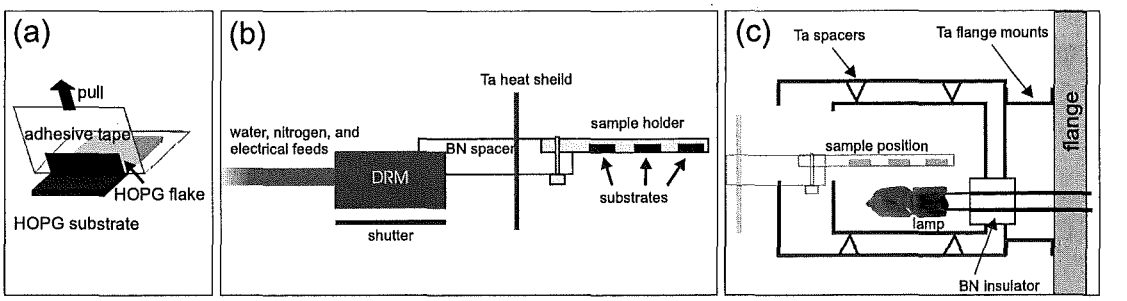

Figure 3.8: Graphite preparation procedure: (a) The samples are cleaved with adhesive tape. (b) Samples are loaded into the sample holder. The sample holder configuration is shown. (c) Samples are thermally cleaned in a radiative oven.

The sample oven is constructed from two concentric tantalum cylinders with an opening for sample insertion, as shown in Figure 3.8(c). Heating to $\sim 420°C$ (recorded with a temporary thermocouple mounted to the sample holder under vacuum) is achieved with a 50 W (24 V) halogen lamp, which is run at 29 V to maximize heat output while minimizing damage to the lamp filament. This is the maximum temperature that could be attained with this configuration. Under these conditions a lamp typically lasts for 20-30 deposition runs, and can be

replaced by venting the system and removing the flange to which the oven is attached. The lamp is then removed through the sample entry hole in the oven, and a new lamp mounted.

Heating under atmospheric conditions can cause thermal oxidation of the graphite surface [110], which results in etching of defect pits into the graphite layers. While this effect is generally severe only at temperatures exceeding 700°C, the oxidation process is still present (and generally initiated at defects) for lower temperatures [111]. To avoid the possibility of this complication, heating is not initiated until the system pressure reaches 1×10^{-6} torr.

Alternative sample heating configurations were trialled prior to the design of the oven in Figure 3.8(c). Their ability to produce clean substrates was judged by comparing the morphology of antimony deposits, with those of the Kaiser group [14], [19], shown in Figure 2.14 (Chapter 2). A series of SEM images are shown in Figure 3.9 (flux = 0.2 Å/s, coverage = 40 ML) for various heating configurations in our system. Figure 3.9(a) shows an image from a heating arrangement with the lamp positioned under the samples in the absence of heat shielding, which provided a maximum temperature of $\sim$ 260°C. Clearly there is a significantly higher island density in our case, and the fingered structures are not observed. Mounting a heat shield to the lamp (but not encasing it as the oven configuration of Figure 3.8(c)) allowed a temperature increase to $\sim$ 330°C, which resulted in branched morphologies only on occasional regions of the substrate (Figure 3.9(b)). Figure 3.9(c) shows a typical region of a deposit obtained with the oven configuration in Figure 3.8(c). Comparison with Figure 2.14 shows that these are of a similar form to antimony aggregates imaged by other workers, and confirms that the oven arrangement in Figure 3.8(c) is adequate to produce clean graphite surfaces.

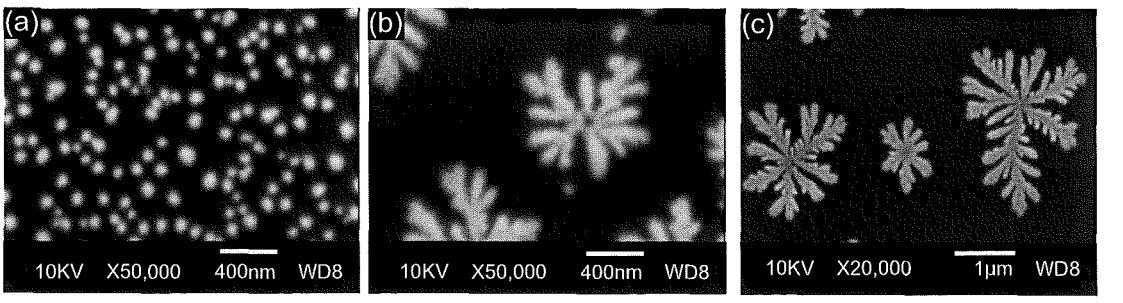

Figure 3.9: Morphology of antimony deposits under various sample heating configurations (flux, coverage, and heating time is the same in all cases). (a) Lamp mounted under samples with no heat shielding. (b) Lamp mounted under samples with minimal heat shielding. (c) Lamp mounted in the heat shielded oven configuration shown in Figure 3.8(b), note scale change.

Ion Shielding

In 1978 Metois and co-workers showed that graphite is particularly sensitive to ion contamination [108]. They found that each ion that bombards the surface can induce an active site for island nucleation. They also reported that high temperature cleaning (T > 1000°C) is required to eliminate the majority of the defect sites, implying that most of the contamination arises as a consequence of very strong adsorbate-surface bonding for ionized particles. However they also found that even after high temperature cleaning, the form of the resulting islands were different to identical depositions performed in a neutral residual atmosphere, implying an irreversible surface modification[4].

Our deposition apparatus has several components that generate ions. The cold-cathode gauge, the RGA, and most notably the ion pump, are all sources of ion contamination from which the substrates must be shielded. This shielding is achieved by simply ensuring that the samples do not have a direct line of sight to any ion sources, since the probability of an ion retaining its charge after a collision with any obstruction (such as a chamber wall) is very small.

Figure 3.4 shows that the cold-cathode gauge is initially located above the graphite surfaces (in the loading port), and the RGA is not operated when the samples are positioned in the 6-way cross (as shown in Figure 3.4(a)). The graphite is shielded from the ion pump by a series of baffles, illustrated in Figure 3.10. They were constructed from 0.5 mm grade 316 stainless steel and designed with three considerations in mind.

1. The baffles needed to obstruct a direct path of any ions from the mouth of the ion pump to the samples. The circumference of the largest diameter baffle is clamped between the top and bottom cross in Figure 3.4. In this configuration, the baffles in conjunction with the crucible serve as an effective obstruction.

2. They must be configured so as not to choke the ion pump. The effective area of each baffle was therefore made as similar as possible, to minimize the restriction of pumping speed.

3. Their role as a focusing mechanism for the atomic beam also had to be taken into account (described in the next section).

Now that the sample preparation has been discussed, we focus our attention on the actual process of deposition.

[4]It is also interesting to note that focused ion beams have been used to intentionally introduce defects, for the purpose of patterning graphite substrates [112].

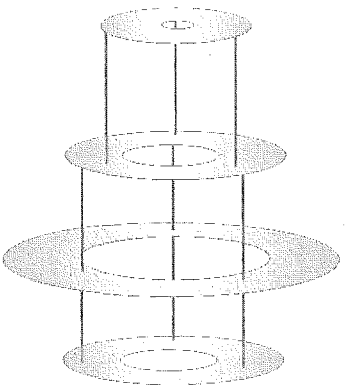

Figure 3.10: Illustration of the baffles used to collimate the atomic beam and to shield the graphite from ion bombardment.

3.2.5 Atomic Beam Generation

In order to generate an atomic beam, we need a source of vapor flux, which requires the change of phase from a solid to a vapor, induced by the input of energy. In this section we consider the process of obtaining the atomic vapor, both within the framework of the kinetic gas theory [113], and from the experimental stance.

Vapor Release From a Surface

The velocity of particles in the gas phase follows a Maxwell Boltzmann distribution with the average velocity given by

$$\nu = \left(\frac{8kT}{\pi m}\right)^{1/2} \tag{3.2}$$

with m= the molecular weight of the particles, k=Boltzmann's constant, and T= the temperature of the vapor.

If a system is in dynamic equilibrium, the pressure of the vapor over a surface is the same as the vapor pressure of the solid or liquid (denoted as the melt), providing the melt and the vapor are at the same temperature. This allows use of Kinetic Gas Theory to describe the process of vapor release from the melt. According to Kinetic Theory, the flux of an ideal gas striking a unit surface from one side is

$$\Gamma[\text{atoms/m}^2\text{s}] = \frac{n\nu}{4} \tag{3.3}$$

where n= the particle density. Therefore under equilibrium conditions this will be the rate of particle release from the melt.

With the help of the ideal gas law, Equation 3.3 can be manipulated into the more useful form

$$\Gamma = \frac{P\nu}{4kT} \tag{3.4}$$

Combining equations 3.2 and 3.4 yields

$$\Gamma = P(2m\pi kT)^{-1/2} \tag{3.5}$$

or

$$\Gamma = 2.65 \times 10^{24} \frac{P}{(mT)^{1/2}} \tag{3.6}$$

with units $P[Pa]$, $m[AMU]$ and $T[K]$.

For deposition experiments, it is more useful if the flux is expressed in units of Å/s. In order to make this conversion, we need to determine the effective inter-atomic distance. This value is always greater than the isolated atomic diameter, since it takes into account that the atoms may not be close packed due to their crystalline arrangement. The number of atoms in a unit volume is given by (ρ/mu), where $\rho[kg/m^3]$= the bulk density of the material, m= the atomic mass $[AMU]$, and u=the nucleon mass = 1.66×10^{-27} kg. The inter-atomic distance is therefore approximated by

$$d_{atom} = \left(\frac{mu}{\rho}\right)^{\frac{1}{3}} \tag{3.7}$$

The atomic flux can then be expressed in terms of the thickness per unit time as

$$\Gamma[m/s] = V[m^3/atom]\Gamma[atoms/m^2s^{-1}] \tag{3.8}$$

$$\Gamma[\mathring{A}/s] = 2.65 \times 10^4 \frac{d_{atom}^3 P}{(mT)^{1/2}} \tag{3.9}$$

with $r[\mathring{A}]$, $P[Pa]$, $m[AMU]$ and $T[K]$. The elemental data for Bi and Sb are shown in Table 3.4.

Element	Melting Point (K)	Bulk Density (kg/m^3)	Atomic Mass Number	Inter-atomic Distance (Å)
Bi	544	9800	208.98	3.3
Sb	904	6620	121.75	3.1

Table 3.4: Element data for Bi and Sb. The melting point, bulk density, and atomic number are standard textbook values. The inter-atomic distance is calculated from Equation 3.7, and gives the average distance between atoms in the bulk, and is also defined as a mono-layer (ML).

The atomic flux released from the melt surface as a function of temperature can be calculated using Equation 3.9 and the vapor pressure-temperature curve for the particular melt element (these curves can be found in the appendix of ref.[107]). Figure 3.11 shows the dependence of the atomic flux on the melt temperature for Bi and Sb. It illustrates that Bi must be heated to well beyond

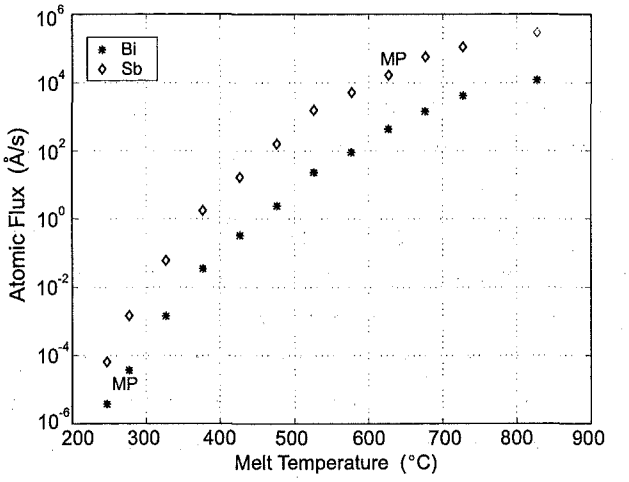

Figure 3.11: Atomic flux as a function of temperature for Bi and Sb. The melting points are indicated on both plots.

its melting point before an appreciable flux can be obtained, while the same flux is emitted from Sb when it is several hundred °C below its melting point.

Thermal evaporation of antimony is known to produce a vapor comprised exclusively of Sb_4 particles [114]. The bismuth vapor contains a mixture of Bi_1 and Bi_2 [115]. We refer to the deposited particles as adatoms, making no distinction between the deposition of single atoms, dimers or tetramers, which are assumed to diffuse as molecules due to their large binding energy (8.9 eV for Sb_4). The deposited dose of material is defined as the coverage, and is expressed in units of mono-layers (ML), where 1 ML is arbitrarily defined as the average distance between atoms in the bulk, and is therefore given by the inter-atomic distance in Table 3.4.

Crucible Configuration

The atomic beam is generated experimentally by thermal evaporation. Bi or Sb is heated in a crucible, with the temperature adjusted by altering the input current. The crucible arrangement is shown in Figure 3.12 in schematic, (a) and photographic, (b) forms. The crucible is constructed from alumina coated tungsten wire from Midwest Tungsten Service, and requires a current input in the range of 8-14 A to produce the flux range required of the materials in this project. The alumina crucible is fitted with a boron nitride lid with an 8 mm opening. Stray atomic vapor is prevented from escaping around the periphery of the lid with a Ta crucible lid. This arrangement is encased within a lidded Ta heat shield, and the configuration is mounted to a high voltage feed-through, as shown in Figure 3.12(b). Note that each of the voltage feed-through arms has a movable segment, which allows adjustment of the crucible position for alignment purposes.

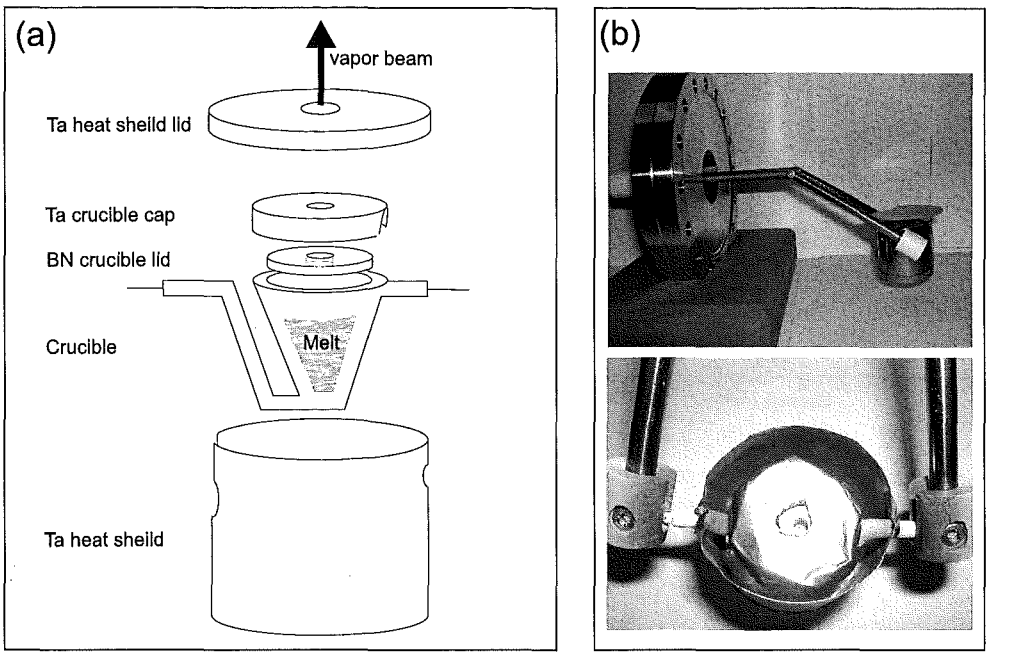

Figure 3.12: (a) Schematic diagram of the crucible and heat shield configuration. (b) Photographs of the crucible arrangement showing the electrical feed-throughs to the flange.

The vapor from the crucible must be restricted to a beam of approximately 8 mm diameter, with a uniform cross-section (i.e. minimal beam spread) at the sample surface, to avoid simultaneous deposition on adjacent samples. This is achieved by allowing an adequate distance of 20 cm between the crucible aperture and the sample holder, in conjunction with the top baffle restricting the diameter to approximately 8 mm.

The baffles in Figure 3.10 also play an integral role in ensuring that the only vapor to reach the graphite, is that which passes through the hole in the top baffle. Caution was exercised in aligning the baffles in relation to the crucible aperture and samples, such that there were no beam shadowing effects. For example if the vertical axis of the baffles was tilted slightly, one of the baffles may cut a line of sight (and hence the vapor beam) from the crucible aperture to the sample. This would result in a non-uniform beam cross-section, and hence a non-uniform substrate coverage.

The beam profile was measured by the following method.

1. Bi is deposited on a SiN wafer.

2. A series of scratches are made across the diameter of the deposit with a Dectak. The Bi film is weakly adhered to the smooth SiN wafer, so the Dectak head cleanly removes fine lines of Bi without damaging the hard SiN surface. The separation of these lines is measured with an optical microscope.

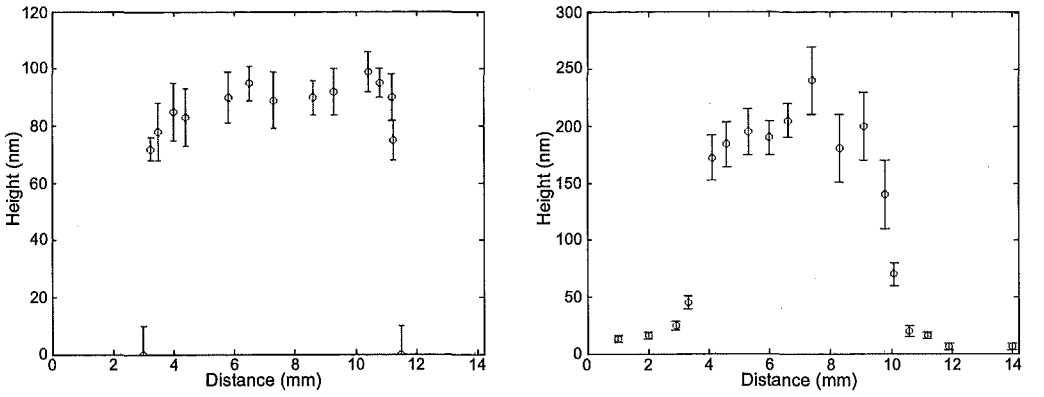

Figure 3.13: Atomic beam cross-sections measured with the AFM: (a) Cross-section generated with apparatus configuration of figure 3.4. (b) Alternative configuration with the baffles replaced with a single aperture, also the sample-crucible distance is reduced, and the sample-aperture distance is increased.

3. The depth of each scratch is measured with the atomic force microscope (AFM) (described in Chapter 4), enabling a beam profile to be determined.

Figure 3.13(a) shows the beam profile for the sample-baffles-crucible configuration described above. It is clear that the thickness of the deposit is relatively uniform across the diameter, within the measurement uncertainties. Figure 3.13(b) demonstrates the effect of reducing the sample-crucible distance and increasing the sample-aperture distance, with the series of baffles replaced with a single aperture with a 3 mm diameter hole. This results in a non-uniform beam profile, which is not suitable for substrate deposition.

Atomic Flux Measurement

The flux is measured directly with a water cooled quartz crystal microbalance (STM-100 from Sycon Instruments). This deposition rate monitor uses the resonant frequency of an exposed 8 mm diameter quartz crystal to sense the mass of deposited film attached to its surface. There is a known relationship between the the frequency of the sensor crystal and the amount of mass accumulated on it [116]. An electronics control unit then calculates the thickness per unit time accumulating on the crystal from its change in frequency. The advantages of using a DRM to measure the flux directly, over relying on estimations from temperature measurements, are numerous. Most notably, it allows real time measurement of the flux at the sample position.

Figure 3.8(b) illustrates that the DRM is positioned slightly (approximately 15 mm) further away from the atomic beam than the samples. However the uniformity of the beam cross-section implies that there will be little difference between the flux deposited to the samples, and that recorded by the DRM. The

biggest variance is likely to arise from alignment problems between the atomic beam and the sensor crystal. If the beam does not entirely cover the crystal, the reduction in mass will erroneously be interpreted as a reduction in flux. To counter this problem, the DRM is independently calibrated by depositing a given thickness of material onto a SiN wafer. The thickness is then measured with the AFM, using the same technique as for the cross-section profiling. It was not necessary to apply a flux correction since no appreciable differences were found.

Changing Evaporant Materials

Before discussing the handling of large quantities of condensed metal vapor, it is important to note that inhalation of heavy metal particulates is hazardous to health. Precautions such as cleaning in a ventilation hood where possible or wearing of a breathing mask, and protection of skin and clothing from contamination should all be exercised.

Changing evaporant materials from bismuth to antimony (and vice versa) requires removal of the crucible configuration from the system. Once the high voltage feed-through flange is removed and stabilized on a work bench, the screws shown in the bottom photograph in Figure 3.12(a) can be removed and the crucible configuration detached from the voltage feed-through arms. The entire crucible configuration is then stored in a sealed container for later use, and a new crucible and heat shield are used for the new material. Evaporant deposits are removed from the copper feed through arms by gently sanding with fine sandpaper, and polishing with acetone and kimwipes, before the new configuration is mounted.

The 4 way cross is removed from the system, and the walls are cleaned by removing large flakes of material, and scrubbing with an scratch free scouring pad. Remaining deposits are removed by wiping with a dilute nitric acid solution (70 ml of 65%HNO_3 mixed with 400 ml distilled water), followed immediately by a rinse with distilled water. Note that while nitric acid does attack stainless steel, it degrades the evaporant materials more rapidly and so wiping with a dilute solution on a tissue does not damage the chamber walls. AR acetone and kimwipe tissues are then used to polish the internal chamber surfaces. The same method is used for cleaning the baffles.

System baking and pumping for several days are required to sufficiently outgas the system before the crucible is heated. It should also be noted that the crucible needs to be heated to produce a particle flux at least once before performing a sample deposition. This is required to outgas contaminants both from the crucible and the pelleted melt material.

3.3 Summary

A UHV system was constructed for the purposes of vapor deposition of bismuth and antimony on graphite substrates. This Chapter has described the bulk structure of Bi, Sb, and HOPG, and the methods used to generate deposited samples. The main components of the system include a 3-stage pumping mechanism, sample holder, sample oven, and crucible. The HOPG substrates are cleaned by thermal treatment, and then deposited with either antimony vapor (Sb_4) or bismuth vapor (Bi_2 and Bi_1) at room temperature. The samples are removed for *ex situ* analysis.

Chapter 4

Film Characterization

This Chapter describes the imaging and diffraction techniques, and image processing methods used to characterize the deposited samples. The first Section describes atomic force microscopy (AFM), in tapping mode. Scanning electron microscopy (SEM) is outlined in Section 4.2. The principles of Electron backscatter diffraction (EBSD) are described in 4.3. Section 4.4 is devoted to an overview of the image processing techniques used in later Chapters of this Thesis.

4.1 Atomic Force Microscopy

A Digital Instruments Dimension 3100 AFM was used in tapping mode for high resolution imaging, and the acquisition of height data for deposited films. We outline the basic principles of operation in this Section, with emphasis placed on tapping mode AFM, and the function of the probe tip. A more comprehensive description can be found the the Digital Instruments AFM manual [117].

The atomic force microscope was invented in 1986 by Binnig, Quate, and Gerber [118], and operates by measuring attractive or repulsive forces between a sharp cantilever tip, which is raster scanned over a surface. The appeal of AFM scanning lies in its ability to provide high resolution 3D imaging, over relatively large scan areas (compared to the small field of view in scanning tunneling microscopy), in ambient conditions.

4.1.1 Tapping Mode AFM

In tapping mode, the AFM operates by scanning the sample with a tip attached to an oscillating cantilever. Tapping results in lower forces and less damage to soft samples compared to the 'contact' mode where the tip is dragged across the sample. Scraping is minimized (lateral forces are virtually eliminated), and higher lateral resolution on most samples is obtained compared to the 'non-contact' mode of operation which hovers the tip above the surface. Due to these reasons, tapping mode AFM is a popular choice for thin film characterization, and is the mode used for the present study. Figure 4.1 shows a schematic diagram of the principles of operation of the tapping mode AFM.

- A cantilever tip oscillates at its resonant frequency (determined by an automated tuning procedure), and is scanned across the sample surface. The tip contacts the surface through the adsorbed fluid layer which is present on the sample surface under atmospheric conditions. The change in cantilever deflection is recorded with a split photodiode detector.

- A constant deflection is maintained between the sample and the tip via a feedback loop, which vertically moves the scanner at each (X,Y) data point to maintain a 'setpoint' deflection. The movement of the tip is achieved by piezoelectric elements.

- The constant cantilever deflection results in a constant force between the tip and sample. The force is calculated from Hooke's law, and typically ranges from nN to μN in ambient environments.

- The vertical distance (Z) moved by the scanner at each surface-plane (X,Y) data point is stored by the computer to form a topographic image of the sample surface.

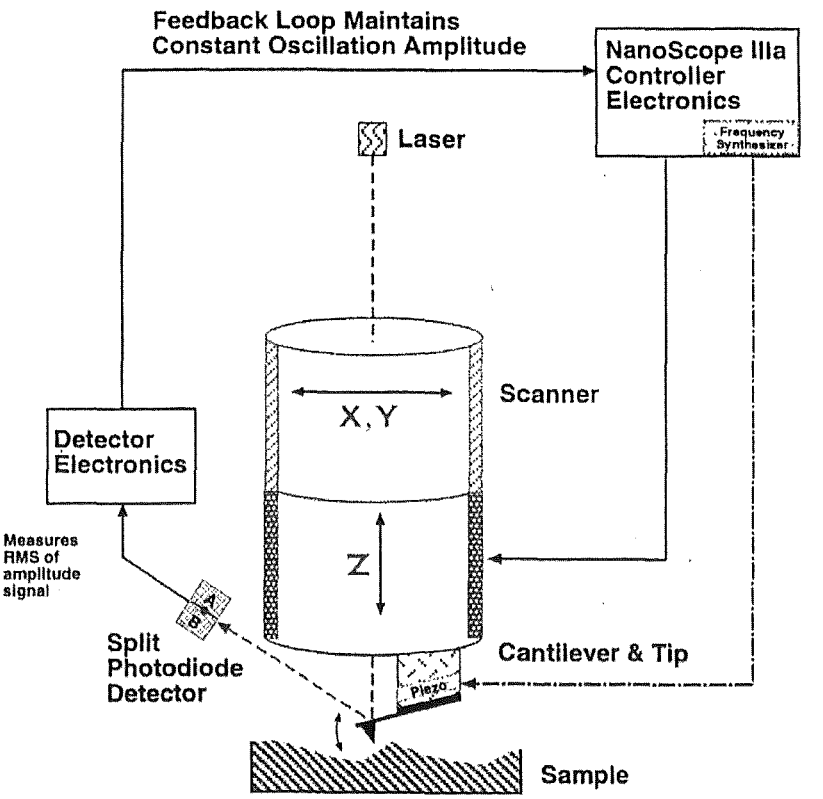

Figure 4.1: Schematic of tapping mode AFM [117].

4.1.2 Probe Tips

The cantilever and tip are an integrated assembly of single crystal silicon. The tip's radius of curvature and side wall angles are the dominant factors in determining the image resolution, as illustrated in Figure 4.2. When the radius of curvature of the tip is greater than the size of the features being imaged, tip broadening results (left image). A sharp tip with a small radius of curvature is capable of resolving smaller features (right image).

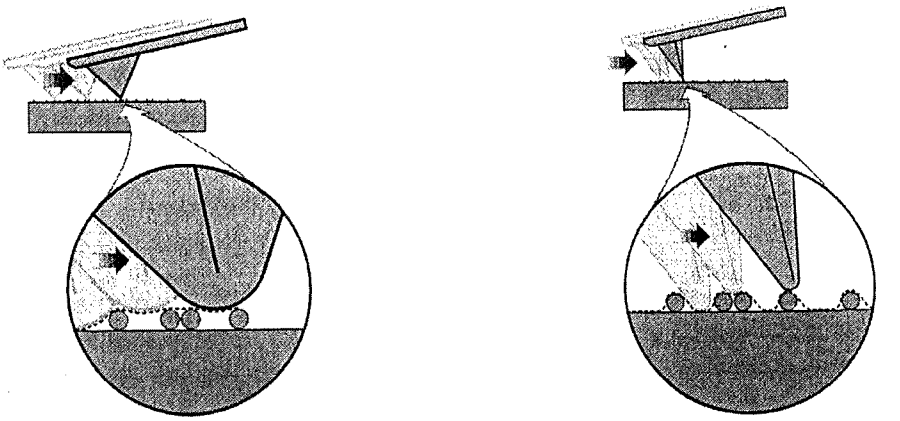

Figure 4.2: Illustration of the effect of tip shape on the resolution of AFM imaging [117].

Other tip properties affecting imaging include the the tip's force constant and resonant frequency. The force constant determines the sensitivity of tip deflections. When the force constant is small, even very small forces can deflect the cantilever. The resonant frequency determines the susceptibility of the cantilever to vibrational instabilities. Though a process of trial and error, the best tips for use with the Bi and Sb aggregates were found to be etched silicon type NCS14 from Micro-Masch. The tips specifications are: radius of curvature < 10 nm, typical resonant frequency ~ 160 Hz, typical force constant ~ 5 N/m).

The resolution of the AFM is limited by the radius of curvature of the tip in the X-Y direction. In the vertical direction, uncertainties in signal noise varied between samples, and are quoted where required in Chapters 5 and 6. It should also be noted that height measurements from the scans required application of a known calibration factor of 1.13 for this instrument.

4.1.3 Examples of AFM Sample Imaging

Successful AFM imaging requires optimization of factors such as the scan speed, and amplitude setpoint of the tip. The amplitude setpoint controls the force between the tip and sample. Increasing the setpoint value (decreasing the force) tends to reduce sample damage, but can result in poor tracking of the surface. The optimum setpoint value for imaging varied between samples, but was typically

slightly lower than the value automatically determined during the tip tuning procedure.

Fast scan rates tend to result in material being picked up by the tip, and damage to surface features. Typically, we used slow scan rates below 0.5 Hz for 5 μm scans (corresponding to a tip velocity of 2.5 μm/s) when imaging bismuth aggregates, which were prone to tip effects. For antimony, the scan rates were not so critical.

Figure 4.3 shows two AFM scans from a bismuth sample that was particularly difficult to image (deposited under high flux conditions, which were generally more prone to AFM induced damage). The left image shows a scan performed at 2.3 μm/s, and shows a general blurring and scraping of the surface features. The right image shows a scan of the same sample performed with a reduced tip speed (1.3 μm/s), and demonstrates a clear improvement in image quality. One of the downsides to the AFM technique is that imaging is slow (typically 15 minutes per scan, but up to 40 minutes for difficult samples), and is complicated by tip effects, which result from the interaction of the probe tip with the sample surface.

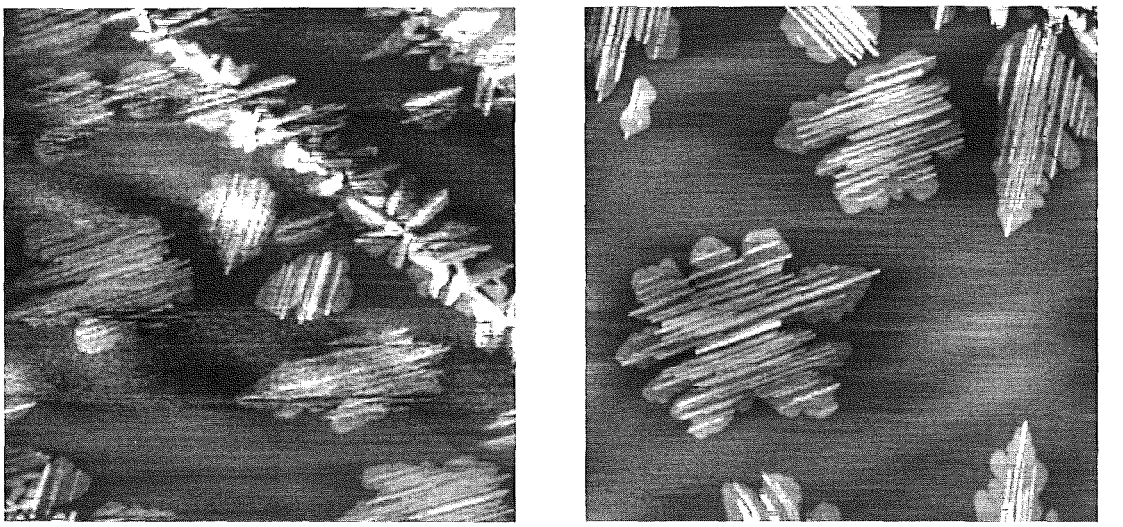

Figure 4.3: Two AFM images of bismuth aggregates taken from the same sample. The left image was scanned with a tip velocity of 2.3 μm/s. The right image was scanned at 1.3 μm/s, and shows an improvement in image quality.

Figure 4.4 shows two examples (antimony aggregates) of the high quality of imaging that is obtained when AFM parameters are sufficiently optimized. The left image is viewed in plane mode, while the right image is presented in 3D mode.

4.2 Scanning Electron Microscopy

Scanning electron microscopy (SEM) is one of the most common imaging techniques used in thin film characterization, and is the topic of many text books

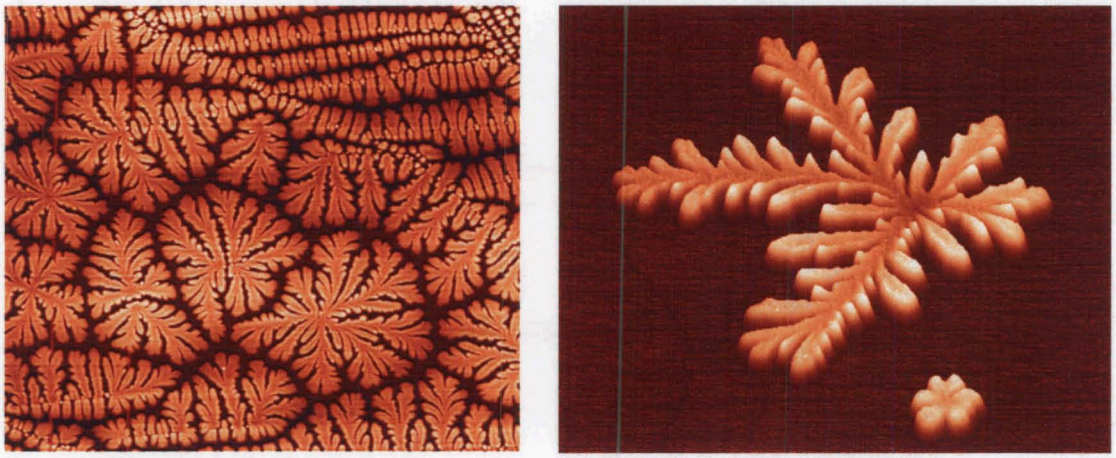

Figure 4.4: Examples of the imaging capability of AFM, when scan parameters are optimized. The images are of antimony aggregates. The left image (15 μm scan size) was featured in the Toronto Star newspaper [119], and appears in the 2005 Veeco calender [120]. The right image (6 μm scan size) was awarded "Top Micrograph Using a Scanning Probe Microscope" at the EIPB conference in San Diego in 2004 [121].

(see for example ref.[122]). We present here a brief overview of its operation, followed by typical system settings for imaging antimony and bismuth aggregates on graphite substrates.

4.2.1 Principles of Operation

An SEM image is formed by a very fine beam of electrons which are focused and then scanned over the surface of the sample, in a vacuum environment. Figure 4.5 shows a schematic representation of a typical SEM configuration. Electrons are thermionically emitted from a cathode filament towards an anode (or alternatively they can be emitted via field-emission). The electron beam typically has an energy ranging between 0.1 keV and 50 keV, and is focused by two successive condenser lenses into a beam with a small spot size (1-10 nm) at the specimen surface. The scanning coils produce the raster scanning of the beam.

Electrons from the beam (primary electrons) strike the sample, and are scattered by atoms just beneath the surface. These scattering events result in the primary electron beam spreading to fill an interaction volume, as depicted in Figure 4.6. The interaction volume varies directly with the accelerating voltage, and inversely with the atomic number of the sample atoms, and generally extends a few microns into the surface. Various types of electrons are emitted from different regions below the surface (see Figure 4.6), but typically it is the low-energy secondary electrons which are collected and detected to produce the SEM image on a television screen.

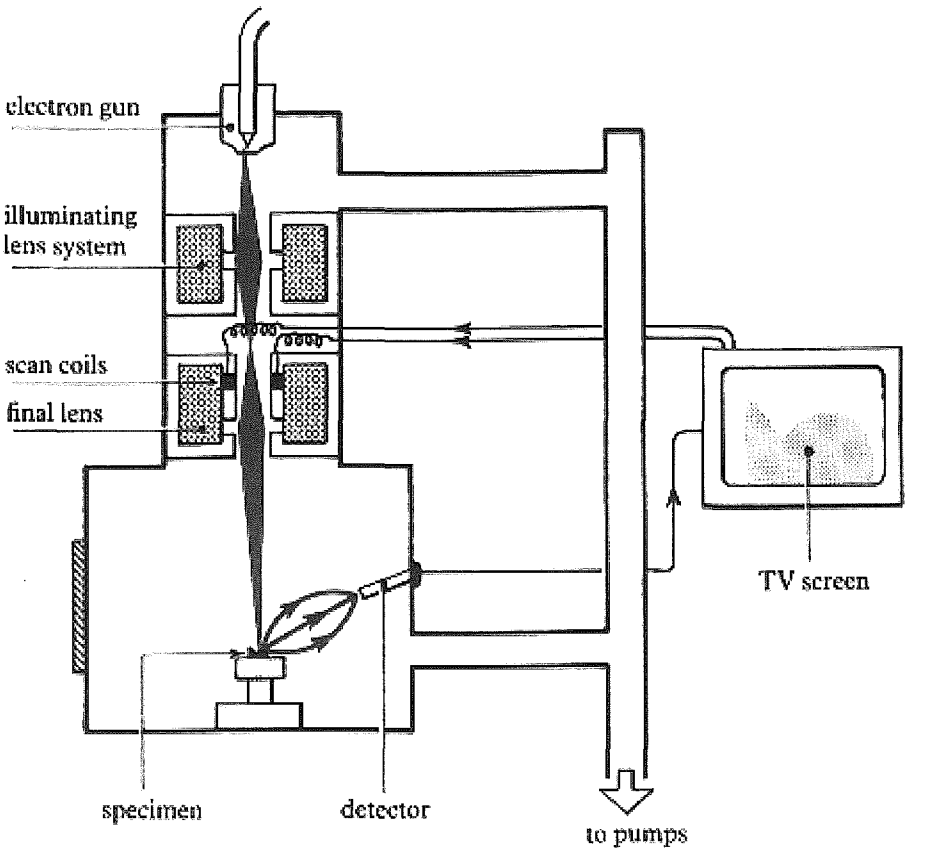

Figure 4.5: Schematic diagram of a scanning electron microscope [123].

4.2.2 SEM Settings and Optimization

SEM imaging was mainly performed with a JEOL JSM6100 instrument. Early in the project it was discovered that the Bi and Sb (to a lesser extent) aggregates are particularly susceptible to beam damage with the SEM in normal operating mode, particularly at high magnifications. Ordinarily the JEOL JSM6100 SEM operates with an accelerating voltage of 12-20 kV, and generally better resolving power is obtained with high accelerating voltages. In the present work, sample damage was minimized by reducing the accelerating voltage to between 6 and 8 kV. The loss in image quality was counter-balanced by moving the anode to the 'up' position, which produces a more intense electron signal.

The working distance defines the distance between the final condenser lens and the sample. Low working distances increase the image resolution, but decrease the depth of field. We used reasonably low working distances ranging from 6 - 12 mm, since a reduction in the depth of field was of little concern due to the flat nature of the samples.

The current of the electron beam determines the number of electrons striking the surface. Higher currents give better resolution, but can also result in charging

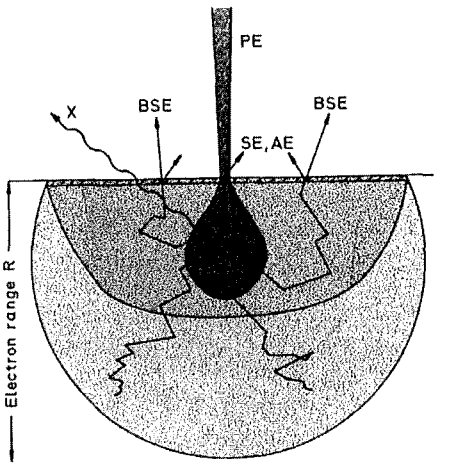

Figure 4.6: Electron interaction volume, showing the origin and depth of secondary electrons (SE), backscattered electrons (BSE), Auger electrons (AE), and x-ray quanta (X) in the diffusion cloud of electron range R for normal incidence of the primary electrons (PE) [122, chap 1].

effects which reduce the image quality. The probe current control was usually set to the '12 O'clock' position on the SEM (numerical values for the probe current are not give on the JEOL JSM6100 instrument).

The maximum magnification for imaging structures while minimizing sample damage was typically found to be 10,000× (although 20,000× was sometimes possible with Sb) . Figure 4.7 shows a typical 10,000× magnification SEM image of some bismuth aggregates, with the imaging parameters optimized as above.

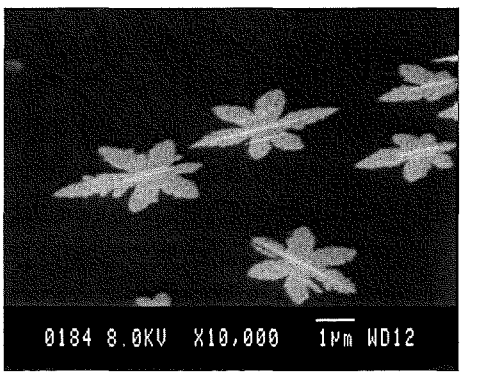

Figure 4.7: Optimized SEM image of bismuth aggregates.

An SEM equipped with a field-emission gun enables imaging with lower accelerating voltages and a higher electron intensity (brightness), and typically provides superior resolution over the thermionic emission of electrons used in regular SEM's. A RAITH 150 electron beam lithography system (used in field-emission imaging mode), and a JEOL JSM 6500F field-emission scanning electron microscope (FE-SEM), were occasionally used for high resolution imaging.

Figure 4.8 shows three images of bismuth films obtained with the RAITH FE-SEM. The left image shows an optimized scan with 20,000× magnification (recall that 10,000× was the maximum magnification possible for these samples with the regular SEM), and an accelerating voltage of 3 kV. The centre image shows the beam damage which results from an increase in magnification (same accelerating voltage as left image, but 50,000× magnification). The islands now display less distinct edges, and were observed to change in a melting-like manner under the electron beam. The substrate between the islands has also become coated with a 'dappled' material, which could be observed rapidly forming under the electron beam. The right image shows a scan with 10,000× magnification, but with the accelerating voltage increased to 10 kV. The beam damage is again obvious, with the left side of the image showing a 'melted' region.

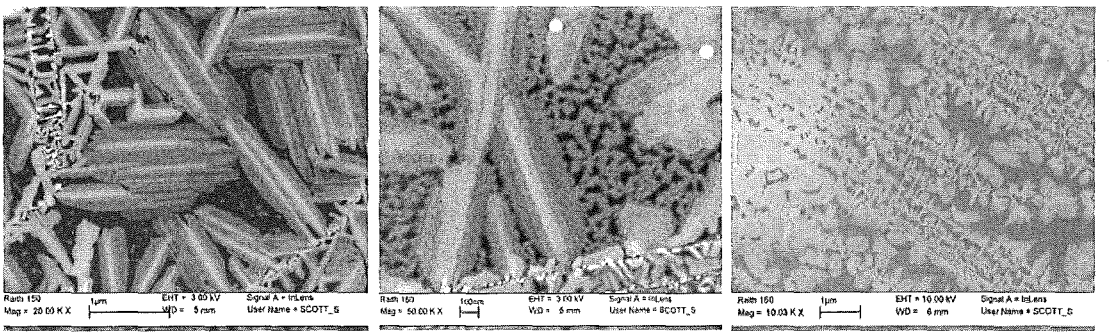

Figure 4.8: FE-SEM images of bismuth films. The left image shows an optimized image with 20,000× magnification and 3 kV accelerating voltage. The centre image shows the same accelerating voltage, but with the magnification increased to 50,000×. The right image has lower magnification (10,000×), but higher accelerating voltage (10 kV).

SEM imaging allows fast sample imaging (typically a few seconds per scan), over a wide range of magnifications. Successful SEM and FE-SEM imaging of Bi/HOPG requires attention to optimizing scanning parameters in order to minimize beam damage. For the Sb/HOPG system, this was generally more straight forward.[1]

4.3 Electron Backscatter Diffraction

Electron backscatter diffraction (EBSD) is an SEM based technique which produces patterns of backscattered electrons (Kikuchi patterns [124]) from a crystal surface. The patterns exhibit the symmetry of the crystal lattice, and so allow determination of the crystal structure and orientation of a sample [125]. The

[1]In Chapters 5 and 6 it is shown that the antimony and bismuth aggregates are of order 20 nm and 1 nm tall respectively. It seems likely that the taller height of the antimony structures allow for easier imaging, as they are more robust.

appeal of this technique lies in its ability to correlate crystal lattice orientation (with submicron resolution), with the film morphology in an SEM image.

EBSD was first developed in 1954 by Alam and co-workers [126], and in the 1970's the technique was applied to metallurgical microcrystallography by Venables and co-workers [127]. Over the last 30 years EBSD has found widespread application in materials science, and is now used for structure determination in applications such as identification of intermetallic phases [128], crystallography of grain boundaries [129], characterization of nanocrystallites formed during electrodeposition [130], and characterization of thin films [131], amongst others.

We now outline the principles of operation and pattern generation in EBSD, which are described in greater detail in the HKL EBSD users manual [132]. The pattern indexing procedure is described in Section 4.3.2, followed by a discussion of pole figures and orientation mapping.

4.3.1 Principles of Operation

The crystal structure of the films in Chapter 6 were investigated by EBSD using an HKL Nordlys II detector and HKL Channel5 software. The samples are loaded into the SEM chamber and tilted at 70° to the *stationary* electron beam, as illustrated in Figure 4.9(a). The electrons strike the sample surface and are scattered, generating electrons traveling in all directions in a small volume which is effectively a point source.

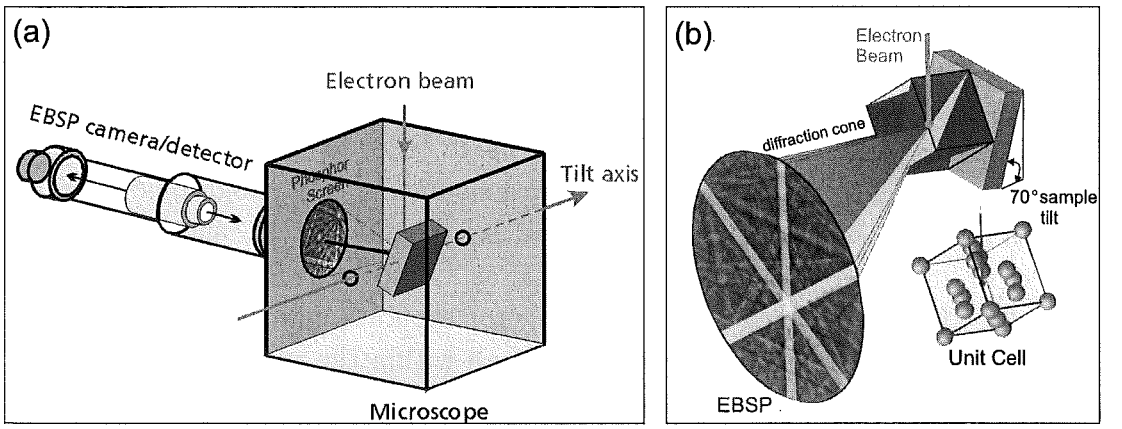

Figure 4.9: (a) The sample surface is tilted at 70° to the electron beam within the SEM. The cone of backscattered electrons are intersected by a phosphor screen. (b) Backscattered Kikuchi bands are generated when electrons arrive at the crystal planes with the Bragg angle. The symmetry of the pattern therefore reflects the symmetry of the crystal lattice. [132]

The multi-directional nature of the scattered electrons means that at every set of lattice planes within a crystal sample, there must always be some electrons arriving at the Bragg angle, θ_B. These electrons can then undergo elastic scattering to produce a strong, reinforced beam. The electrons form two cones for

each crystallographic plane, which are intersected as hyperbolae by a phosphor imaging screen, which is itself imaged by a CCD camera, allowing digital recording of the pattern. These are the Kikuchi lines, and their spacing is an angular distance of $2\theta_B$, which is proportional to the inter-planar spacing through the Bragg condition ($n\lambda = 2d_{(hkl)}\sin\theta_B$). A schematic diagram of Kikuchi bands (pairs of Kikuchi lines) generated from the crystallographic planes of a sample is shown in Figure 4.9(b). Note that the lines appear to be almost straight, because the apex angle of a diffraction cone is close to 180°, so the cones are almost flat.

Each Kikuchi band corresponds to a family of crystal lattice planes. The intersection of bands corresponds to a zone axis (or pole), and major zone axes are recognized by the intersection of several bands. The entire pattern of Kikuchi bands is also referred to as an electron backscatter diffraction pattern (EBSP), and it essentially represents all the angular relationships in a crystal, and therefore the crystal symmetry.

4.3.2 Indexing

Indexing is a process which involves assigning a particular crystallographic orientation to an EBSP recorded by the phosphor screen. The HKL Channel5 software automatically interprets the EBSP's. A comprehensive account of this process is given in the Channel5 users manual [132], we simply present an overview here.

The Flamenco program detects the location of Kikuchi bands on the EBSP, and assigns indices to the visible zones, as shown in Figure 4.10. When indexing an EBSP, Flamenco needs a list of possible phases which the EBSP may have been produced from (for example rhombohedral bismuth in our case). The software can then generate lists of Kikuchi bands and relative intensities, and compares them to the experimentally obtained patterns, in order to assign the indices.

Flamenco automatically suggests solutions for the crystallographic orientation (an index) based on model fits to the experimental pattern, and ranks them in order of 'mean angular deviation' (MAD) as an indicator for 'goodness of fit'. Typically, MAD<1 is considered acceptable for accurate index solutions. In this study, the MAD for accepted solutions were all within the range of 0.2 - 0.8.

To correlate crystallographic orientation with film morphology, an SEM image of the area of interest is first acquired, then the electron beam is used to probe the structure at various locations in the image. It should be noted that because the sample is mounted at 70° to the electron beam, the SEM image is automatically tilt corrected to provide a true representation of the surface features.

4.3.3 Pole Figures

A pole figure is the spherical projection of a particular family of crystallographic plane normals, displayed in a plane representing the upper or lower hemisphere,

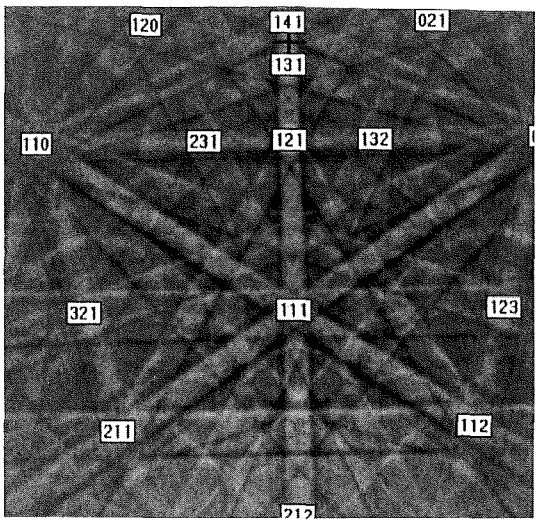

Figure 4.10: An the assignment of indices to the visible zones of an experimentally generated EBSP [132].

and is a convenient way to display the index solutions. Pole figures are generated automatically by the Mambo program, and are represented in stereographic projection.

An illustration of the construction of a pole figure in stereographic projection is shown in Figure 4.11, for a cubic crystal. The orientation of a crystallographic unit cell is shown with respect to the sample orientation in (a). If the unit cell is placed within a sphere, the {100} plane normals intersect the sphere as shown in (b), and a plane parallel to the sample surface would intersect the sphere as a circle. Figure 4.11(c) shows the points where the {100} plane normals intersect the top of the sphere, connected to the opposite pole of the sphere. (d) shows the circle that was inscribed in the sphere, and demonstrates that the 3D crystallographic directions have been converted into points on a circular plane. This is the pole figure, and it represents the crystallographic orientation of a sample. Note that the filled-in circles represent the crystallographic plane normals for the top hemisphere, and the unfilled circles depict those which intersect the bottom hemisphere (not shown in (c)).

Many index points can be imported into a single pole figure, allowing the distribution of crystallographic orientations within a sample to be visualized, as will be demonstrated in Chapter 6.

4.3.4 Orientation Mapping

The indexing described thus far, uses a stationary electron beam to probe the crystal structure. However EBSD can also be used in scanning mode to allow automated sampling of a grid of points. The EBSP from each point is automatically solved to give an index solution. The index solutions (up to several thousand)

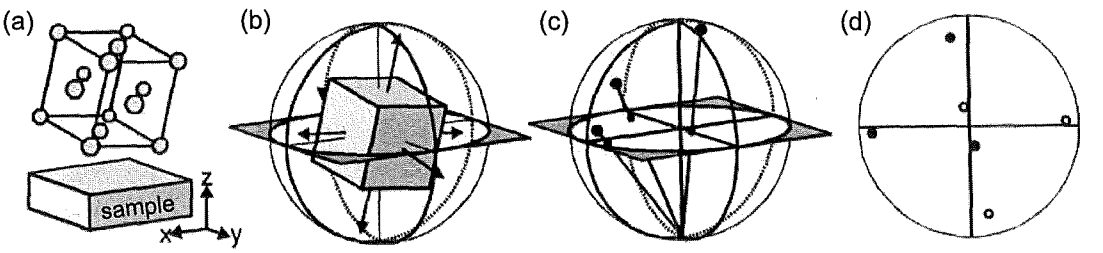

Figure 4.11: Construction of a pole figure for a cubic system. (a) Orientation of a crystallographic unit cell with respect to the sample. (b) projection of {100} plane normals onto a sphere. (c) Lines connecting the points where the {100} plane normals touch the sphere with the opposite pole of the sphere, and their intersection with a plane. (d) The 2D pole figure [132].

are outputed in the form of an orientation map (as will be shown for bismuth in Chapter 6), which depicts the crystallographic structure of the sample surface.

4.4 Image Processing and Analysis Procedures

This Section describes the techniques used to convert greyscale SEM images into binary images, and processing steps for obtaining quantitative data on the island characteristics. Image filtering steps are first described, followed by the thresholding procedure. Finally, an overview of island area and density calculation and the method for analyzing island edge statistics, is given.

4.4.1 Image Filtering

In SEM micrographs, the islands appear as bright features on a dark background. The SEM images were processed by removing noise and equalizing the background across the image, so that a threshold value could be be applied to the entire image, resulting in conversion to binary (black and white) form. A program that was developed by Hall [133], and implemented by Hyslop [134] to process clusters from transmission electron microscope images, has been utilized.

- Mean filters (3 × 3 pixels) and median filters (7 × 7 pixels) are applied to the image to aid in noise reduction.
- The image is subdivided into smaller sections and the peak of the greyscale histogram for each section is determined by fitting a Gaussian function over the greyscale histogram of each area. The background levels are then 3 × 3 median filtered, then interpolated to produce a background surface, which is removed from the filtered image.

The results of this procedure are illustrated in Figure 4.12. A raw SEM micrograph is shown in Figure 4.12(a). The same image is shown after the filtering process in Figure 4.12(b), demonstrating that the islands now appear

more distinct from the background. Figure 4.12(c) shows the greyscale histogram for the processed image, and represents a typical example for the bismuth films. The first (and dominant) peak results from the abundance of dark grey in the image, the smaller and broader secondary peak centered around a greyscale level of 200, arises from the lighter shaded islands.

Figure 4.12: A comparison of SEM images: (a) before filtering, (b) after filtering, (c) greyscale histogram for the processed image.

4.4.2 Thresholding

Thresholding converts an image from greyscale to black and white, so that the histogram shown in Figure 4.12(c) is converted to only black (greyscale 0) and white (greyscale 255) pixel values, which are interpreted as 0's and 1's by Matlab when calculating statistics such as island area and projected surface coverage. The calculated island statistics therefore depend on the choice of threshold value.

Figure 4.13(a) shows a processed SEM image (the area of interest is isolated and surrounding regions are removed). The calculated fraction of this region that is covered with islands (surface coverage), as a function of the threshold level, is shown in Figure 4.13(b). For greyscale values between 90 and 140, the calculated value of the surface coverage is not strongly dependent on the choice of threshold level. However, for lower threshold levels, the value rapidly increases. For higher levels it begins to diminish. Figure 4.13(c) shows three thresholded images, with the threshold value indicated on each image. The left image shows that low threshold values result in an artificial enlarging of the islands, and also the emergence of small islands, which are actually just noise. The centre image shows the correct threshold level for the image in Figure 4.13(a), as determined by a visual comparison of the thresholded images with the original (automated detection was not possible, since the image quality and greyscale contrast varied between samples, particularly for bismuth). Figure 4.13(c) shows an image thresholded at 180 greyscale levels, and demonstrates that setting the level too high results in erosion of the island edges, to produce smaller and fragmented morphologies. The correct threshold level could typically be determined to within ± 5 threshold steps, yielding an estimated uncertainty in the island size (described below) of $\pm 10\%$.

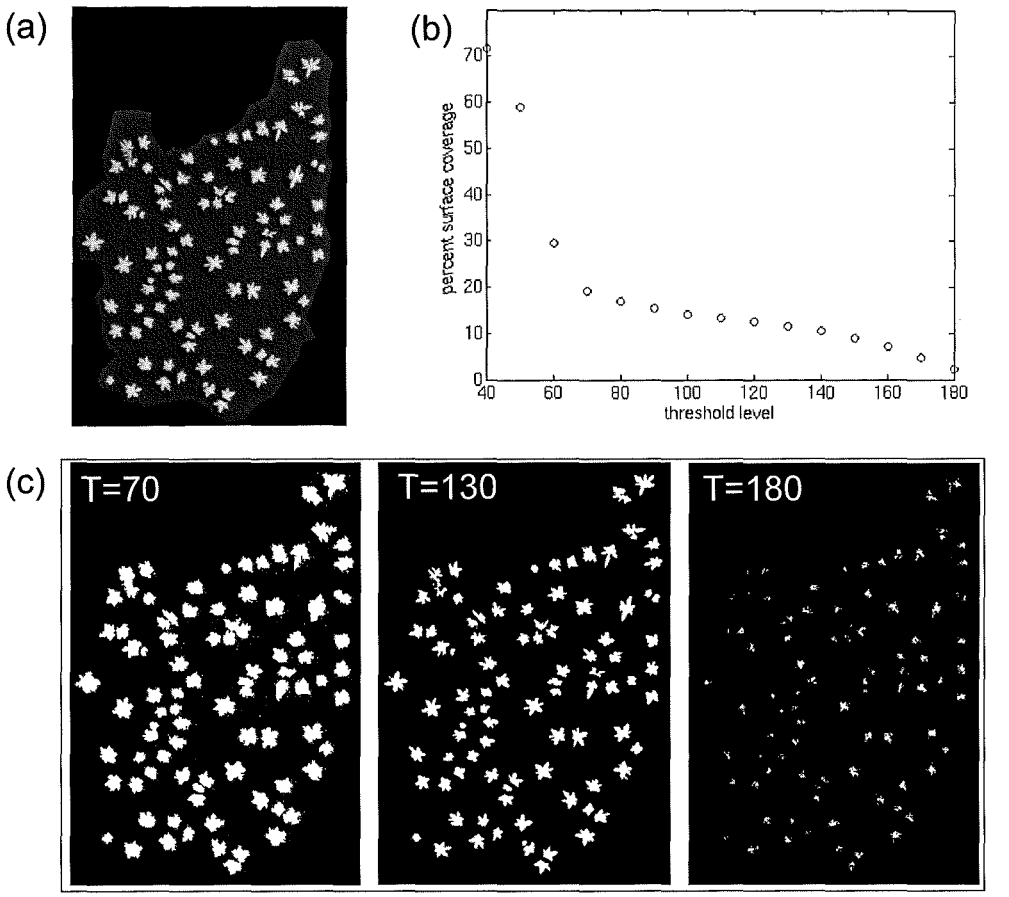

Figure 4.13: Thresholding procedure. (a) A filtered SEM image, with the region of interest isolated and the remainder of the image removed. (b) Plot of the fraction of the region of interest that is covered with islands, as a function of the threshold level. (c) Thresholded images, with the threshold level indicated on each image.

4.4.3 Island Area and Density Analysis

Multiple SEM images were used from different areas of each sample, and in many cases multiple samples, in order to produce representative data sets for the island area and density statistics. Matlab programs were developed which allowed automated calculation of island statistics from the binary images, averaged over all images.

Background noise in the SEM images dramatically effects the analysis. Noise reduces the mean island size, since small islands which appear in the background will be included in the mean area calculation. It also increases the island density for the same reason. Noise filters were included in the programs, which discard any islands below a predefined size, to avoid this complication.

Island densities were calculated from low magnification images (such as in Figure 4.13(a), which feature a large number of islands for analysis. Island areas were typically calculated from higher magnification images (such as in Figure 4.12) since a small amount of erosion around the island edges does not significantly effect the area calculation for such large islands. However, the reduced

number of islands featured in each image required the inclusion of significantly more images in the data sets, than was required for the density analysis. The island density and area calculations are described further in Chapter 6, where they are implemented for the characterization of the bismuth films.

4.4.4 Island Edge Analysis

The erosion of island edges that results from the thresholding procedure is problematic for calculation of statistics such is the island perimeter and fractal dimension.

Figure 4.14 demonstrates the thresholding effect on the island perimeter. The left image shows an SEM scan, filtered as described above. The centre image shows the thresholded image, with the inset showing a region with increased magnification. It is clear that the erosion results in a pixelation artifact, rendering analysis of edge statistics problematic.

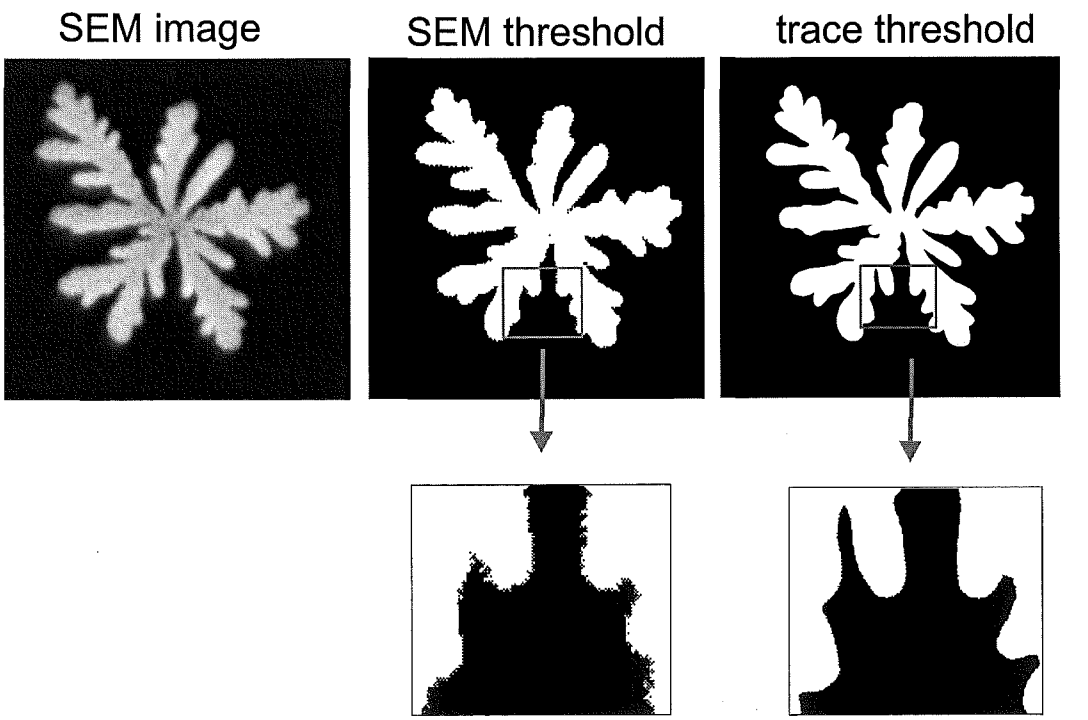

Figure 4.14: Effect of thresholding on the island edges. The left image shows a filtered SEM image. The centre image shows the thresholded SEM image, with the inset showing a higher magnification region of the image. The right image shows a thresholded image which was taken from a trace of the filtered SEM image, note the clear improvement in the quality of the edges.

To improve the results of the automated procedure, a manual trace of the island boundaries from the filtered SEM images was performed, and converted into binary form with a digital scanner. This is shown in the right image in Figure 4.14. The increased magnification inset shows a distinct improvement in the quality of the island edges. This tracing procedure was implemented for

all islands which required analysis of island edge statistics (such as calculation of the perimeters as a function of area, and fractal analysis, in Chapter 5). The thresholded SEM images were exclusively used where only area and density statistics were required (data presented in Chapter 6), since the tracing procedure is significantly slower.

4.5 Summary

This Chapter has described the use of AFM and SEM techniques for obtaining images of deposited samples, EBSD for structure determination, and image processing methods.

Tapping mode AFM uses an oscillating cantilever and tip assembly to raster scan the topology of a surface. It is useful technique for obtaining high resolution images, and allows the acquisition of height data. However, sample imaging is slow (typically 15 minutes per scan, but up to 40 minutes for difficult samples), and is complicated by tip effects, which result from the interaction of the probe tip with the sample surface.

The SEM allows rapid imaging, over a wide variety of magnifications. Beam damage restricts the maximum magnification, and low accelerating voltages are required to further reduce this effect. SEM used in conjunction with AFM allows the film morphology to be characterized in 3D, and in high resolution over a wide range of length scales.

EBSD allows direct correlation of crystallographic structure with the films morphology, with submicron resolution. The HKL Channel5 software allows automatic indexing of EBSP's which are comprised of a series of Kikuchi bands reflecting the symmetry of crystal lattice at the point of indexing.

The final Section gave an overview of the techniques used to extract quantitative data on the island characteristics from the SEM images. Filtering and thresholding steps were discussed, followed by an overview of island area, density, and perimeter analysis.

Chapter 5

Antimony/HOPG: Diffusion and Aggregation

This Chapter presents a discussion of the diffusion of antimony tetramers on HOPG substrates (grade ZYH), and their subsequent aggregation into islands. This system has been extensively investigated previously [86], [135], [19], [14], allowing comparison of our island morphologies with those generated by other experimental apparatuses, as will be discussed in the following Sections. The coverage range of 5 ML - 40 ML, with the flux varied between 0.005 Å/s - 2.0 Å/s, is the primary focus of the study.

The general island morphologies observed in SEM images are discussed in Section 5.1, with emphasis on the variation in morphology with increasing coverage (θ) and flux (F). A statistical study of the degree of island branching is presented in Section 5.1.3. Analysis of the island heights from AFM scans (which have not been performed previously), are presented in Section 5.2. Next, a brief account is given of a second island type which is observed to co-exist with the more regular morphology, followed by a discussion of the evolution of film morphology in the high coverage limit. The Chapter concludes with a summary of the Sb/HOPG system, highlighting the aspects of the present study which go beyond previous observations in the literature.

5.1 Island Morphologies from SEM scans

This Section describes the dependence of the island morphologies on the deposited coverage, and the particle flux. Next, the degree of branching is quantitatively characterized, and fractal dimensions are investigated.

5.1.1 Variation in Morphology with Coverage

Representative SEM images of the evolution of island morphology with increasing coverage are shown in Figure 5.1, for a fixed flux of 0.03 Å/s. Island formation (Volmer-Weber growth mode) is observed on the graphite surface, with the highest density of islands occurring along the HOPG step edges. The θ=5 ML image shows a mixture of small circular (compact) islands, and slightly larger islands

featuring irregularities around their perimeter, with the most pronounced resulting in a fingered morphology. The step edge aggregates are generally compact. An increase in coverage to 10 ML produces larger islands with a branched morphology on the graphite terraces. Step edge decoration is a mixture of compact and fingered aggregates. A further coverage increase to 40 ML results in large branched islands which cover an appreciable fraction of the substrate surface. The step edge structures that face towards the large graphite terrace (centre of the image) feature long and branched morphologies, while those nucleated on closely spaced step edges (right in image) tend to be compact.

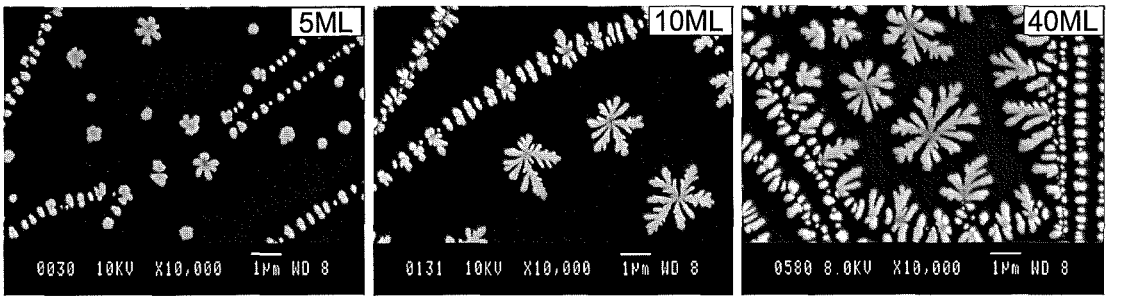

Figure 5.1: Representative SEM micrographs of the evolution of surface morphology with increasing coverage. The flux is held constant at 0.03 Å/s.

It is clear that there is a transition from compact to branched morphologies with increasing island size. The shape of diffusion aggregated islands depends on two characteristic times [85]: an arrival time t_a, which defines the time between subsequent arrivals of Sb_4 clusters to the island boundary (the growth front), and a coalescence time t_c, which defines the time required for an island to incorporate the cluster and rearrange into a thermodynamically favored compact shape.

$$\begin{aligned} t_a > t_c &\longrightarrow \textit{compact islands} \\ t_a < t_c &\longrightarrow \textit{branched islands} \end{aligned} \tag{5.1}$$

The time taken for an island to rearrange into a compact shape increases as the island grows larger, however t_a stays relatively constant under constant flux conditions[1]. Small islands are therefore compact since $t_a > t_c$, but as the islands grow t_c increases and eventually t_a becomes comparable to t_c, inducing a cross-over from compact to branched shapes. The general morphology, and the transition from compact to branched morphologies with increasing coverage, is consistent with other studies of the Sb/HOPG system (see for example [14], [19]). It is also worth mentioning that several studies have been performed with varying

[1]Note that this assumes that the islands are small enough that the increasing island size does not significantly deplete the diffusion field. This will not be the case at high coverage when the islands almost touch and t_a rapidly increases as the arrival of adatoms to the island perimeters slows down.

Sb cluster size [86], [85], [15], which affects the coalescence time, since it takes longer for larger incident clusters to be incorporated into an island.

The fingered growth observed in Figure 5.1 is a consequence of the well known Mullins-Sekerka type tip instabilities. In their original paper [75], Mullins and Sekerka considered the shape evolution of an initially spherical particle whose growth was controlled by either diffusion of material or heat flow. They found that beyond a critical radius, perturbations in the spherical growth front cannot be smoothed, and the sphere becomes unstable.

Mullins-Sekerka instabilities manifest themselves in many structures which grow from a Laplacian field [136]. An often cited example is that of the Hele-Shaw cell [137], [138], [139] which demonstrates viscous fingering in hydrodynamics. In a typical Hele-Shaw experiment, glycerin is trapped between two slightly separated glass plates. A less viscous fluid is injected through a hole in the top plate, displacing the glycerin. Figures 5.2(a)-(c) show examples of viscous fingering patterns, which bear obvious similarity to the antimony islands. Initially the 2-fluid interface is circular, (a) but as more fluid is injected instabilities develop, (b) and eventually grow into fingered patterns (c).

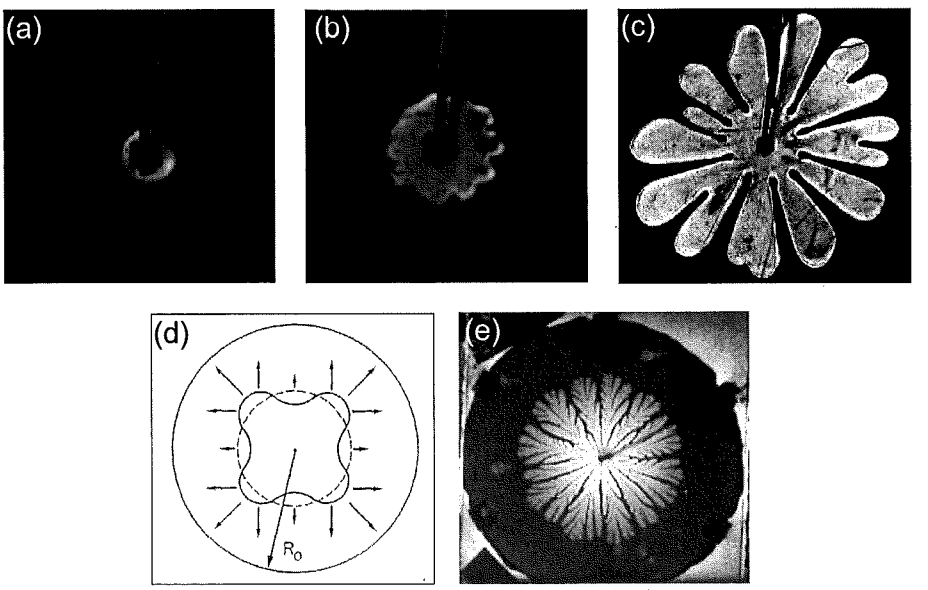

Figure 5.2: Pattern formation in the Hele-Shaw cell, where a viscous fluid is displaced by the injection of a less viscous fluid. (a) During early stages of fluid injection the 2-fluid interface is circular. (b) As injection proceeds, Mullins-Sekerka instabilities develop. (c) Fingered patterns eventually form [140]. (d) Schematic of the growth mechanism (see text), reproduced from ref.[136]. (e) An example of a fingered pattern formed under increased kinetic influence (by either increasing the viscosity difference between the two fluids, or increasing the injection rate).

In the case of the Hele-Shaw cell, the morphology results from of an interplay between surface tension and a pressure gradient at the 2-fluid interface. Surface tension tends to stabilize the interface, keeping it uniform. A pressure gradient

tends to destabilize the interface, causing fingering. Figure 5.2(d) illustrates the basic concept. The dashed line depicts the initially compact interface which is maintained by surface tension. As its radius increases by fluid injection, instabilities develop (solid line). The 4 bulges are closer to the outer boundary (large solid circle of radius R_o), so the pressure gradient and velocity of the interface (arrows) are greater at these bumps. This results in rapid and unstable growth, which can not be smoothed by surface tension, and the formation of Saffman-Taylor [141] fingers. Figure 5.2(e) presents an example of viscous fingering under conditions of increased instability, which is achieved by either increasing the viscosity difference between the two fluids, or increasing the injection rate.

In the case of pattern formation in the antimony islands, it is the cluster diffusion field that serves as the destabilizing influence on the morphology (analogous to the pressure gradient), and edge diffusion which attempts to smooth perturbations (analogous to surface tension). For small island sizes, edge diffusion smooths the island perimeter, maintaining a compact morphology. Eventually protrusions develop along the growth front and extend further into the diffusion field, and so capture a larger portion of material. These protrusions also become susceptible to instabilities, and tip splitting manifests itself in the morphologies, resulting in the highly branched islands observed in the 10 ML and 40 ML images in Figure 5.1.

5.1.2 Variation in Morphology with Flux

Figure 5.3(a) shows the evolution of surface morphology with increasing flux, for a fixed coverage of 10 ML. The low flux (F=0.005 Å/s) image shows aggregates with a fingered morphology. As the flux is increased the islands become progressively more branched, with the the high flux (F=2.0 Å/s) environment producing aggregates which are similar to many fractal islands observed in the literature [142], [77], [143]. It is also apparent that the aggregates project a greater surface area onto the substrate when the flux is increased, suggesting a reduction in height with increasing flux (this will be explored in Section 5.2). Figure 5.3(b) shows higher magnification SEM images of islands from two different flux regimes, for a fixed coverage of 40 ML. It is again clear that the lower flux islands are more compact, and project less surface area onto the substrate.

As the deposition flux increases, the arrival rate of clusters to the island perimeter also increases (t_a is reduced). For any given island size, a low flux growth environment will produce more compact shapes according to Equation 5.1, i.e. in a high flux regime, the island has less time to rearrange (via processes such as edge diffusion) to a compact shape before more clusters arrive to its perimeter. Increasing the particle flux results in faster island growth, and consequently more branched shapes. This is again consistent with other studies of the Sb/HOPG system [14]. The analogous case in the Hele-Shaw cell (shown in Figure 5.2(e)) is to increase the rate of fluid injection.

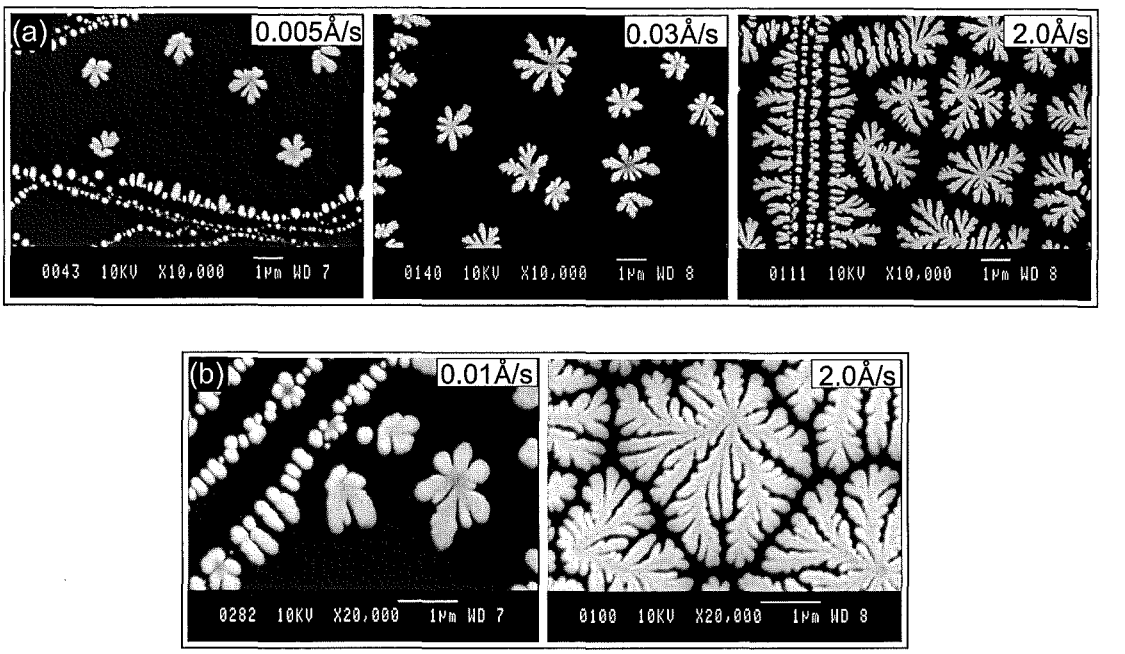

Figure 5.3: Representative SEM micrographs of the evolution of surface morphology with increasing flux. (a) The coverage is held constant at θ=10 ML. (b) Higher magnification images, θ=40 ML.

Competitive Capture

The local flux surrounding an island varies depending on the proximity of neighboring islands which compete for capture of particles from the diffusion field (competitive capture). Figure 5.4(a) shows two islands from a θ=40 ML, F=0.01 Å/s sample. Figure 5.4(b) shows the capture zones for each of these islands. Capture zones are constructed by drawing perpendicular bisectors between neighboring aggregates, and are known as Voronoi polygons [144], named after the Russian mathematician. Any particle deposited within a particular capture zone has a maximum probability of contributing to the growth of the island nucleated within it (indicated by black dots). The two arrows in Figure 5.4(b) highlight that the length of the capture zone surrounding an island varies depending on the proximity of its neighbors.

Island branches tend to grow longer towards regions which are void of other islands, since there are more diffusing particles available (larger capture zones) and consequently a faster impingement rate to the branches' growth front. Long branches have therefore grown more rapidly than their shorter counterparts, allowing less time for rearrangement into compact shapes. This is demonstrated by the top island in Figure 5.4(a), where the more branched island arm extends in the direction of the long arrow in Figure 5.4(b).

Figure 5.4(c) shows a striking example of competitive capture. The structures nucleated along the closely spaced step edges to the left and right in the

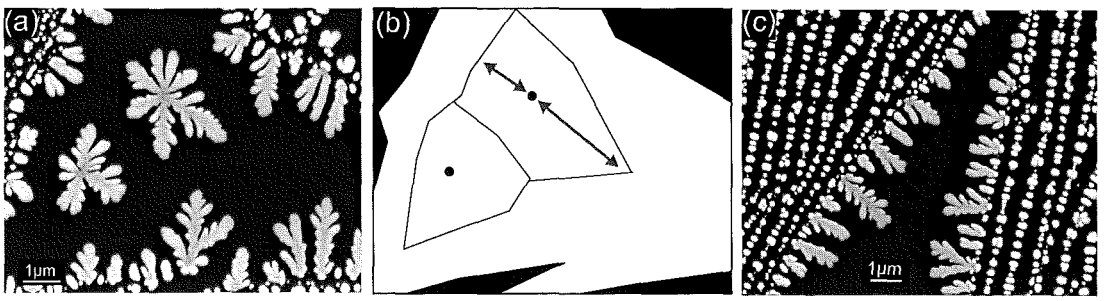

Figure 5.4: The effect of competitive capture on the island morphologies. θ=40 ML, F=0.01 Å/s. (a) SEM image showing two terrace nucleated islands. (b) Voronoi polygons for the two islands in (a). (c) Compact structures nucleated along closely spaced step edges, and branched structures protruding from widely spaced step edges (centre).

image tend to feature compact morphologies, where the local diffusion field is reduced by the high density of closely spaced aggregates. The two widely spaced step edges in the centre of the image feature branched morphologies, since the local diffusion field is increased in this region, resulting in faster and less stable growth.

5.1.3 Quantitative Analysis of Island Branching

This section quantifies the amount of branching observed in the SEM images, by characterizing the island perimeters (the contour length) as a function of island size (area of the island projected onto the substrate) for various deposition fluxes. Only islands found in regions of the sample which feature a low density of islands on large terraces (indicating a low defect density on the substrate) are included in the data sets.

Figure 5.5(a) shows a plot of the island perimeter as a function of increasing island area for multiple samples with different coverages, with the flux fixed at 0.03 Å/s. The black dots represent the experimental data. The red curve is the dependence of a circle's circumference on its area, for comparison with the experimental data. Note that only data for islands smaller than 0.6 μm^2 are plotted here, in order to show detail in the plot for small island sizes. Initially the experimental data lies on the plot for a model circle, showing that the islands are compact. At an island size of approximately 0.25 μm^2, the data departs from this curve, indicating the transition to branched morphologies. The dashed line in Figure 5.5(a) is a least squares fit to the data points which lie beyond this transition (determined from the complete data set in Figure 5.5(b)).

Figure 5.5(b) shows the complete data set for F=0.03 Å/s, where the dashed line is the same linear fit described above. From this plot it is clear that the perimeters of the branched islands have a linear relationship to the island area for $A > 0.25$ μm^2. Figure 5.5(c) presents a similar plot for multiple fluxes (indicated by the legend). All fluxes exhibit a linear dependence of the perimeter on the

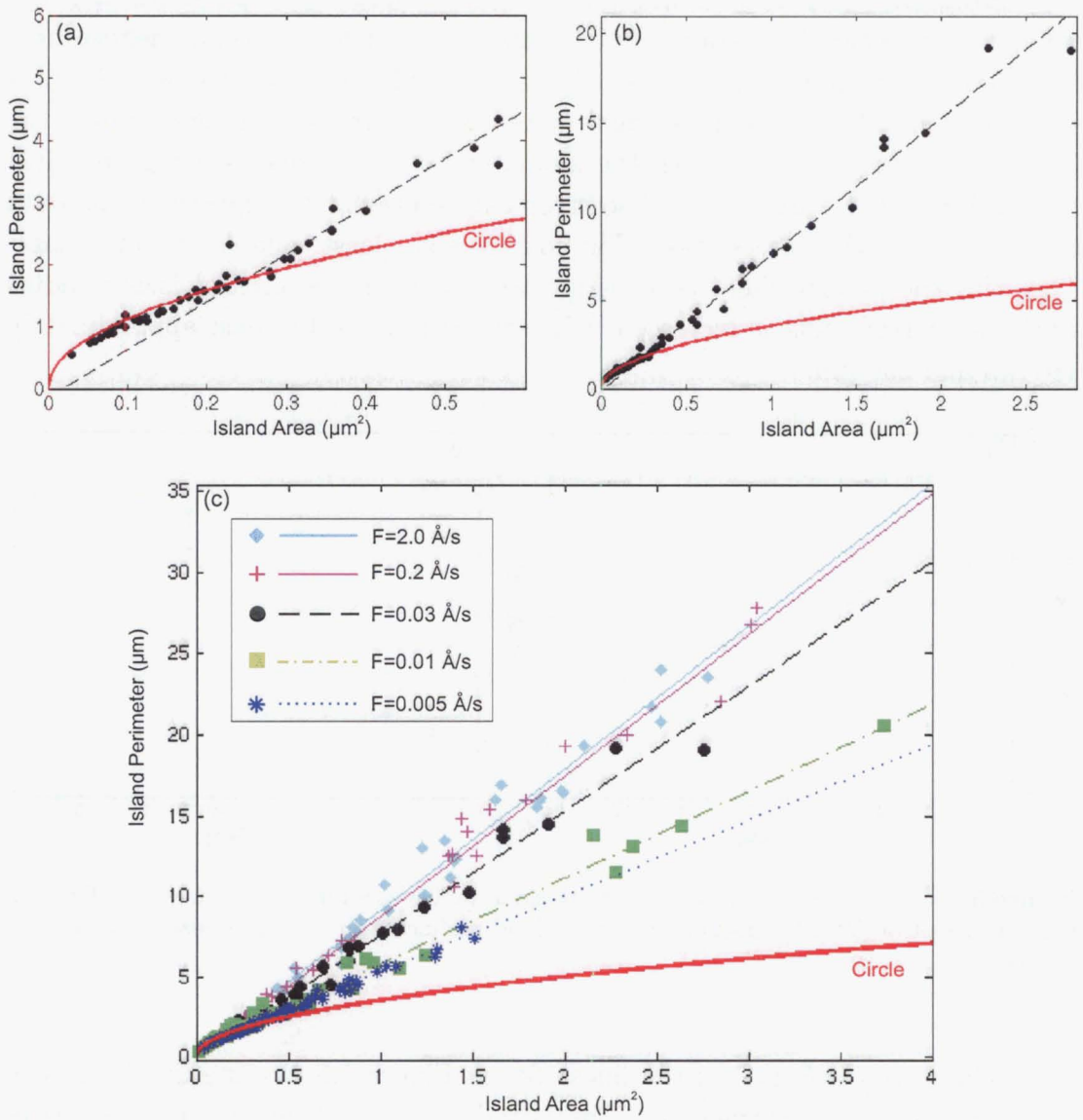

Figure 5.5: Plots of the island perimeters as a function of projected island area. The red curve plots the dependence of a circles circumference on its area, for comparison with the experimental data. (a) Island perimeter as a function of island area for multiple coverages (F=0.03 Å/s), only data for islands smaller than 0.6 μm^2 is plotted here. (b) Complete data set for F=0.03 Å/s. (c) Plot of the variation of island perimeter with increasing island size for multiple fluxes (indicated by the legend).

island size, after the transition to branched islands. It is also clear that the slope of the linear fits increase with increasing flux, indicating an increase in the degree of branching, in agreement with the qualitative observations from SEM images in the previous Section.

From the data set shown in Figure 5.5(c), we can extract the island radius at which the transition from compact to branched morphologies occurs, defined here as the critical island radius. Figure 5.6(a) shows a plot of the critical island radius as a function of flux. The data points were obtained from the intersection of the linear fits in Figure 5.5(d) with the model curve for a circle (see Figure 5.5(a) for the F=0.03 Å/s example). The error bars represent the spread in the data to both sides of this intersection. The solid line is a least squares fit to the data. This plot shows that there is a distinct reduction in the critical island radius when the particle flux is increased, with values ranging between approximately 180 nm and 290 nm.

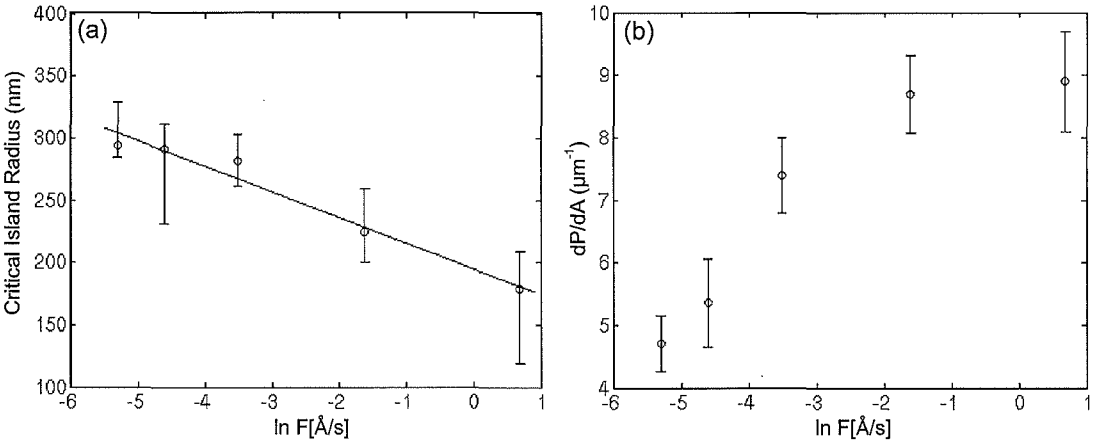

Figure 5.6: (a) Log-linear plot of the critical island radius as a function of increasing flux. (b) Log-linear plot of dP/dA (dependence of the island perimeter on the island size) as a function of flux.

The slopes (dP/dA) of the linear fits in Figure 5.5(c) quantify the dependence of the island perimeter on the island size, and hence define the degree of branching for the various fluxes. Figure 5.6(b) shows a plot of dP/dA as a function of flux. Each data point is comprised of at least 30 typical islands taken from multiple samples, so should provide an adequate representation of the particular flux environment. The error bars represent the standard deviation in the raw data. From this plot it is evident that the islands become significantly more branched with increasing flux, but this trend seems to level off in the high flux limit. This implies that there is a maximum degree of branching reached at F$\sim$0.2 Å/s corresponding to $dP/dA \sim 8.5\ \mu\text{m}^{-1}$. However, it was not possible to perform higher flux experiments to further investigate this effect, owing to difficulties in performing sufficiently short depositions to allow observation of

isolated islands (recall that the island area projected on to the substrate increases with increasing flux). For this reason we conclude that the degree of branching increases with increasing flux, but may reach a maximum perimeter to area ratio at F$\sim$0.2 Å/s.

The values of the critical island radius plotted in Figure 5.6(a) only apply to islands nucleated on regions of the substrate with a low defect density. Figure 5.7 shows an example (high magnification) of island nucleation on a defect contaminated substrate terrace (θ=10 ML, F=0.03 Å/s). The morphology is characterized by a high density of irregularly shaped islands, many of them with crescent shapes. These islands are smaller than the critical island radius for this flux, which is 280 ± 20 nm from Figure 5.6(a). It seems that defects effect the shape formation in antimony islands, inducing the fingering morphology at significantly smaller island sizes.

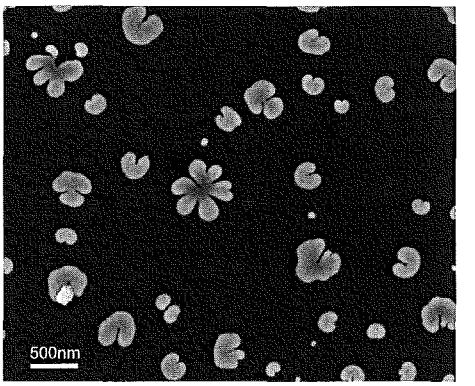

Figure 5.7: FE-SEM image of island nucleation on a defect contaminated substrate. θ=10 ML, F=0.03 Å/s.

Kaiser *et al* [19] report a critical island radius of about 60 nm (and note that compact islands are never observed beyond this radius), which is significantly smaller than we present in Figure 5.6(a). Their SEM images of compact islands feature a significantly higher island density than in our case, indicating the likelihood of nucleation on defects.

5.1.4 Fractal Dimension

The fractal dimension provides another means of quantifying the island morphology. For DLA-type island growth, the fractal dimension is often quoted in the literature to quantify coarsening effects which come into play during island annealing [143], [77].

The fractal dimension, f_D is calculated here by the box counting method [145], which involves superimposing a grid of square boxes over a thresholded island, and varying the size of the boxes. The number of boxes of a particular size which are filled by the island (box count) are plotted on a log-log graph as

a function of the box length (in units of pixels). For the pattern to be classed as fractal, the data should be linear, and $1 < f_D < 2$, i.e. between a straight line (1D) and a completely filled in plane (2D).

Figure 5.8(a) shows an example of the the box counting method applied to a θ=10 ML island deposited at 2.0 Å/s, where the box lengths are indicated in the Figure. It is evident that beyond some particular box length, the analysis runs out of statistics, as the pattern size approaches the box size. Additionally at very small box sizes, pixelation of the image around the island perimeter effects the analysis. These two effects are demonstrated in Figure 5.8(b), which shows a log-log plot of the box count as a function of box length, for box lengths ranging from 1-255 pixels. The data deviates from a straight line at very small box lengths, demonstrating the pixelation artifact. Very large box lengths produce noisy data, and no longer represent the scale invariance of the pattern. Figure 5.8(c) shows the same plot, but with the data below a box length of 5 pixels and above 34 pixels removed, to ensure an accurate calculation of fractal dimension. The linear fit to the data yields $f_D = 1.83 \pm 0.05$. A comprehensive discussion of confidence limits in the scaling behavior of DLA-type fractals can be found in ref.[146].

Figure 5.9 shows a plot of the fractal dimension for various fluxes, where each data point represents a single island. It is clear that there is no distinguishable trend in the fractal dimension as a function of flux. The average fractal dimension for the complete data set is 1.77 ± 0.05 (the uncertainty is taken as the standard deviation), which is consistent with values obtained for other DLA-type structures [71], [77]. It seems likely that the spread in the data in Figure 5.9 is a result of difficulty in determining appropriate upper and lower cut-offs in the data set, particularly as the flux is reduced, since the structures' perimeter smoothens as a result of increased edge diffusion.

The smoothing of the growth front, brought about by a reduction in flux, is analogous to increasing the temperature of the system, since both lead to a general compacting of DLA-type structures. A transition must occur from fractal to compact geometries with either increasing temperature or decreasing particle flux. This transition has been observed in KMC simulations of MBE growth at substrate step edges in the Cu/W(110) system [147]. DLA type structures with $f_D = 1.7$ are observed at low temperature, in agreement with STM investigations of Cu/W(110) [148]. With increasing temperature the branches begin to widen and smoothen (with initially no change in the fractal dimension). Beyond a critical temperature, the fractal dimension rapidly increases to 2, signifying a transition to compact (2D) structures at the step edges. It seems likely that if the flux could be sufficiently reduced in the Sb/HOPG system, a similar transition may be observed.

In the previous Section it was shown that the perimeter to area ratio of the islands clearly decreases as the flux is reduced, consistent with the compacting of the island shapes observed in the SEM images in Figure 5.3. The fractal dimen-

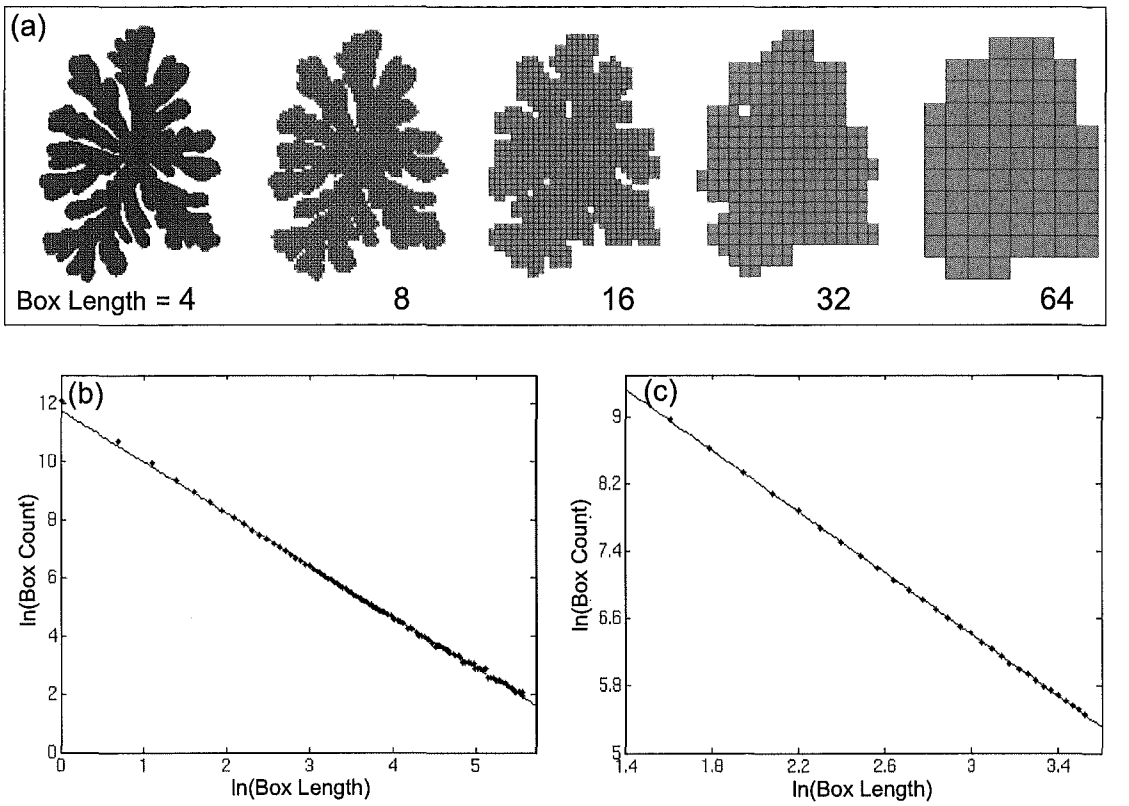

Figure 5.8: An example of the box counting method of fractal analysis, applied to a θ=10 ML island deposited at 2.0 Å/s. (a) Box mesh superimposed over an island, the box lengths are given for each illustration (in units of pixels). Log-log plots of the box count as a function of box length for: (b) Box lengths ranging from 1 to 255 pixels. (c) Box lengths ranging from 5 to 34 pixels.

sion analysis seems somewhat contradictory to this, since the fractal dimension is found to be independent of flux.

Stegemann *et al* have also performed a fractal analysis of antimony islands as a function of flux [14] for a similar flux range to that used in our study. They report values of f_D ranging from 1.45 to 1.67, with f_D *increasing* with increasing particle flux. This is also in clear contrast to the present case. The reason for this discrepancy between two studies of the same system is unknown at this stage.

5.2 Island Heights From AFM Scans

This Section explores the island heights, obtained from AFM scans. The variation in height with increasing coverage is first investigated. Next the influence of flux on the heights is discussed, including the effects of competitive adatom capture. Section 5.2.3 addresses a build up of material which is found to exist around the island perimeters.

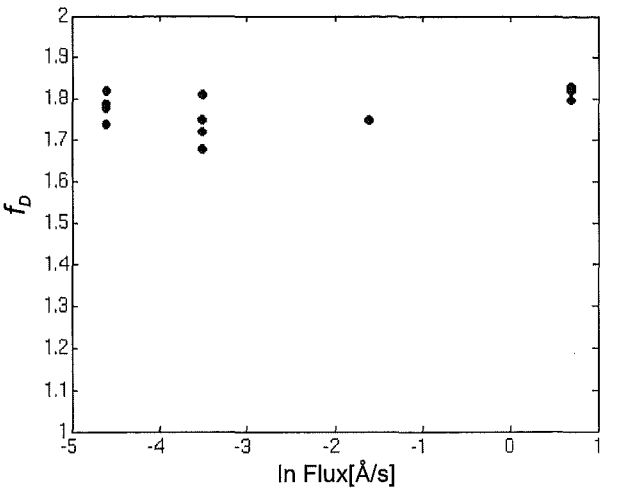

Figure 5.9: Plot of the fractal dimension, f_D as a function of flux, where each data point represents a single island.

5.2.1 Variation With Coverage

Figure 5.10 shows two AFM images (in 3D plotting mode) of islands from a θ=10 ML, F=0.03 Å/s sample. The increase in image resolution compared to the SEM scans from the previous Section is immediately obvious. Note however, that while the AFM technique is a useful compliment to SEM imaging, it is not suitable to completely characterize the film morphology independently. AFM scans typically take 30 minutes for reasonable image quality, which prohibits analysis of a large number of images from each sample. Additionally, high speed low magnification imaging is required to initially assess the film morphology, which is generally not possible with the AFM since fast tip scanning tends to damage the islands and contaminate the cantilever tip.

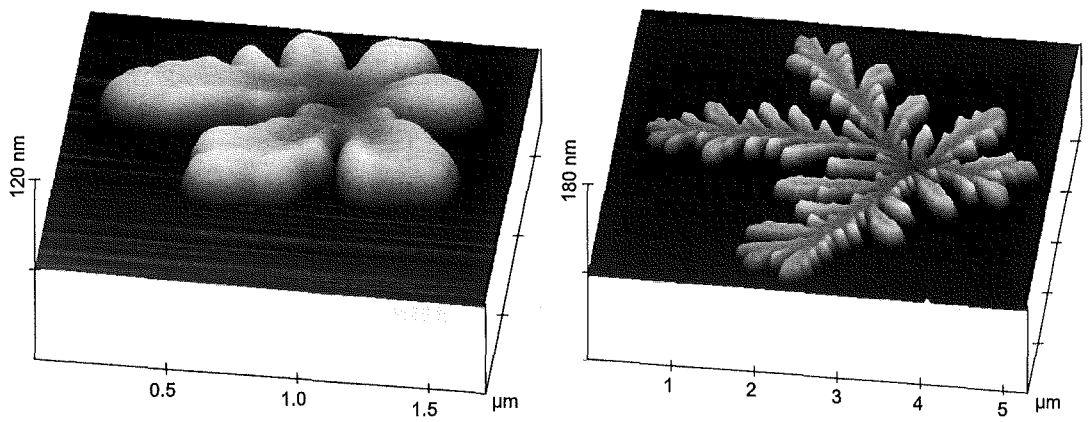

Figure 5.10: AFM images of two antimony islands from a θ=10 ML, F=0.03 Å/s sample, note the scale change between the two images.

Figure 5.10 reveals that there are height variances within individual islands, requiring that AFM cross-sections are taken at multiple locations, to ensure a representative account of the 3D morphology. Figure 5.11 shows a plot of the branch height (measured at the tip) as a function of the branch length for multiple coverages (indicated by the legend), deposited at a fixed flux of 0.03 Å/s. The data for each coverage is taken from multiple islands, and in some cases multiple samples to ensure that the heights are representative of the particular deposition parameters. It is apparent from this plot that for any given coverage, longer branches tend to be flatter (which will be addressed in the next Section). For this reason, the island heights are characterized in terms of branch length, rather than quoting a mean height to represent a given flux and coverage. Figure 5.11 also shows that the branch heights increase with increasing coverage. In previous sections it was shown that low coverage samples feature more compact islands. The 2 ML and 5 ML data sets in this plot are taken from predominantly compact islands, where in such cases the branch length is taken as the radius of a circular island.

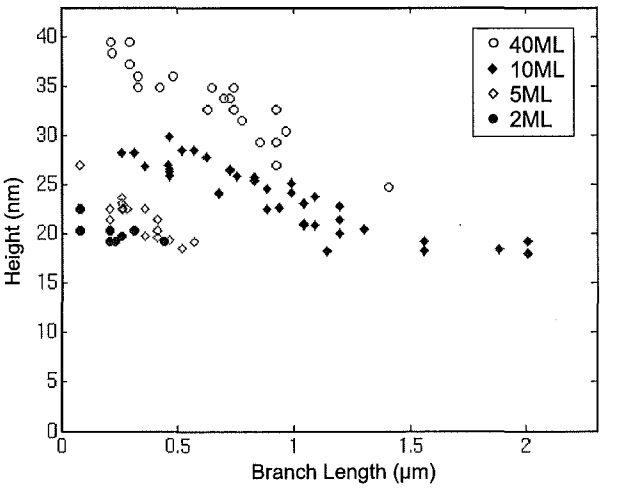

Figure 5.11: Plot of the island branch height as a function of branch length, for various coverages (indicated by the legend). The flux fixed at 0.03 Å/s.

The increase in the general island heights with increasing coverage in Figure 5.11 shows that as deposition proceeds, a portion of the new material arriving to the growth front is transported upward. However, the majority of material seems to contribute to lateral (2D) island growth. For example, the F=0.03 Å/s (θ=10 ML) data set in Figure 5.11 reveals island heights between 17-30 nm, and the 10 ML SEM image at the same flux in Figure 5.1 shows that the islands are typically greater than 1μm lateral diameter, giving an aspect ratio of order 0.02.

5.2.2 Variation With Flux

Figure 5.12 presents a plot of the branch height as a function of branch length for various fluxes (indicated by the legend), with the coverage fixed at 10 ML. The data points for each flux are taken from multiple islands and multiple samples, ensuring a representative data set. This plot shows that for each flux, the branches become flatter with increasing length, and it appears that the very long branches level off to some minimum height for each flux. Figure 5.12 also shows that that the islands become flatter with increasing deposition flux, confirming the qualitative observation from SEM images in Figure 5.3.

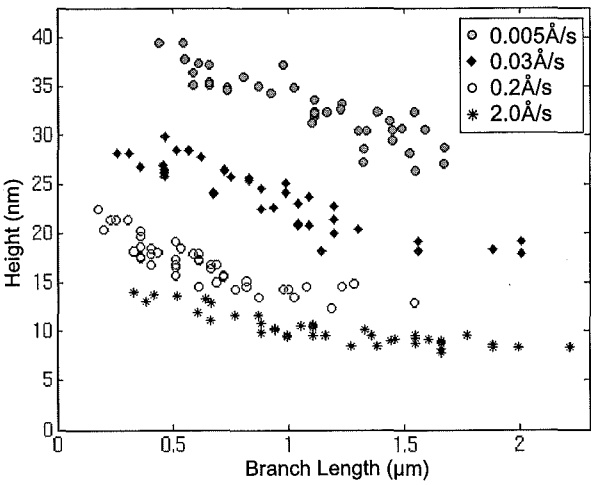

Figure 5.12: Plot of the island branch height as a function of branch length, for various fluxes (indicated by the legend). The coverage is fixed at 10 ML.

Increasing the particle flux reduces the available time for transport of particles from the the perimeter to the top of the island (rearrangement to 3D morphologies), before the next particles arrive from the diffusion field and 'pin' the previous material in place. This accounts for the reduction in island height with increasing deposition flux demonstrated in Figure 5.12.

The flattening of the island branches with increasing length in Figure 5.11 and Figure 5.12, is consistent with the increased growth rate for longer branches compared to their shorter counterparts, as was discussed in Section 5.1.2, since faster growth rates allow less time for 3D rearrangement. Figure 5.13 shows a typical example of the effect of competitive capture of the diffusion field on the height profile. The AFM image shows two small islands nucleated close to each other, with an absence of other islands in their vicinity. The associated height profile taken through the horizontal line in the image, reveals that the sides of the islands facing each other are taller than other parts of the islands. The capture zone for diffusing particles is significantly reduced between the two islands, resulting in slower growth, and consequently a more compact and 3D

morphology.

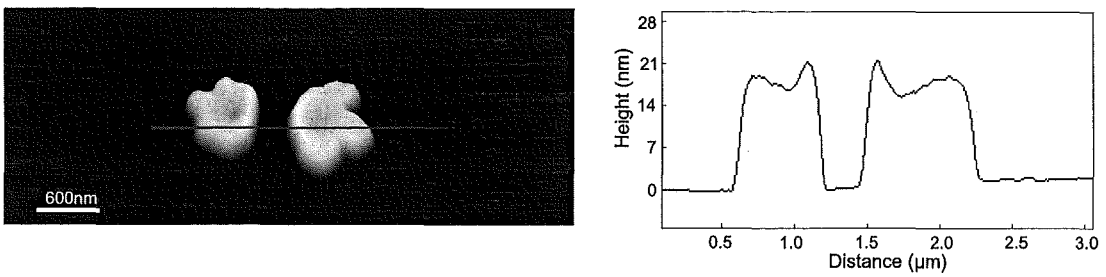

Figure 5.13: The effect of competitive capture of the diffusion field on the island height profiles, θ=5 ML, F=0.03 Å/s. Left: AFM image, with the position of a height cross-section indicated by the horizontal line. Right: Height cross-section.

5.2.3 Island Perimeters

In many of the AFM scans, a build up of material was found to exist around the island perimeters. Figure 5.14(a) shows a particularly pronounced example of the effect, where the branches have an increase in grey scale intensity around their edges, indicating an increase in height. Figure 5.14(b) shows an FE-SEM image from a different sample with different deposition parameters. The increased brightness around the edges of the branches is again present, excluding the possibility of this feature being attributed to an AFM tip effect.

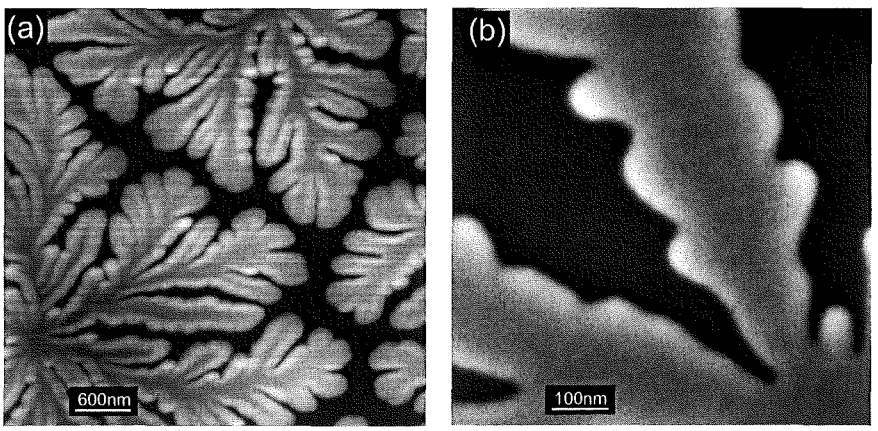

Figure 5.14: Images demonstrating the build up of material around the perimeter of the island branches. (a) AFM image, θ=40 ML, F=2.0 Å/s. (b) FE-SEM image θ=10 ML, F=0.03 Å/s.

At the end of deposition, $t_a \rightarrow \infty$ since the diffusion field is diminished when the last clusters arrive to the islands' growth front. It seems likely that this allows for more 3D rearrangement of material during the final stages of island growth, leading to the build up of material around the edges of the fingered structures.

Figure 5.15 shows representative AFM images and height profiles for two islands with 10 ML coverage, deposited at F=0.03Å/s (a), and F=0.005 Å/s (b). The height profile for the higher flux example clearly shows the elevated height at the branch edges, while this feature is absent in the profile from the low flux island. A low flux growth environment allows taller more thermodynamically favorable (compact) shapes to aggregate. It therefore seems likely that there would be less tendency for further 3D aggregation at the end of deposition.

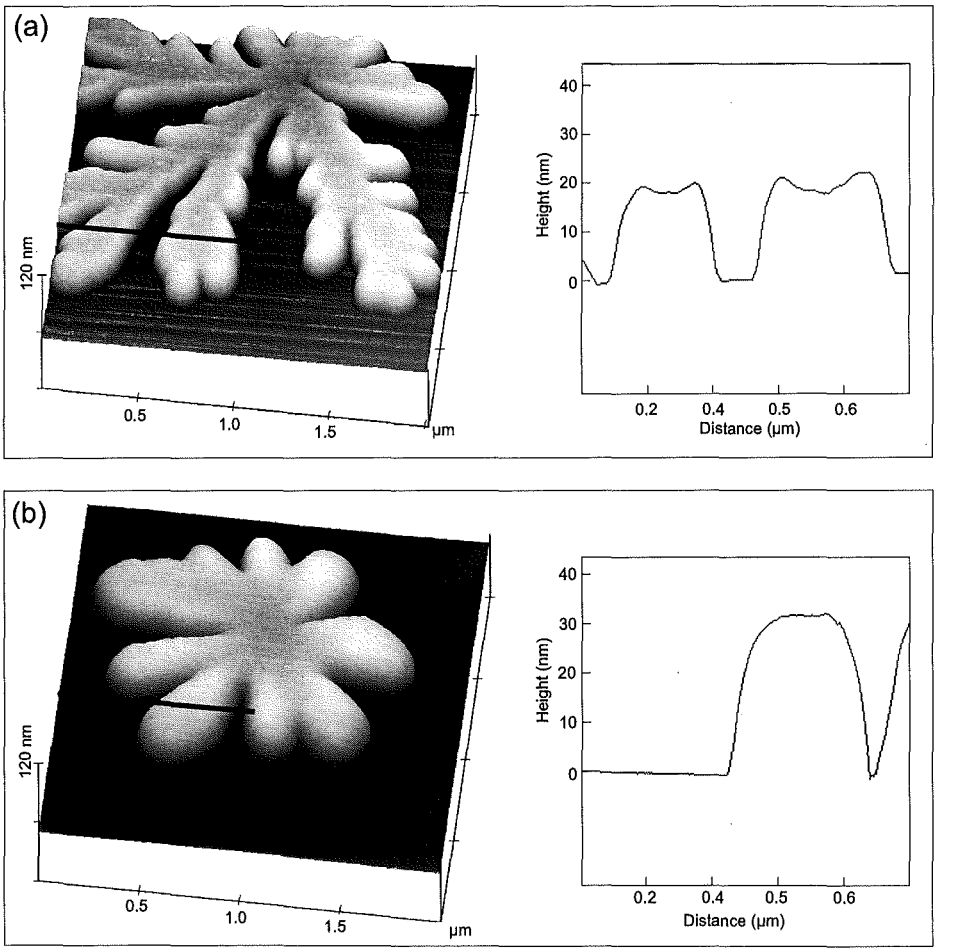

Figure 5.15: 3D AFM images and height profiles for islands with 10 ML coverage. (a) F=0.03 Å/s, the height cross-section (right) shows elevated heights at the edges of the branches. (b) F=0.005 Å/s, the height cross-section (right) does not feature the elevated height at the island edges.

5.3 Co-existing Morphologies

A different type of aggregate to those discussed in previous Sections was occasionally observed to co-exist on some samples, and is shown in Figure 5.16. These new structures (dendrites) were typically found in regions of the substrate with

a high defect density (such as step edges), as demonstrated in Figure 5.16(a). The FE-SEM scan in Figure 5.16(b) shows a higher magnification image. Note that the FE-SEM image was obtained with the microscope stage tilted at 70°, and the image subsequently tilt corrected, which produces the shadowing around the islands and gives an impression of height. This image shows an example of a new structure which surrounds a fingered island, and therefore has grown after the more typical island. From the shadowing effect, it seems that the dendrites are significantly flatter than the fingered islands. Their heights could not be quantified with AFM measurements, since the sparseness of the structures prohibited their location with the AFM's relatively small field of view.

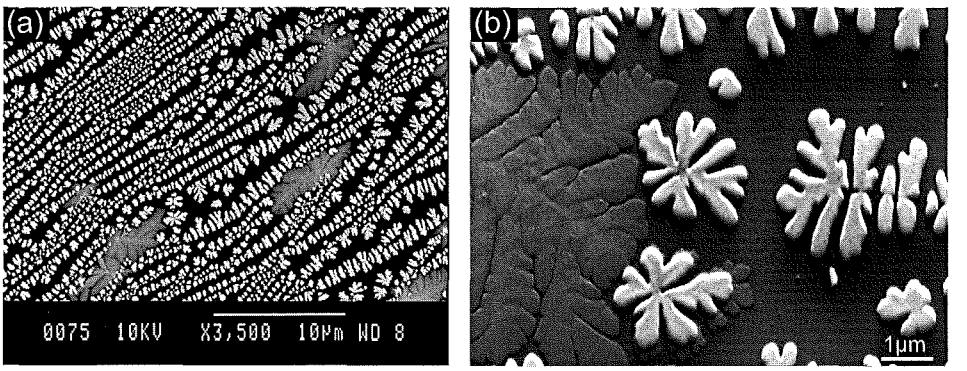

Figure 5.16: Micrographs of dendrites which were found to occasionally co-exist with the more typical fingered morphology. F=0.03 Å/s, θ=40 ML (a) SEM image (b) FE-SEM image.

The manifestation of the flat dendritic morphology was not reproducible for a given set of deposition parameters. It is however worth noting that the new morphology was never observed above deposition rates of 0.03 Å/s, indicating that it is probably a low flux effect. This dendritic morphology has also been reported by Kaiser *et al* [19] in a low flux environment, and observed in islands grown by diffusion of large antimony clusters [135].

5.4 The High Coverage Limit

The preceding Sections have considered the regime where island growth occurs mainly by diffusion of clusters across the substrate, and subsequent incorporation at the island perimeter. When the coverage (or in this case, also the flux) is increased, the islands project a greater surface area onto the substrate, and occupy an increasing region of their original capture zone (see for example the left image in Figure 5.3(b)). At sufficiently high coverages, the capture zone will entirely fill, bringing about island coalescence.

Figure 5.17 presents SEM images of the evolution in film morphology with increasing coverage, in the high coverage regime (F=2.0 Å/s). In the 200 ML

image a small portion of each aggregates capture zone is still visible. At θ=400 ML the capture zones are virtually absent, but island boundaries are still clearly visible. Increasing the coverage to 1000 ML results in barely distinguishable island boundaries, and by 2000 ML they have entirely disappeared, after coalescing to form a continuous film. The inset in the 2000 ML image shows that the film is now characterized by a coarse grained morphology, which was not present at any other coverage.

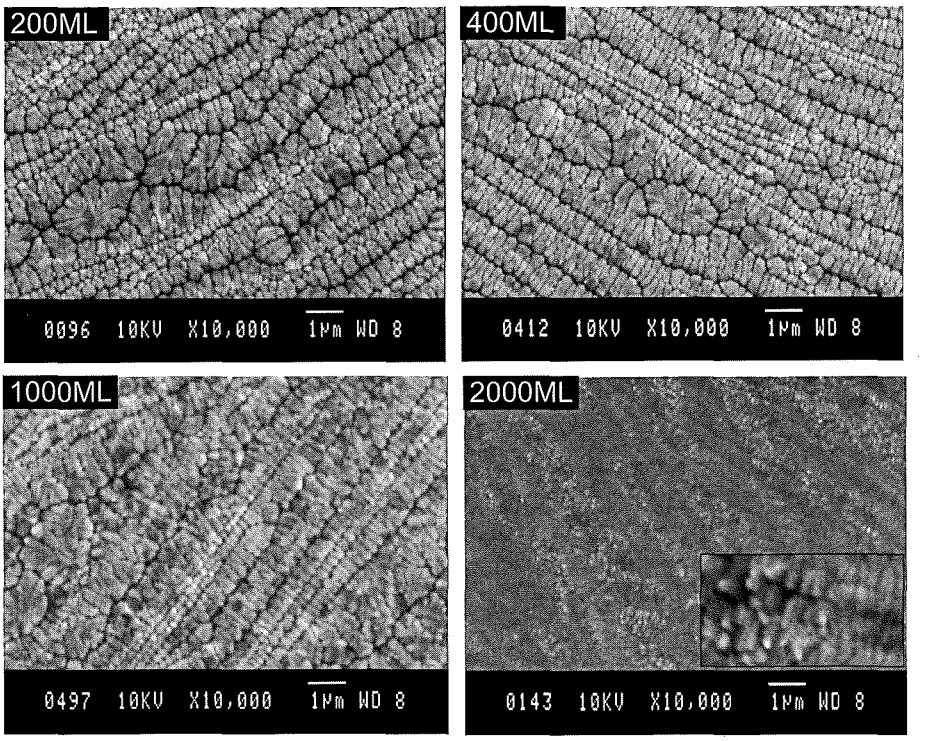

Figure 5.17: SEM images of films in the high coverage limit. The coverage is indicated on each image, the flux is fixed at 2.0 Å/s. The inset in the θ=2000 ML image shows a higher magnification region of the film (image size 2×1 μm).

Kaiser *et al* [19] have shown a coverage dependent transition from large branched islands to a film with small crystallites (see Figure 2.13 in Chapter 2). In their case there is a transition from large islands to a granular film with increasing coverage. It is this granular morphology which adopts the hexagonal symmetry of the small crystallites shown in Figure 2.13 [149]. This seems to be a similar result to the transition observed in Figure 5.17, where the fingered structures eventually evolve into a granular morphology. However, the resolution of our SEM imaging did not allow the precise morphology of the granular film to be distinguished (higher resolution AFM imaging of these samples was prohibited by a tendency for tip contamination). It is also worth noting that in the case of Kaiser *et al*, the transition is already complete at a coverage of 200 ML, while we still observe island growth at coverages up to at least 1000 ML.

5.5 Summary of Sb/HOPG

This Chapter has examined the morphology and growth characteristics of antimony aggregates on HOPG substrates. The deposition parameters of coverage and flux were altered, and resulting variation of the island morphology investigated. Using SEM and AFM we have observed the growth of both compact and branched island types, and an occasional coexisting dendrite morphology in low flux growth environments.

With increasing coverage, the islands undergo a transition from compact to branched morphologies, demonstrating the manifestation of Mullins-Sekerka instabilities. The heights also increase with increasing coverage. In the high flux limit, there is a transition to a continuous film at ~2000 ML

When the deposition flux is increased, flatter islands form, with a significantly more branched morphology for any given coverage. With increasing flux, the critical island radius for the transition from compact to branched morphologies reduces from ~290 nm (F=0.005 Å/s) to ~180 nm (F=2.0 Å/s). After this transition, the island perimeter scales linearly with the projected island area ratio for each flux. However, the perimeter/area ratio increases with increasing flux, in accordance with the increased branching observed in the SEM images. The proximity of neighboring islands also effects the branching and heights, since the local growth rates (and hence time for rearrangement) are altered due to competitive capture of the diffusion field. Flatter and more branched islands are found to extend toward regions where there is an absence of other islands.

The general island morphologies, and compact to branched transition, are consistent with other studies of the Sb/HOPG system, allowing confidence that the UHV system described in Chapter 3 is sufficiently optimized for diffusion and aggregation studies. However, this investigation has differed from previous studies by showing a flux dependence in the transition from compact to branched morphologies. Additionally, the island heights have been characterized, providing a more in-depth picture of the the 3D morphology. This Chapter has shown that the aggregation of antimony islands on HOPG represents a classic system where the interplay between kinetics and thermodynamics determines the 3D morphology. Low fluxes shift the balance towards more thermodynamically favorable compact shapes, while higher fluxes increase the kinetic dominance, resulting in flatter and more branched morphologies.

Chapter 6

Bismuth/HOPG: Diffusion, Nucleation, and Growth

This chapter involves an investigation of the diffusion, nucleation, growth, and coalescence of bismuth islands on HOPG (grade ZYB) substrates. The coverage range of 0.2 ML - 100 ML is studied with the flux varied between 7×10^{-4}–1.0 Å/s. The first section discusses the morphology and growth of islands on relatively defect-free regions of the substrate. The main focus here is the effect of altering the experimental parameters of flux (F) and coverage (θ) on the shape, size, and density of the islands. Section 6.2 explores a striping detail that was discovered within individual islands in the previous Section. Section 6.3 examines the large coverage limit, where islands begin to coalesce, and eventually form a continuous thin film. This leads to an investigation of the aggregates' crystal structure in Section 6.4, where an orientation transition is identified. The nucleation and growth of aggregates at natural step edges on the graphite surface are considered in Section 6.5, with the morphology again studied as a function of varying flux and coverage. The dependence of island morphologies on post deposition vacuum time, and the stability of the structures in ambient conditions are detailed in Section 6.6. Section 6.7 considers the effect of increasing the surface defect density by reducing the annealing temperature during the substrate cleaning process.

6.1 Island Morphologies: Growth and Kinetic Influences

This section focuses on the effects of shifting the balance between thermodynamic stability and kinetically determined morphologies by altering the coverage and flux. The evolution of island shapes and heights are first investigated, followed by a statistical analysis of the island density and size. Finally we consider the degree of adsorbate condensation on the graphite surface.

6.1.1 Variation in Morphology With Coverage

The evolution in island shape as the coverage is increased is depicted in Figure 6.1, for the F=0.005 Å/s (low flux) case. SEM images for different coverages showing groups of islands, are presented in Figure 6.1(a). The magnification of

$10,000\times$ was chosen because it allowed imaging of multiple islands within a single scan. This magnification was also the maximum that could be obtained without significant beam damage to the islands (see Chapter 4). In order to observe detail of individual islands, AFM scans were required to obtain the necessary resolution. Single representative islands are shown in Figure 6.1(b). It is clear that the islands feature stripes, which will be explored in detail in Section 6.2. This Section focuses on the morphology of the island bases, hence the stripes are only referred to qualitatively where necessary in the following discussions.

The θ=0.2 ML SEM image shows a mixture of compact and slightly branched island morphologies. The smaller islands are compact, while the slightly larger islands tend to feature branched-like perimeters. The AFM image of a compact island reveals that these small islands are generally elongated hexagons. The θ=0.5 ML SEM image shows an increase in the island size. It is also apparent that the majority of these islands have a 6-point star shape. As the coverage is increased further, the islands continue to increase in size, with no obvious evolution of the island density. Most islands maintain the 6-point star morphology. The islands in the θ=1.5 ML SEM scan begin to show a small amount of edge splitting around the island perimeter, a feature which is particularly obvious in the accompanying AFM scan, and is also observed in the θ=2.0 ML sample. It is therefore clear that there is an evolution in island shape from compact islands with elongated hexagonal shapes, to 6-point star morphologies with increasing island size in the 0.005 Å/s flux environment.

The Bi/HOPG system has been investigated previously [87], but in that case the samples were not cleaned via UHV thermal treatment prior to deposition. Consequently, the resulting morphology is quite different to the present case, and consisted of a high density of small compact elongated particles, consistent with surface defect decoration.

The island morphologies in Figure 6.1 are consistent with a kinetic influence becoming increasingly active with increasing coverage (in contrast to the Sb aggregates in Chapter 5, there is a high degree of symmetry in the Bi island shapes, the origin of which will be addressed in Section 6.4). During the early stages of growth (at low coverage), the islands have time to rearrange, via edge diffusion, into a thermodynamically favorable compact morphology before the arrival of more material to the island boundaries. As deposition proceeds, the points of a hexagon will capture a larger portion of the diffusing material than the straight island edges, since they protrude further into the diffusion field. For small island sizes in a low flux environment, adatoms arriving at these corner sites are able to be transported via edge migration along the sides of the hexagon, hence maintaining a compact morphology. As the length of the hexagon faces increase with the growing island, eventually the material will not have time to evenly disperse along the faces. It is at this stage that the hexagons corners begin to grow more rapidly than the faces, and we observe a transition from hexagonal

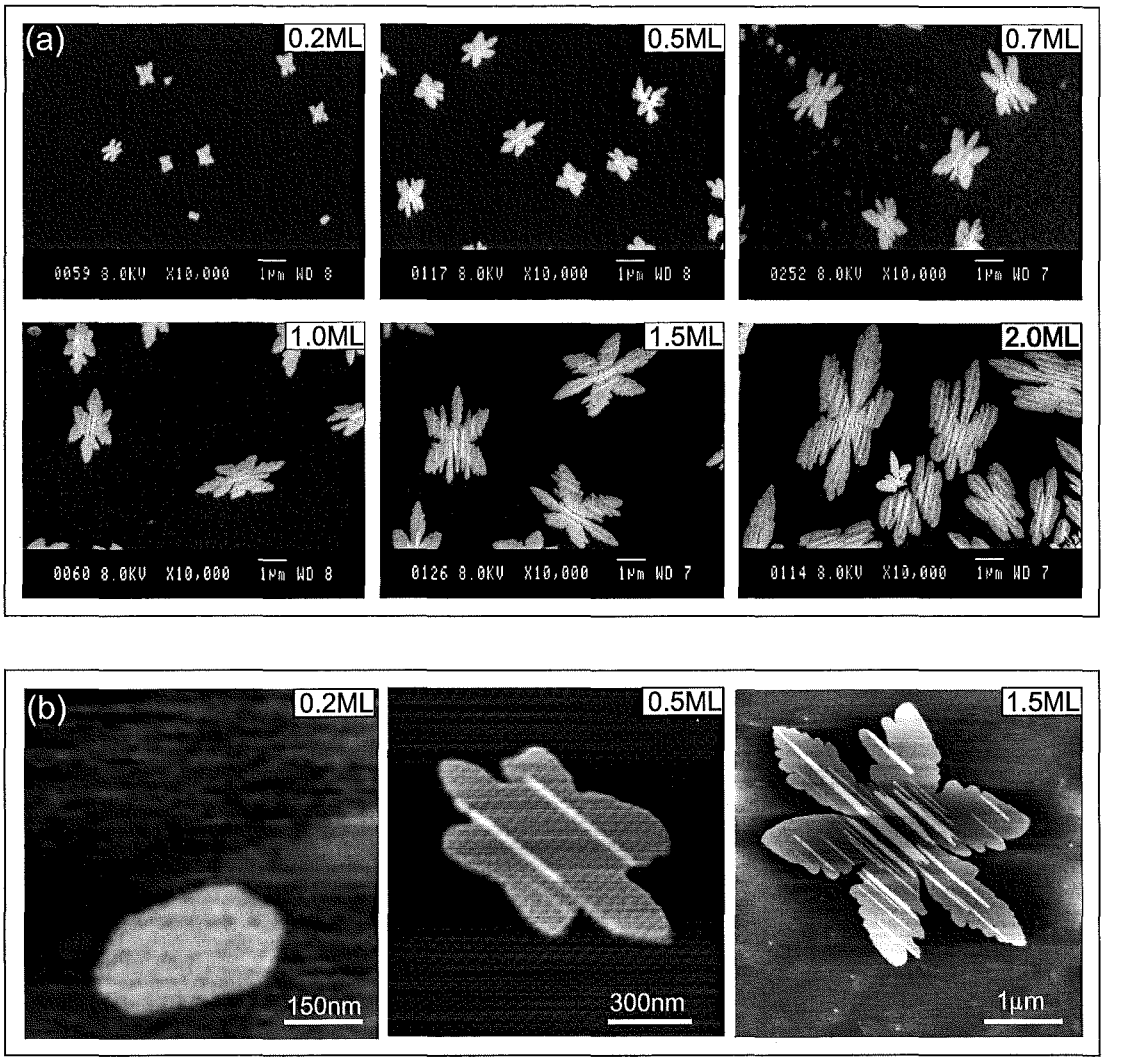

Figure 6.1: SEM micrographs (a), and AFM scans (b), of the evolution of island morphology with increasing coverage. The flux is held constant at 0.005 Å/s.

islands to 6-point stars. As the coverage is increased further, the islands continue to grow, with the star points capturing an increasing amount of the diffusion field. Instabilities which result in edge splitting develop around the growth front, which is no longer able to cope with the transport of adatoms over the long distances of the edges of the star points.

6.1.2 Variation in Morphology With Flux

Altering the deposition flux allows further examination of the influence of kinetics on island growth. Low deposition rates allow longer time scales for rearrangement to energetically favorable morphologies, before subsequent adatoms are incorporated into the islands. Conversely, kinetic effects should become apparent when the flux is increased, as the time scale for stable morphologies to be attained is reduced.

Figure 6.2 shows the evolution of island shape with increasing coverage in the F=0.2 Å/s (high flux) case. It is clear that there is a higher density of smaller islands than in the low flux example, which will be discussed in Sections 6.1.5 and 6.1.6. The island sizes increase with increasing coverage, with no notable variation in the island density. The θ=0.2 ML SEM image shows that the small islands are relatively compact at the resolution of the image. The AFM image however shows that the perimeter features some degree of irregularity. Also there is no obvious symmetry associated with the island shape. At a coverage of 0.5 ML the islands have become branched. Some islands appear to have a 6-point star morphology, but many do not feature this symmetry. The θ=1.5 ML images show a large degree of edge splitting, with many of these instabilities comparable in length to the primary arms of the islands.

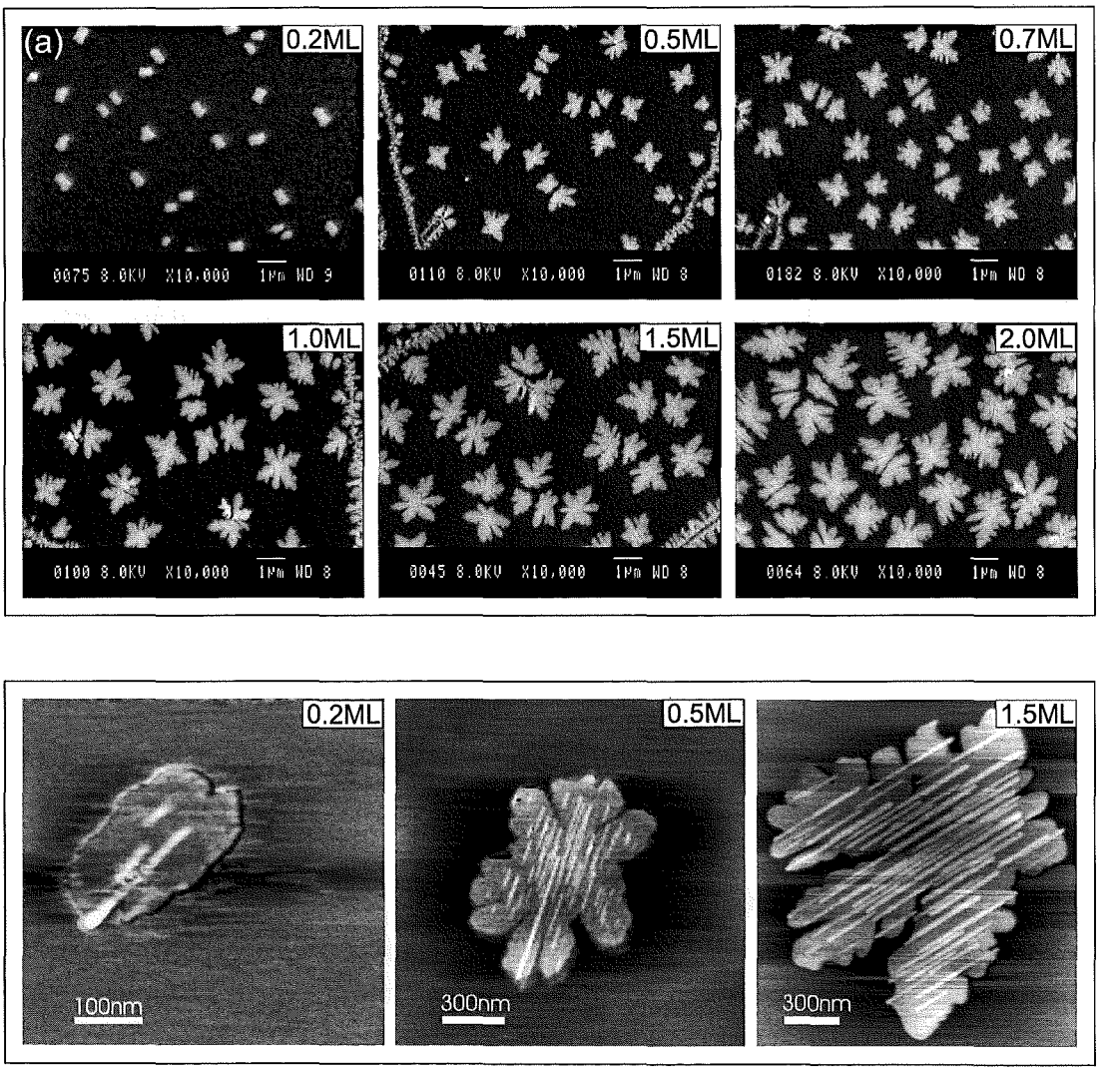

Figure 6.2: SEM micrographs (a), and AFM scans (b), of the evolution of island morphology with increasing coverage. The flux is fixed at 0.2 Å/s.

A comparison of Figure 6.1 and Figure 6.2 reveals that the transition from compact hexagonal to 6-point star is less prevalent in the higher flux case. Kinks that protrude from the perimeter of small islands will grow more rapidly than other parts of the island. In the low flux case these were at the corners of hexagons, resulting in a star shaped morphology with increasing size. The absence of symmetry in the positioning of kink sites in many of the small islands in the high flux case results in a more random growth shape with increasing island size. This is made particularly obvious by a comparison of the θ=1.5 ML AFM images in Figure 6.1 and Figure 6.2.

Figure 6.3 presents a series of SEM images, showing representative islands from various fluxes (indicated on the image), at a fixed coverage of 1.5 ML. The F=7×10^{-4} Å/s image shows two different island types which were found to coexist. One is an elongated hexagonal shape with a smooth perimeter, and the other is a very elongated and larger star shaped island. The F=0.005 Å/s image shows a more pronounced star shape, with a clear elongation, and a few small instabilities around the growth front. An increase in flux to 0.03 Å/s produces a less elongated star shape, with more edge instabilities. The 0.2 Å/s flux produces large scale edge splitting around the perimeter, and no notable island elongation. A further flux increase to 1.0 Å/s results in a more random growth shape, which is characterized by instabilities and edge splitting. In this very high flux example, the primary arms of a star are not generally present, since the growth of instabilities competes with the growth of any primary arms, and eventually dominates the morphology.

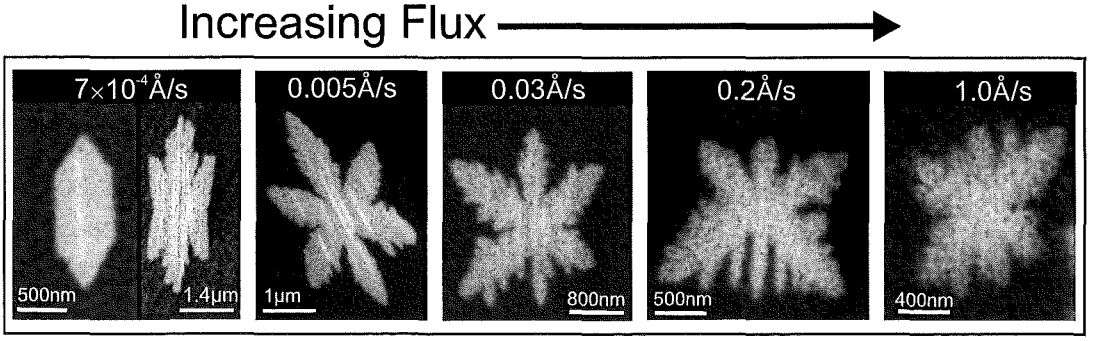

Figure 6.3: Representative SEM images of the evolution in island morphology with increasing flux. The coverage is held constant at 1.5 ML.

With increasing flux the islands undergo a transition from compact hexagonal, to 6-pointed star, to branched and disordered growth. The case of the hexagonal islands in the low flux limit (F=7×10^{-4} Å/s) is particularly interesting, since it demonstrates the competition between kinetics and thermodynamics. When the flux is extremely low, edge diffusion is successful in preventing the accelerated growth of the hexagonal corners. With increasing flux, kinetics controls the morphology, resulting in star shaped islands, and eventually quite disordered growth.

This type of morphology was observed previously on low coverage samples (see the 0.2 ML AFM image in Figure 6.1). However in this extremely low flux, high coverage example, the hexagonal islands are significantly larger, enabling clear resolution of the hexagonal faces in the SEM images. The co-existence of both hexagonal and star shaped islands on the same sample indicates that the 7×10^{-4} Å/s flux is just at the limit of the compact-branched transition. Figure 6.4 shows two SEM images of the coexisting morphologies. A region where star shapes and hexagonal morphologies are more prevalent is shown in (a) and (b) respectively. Figure 6.4(b) represents the more typical morphology for this coverage and flux. It should be noted that difficulties in stabilizing the flux on the deposition rate monitor leads to a large margin of error in the magnitude of the flux and coverage in the 7×10^{-4} Å/s flux example. For this reason it was not possible to produce lower flux samples, or perform a comprehensive study of this flux with the current apparatus.

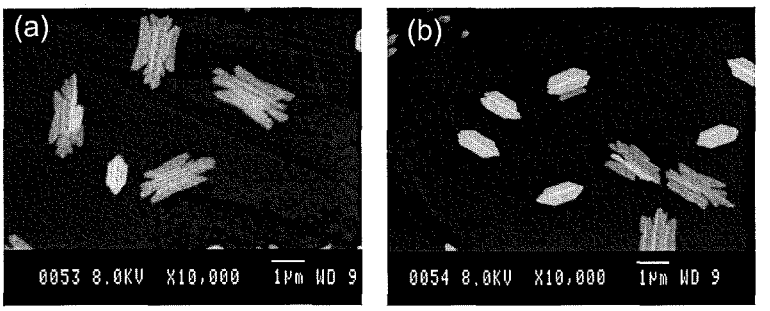

Figure 6.4: SEM images showing regions of a F=7×10^{-4} Å/s, θ=1.5 ML sample where: (a) The star shaped islands are more prevalent. (b) The hexagonal islands are more prevalent, this represents the typical morphology.

Now considering the high flux, high coverage case, it seems that there are two effects that contribute to the lack of symmetry in this growth environment. The large islands tend to evolve from small islands without prominent hexagonal symmetry (as seen in Figure 6.2), which inhibits the formation of primary arms in the orientation of 6-point stars. Also any small islands which may have attained the hexagonal shape tend to lose their 6-fold symmetry as they grow, due to the rapid onset of side splitting and edge instabilities which eventually competes with the growth of the primary arms.

6.1.3 Edge Diffusion and Island Elongation

It was clear in Figure 6.3 that the islands tend to become increasingly elongated as the flux is reduced, which will now be discussed in terms of edge diffusion.

The existence of elongated islands in a low flux environment requires that the energy barriers for edge diffusion are higher along some directions than others (anisotropic edge diffusion). Also, the interplay between corner rounding and edge diffusion is important, since higher barriers for corner crossing compared to edge

diffusion are required to produce anisotropic shapes. Figure 6.5 depicts a small and initially hexagonal island. If we allow edge diffusion to proceed more easily along face a than in any other direction, then as growth proceeds the island will elongate along an axis parallel to a (this is shown to be a Bi$\langle 11\bar{2}0 \rangle$ direction in Section 6.4). In a low flux environment, there is time for an adatom arriving at some site along the a face to be transported to an energetically favorable site before the next adatom arrives from the diffusion field, producing island elongation. This tendency for elongation is obscured at higher fluxes by the more rapid arrival of new adatoms at the perimeter, which "pin" the edge adatoms in place, ending their diffusion.

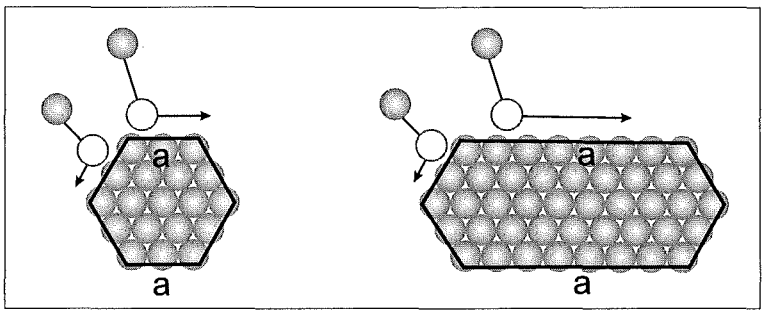

Figure 6.5: An illustration of anisotropic edge diffusion resulting in elongated islands. The left drawing is of an initially hexagonal island. If diffusion barriers are lower along a edges than in other directions, then diffusion is faster in this direction, producing an elongated island like that depicted in the right drawing.

Anisotropic edge diffusion has other effects on the general island morphology. Figure 6.6(a) shows a histogram of the orientation of the long axes of the islands on the substrate (the azimuthal orientation) for several flux and coverage examples, and shows that the islands are preferentially oriented at 60° to one another (see for example the θ=1.5 ML SEM image in Figure 6.1) . This corresponds to the symmetry directions of the hexagonal graphite lattice, and shows that the substrate influences the island orientation (this will be described in more detail in Section 6.4). It would be reasonable to expect that if one axis of a 6-pointed star is aligned with a symmetry direction of the substrate, that the other arms of the star (secondary arms) should also be oriented at 60°. Figure 6.6(b) shows the average angle of the secondary arms from the elongation axis, as a function of increasing coverage, for various fluxes (indicated by the legend). Note that each data point is an average of islands from several different regions of the substrate. The inset is an SEM image of a star shaped island, showing the angle between secondary arms. Clearly, the secondary arms are oriented at angles greater than 60°. There is negligible dependence of the angle on coverage, however it decreases as the the flux is increased, as shown in Figure 6.6(c). The error bars correspond to ± 1 standard deviation of the data about the mean value, with a data set of over 600 islands.

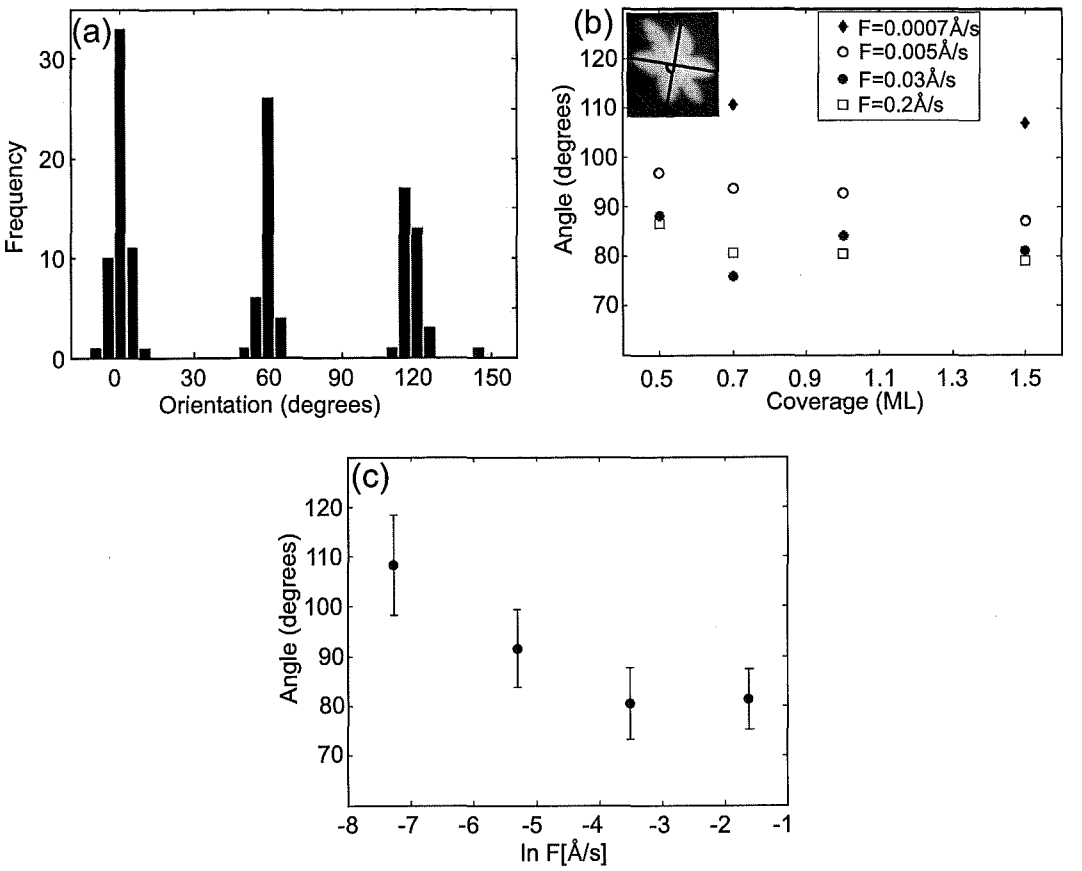

Figure 6.6: (a) Histogram of the azimuthal orientation of the islands on the substrate. (b) Plot of the angle between the secondary arms of the star shaped islands (this angle is indicated in the SEM image inset), as a function of increasing coverage, for the fluxes shown in the legend. (c) Plot of the average angle between the secondary arms the of star shaped islands, as a function of flux, with the data averaged over all coverages.

The notion of anisotropic edge diffusion is consistent with the observation that the arms of the star opposite the long axis are flattened towards the axis (i.e. the angle between the secondary arms increases) with a reduction in flux. The increased fraction of the diffusion field captured by the corners of a hexagonal island (compared to the flat faces), will have longer to diffuse away from the corners at low fluxes. Because adatoms diffuse more easily along *a* edges (than in other directions), this will tend to smooth (flatten) face *a*, rather than producing the long protruding star arms featured in the slightly higher higher flux cases (for example F=0.03 Å/s in Figure 6.3).

The effect of faster diffusion along *a* faces also manifests itself in the morphology of the edge instabilities. Any deformity protruding from the island perimeter will be amplified along the elongation direction. This can be seen in Figure 6.3, where instabilities and splitting of the growth front tend to be aligned parallel to the direction of island elongation.

6.1.4 Island Base Heights

The heights of the star shaped island bases (this excludes the stripes which sit on the bases) have been measured from AFM scans. The primary focus of this study is the flux range 0.005 Å/s - 0.2 Å/s, for coverages between 0.2 ML and 2.0 ML, since these deposition parameters were easily reproduced and allowed data to be obtained from several samples. It should be noted that the uncertainty in the height measurements is approximately ±0.2 nm, arising from the signal noise in the AFM scans. The heights of the hexagonal islands from the low flux limit are considered at the end of this Section.

A typical base height profile is shown in Figure 6.7. It reveals that the island bases have a flat height cross-section (excluding the peak in the centre of the island which results from the stripe featured in the image), implying that they are some uniform multiple of atomic layers tall. This type of flat profile is observed for all the bismuth island bases. However it is not generally possible to attribute a particular multiple of atomic layers to a base height, given the signal noise in the AFM scan, and the *ex situ* nature of the measurements.

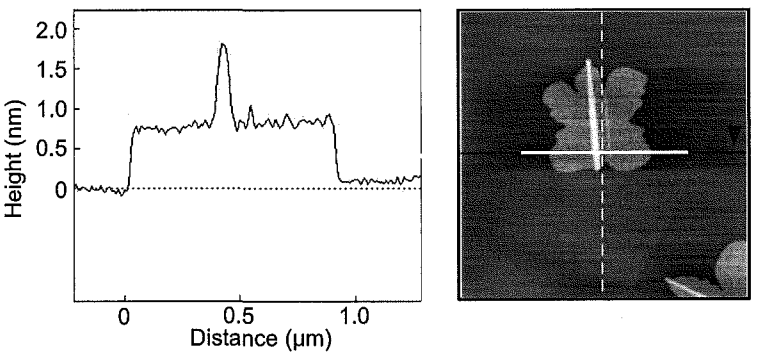

Figure 6.7: A representative AFM height cross-section (left), taken through the solid horizontal line in the AFM image (right) (θ=0.7 ML, F=0.03 Å/s).

Figure 6.8(a) presents histograms of the island base heights for the 0.2 Å/s flux, showing that the island bases are always less than 2 nm tall for the coverage range 0.2 - 2.0 ML. Figure 6.8(b) shows the mean island base height as a function of increasing coverage for F=0.2 Å/s. The error bars represent the standard deviations of the histograms in Figure 6.8(a), and so give an indication of the spread in the mean island heights. It is apparent from this plot that there is no distinguishable evolution in the mean island height with increasing coverage, and we observe a constant mean island height of order 1 nm. Figure 6.8(c) is a combined histogram of the island heights for all the coverages featured in Figure 6.8(a). From this histogram we find a mean island base height of 1.1nm for this flux, with a standard deviation of σ=0.25 nm.

Figure 6.9(a) presents histograms for the 0.03 Å/s flux, which all show

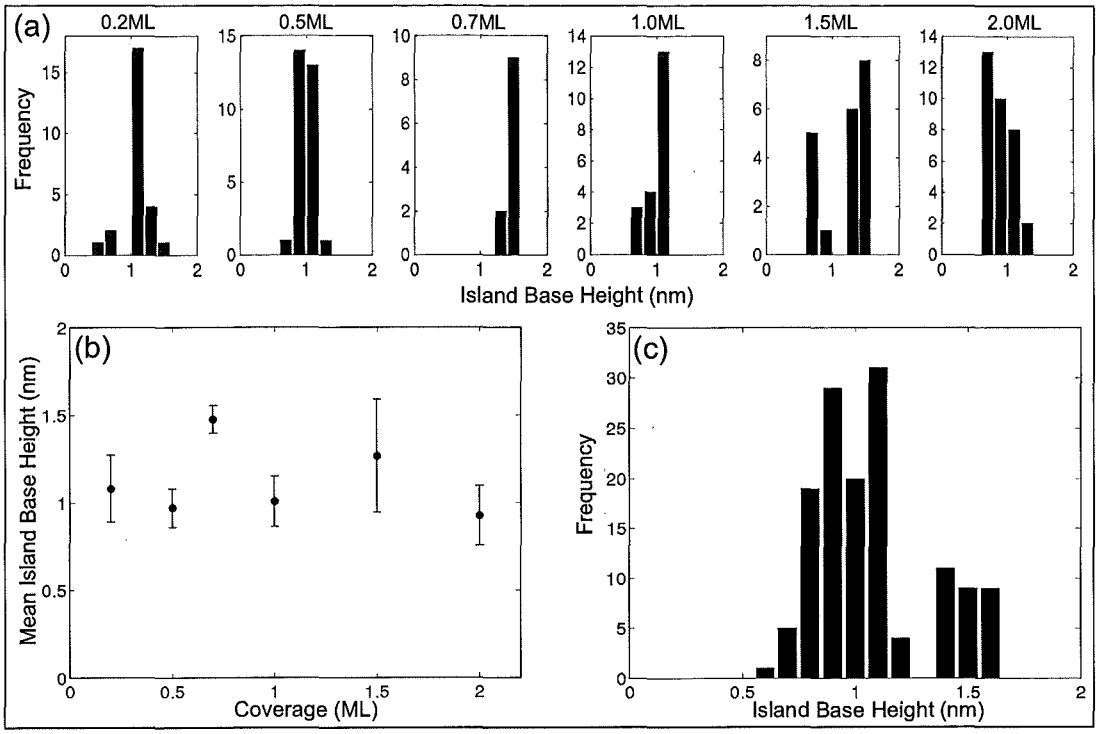

Figure 6.8: Island base height data for F=0.2 Å/s. (a) Height histograms for the coverage range 0.2 - 2.0 ML. (b) Mean base height as a function of increasing coverage. (c) Combined histogram of the island heights for all the data from (a).

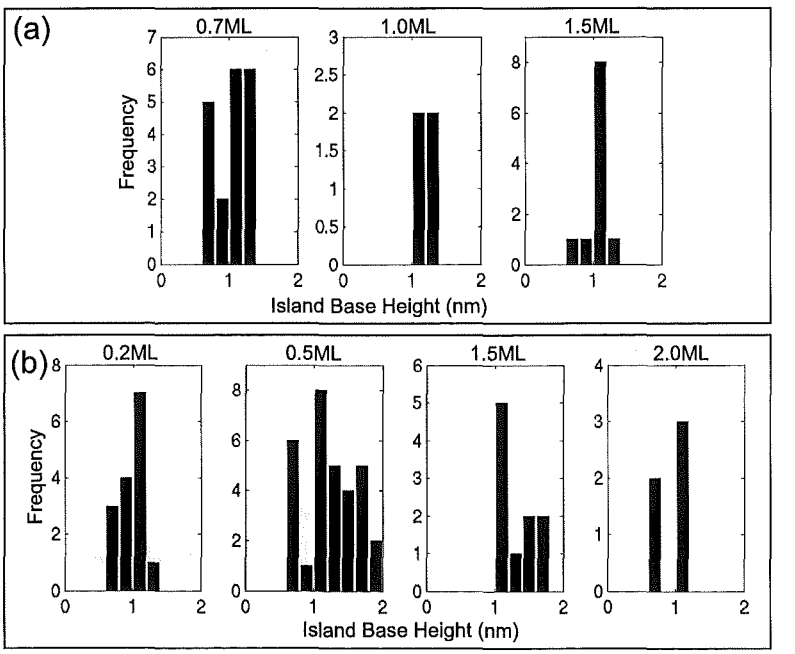

Figure 6.9: (a) Histograms of the island base heights for (a) F=0.03 Å/s, and (b) F=0.005 Å/s.

island heights of order 1 nm. Figure 6.9(b) shows histograms for F=0.005 Å/s. We again find a distribution in the island heights, which are always less than 2 nm, and no obvious trend with increasing coverage. The entire coverage range was not measured for these two fluxes, due to the time required to obtain each AFM scan. Instead, a selection of coverages were chosen to enable a comparison with the complete data set obtained for the F=0.2 Å/s case.

Figure 6.10 presents combined height data for the entire flux and coverage range ($\theta = 0.2 - 2.0$ ML, F = 0.005 - 0.2 Å/s). Figure 6.10(a) shows the mean island height as a function of coverage, for the three fluxes (indicated by the legend), the error bars represent ± 1 standard deviation of data about the mean value. This plot shows that there is no clear dependence of the mean island height on either flux or coverage. A combined histogram of base heights for all coverage and flux environments is shown in Figure 6.10(b). We find a mean height of 1.1 nm with a standard deviation of σ=0.3 nm for the bismuth island bases.

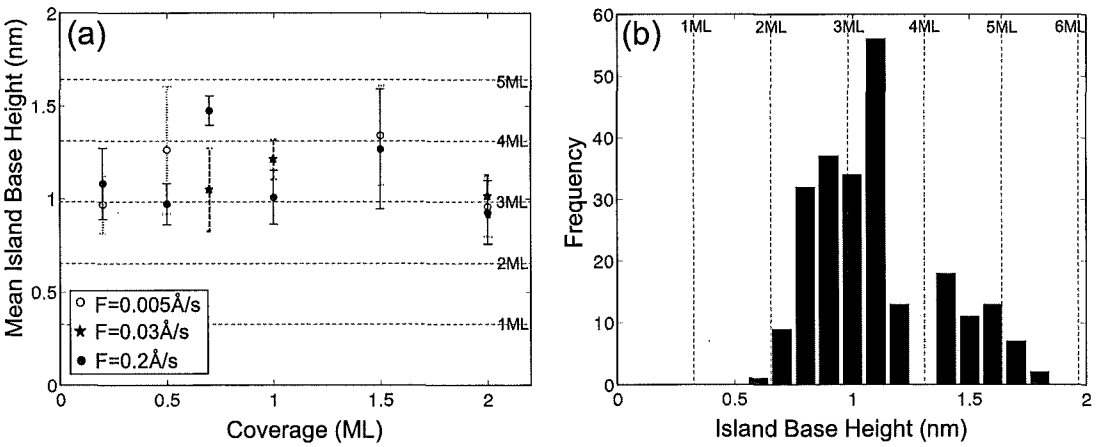

Figure 6.10: Island height data combined from all flux and coverage environments. (a) The mean base height as a function of increasing coverage, the error bars denote the standard deviation in data. (b) A histogram of the island base heights. The dashed lines in the plots indicate multiples of atomic layer thickness.

The data in Figure 6.8, Figure 6.9, and Figure 6.10 show that there is a fairly narrow distribution of island base heights, which appear to be independent of flux and coverage. Although there is a distribution of heights, the independence of the distribution on coverage implies that the majority of islands aggregate to a height within the approximate range of 0.8 nm - 1.4 nm, and then the base growth proceeds horizontally at a fixed height. It is clear that this aggregation to a fixed base height must occur during the earliest stages of growth, since by θ=0.2 ML we already find the heights to be of order 1 nm.

In Section 6.4 it is shown that these bismuth islands are oriented with $\{01\bar{1}2\}$ crystallographic planes parallel to the substrate, which corresponds to an inter-planar distance of 0.33 nm. Dashed lines representing multiples of atomic

layer thicknesses are shown in Figures 6.10 and 6.11 for comparison with the experimental data. While correlation of island heights with precise atomic layer heights is not possible, the absence of any islands which could be consistent with a single layer height is obvious. This suggests that the island bases of a single atomic layer are not energetically favorable.

It is clear that the height characteristics for bismuth islands are very different to those of antimony (Chapter 5), where 3D aggregation was demonstrated. The 2D (but multi-layer) growth of the island bases in the Bi/HOPG system, implies a high energy barrier for upward adatom migration from the side faces to the top faces of the islands (Erlich-Schwoebel [150] type barrier). This is also found in the Au/graphite system [16], which features the aggregation of very flat islands with heights comparable to the present case.

We now consider heights of both the large hexagonal islands and the star-like islands found in the low flux limit. Figure 6.11 presents island height data for F=7 $\times$ 10^{-4} Å/s (black bars), along with the combined height data from all other fluxes (grey bars, data from Figure 6.10(b)). The star-like and hexagonal islands are approximately 1.8$\pm$0.2 nm tall 2.5$\pm$0.2 nm tall respectively. It seems that the star-like islands may be marginally taller than most of the islands from other fluxes, however the uncertainty in the AFM height measurements makes it difficult to conclusively identify a difference. It is immediately obvious however that the hexagonal islands are significantly taller than islands from any other flux studied thus far (which also accounts for the smaller size of the hexagonal islands, compared to their star shaped counterparts in Figures 6.3 and 6.4). This is consistent with a thermodynamic tendency to minimize the free energy of the system, leading to compact and 3D shapes. The reduction in flux allows more time for upward adatom migration (time to overcome Erlich-Schwoebel type barriers) and subsequent growth in a direction perpendicular to the substrate [54].

It is therefore clear that a transition in growth mode occurs for islands grown in flux environments lower than 7 $\times$ 10^{-4} Å/s, from kinetically dominated star shaped dendrites with negligible variation in height with flux, to taller more compact morphologies. This transition to taller more compact shapes with decreasing flux is analogous to the more compact island morphologies which are typically observed at elevated temperatures in many systems [91], where edge diffusion and corner crossing become more rapid, resulting in more thermodynamically favorable shapes [79]. Note that the low flux limit will not be considered further until step edge decoration is discussed in Section 6.5.

The range of thin film growth modes on graphite is extensive, and depends on an array of experimental variables, of which temperature is particularly important. Layer by layer growth has been observed for Ru adsorption on graphite [151], however Binn *et al* find that island growth is more typical for metals deposited on graphite [99]. They observe that Cr and V islands grow on graphite at a temperature of 423 K, via 3D aggregation to a height

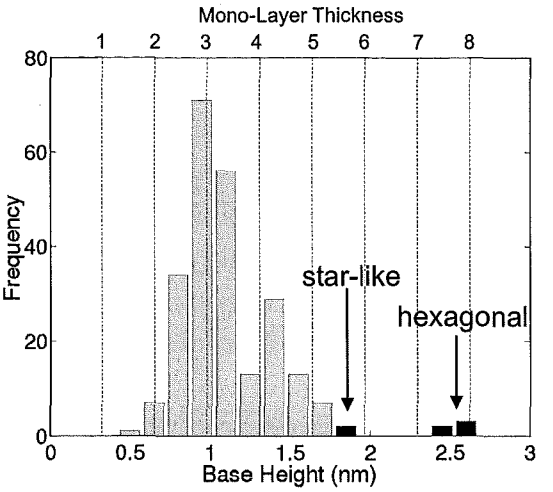

Figure 6.11: Island height data for F=7 $\times$ 10^{-4} Å/s (black bars). The grey bars represent the combined height data from all other fluxes (taken from Figure 6.10(b)). The dashed lines indicate multiples of atomic layer thickness.

of order 10 nm, and subsequent lateral island growth at this fixed height for the remainder of deposition. These investigations were performed with X-ray and ultraviolet radiation (XUV) reflection techniques, which indirectly determine the film's morphology from the reflectivity of a synchrotron beam. This makes a comparison with the shape of our Bi islands impossible. However it does indicate that lateral island growth at a fixed height on graphite is certainly not unique to Bi adsorbates. It would be interesting to observe if any of the Cr or V islands feature the flat tops found for Bi.

Most high resolution investigations of island heights in the literature are limited to small islands, which enables STM imaging [152], [153]. The growth of 1 ML tall islands is fairly common, and is often observed in metal/semiconductor and metal/metal systems [154]. In these examples the substrates often have dangling surface bonds, which results in strong adsorbate/substrate bonding, favoring 2D aggregation. These cases are fundamentally different from the Bi/HOPG island bases, since the islands do not aggregate to a multi-layer height and then grow 2-dimensionally at this height. Instead they grow 2-dimensionally at the single mono-layer height until they touch and coalesce, often forming a wetting layer. The metal/graphite binding energy should be much weaker (see for example ref.[54] for Au/HOPG) since it is mainly due to Van der Waals interactions [18], hence favoring 3D growth.

2D growth of multi-layer islands which exhibit preferred heights have been observed in several adsorbate/substrate systems (for example Pb/Cu [155] and various metals on semiconductor surfaces [156], [157]), where these flat islands were attributed to a quantum size effect. In those cases, the electronic energy of the islands in the Z-direction oscillates with film (or island) thickness due to the confinement of electrons between the substrate-film and the film-vacuum

interface. Some island heights are therefore more energetically favorable than others, and so appear far more frequently in the STM images at low temperature. The AFM signal noise prohibits any conclusive correlation of our island base height with multiples of atomic layers, although layer heights are shown in Figures 6.10 and 6.11 for ease of reference. It would be interesting to observe with *in situ* STM if particular multiples of atomic layers are preferred in the base heights. It does however seem unlikely that the flat bases could be attributed to quantum confinement, since our system is at room temperature, and in no other such system has layering (such as stripes) been observed on top of the flat island bases.

A similar 2D growth mode has however recently been reported in the Bi/Si system at room temperature [158], where island growth proceeded laterally at a constant height of 1.3 nm, and where only islands of even multiples of atomic layers were stable. The preferred heights were accounted for by a layer-pairing of Bi$\{01\bar{1}2\}$ planes which saturated dangling covalent bonds, rather than by electron confinement. It is shown in Section 6.4 that the islands observed here are also $\{01\bar{1}2\}$ oriented in the Bi/HOPG system. However the inability to resolve preferred heights makes further comparison with the Bi/Si system in terms of mechanisms for lateral growth difficult. Regardless of the precise mechanism for the flat island bases, the multi-layer 2D growth results in the formation of islands with lateral dimensions orders of magnitude greater than the thickness.

6.1.5 Island Densities

The evolution of island densities with varying experimental conditions allows investigation of the mechanisms responsible for island nucleation. Island densities have been determined by counting the number of islands within a manually defined capture zone area, from the SEM images, as shown in Figure 6.12. We select regions on large terraces that appear to be relatively defect free, as indicated by a low density of large islands for the particular sample. For each coverage we typically select 4 such regions from different areas of the sample, to ensure a representative data set. Relatively low magnification ($\times$3500) SEM images are used to ensure that a statistically significant number of islands are available for analysis.

Saturated Island Densities

Figure 6.13 shows the island density as a function of coverage for the flux range 0.005 Å/s - 1.0 Å/s (indicated by the legend). We observe that there is no distinguishable dependency on coverage for any flux. Once island nucleation is completed, the remainder of the deposited adatoms will be captured by existing islands and contribute primarily to island growth. This is the so called post-nucleation (pure island growth) regime, where the island density has reached

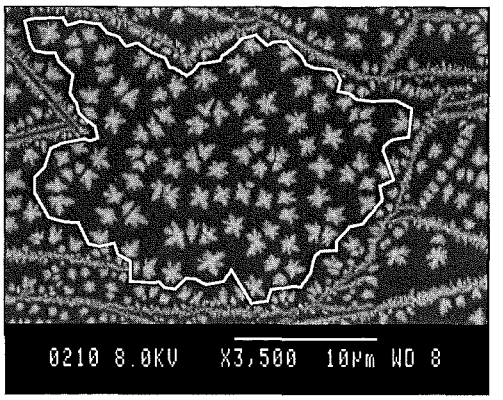

Figure 6.12: An example of a region selected to determine island densities (F=0.2 Å/s, θ=1.5 ML). Note that uniform regions on large terraces are chosen, avoiding step edges.

a maximum, defined as the saturated island density, N_s. The approximately constant island density with increasing coverage shown in Figure 6.13, means that by θ=0.2 ML the nucleation of new islands is virtually completed, and the saturated island density has been reached.

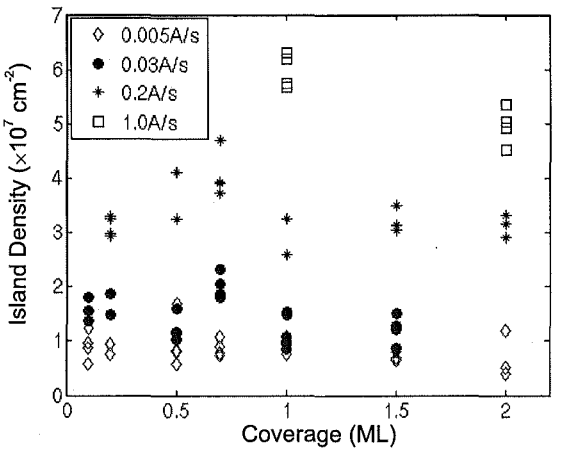

Figure 6.13: The dependence of island density on coverage for the flux range of 0.005 Å/s - 1.0 Å/s (indicated by the legend).

Homogeneous Versus Heterogeneous Nucleation

The independence of the island density on the coverage can result from post-nucleation growth of islands which have nucleated either on defect traps (heterogeneous nucleation) or from adatom-adatom collisions (homogeneous nucleation). We now explore these two possibilities.

The particle flux controls the diffusion length between adatom-adatom collisions by altering the concentration of diffusing adatoms on the surface. High fluxes result in a higher concentration of diffusing adatoms, which travel short distances before colliding with other adatoms. Conversely, if the flux is sufficiently

low that the adatom-adatom collision distance is greater than the distance between defects, island nucleation will occur primarily by defect trapping, and the island density will be independent of flux.

Figure 6.14 depicts the two regimes of nucleation. Heterogeneous nucleation is indicated by the dashed line, where the island density is independent of flux. As the flux is increased, the adatom-adatom collision distance decreases, and eventually there is a cross-over from heterogeneous to homogeneous nucleation (solid line), and the island density begins to increases with increasing flux. Mean field nucleation theory predicts from a rate equation analysis [159], that for homogeneous nucleation, the saturated island density has a functional dependence on the flux of the form

$$N_s \propto F^{\chi} \tag{6.1}$$

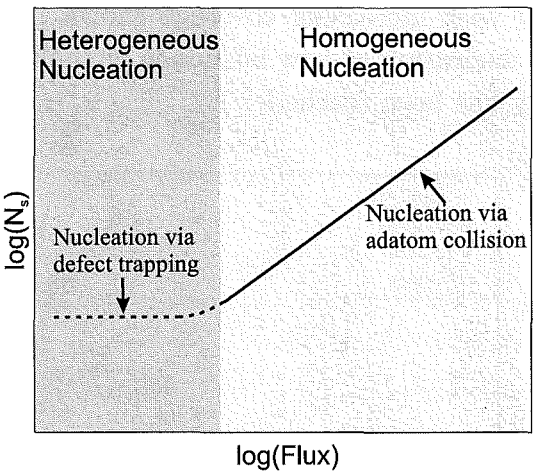

Figure 6.14: Schematic representation of the two types of island nucleation. The saturated island density, N_s is independent of flux in the case of heterogeneous nucleation, and increases with flux in the case of homogeneous nucleation.

Figure 6.15 presents a log-log plot of the saturated island density as a function of increasing flux. N_s has been calculated by averaging over all the island densities from multiple deposits at each flux in order to reduce the uncertainties to an acceptable level. Typically, each data point in Figure 6.15 is an average of 20 different regions taken from a variety of samples with different coverages (since the island density was found to be independent of coverage). The error bars are taken to be the standard deviation of the mean island density ($\sigma_{\overline{x}} = \frac{\sigma_x}{\sqrt{n}}$, where n is the number of samples in the data set).

The relationship between the saturated island density [cm^{-2}] and the deposition flux [Å/s] is determined from the least squares fit to the data points. It follows the power law relation

$$N_s = (5.7 \times 10^7) F^{0.36 \pm 0.03} \tag{6.2}$$

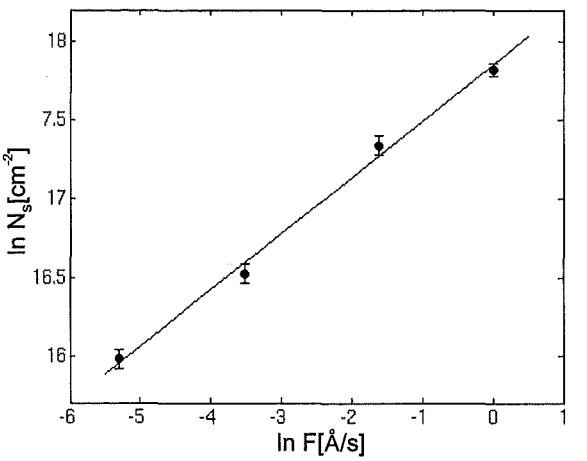

Figure 6.15: A log-log plot of the saturated island density, N_s as a function of flux. The line is a least squares fit to the experimental data points.

for more than two orders of magnitude in flux. The agreement of the form of this experimental fit with Equation 6.1, shows unambiguously that the Bi islands are nucleated via adatom-adatom collisions in the flux range of this study. We would expect this relation to break down in the limit of extremely low flux where heterogeneous nucleation would eventually prevail, and for extremely high fluxes, where the adatom arrival rate to the surface becomes rapid enough to prevent any appreciable diffusion. However neither of these regimes are experimentally accessible with our apparatus. We can now generalize to say that we are working in the post nucleation growth regime, and that islands are formed by homogeneous nucleation.

The island density in the lowest flux environment also gives us an estimation of an upper bound on the defect density in the clean regions of the graphite substrates of 9×10^6 cm^{-2}. This value is considerably lower than reported in other studies of adsorbates nucleated on the HOPG basal plane. For gold particles Darby and Wayman [54] obtain island densities of 4×10^7 cm^{-2} for vacuum cleaved graphite (recall our substrates were air cleaved). Anton and Kreutzer [91] find gold island densities of order 10^9 cm^{-2} in the cleanest regions of HOPG prepared in a similar manner to our substrates. Their densities were independent of deposition temperature, which implies an intrinsic graphite defect density. It seems unlikely that the defect density of our substrates would be any lower than in these studies, given the similarity of substrate preparation and vacuum environments.

It should be noted that the Bi inter-island spacing is similar to that of antimony, both in our study and in the work of other groups [19]. This then raises the possibility that Bi and Sb may be less sensitive to defects than many other adsorbates. It is however clear that terrace defects are not transparent to the diffusing adatoms, since some graphite terraces are decorated with islands many orders of magnitude denser than in the clean regions selected for this study, as

illustrated in Figure 6.16. It will also be demonstrated in Section 6.7 that lowering the substrate cleaning temperature introduces a significantly higher density of defect nucleated islands.

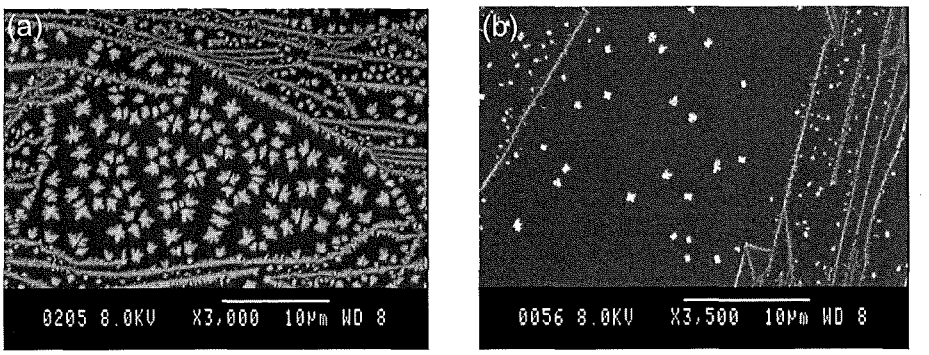

Figure 6.16: Variation of island densities on different graphite terraces. Note that the small terraces tend to be characterized by higher island densities. (a) θ=1.5 ML, F=0.2 Å/s. (b) θ=0.2 ML, F=0.005 Å/s.

The Critical Island Size

The influence of the particle flux on the saturated island density provides information on the critical island size i, above which islands are stable against dissociation (measured in units of number of particles) [48]. Standard rate-equation theory predicts that the exponent in Equation 6.1 depends on the critical island size through the relation

$$\chi = \left(\frac{i}{i+2}\right) \tag{6.3}$$

Equation 6.3 assumes that diffusion is 2D and isotropic [1] which is a reasonable approximation for the graphite substrate. It also ignores the possibility of diffusion of stable islands, which is not *a priori* obvious for our system. A transition from $i = 1$ to $i > 1$ is expected with increasing temperature, as dissociation becomes active. However a complication to this scenario may arise if small cluster diffusion becomes activated before island dissociation. Villain *et al* [161], [162] have shown that a modified form of the scaling relation is required to account for the possible influence of small island mobility on the island density. They calculate a value of $\frac{2}{5}$ for the exponent in Equation 6.1 for the case where $i = 1$ and small clusters are able to diffuse. Bartelt *et al* [163] present a discussion of the likelihood of requiring consideration of a modified scaling relation in practical systems. In the homoepitaxial metal cases they review, it seems that the island

[1] For the case of highly anisotropic and 1D diffusion $\chi = \left(\frac{i}{2i+2}\right)$. A list of the possible values of the exponent for different physical regimes is given in Table 11.1 of ref.[160]

density is not significantly effected by a small degree of cluster mobility, and the classic form of the scaling exponent given in Equation 6.3 remains valid.

A comparison of Equations 6.1 and 6.2 yields an exponential factor of $\chi = 0.36 \pm 0.03$ for the Bi/HOPG system. It is clear that our exponent fits Equation 6.3 for $i = 1$, implying that the smallest stable island size is comprised of two adatoms in this system. It is therefore assumed that there is no Ostwald ripening for this system at room temperature. It should be noted however, that the exponent is also very close to the value $\chi = \frac{2}{5}$ determined for the regime of $i = 1$ with rapid small cluster mobility. Based on the above discussion, it is not possible to comment on the possibility of small cluster diffusion in this system solely from the scaling of the saturated island density with the particle flux, even though Equation 6.3 assumes that small clusters are immobile. This information requires STM studies of the scaling of the island size distributions with coverage [163].

Diffusion Lengths

The values obtained for the island densities allow estimation of the mean adatom diffusion length, L for each flux since $N_s^{-1} \sim L^2$. We define L as the mean distance traversed by an adatom before it collides with another diffusing adatom to nucleate an island (the inter-island distance). The average value of this length is in the region of 3.4 μm for F=0.005 Å/s, 2.7 μm for F=0.03 Å/s, and 1.7 μm for F=0.2 Å/s.

The diffusion coefficient, D describes the mean square displacement, $\langle r^2 \rangle$ of an adatom (undergoing Brownian motion) in a given time interval, t [36] and is given by the Einstein relation

$$D = \frac{\langle r^2 \rangle}{4t} \tag{6.4}$$

Knowledge of the time taken to travel the diffusion length would allow a crude estimate of the room temperature diffusion coefficient for the Bi/HOPG system via Equation 6.4. Since we have determined that the island densities have saturated by θ=0.2 ML for each flux, we can estimate a lower limit for the diffusion coefficient. Given that L is of order 1.7 μm for F=0.2 Å/s, and it takes less than 3.4s (the deposition time for θ=0.2 ML) for the adatoms to traverse this distance[2], we estimate that $D > 10^{-9}$ cm^{2}s^{-1}. The accuracy of this value could be greatly improved if we were able to ascertain the actual coverage at which the island density saturates, rather than just relying on an upper bound. However

[2]This assumes that all islands are nucleated within the time frame of deposition. In Section 6.6 we show that this is a reasonable assumption, based on the absence of a morphology change when the diffusion process is frozen immediately at the end of deposition (chamber immediately vented), compared to when there is a time delay between the end of deposition and removal of the sample from the chamber.

this is prohibited by the resolution of the SEM, and by timing accuracy of the deposition at high fluxes.

This lower limit of the diffusion coefficient for Bi/HOPG is significantly larger than in many other adsorbate/substrate combinations. For Ir/Ir(100) at T=270 K, $D = 10^{-16}$ cm^2s^{-1} [164]. Studies of Pd diffusion on sapphire at a temperature of 798 K yield $D = 1 \times 10^{-10}$ cm^2s^{-1} [165]. It has also been shown in numerous cases that large clusters are able to diffuse. Sb_{36} diffuses on amorphous carbon with $D = 2 \times 10^{-12}$ cm^2s^{-1} [164]. We would expect the diffusion of adsorbates on HOPG to be more rapid than in the above cases, due to its extremely weakly interacting nature. For the case of antimony cluster diffusion on graphite at room temperature, Bardotti *et al* [166] find diffusion coefficient values of order 10^{-8} cm^2s^{-1} (10^8 times higher than studies of cluster diffusion on other substrates). Diffusion of gold clusters on graphite at room temperature also yields a diffusion coefficient of order 10^{-8} cm^2s^{-1} [167]. Molecular dynamics simulations of diffusion of large gold clusters on graphite have shown that the diffusivity of these clusters is comparable to that of single adatoms [168]. These values for diffusion of clusters on graphite are larger than our lower bound on the diffusion coefficient for Bi adatoms on graphite. This further indicates that island nucleation is completed well within the time frame of deposition.

6.1.6 Island Sizes

The evolution of island area with increasing coverage has been investigated for fluxes in the range 0.005 Å/s - 0.2 Å/s. In all cases we are concerned with coverages below 2 ML to avoid the complication of island coalescence. It should be noted that all equations in this Section express flux in units of [Å/s], coverage in [ML], area in [μm^2], and time in [s], in order to maintain intuitive expressions that can easily be compared to SEM images and data plots.

Figure 6.17 presents an example of the island size distribution for various coverages at a fixed flux of 0.2 Å/s. The histograms show an approximately normal distribution of island areas. The standard deviation in the histograms is in all cases within the range of 30-40% of the mean island area, indicating that the distribution in the island sizes about the mean is independent of coverage.

The absence of any obvious asymmetry in the size distributions in Figure 6.17 allows us to rule out some secondary island aggregation processes. If small islands were able to diffuse, we would expect to observe an asymmetrical distribution with an increase in the number of large islands, at the expense of the number of small islands which have diffused and coalesced to form them. Also, double peaks have been observed in size distributions when islands are able to migrate after they reach some critical size [169]. The approximately normal size distributions observed for bismuth therefore support the conjecture of a simple deposition, diffusion, nucleation and growth model for this system.

The mean island areas have been calculated for each coverage within a given

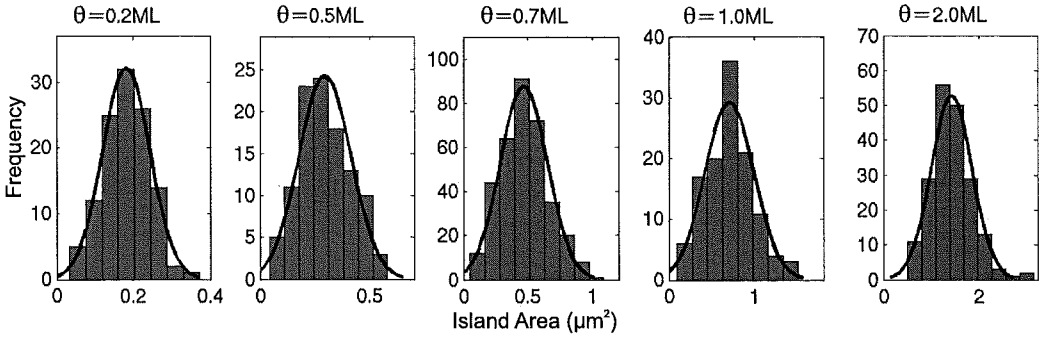

Figure 6.17: Histograms of island size distributions for F=0.2 Å/s, note scale changes. The superimposed curves are normal distribution fits to the data.

flux environment from the size distributions, and are presented in Figure 6.18. The x-axis has also been rescaled into the time domain using $\theta = Ft/3.4$. The uncertainty is taken to be the standard deviation in the mean. However, these were typically 3% of the data value, yielding error bars smaller than the data symbol size. Error bars of $\pm 15\%$ of the data values have been chosen, to reflect uncertainties in the deposited dose of bismuth, and uncertainties in the thresholding procedure for determining the island areas from the SEM images.

The three plots show a linear increase of the mean island area, A with increasing coverage for all fluxes, with the dependence

$$\begin{aligned} A &= (2.3 \pm 0.2)\theta - 0.39 \pm 0.02 \quad \text{for F=0.005 Å/s} \\ A &= (1.3 \pm 0.2)\theta - 0.17 \pm 0.08 \quad \text{for F=0.03 Å/s} \\ A &= (0.67 \pm 0.9)\theta \quad \text{for F=0.2 Å/s} \end{aligned} \tag{6.5}$$

Rescaling into the time domain (this will be used later to determine growth rates), yields

$$\begin{aligned} A &= (0.33 \pm 0.04 \times 10^{-2})t - 0.39 \pm 0.02 \quad \text{for F=0.005 Å/s} \\ A &= (1.2 \pm 0.2 \times 10^{-2})t - 0.17 \pm 0.08 \quad \text{for F=0.03 Å/s} \\ A &= (3.9 \pm 0.6 \times 10^{-2})t \quad \text{for F=0.2 Å/s} \end{aligned} \tag{6.6}$$

The linear dependence of the island area on coverage confirms the initial observation from the AFM scans that the islands grow at approximately fixed heights (since the island density is constant with coverage). If significant 3D aggregation was active, the area of the islands projected onto the substrate should follow a power law relation [170]. The plots also confirm that the mean area of the low flux islands is larger than that of their high flux counter parts, for a given coverage, as was qualitatively observed in the SEM images in Figures 6.1 and 6.2. This is due to the increased island density in the high flux case, which results in less material available per island due to competitive adatom capture.

The offset from zero in the linear fits can perhaps be understood within the context of the initial stages of island nucleation. When the first particles

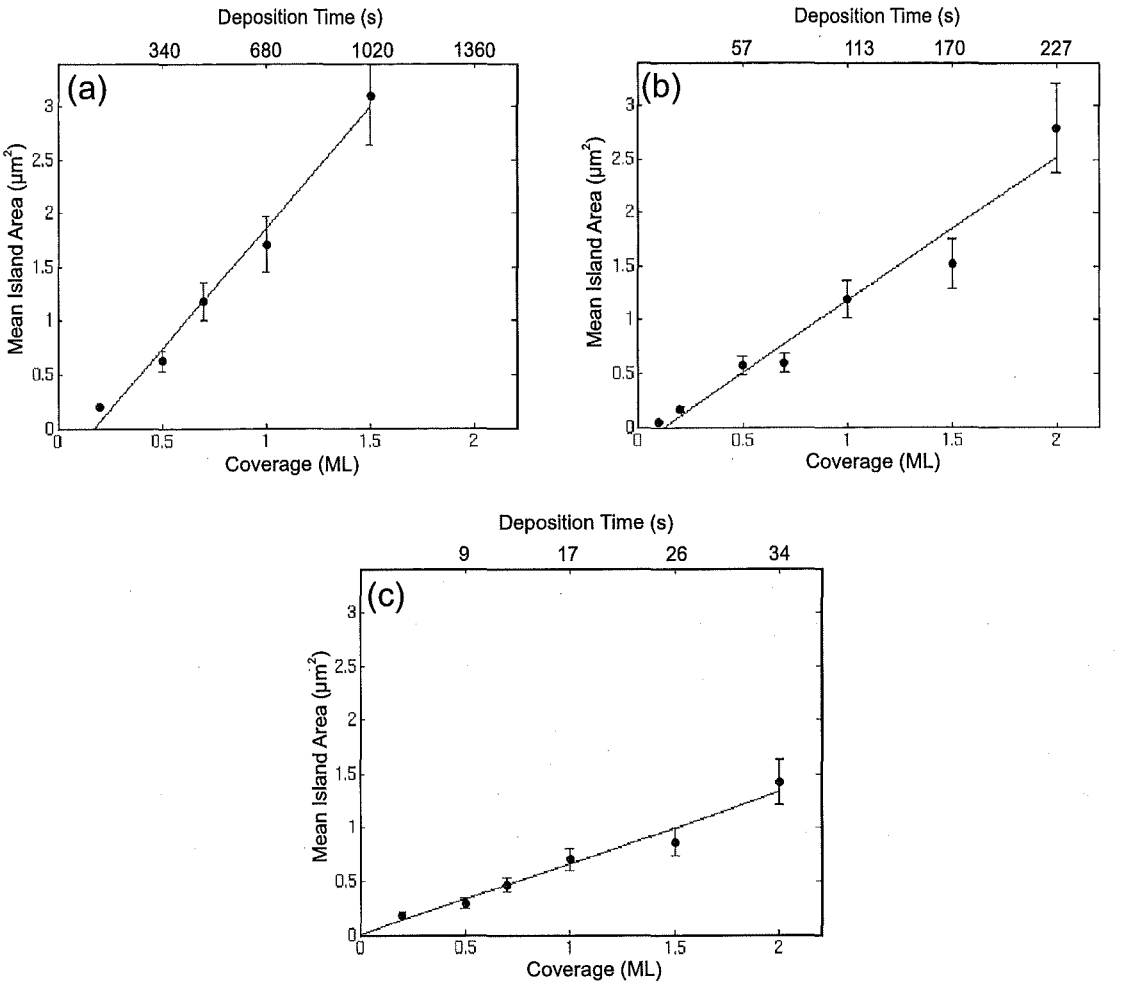

Figure 6.18: The evolution of the mean island size with increasing coverage for (a) F=0.005 Å/s, (b) F=0.03 Å/s, (c) F=0.2 Å/s.

arrive at the graphite surface from the vapor beam, they diffuse uninterrupted by islands. The adatom migration is ended by an encounter with another diffusing adatom, and the subsequent binding to nucleate an island. The time scale of this uninterrupted diffusion, t_{ud} will depend on flux, since higher fluxes result in a more rapid rate of adatom collisions, and hence a reduction in the uninterrupted diffusion time. This is consistent with the observation that the offset in the linear fit is reduced as the flux is increased in Figure 6.15. We obtain an uninterrupted diffusion time of $t_{ud} = 120 \pm 70$ s for F=0.005 Å/s, $t_{ud} = 14 \pm 8$ s for F=0.03 Å/s, and $t_{ud} = 0 \pm 2$ s for F=0.2 Å/s.

The offsets in the mean island area as a function of the particle flux are plotted in Figure 6.19(a). A linear fit to the data points yields the relation

$$A_{offset} = 0.11ln(F) + 0.17 \tag{6.7}$$

The scatter in the experimental data points in Figure 6.18 results in uncertainties of order ±60% in Equation 6.7. This prohibits a correlation of the uninterrupted

diffusion time with the particle flux with any reasonable degree of accuracy, but nonetheless serves to describe the limited data set in Figure 6.19(a).[3]

The mean island growth rate, $dA/dt[\mu m^2 s^{-1}]$ for each flux is given directly by the linear fits in Equation 6.6, and is plotted as a function of the particle flux in Figure 6.19(b). We observe that the growth rate increases as the flux is increased, which is intuitively obvious, since increasing the flux results in a more rapid arrival rate of adatoms to the island perimeters. The log-log plot of the growth rate as a function of flux yields a linear fit, from which we determine

$$dA/dt = (0.12 \pm 0.02)F^{0.67\pm0.07} \tag{6.8}$$

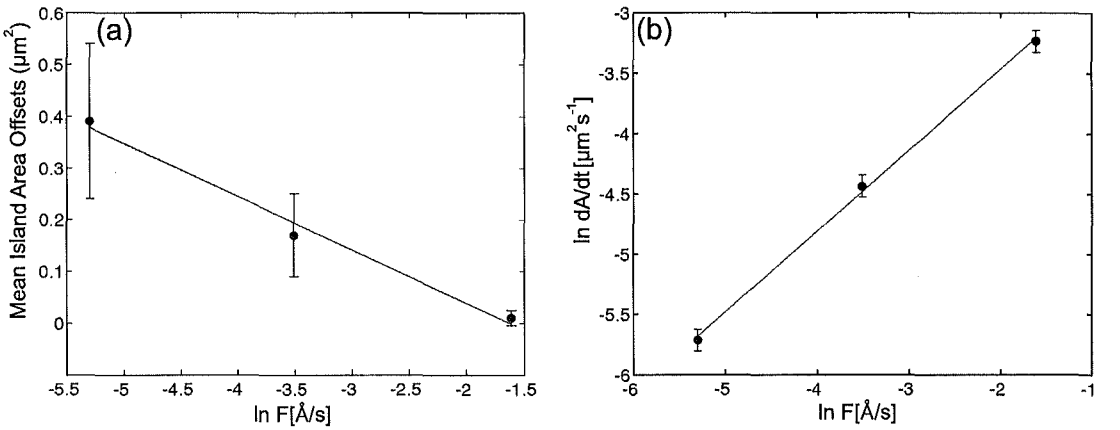

Figure 6.19: (a) The dependence of the offsets in the mean island area (from Figure 6.18) on the particle flux. (b) The dependence of the mean island growth rate on the particle flux.

The mean island area at a given coverage depends on both the growth rate and the time at which the islands start growing (given by the uninterrupted diffusion time). Combining Equation 6.7 and Equation 6.8 (and using $\theta = Ft/3.4$) allows the mean island area to be expressed in terms of experimental parameters, as

$$A = (0.41 \pm 0.04)\theta F^{-0.33\pm0.03} + (0.11ln(F) + 0.17) \tag{6.9}$$

Figure 6.20 shows experimental data points of the mean island area as a function of coverage. The solid lines are linear fits to the data using Equation 6.9 (note that in Figure 6.18 the solid lines were least squares fits to the data set for each flux) and the dashed lines are fits with the offset due to the uninterrupted diffusion time (second term in Equation 6.9) neglected. It is clear that the offsets represent only a small correction to the mean island area, and become less important with increasing flux and/or increasing coverage.

[3]Note that using values of t_{ud} in Equation 6.4 should narrow down the range of the diffusion coefficient. However, the large uncertainties quoted here yield diffusion coefficients consistent with that calculated by using the deposition time for θ=0.2 ML.

The exponent of -0.33 in the first term of Equation 6.9 results because the mean island area is directly proportional to N_s^{-1}, since higher island densities result in smaller islands. The large uncertainty in the second term of Equation 6.9 (of order ±60%) makes any analysis of the meaning of its functional form difficult. The best we can say is that it probably exists due to a time delay between particle deposition and the nucleation of islands (an uninterrupted diffusion time). For the purpose of this study, it is included in Equation 6.9 as a minor correction to the island area, in order to fit the experimental data in Figure 6.18.

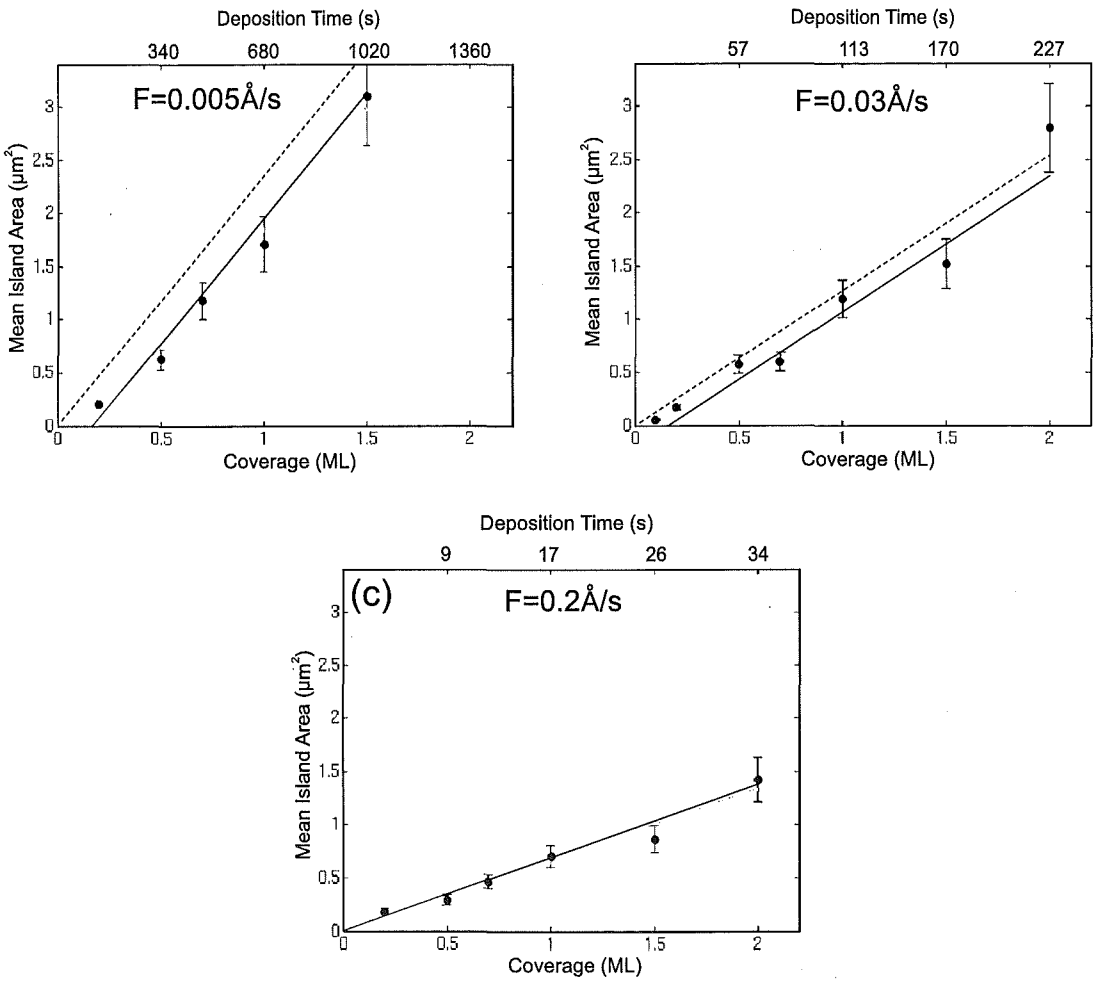

Figure 6.20: Mean island area as a function of coverage. The symbols are the experimental data points (reproduced from Figure 6.18). The solid line is a fit to the data using Equation 6.9. The dashed line is a fit to the data using Equation 6.9 with the second term neglected.

Equation 6.9 allows prediction of the mean island size for the Bi/HOPG system for any given flux and coverage within the range of this study. Knowing that the island density scales with flux according to Equation 6.2, allows tuning of flux and coverage to obtain predictable island densities and sizes from homogeneous nucleation.

6.1.7 Adsorbate Condensation

The calibration of the deposition rate monitor by thickness measurements of Bi deposited on a SiN wafer in Chapter 3, allows confidence in the measurement accuracy of the amount of material arriving at the substrate surface from the particle beam. However it does not provide any information on the degree of condensation on the HOPG surface, which may be markedly different to that of SiN, due to its extremely clean and weakly interacting nature.

Incomplete condensation arises when the adsorption energy between the adatom and substrate is low, resulting in evaporation of diffusing adatoms from the substrate. In this regime, particles deposited on a surface will diffuse until they either evaporate, or collide with another diffusing adatom, island, or defect trap and remain permanently on the substrate. The lifetime of adatoms migrating on the surface is therefore determined by the outcome of a competition between the evaporation time τ_e, and the time for collision τ_{col}, with another diffusing adatom, aggregated island, or defect trap.

$$\begin{aligned} \tau_e > \tau_{col} &\longrightarrow \textit{complete condensation} \\ \tau_e < \tau_{col} &\longrightarrow \textit{incomplete condensation} \end{aligned} \tag{6.10}$$

The degree of adatom condensation on a surface is quantified by the condensation coefficient, which is given by the fraction of adatoms which satisfy $\tau_e > \tau_{col}$ (i.e. condense on the surface). Other workers have demonstrated that the adatom-graphite binding energy, which is predominantly due to Van der Waals forces, is low in relation to adatom-adatom binding energies [54]. We now discuss the degree of bismuth condensation on the graphite surface.

A simple measure of the condensation coefficient is obtained by comparing the volume of material aggregated into islands, with the amount of material deposited within their adatom capture zone. A capture zone was defined around a group of islands from a θ=1.5 ML sample deposited at F=0.2 Å/s as shown in Figure 6.21. This AFM scan has the best signal to noise ratio of all our data (the island density in this region is slightly higher than for typical non-defect nucleated islands, however it is irrelevant whether the island morphology is typical for this purpose). The area within this zone multiplied by the deposited dose of bismuth gives the total volume of material available for island formation within the capture zone, and was calculated to be $(2.1 \pm 0.2) \times 10^{-3}$ μm^3.

The total volume of material condensed into islands was measured from the AFM image. The volume of the island bases were calculated from their area projected on to the substrate, and their heights. The contribution to the island volume by the striped layers was also included by measuring each stripe's area and height. We find that the total volume of bismuth condensed into islands within the capture zone is $(1.7 \pm 0.25) \times 10^{-3}$ μm^3.

The accuracy of the height measurements were limited by the AFM signal noise to within 10% in this case. The uncertainty in the deposited volume arises

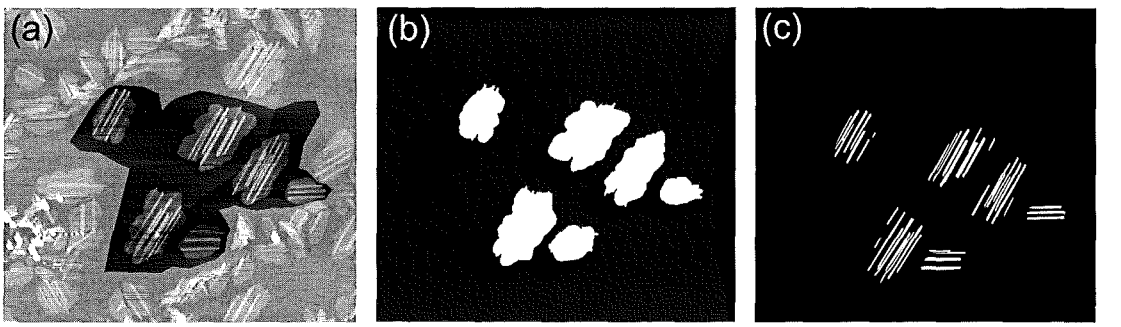

Figure 6.21: (a) The AFM image used for calculating the ratio of deposited to condensed material, the scan size is 5 μm. The darker central region defines the capture zone for the 6 islands. (b) and (c) are the binary island base and stripe areas for individual height calculation.

mainly due to experimental factors, such as the stability of the particle flux. The manual definition of the capture zone, island bases and island stripes contributed negligible uncertainties in comparison to the experimental measurements.

The agreement of these two values indicates that complete condensation is achieved for this flux (at least within the margin of error of the experimental parameters). This implies that $\tau_e > \tau_{col}$, and also excludes the possibility of a significant fraction of particles bouncing off the substrate at the moment of deposition.

This really only directly confirms complete condensation for the θ=1.5 ML and F=0.2 Å/s growth environment. It would be beneficial to investigate other coverages and fluxes to generalize for the entire system, especially for the low flux where τ_{col} is much larger. However, the low density of islands in the low flux case prohibits obtaining AFM scans that include enough islands to define a capture zone, while still being able to get accurate height and island area resolution. Also, the noise levels in the AFM scans are generally much higher for low coverage islands grown in a high flux environment, thus prohibiting evaluation of the condensation coefficient for lower coverages.

Anton and Schneidereit found a condensation coefficient for Au/HOPG at room temperature of 0.3±0.2 for a projected coverage of about 5%, which rapidly approached unity as deposition progressed [16]. Arthur and Cho find very low condensation coefficients during the early stages of Cu/HOPG and Au/HOPG deposition at room temperature [17]. Our study however, only considers the coverage range beyond θ=0.2 ML, and our sample is located at a greater distance from the crucible than is suggested by the chamber configuration in ref.[17], which may result in less sample heating. Other workers just note that the quantity of material on the substrate agrees with the deposited amount determined by a deposition rate monitor [171].

Based on the complete condensation of the θ=1.5 ML and F=0.2 Å/s sample, we assume that evaporation of adatoms from the graphite surface is not a major consideration in the range of our study.

6.1.8 Summary of Island Morphologies

We have demonstrated that altering the flux and coverage has a marked effect on the island morphologies. In a low flux environment, we observe a transition from compact and elongated hexagonal islands to 6-point star shaped islands with increasing coverage. In a high flux environment, the islands are less compact, and large islands feature edge instabilities and splitting. The island bases were found to be of order 1 nm tall, independent of coverage and flux. A low flux limit was also investigated, and it was shown that large hexagonal islands with heights of order 2.5 nm populate this growth environment, representing a crossover to more energetically favorable morphologies.

Island densities saturated at coverages below θ=0.2 ML for all fluxes. The densities increased with flux according to Equation 6.2, from which it was determined that islands form via homogeneous nucleation, and that a particle comprised of two adatoms was the smallest stable island size. The island densities also allowed us to estimate a lower bound on the room temperature diffusion coefficient of $D > 10^{-9}$ cm^{2}s^{-1}.

The mean island size increased linearly as the coverage was increased, confirming a predominantly 2D growth mode in the coverage range of the study. Also, the slope of this linear dependence changed with flux, showing that for a given coverage the mean island size decreases with increasing flux. A single expression was found (Equation 6.9) to characterize the mean island area for the flux and coverage range of 0.005 Å/s - 0.2Å/s and 0.2 ML - 2.0 ML respectively. The final section confirmed that the dose of bismuth offered to the substrate is completely condensed into islands.

We therefore conclude that altering the flux and coverage allows a large degree of control over the shape, size, and density of bismuth islands grown from homogeneous nucleation on HOPG surfaces.

6.2 Island Striping

We now turn our attention from the general island morphology, and explore the striping detail observed on the individual islands in Section 6.1. This striping morphology can be seen in the AFM images of Figure 6.1(b) (F=0.005 Å/s), and Figure 6.2(b) (F=0.2 Å/s), where it is clear that the stripes on an individual island are always parallel to one another. Also, the stripes are always oriented parallel to the island's elongation direction.

In this Section we first examine the origin of the striping material, followed by characterization of the stripe density with changing flux and coverage. We then investigate the evolution of the striping morphology with changing flux and coverage. This Section uses data obtained from AFM scans, which in addition to height information, allow greater resolution than the SEM scans on the scale of individual islands. However, obtaining high quality AFM scans can be problem-

atic due to tip effects. Also, the time to capture an image is significantly greater than for SEM imaging. For these reasons, it was not always possible to obtain complete data sets.

6.2.1 Direct Impingement of Particles to the Island Bases

Given the 2D growth of the bismuth island bases demonstrated in Section 6.1.6, it seems likely that the material involved in the striping morphology may have come from direct impingement of the particle flux onto the island base, rather than from upward adatom migration. We now test if the amount of directly impinged material can account for the total volume of bismuth contained in the striped layers.

The integrated contribution to the island volume from direct impingement, V_{DI} can be calculated from the experimental flux and the increase with time of the projected island base area, $A(t)$ which collects the flux (all in SI units), i.e.

$$V_{DI} = F \int_0^{t=t_f} A(t)dt \tag{6.11}$$

It is not possible to determine $A(t)$ directly in this case, since we can not image individual islands during growth. However we can approximate by using the mean island area given by Equation 6.6 (with an adjustment of a factor of 10^{-12} to obtain SI units), which has the general form

$$A(t) = at + b \tag{6.12}$$

where a and b are the flux specific constants. We can neglect b to a first order approximation, which gives

$$A(t) \sim at \tag{6.13}$$

Substituting Equation 6.13 into Equation 6.11 then integrating and solving for V_{DI} at the end of deposition ($t = t_f$) yields

$$V_{DI} = \frac{Fat_f^2}{2} \tag{6.14}$$

This can be simplified by noting that at_f is just the mean island area at the end of deposition and $\theta = Ft$, to obtain

$$V_{DI} = \frac{A_f\theta}{2} \tag{6.15}$$

or expressing in units of $V_{DI}[\mu m^3]$, $A_f[\mu m^2]$, and θ[ML]

$$V_{DI} = (3.4 \times 10^{-4})\frac{A_f\theta}{2}$$

Equation 6.15 allows calculation of the contribution to an individual island's volume from direct impingement, and is particularly convenient because it only

requires measurement of the projected island area from the AFM scan. It should be noted that this equation is only valid for coverages up to 2 ML. Beyond this, the growth rate of the island bases is likely to become non-linear, since the islands eventually grow large enough that they begin to touch, effectively halting lateral growth. The simplicity of Equation 6.15 results from the linear island growth in this system, however more complicated functions could be introduced into Equation 6.11 to describe the growth in non-linear cases such as the high coverage limit.

The actual volume of material contained within a particular island's stripes, V_m is measured by calculating the volume of each stripe by multiplying its height (from the AFM scan) with its projected area onto the island base, and summing over all stripes on the island. We estimate that the uncertainty in V_m from this procedure is of order $\pm 20\%$, with around 10% due to AFM signal noise and another 10% arising from the procedure of tracing the stripe outlines. The uncertainty in V_{DI} is estimated to be in the region of $\pm 8\%$, with the majority arising from the stability of the particle flux which effects the coverage.

We now test weather $V_{DI} = V_m$ for the two islands shown in Figure 6.22. An island from the 0.2 Å/s flux is shown in Figure 6.22(a). For this island we find that $V_{DI} = (1.06 \pm 0.08) \times 10^{-4}$ μm^3 and $V_m = (1.13 \pm 0.23) \times 10^{-4}$ μm^3. The agreement of these two values shows that striping arises from direct impingement (at least within the range of the uncertainty) for the 0.2 Å/s flux. Figure 6.22(b) shows an island from the 0.005 Å/s flux. In this case $V_{DI} = (1.57 \pm 0.13) \times 10^{-3}$ μm^3 and $V_m = (1.22 \pm 0.24) \times 10^{-3}$ μm^3. The agreement of these two values now enables us to generalize across the entire flux range, to conclude that the striping morphology results predominantly from the direct impingement of the particle flux onto the island bases. Of course we can not entirely exclude a small degree of upward and downward adatom migration given the magnitude of the uncertainty.

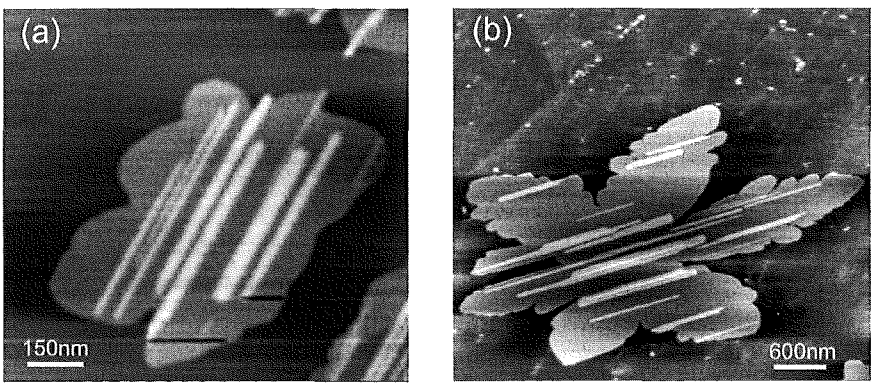

Figure 6.22: Islands selected to measure the ratio of directly impinged to aggregated material in the stripe morphology. Coverage is fixed at 1.5 ML. (a) $A_{island} = 0.418 \pm 0.008$ μm^2, F=0.2 Å/s. (b) $A_{island} = 6.16 \pm 0.12$ μm^2, F=0.005 Å/s.

The confinement of directly impinged material to the top face of the island bases, is consistent with the observation that the base heights are independent of coverage, since this implied a large Erlich-Schwoebel barrier at the island edges. This barrier also prevents significant migration from the top face to the side faces of an island. A similar effect was reported for the Au/HOPG system [16], where small increases in island height could be entirely accounted for by directly impinged material. However, in that system the material seemed to be evenly dispersed across the top face of the island, rather than aggregated into structures on top of the island base.

6.2.2 Stripe Densities

The number of stripes per island, n have been counted for islands deposited under various flux and coverage conditions. Figure 6.23(a) shows a plot of n as a function of the island area, for a fixed flux of 0.03 Å/s. The number of stripes per island increases approximately linearly with increasing island size. The plot includes data from 4 coverage examples, as indicated by the data legend, and we observe that there is no obvious distinction between the different coverages. Figure 6.23(b) shows a plot of the number of stripes per island as a function of increasing island area (combined data from all coverages) for three flux environments. All fluxes show an approximately linear increase in the number of stripes per island with increasing island area, implying a constant stripe density, ϱ for a fixed flux, since $\varrho = dn/dA$. The stripe density increases with increasing flux from 3.3 ± 1.0 μm^{-2} at F=0.005 Å/s to 50 ± 12 μm^{-2} at F=0.2 Å/s. The increase in stripe density can also be observed by comparing the AFM images in Figure 6.1 (F=0.005 Å/s) and Figure 6.2 (F=0.2 Å/s).

Figure 6.23(c) shows a log-log plot of the stripe density as a function of the particle flux. It is clear that the stripe density increases dramatically when the flux is increased from F=0.03 Å/s to F=0.2 Å/s. It also appears that there is little change in density from F=0.005 Å/s to F=0.03 Å/s.

The constant stripe densities for all islands in a given flux environment, and the increase in the stripe density with increasing flux, can be explained if we assume the island bases serve as finite bismuth substrates for the diffusion and nucleation of directly impinged material into stripe-like islands. When the particle flux is increased, the time between collisions with other diffusing adatoms is reduced. This results in an increased aggregate density, as we have already demonstrated for the Bi/graphite system. For the case of Bi/HOPG, the log-log plot of the island density (Figure 6.15) showed a linear increase with increasing flux, consistent with nucleation via adatom collisions. It is immediately apparent from Figure 6.23(c) that this is not the case for the Bi/Bi system. Instead we observe a similar stripe density for the two low flux cases, implying that nucleation via adatom collision is not relevant. This trend may be indicative of nucleation on defects at low flux, followed by a crossover to nucleation via adatom collision at

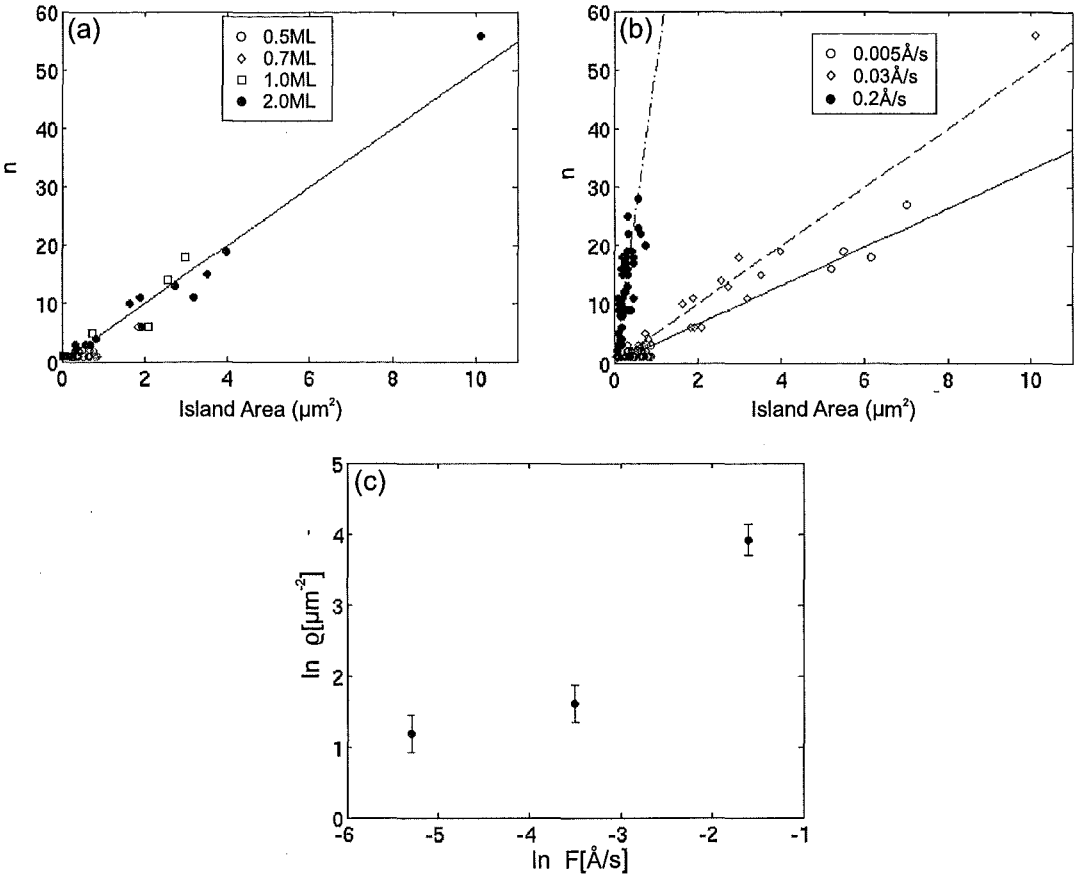

Figure 6.23: (a) Plot showing the linear increase in the number of stripes present on an island, n as a function of island size, for a range of coverages at a fixed flux of F=0.03 Å/s. The line is a least squares fit to the entire data set. Note there is no distinguishable variation with coverage. (b) Plot showing the increase in the number of stripes with increasing island size for various fluxes, all coverages are included in the data set, the lines are least squares fits to the experimental data. (c) The evolution of the stripe density, ϱ with increasing flux, note the dramatic increase from F=0.03 Å/s to F=0.2 Å/s.

some critical flux, as was demonstrated schematically in Figure 6.14. However, it is of course impossible to state this definitively given the limited data set. Difficulty in scanning high flux samples with the AFM prohibits a more complete picture from being obtained.

6.2.3 Evolution of Striping Morphology With Flux

Figure 6.24 presents AFM images of the evolution of striping morphology with increasing flux, at a constant coverage of 1.5 ML. It is clear that the width of the stripes are similar in the F=0.005 Å/s and F=0.03 Å/s environments, but dramatically decreases when the flux is increased to 0.2 Å/s. This is consistent with the observation of similar stripe densities for F=0.005 Å/s and F=0.03 Å/s, and the increase in island density for the 0.2 Å/s flux, in the previous Section. This parallels the behavior of a surface diffusion and nucleation system, where an increased island density reduces the adatom capture zone per island, resulting in

smaller islands, or in this case narrower stripes. The wider stripes in the low flux environments often feature striping themselves, resulting in layered morphology. This second layer of stripes is most likely due to the direct impingement of the particle flux on to the stripes themselves, in much the same way as the first layer of stripes aggregate from the direct impingement of particles on to the island bases.

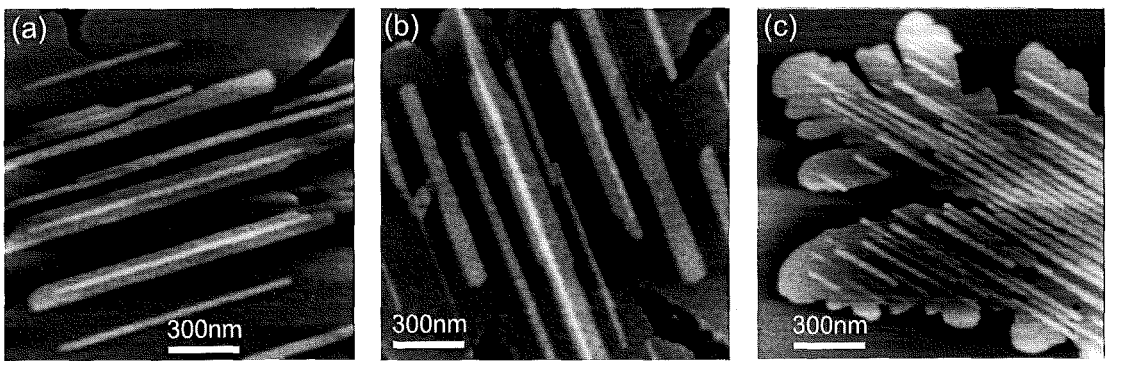

Figure 6.24: The evolution of striping morphology with increasing flux. (a) F=0.005 Å/s, (b) F=0.03 Å/s, (c) F=0.2 Å/s. The coverage is fixed at 1.5 ML. The wider stripes from the lower flux case often feature multiple layers of striping at this coverage. Note the dramatic change in stripe width when the flux is increased from 0.03 Å/s to 0.2 Å/s.

Figure 6.25 shows two islands from the F=0.005 Å/s and F=0.2 Å/s flux environments, both with the same coverage of 1.5 ML. It is apparent from the low flux image that the stripes tend to be wider towards the centre of the island. This can be understood if we consider the stripe morphology in terms of bismuth deposition and diffusion on island bases that are growing with time. At the end of deposition, the innermost regions of the island base have been exposed to the direct impingement of particles for longer than the outer regions, since they formed first. Consequently, more material is available for stripe aggregation here, leading to broader stripes towards the centre of islands, and narrower stripes towards the more recently formed outer island regions. This feature is less obvious in the high flux image, probably because the high density of stripes prevents the effect from becoming so pronounced. The insets in Figure 6.25 (b) show that the innermost stripes do tend to be wider, but there is little free space to accommodate the broadening. Instead, the stripes grow into each other and coalesce.

The stripe heights have been measured from AFM scans. Figure 6.26 shows the height of individual stripes as a function of their projected surface area for (a): F=0.005 Å/s and (b): F=0.2 Å/s, at a fixed coverage of 1.5 ML. Both plots contain data from multiple islands. It is evident for both fluxes that the stripe height increases with increasing stripe area, and eventually levels off to a maximum height. The high flux stripes tend to be flatter than those featured on the low flux islands, with a maximum stripe height of approximately 1.1 ± 0.15 nm

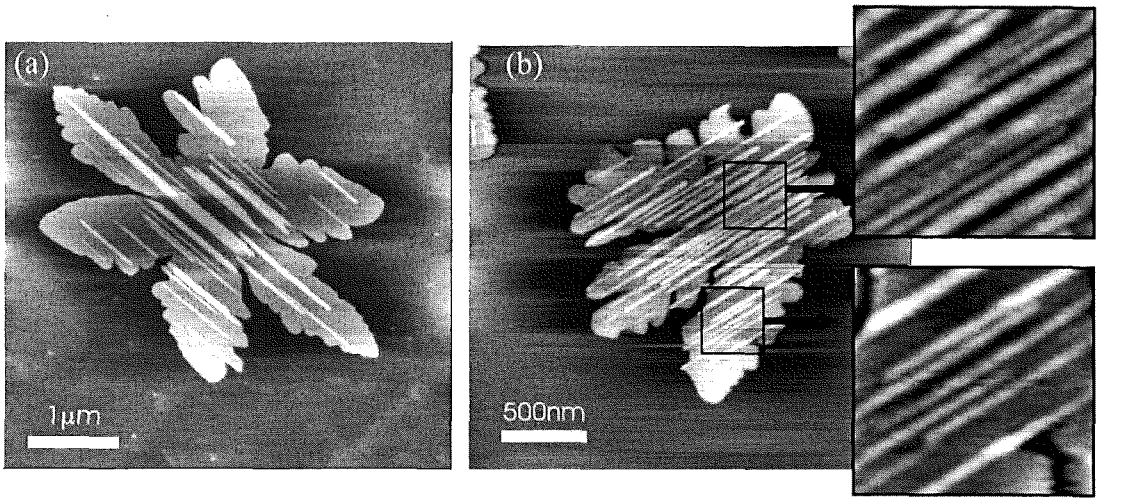

Figure 6.25: Variation of stripe width across the island base. (a) F=0.005 Å/s, (b) F=0.2 Å/s. Coverage is fixed at 1.5 ML.

for F=0.005 Å/s, and 0.8 ± 0.15 nm for F=0.2 Å/s. It is interesting to note the contrast of the stripe heights with those of the island bases. The stripes vary in height with increasing area, from approximately 0.3 nm (corresponding to 1 atomic layer) and the maximum height is flux dependent. The island base heights did not depend on area or flux, and were never as flat as 0.3 nm.

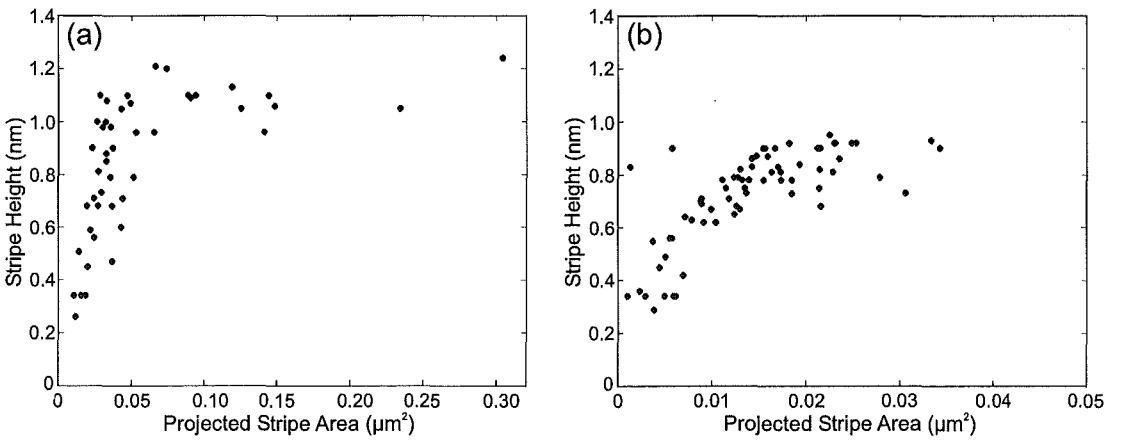

Figure 6.26: The stripe heights measured from AFM scans. Each plot contains stripe data from several islands (a) F=0.005 Å/s, θ=1.5 ML (b) F=0.2 Å/s, θ=1.5 ML.

6.2.4 Evolution of Striping Morphology with Coverage

The evolution of the striping morphology with increasing coverage can be observed in the AFM images in Figure 6.1, for the low flux environment, and in Figure 6.2 for the high flux case. A study of the striping behavior as a function of coverage is presented in Figure 6.27. The fraction of an island covered with stripes (defined here as the striping fraction, ξ) as a function of the island base

area for different coverages, is shown in Figure 6.27(a), where each data point is from a single island. This plot shows that for a fixed coverage, there is negligible dependence of the striping fraction on the island size. This is clearly what is expected for the case of direct impingement. The surface area of an island that is projected on to the substrate defines a finite collection area for the capture of directly impinged particles. Larger island bases capture proportionately more directly impinged material, thus keeping the striping fraction constant.

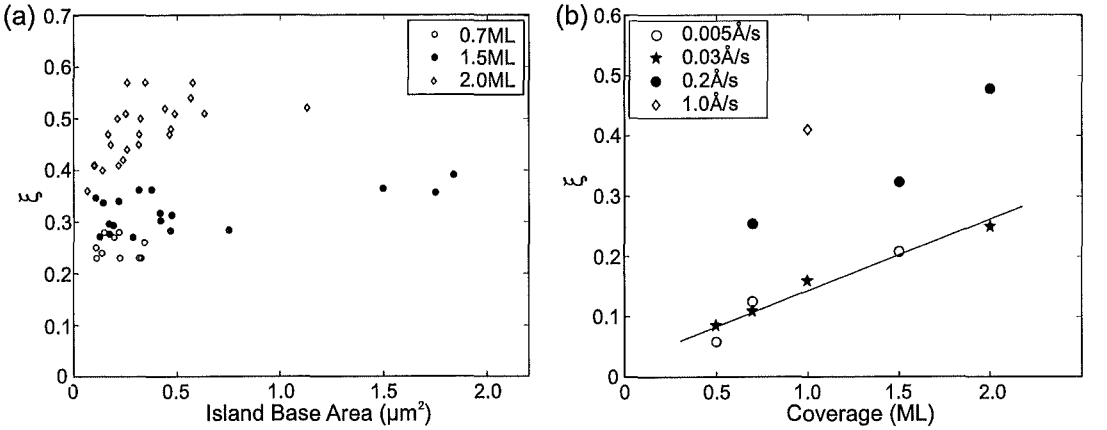

Figure 6.27: Plots of the fraction of an island base that is covered by stripes, ξ. (a) Variation with island base area for different coverages, the flux is fixed at 0.2 Å/s. (b) Variation with coverage (data averaged across all island sizes) for different fluxes, the line is a linear fit to the F=0.03 Å/s data.

It is apparent from Figure 6.27(a) that the striping fraction increases with increasing coverage. Figure 6.27(b) shows a plot of the average striping fraction as a function of coverage for various fluxes (averaged data across all island sizes for a given coverage, since there was no obvious dependence). The linear increase in striping fraction with coverage is evident in this plot for all fluxes. The line in Figure 6.27(b) is a linear fit to the F=0.03 Å/s data. We also observe that the 0.005 Å/s flux follows approximately the same linear fit. The striping fraction is greater for the F=0.2 Å/s and F=1.0 Å/s cases than it is in the lower flux examples.

The increase of the striping fraction with increasing coverage observed in Figure 6.27(b) is consistent with the direct impingement of particles on to the island bases. Island bases collect directly impinged material from the moment they form. As deposition proceeds, the islands grow larger and project a greater surface area on to the substrate, thus collecting more directly impinged adatoms. The longer the deposition time (increasing coverage), the more time the bases have to collect the material, leading to an increasing fractional coverage with time.

The increase in the striping fraction for the higher fluxes in Figure 6.27(b) implies that either there is more material involved in striping in the higher flux

cases, or the stripes are flatter and hence project a greater surface area on to the island base. In Section 6.2.3 we found that the lower flux stripes tended to be taller than those aggregated in a high flux environment. We also noted that the wider low flux stripes often feature a multiple stacking of stripes, therefore the projected surface area of these stripes will be less than for the single layer stripes containing the same amount of material. The combination of these two observations indicates that the greater projected surface area of the stripes in the high flux environment is most likely due to the material being dispersed into flatter stripes than their low flux counterparts.

Although direct impingement successfully accounts for the stripe morphologies discussed thus far, it is not consistent with the low coverage, low flux environment. The vast majority of islands in the θ=0.2 ML, F=0.005 Å/s deposits (shown in Figure 6.28(a)) exhibit no striping at all, and occasional islands have continuous layering featuring significantly more material than could be accounted for by direct impingement. It seems that we must admit both upward and downward adatom migration for these islands. At higher coverages this morphology is never observed. Beyond some particular size limit the upward adatom migration seems to cease, and the base layer remains intact with subsequent island growth proceeding at the same height as the regular island bases (see for example the middle island in Figure 6.28(a)). The agreement of the deposited and aggregated contribution to the island from direct impingement calculated in Section 6.2.1 indicates that this deviation from the standard direct impingement of striping material has negligible effect on the overall striping morphology in the low flux environment, probably because it is only observed for small islands.

Figure 6.28(b) shows an AFM image of small islands from the 0.2 Å/s flux. We observe that the islands feature the regular striping morphology in this high flux case. This demonstrates that the processes of upward and downward adatom migration do not appear to be active in the high flux environment, even for small islands comparable in size to those in the low flux case where these processes appear to dominate the morphology. It therefore seems that upward and downward adatom mobility are processes which require relatively long time scales to become active. This is also consistent with the observation of increased island heights for the hexagonal islands in the θ=1.5 ML, F=7×10^{-4} Å/s environment in Section 6.1.4, where the time available to allow upward adatom migration was increased.

6.2.5 Striping Summary

The structure on top of the island bases features a striping morphology, which arises mainly from the direct impingement of the particle flux on to the growing island bases. Subsequent diffusion of these adatoms on the bases results in many characteristics analogous to island nucleation and growth on substrates. We observe that the stripe densities are approximately independent of coverage

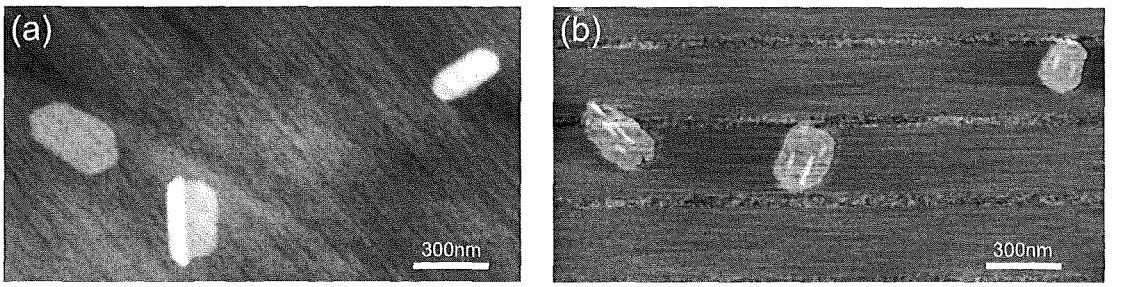

Figure 6.28: (a) AFM scan demonstrating the absence of the regular striping morphology in the low flux and low coverage environment, the island bases are typically of order 1 nm tall, however under these deposition conditions some bases have continuous layering to produce a base height of order 2 nm. θ=0.2 ML, F=0.005 Å/s. (b) The regular striping morphology is present in the high flux (F=0.2 Å/s)case at the same coverage (θ=0.2 ML).

beyond θ=0.2 ML. There is little change in density when the flux is increased from 0.005 Å/s to 0.03 Å/s, but a large increase results when the flux is further increased to 0.2 Å/s. Correspondingly, the stripe widths also decrease with the increased density. The fraction of the island base covered with stripes (striping fraction) is independent of island size beyond θ=0.2 ML for a fixed flux. However the striping fraction increases with increasing coverage.

It therefore seems that striping can be accounted for by a model involving the deposition and diffusion of particles onto a finite bismuth substrate that is growing in size with time. However it should be noted that in the low flux low coverage case (θ=0.2 ML, F=0.005 Å/s), we observe a departure from the direct impingement model. In this environment upward and downward adatom mobility appear to be active, and prevents the formation of stripes.

6.3 Island Coalescence and a Transition to Trigonal Symmetry

We now depart from studying low coverage island morphologies, and instead focus on the evolution of the films as the coverage is increased beyond 2 ML. This Section explores the coverage range of 5 ML - 100 ML (with the flux fixed at 0.03 Å/s), allowing investigation of the interaction between large islands that are in close proximity.

6.3.1 Morphology: An SEM and AFM study

A series of SEM images (top), AFM images (middle), and AFM height cross-sections (bottom) of the film morphology for 5 ML, 12 ML, and 100 ML coverages are presented in Figure 6.29.

The 5 ML SEM image in Figure 6.29 shows large branched islands which cover most of the surface. We also note a small region in this image with a morphology different to the rest of the film (circled for ease of identification). It

is characterized by an increase in image brightness, which is often indicative of an increase in film height. The AFM image of the more typical island morphology reveals an increase in the number of stripes present on the island surfaces compared to the lower coverage images presented in previous Sections, with multiple stripe layering. It is clear from this image that the stripes are again parallel within individual islands. The AFM image inset shows a high magnification region where two islands have grown together and begun to coalesce. The height cross-section shows that the stripes are of order 1 nm tall, consistent with the heights reported for the low coverage islands in Section 6.2.

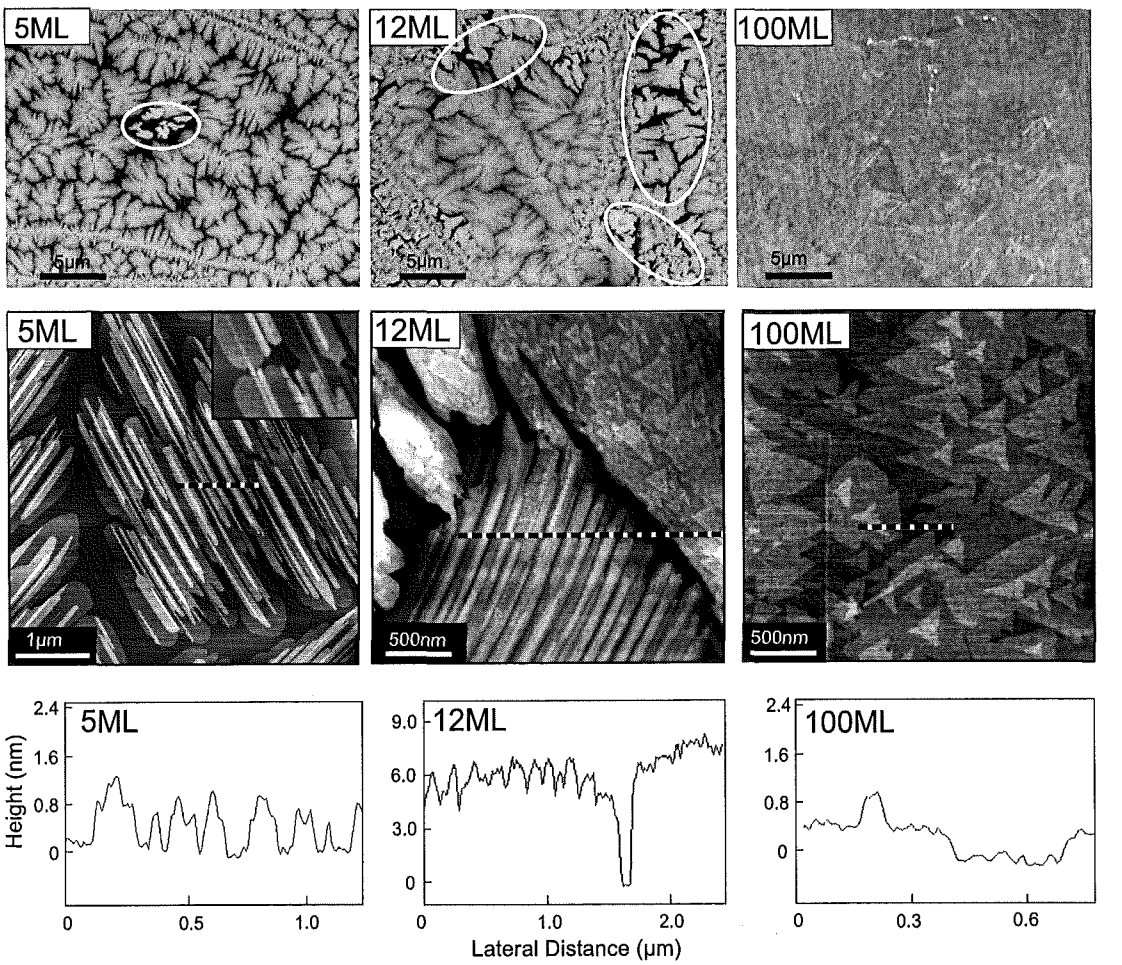

Figure 6.29: Top panel: SEM images of bismuth films for 5 ML, 12 ML, and 100 ML (F=0.03 Å/s). The circled regions in the 5 ML and 12 ML images indicate the restructured morphology referred to in the text. Bottom panel: AFM images (higher magnification) of the 5 ML, 12 ML, and 100 ML films (F=0.03 Å/s), the inset in the 5 ML image shows a higher magnification region with image size 820 nm × 650 nm. The dashed black and white lines in the AFM images indicate the positions of height cross-sections, which are shown in the bottom panel.

In DLA, when large islands grow towards each other, their capture zones become significantly reduced due to the increasing size of the islands, resulting

in slower lateral growth. The majority of island growth will then be vertical due to direct impingement of the flux on to the island base (and aggregation into stripes). If 3D rearrangement is possible, as was the case for antimony, the reduction in capture zone area is slow since material can be transported from the growth front into vertical island growth, and island coalescence is postponed. For antimony, capture zones were still visible at θ=200 ML, and island growth was observed up to θ=1000 ML. Conversely for Bi, there is negligible transport from the growth front into 3D growth, resulting in faster growth along the plane of the substrate (2D growth). The islands touch when the capture zone is eventually filled, and begin to coalesce, as shown in the AFM image inset in Figure 6.29, where two islands have joined together and the stripes begin to form continuously over both islands.

The 12 ML SEM image shows a dramatic increase in the new morphology (circled in the image), resulting in two coexisting island morphologies on the surface. It is clear that the new morphology projects less surface area on to the substrate than the regular islands, as evidenced by the increase in exposed substrate between these islands. The accompanying AFM image shows both morphologies. The large island in the bottom of the image exhibits the stripes. In contrast, the island in the top right of the AFM image, which is typical of those shown in the circled regions in the SEM image, shows a different morphology with triangular surface features. Also, the accompanying height profile confirms that this new morphology (represented in the right of the cross-section) is slightly taller than the striped islands (represented in the left of the cross-section). This redistribution of the island volume into taller islands with less projected surface area implies a restructuring of the islands as a whole.

The 100 ML SEM image shows a relatively uniform and continuous film at this magnification. There is no evidence for any island boundaries, confirming the large scale island coalescence and a transition to a continuous film. The corresponding AFM image shows a continuous film with a pancake-like layer stacking of triangular surface steps. The AFM cross-section represents a height profile through two such layers. Although the profile is of poor quality, it is sufficient to determine that each layer has a height of approximately 0.4 ± 0.1 nm. It is shown in Section 6.4 that these films have their $\{0001\}$ crystallographic planes oriented parallel to the substrate, corresponding to an inter-planar spacing of 0.39 nm. Therefore, each triangular step has a single atomic layer thickness.

Growth of the triangular film morphology proceeds in a similar manner to the striped island growth. In the case of the striped islands studied in Section 6.2, stripes frequently coalesced, and new stripes also formed on top of existing ones, producing a multiply layered morphology. In the case of the triangular surface steps, adjacent triangles also coalesce to form layers, but an entirely continuous layer is also not achieved before the next layer begins. This is demonstrated in Figure 6.30 (θ=30 ML), which shows 6 such height layers (indicated by grey-scale

intensity), with many merging triangles, and holes in the film, where complete coalescence has not been achieved. The accompanying height profile through the dashed line in the image shows again (with better resolution than the θ=100 ML profile in Figure 6.29) that each layer is consistent with a single atomic height.

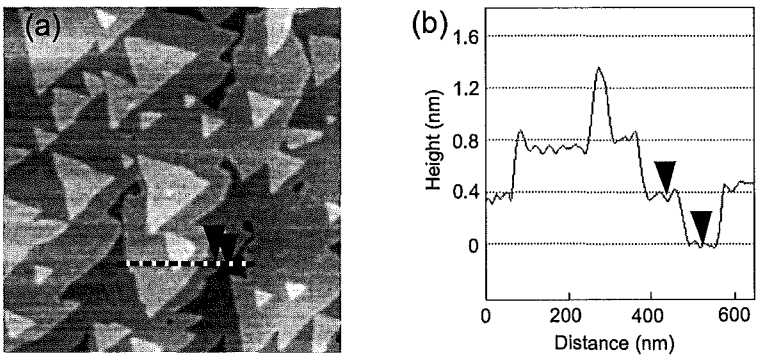

Figure 6.30: (a) AFM image from a trigonal film (θ=30 ML, F=0.03 Å/s). (b) Height cross-section through the line indicated in the AFM image.

6.3.2 Summary of Island Coalescence and Transition to Trigonal Symmetry

It is evident that the Bi/HOPG system begins growth with a striped island phase, followed by a transition to a continuous trigonal morphology with increasing thickness. The transition seems to begin with the restructuring of some striped islands into taller islands with triangular steps at a deposited dose of ~12 ML. As deposition proceeds, the film becomes continuous, with trigonal symmetry. The next Section investigates the crystal structure of both the striped islands and the trigonal film.

6.4 Crystal Structure and Orientation: An EBSD Study

This Section discusses use of the EBSD technique to investigate the crystallographic orientation of the substrate, islands, and continuous film. This allows determination of the orientation relationship between the adsorbate and substrate crystallographies. First, the orientation of the bare substrate is discussed, followed by that of the striped islands and the underlying substrate. The evolution of the crystallography with increasing coverage is explored, and discussed within the context of the changing film morphology observed in the previous Section, showing a thickness dependent orientation transition in the Bi/HOPG system. The interaction of the bismuth and graphite lattice meshes is also discussed. Finally, the crystal structure is then used in conjunction with edge diffusion effects to describe the shape formation.

6.4.1 Substrate Orientation

To allow correlation of film and substrate crystallographies, it is necessary to determine the uniformity of the graphite substrate over different length scales. Figure 6.31(a) shows a typical EBSP from a freshly cleaved HOPG substrate (top), showing the series of Kikuchi diffraction bands. The orientation solution is also shown (bottom). Figure 6.31(b) shows pole figures for 30 index points taken within a 350 μm^2 region of the substrate. The {0001} pole figure shows the stereographic projection of the HOPG{0001} plane normals, showing that the substrate surface always reveals the HOPG{0001} plane (as expected, since cleaving breaks the weak interlayer Van der Waals bonds of the layered graphite structure). The $\{10\bar{1}0\}$ pole figure shows the 6 equivalent $\{10\bar{1}0\}$ plane normals, which all intersect the edges of the stereographic projection (since the $\{10\bar{1}0\}$ and {0001} crystallographic planes are perpendicular), revealing the same in-plane orientation for all 30 data points. It is therefore clear that the crystallographic orientation of HOPG is uniform within this 350 μm^2 region.

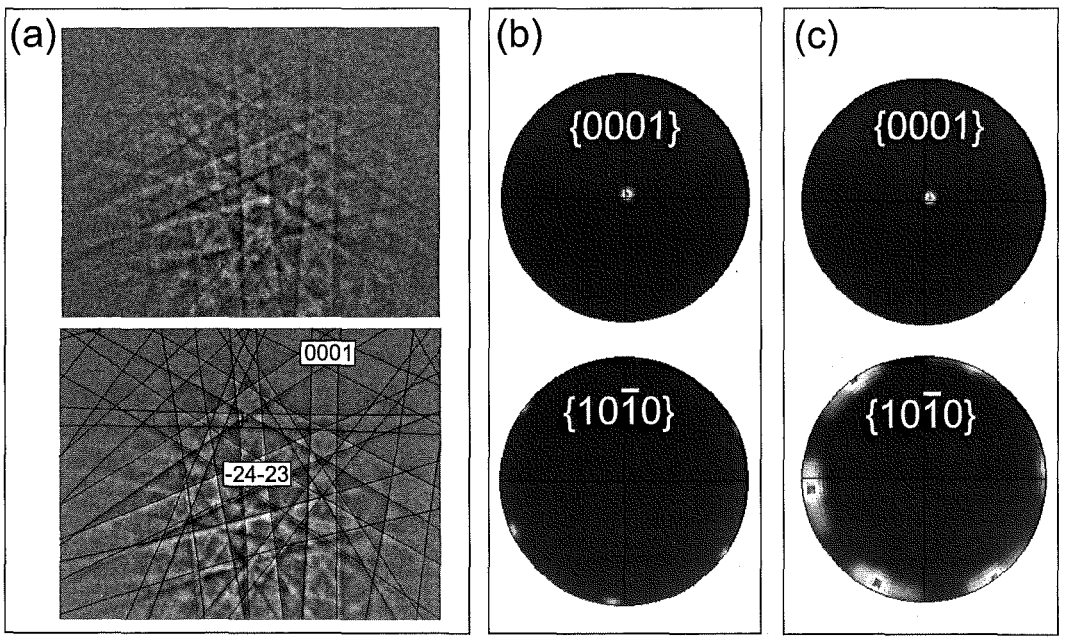

Figure 6.31: (a) Typical EBSP from the bare graphite substrate. (b) Pole figures (stereographic projections) for a 350 μm^2 region of HOPG. (c) Pole figures for a 4×10^4 μm^2 region of HOPG.

Figure 6.31(c) shows pole figures for 30 data points taken from a 4×10^4 μm^2 region. The smearing of the poles in the $\{10\bar{1}0\}$ pole figure shows that over relatively large areas there is some basal plane rotation. Consequently, the substrate and film patterns must be obtained from the same area to allow precise correlation of substrate and film crystallography.

6.4.2 Orientation of Bismuth Films

The EBSD instrument requires a minimum film thickness of order 10 nm to index crystallographic orientations. This obviously excludes the possibility of directly indexing the island bases in the coverage range of 0.2-2.0 ML, which were typically of order 1 nm tall. Indexing was attempted on thicker islands from higher coverage deposits (see for example the θ=12 ML AFM cross-section in Figure 6.29 from the previous Section). However, it should be noted that these islands are still significantly thinner than samples that are usually used in EBSD studies. Consequently, obtaining EBSPs is non-trivial and requires careful optimization of SEM parameters, as will be described below.

10 ML Film

Indexing was first attempted on a 10 ML coverage sample, in order to find the thinnest film capable of producing Kikuchi bands for the bismuth lattice. Figure 6.32 shows an EBSP taken from a θ=10 ML bismuth island. Comparison with Figure 6.31(a) shows that it has the same set of Kikuchi bands as the substrate, and the automated EBSD indexing software confirmed the solution as being that of the hexagonal graphite lattice. The implication is that for coverages $\lesssim$ 10 ML, the electron beam penetrates the bismuth islands to produce Kikuchi diffraction bands from the underlying substrate.

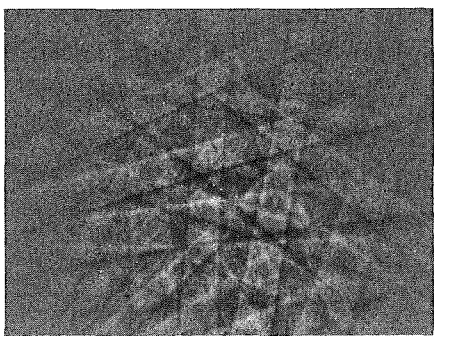

Figure 6.32: EBSP for an island from a θ=10 ML bismuth film, which was indexed as the graphite structure.

12 ML Film

A 12 ML coverage sample (corresponding to a deposited dose of 4 nm, aggregated into islands approximately 5-7 nm tall), was the thinnest film which exhibited EBSPs that could be indexed for bismuth. Figure 6.33(a) shows an FE-SEM image of the island morphology from a θ=12 ML sample, where the striped features are clearly visible. Note that this image has been tilt corrected (from the 70° orientation required for EBSD). The FE-SEM accelerating voltage and probe current were set to 10 kV and 11 (unitless) respectively. These were

not optimum imaging parameters, but were a necessary compromise between obtaining sufficient image resolution, and optimizing the intensity of the Kikuchi bands. Often higher accelerating voltages produced better image resolution but poorer quality EBSPs. However different regions of the sample required different settings, which could typically only be found by trial and error.

In order to determine the crystallinity of the islands, index points were taken at 6 different locations within the highlighted region of the image, which all have the same stripe direction. An EBSP from one such location is shown in Figure 6.33(b). This pattern is the most intense that was able to be obtained from a θ=12 ML film, often the Kikuchi bands were significantly weaker. Consequently, automated band detection was often not successful, requiring the bands to be defined manually, and negating the possibility of automated orientation mapping.

Figure 6.33(c) and (e) show pole figures for the 6 index solutions, and are interpreted as follows.

- The pole cluster in the centre of the $\{01\bar{1}2\}$ pole figure in Figure 6.33(c) shows that the islands have a $\{01\bar{1}2\}$ plane parallel to the substrate plane ($\{01\bar{1}2\}$ oriented). The two pole clusters near the edge of the figure originate from the other equivalent $\{01\bar{1}2\}$ planes.

- The three equivalent $\{01\bar{1}2\}$ crystallographic planes are shaded in the rhombohedral bismuth cell in Figure 6.33(d), with their plane normals indicated. When one $\{01\bar{1}2\}$ plane normal is perpendicular to the surface (centre cluster of poles), the other two are oriented as shown, producing the poles (plane normals) near the edges of the pole figure [4].

- The $\{0001\}$ pole figure shown in Figure 6.33(e) demonstrates the relationship between the $\{01\bar{1}2\}$ and $\{0001\}$ crystallographic planes (which will be required later, when the pole figures are comprised of multiple island orientations). An island with a $\{01\bar{1}2\}$ orientation projects a single $\{0001\}$ plane normal onto the upper stereographic hemisphere, as indicated in (d). The angle between the $\{01\bar{1}2\}$ and $\{0001\}$ crystallographic planes (and hence plane normals) is 54° according to Equation 3.1. Hence, the $\{0001\}$ pole appears at 54° on the pole figure.

The pole figures in Figure 6.33 demonstrate a single orientation for all indexed points within the highlighted region of the FE-SEM image, showing that the islands (all with stripes in the same direction) are single crystal. We now proceed with a description of the various island and substrate orientations.

[4]Note that if the $\{01\bar{1}2\}$ islands were indexed as perfectly parallel to the substrate plane there would be 4 pole clusters on the outer edges of the $\{01\bar{1}2\}$ pole figure. The two missing clusters are a result of a slightly off-centre indexing, which push the poles into the lower hemisphere of the stereographic projection. This is also observed to some extent in the graphite pole figures, indicating that it is the result of a slight sample-beam geometry misalignment.

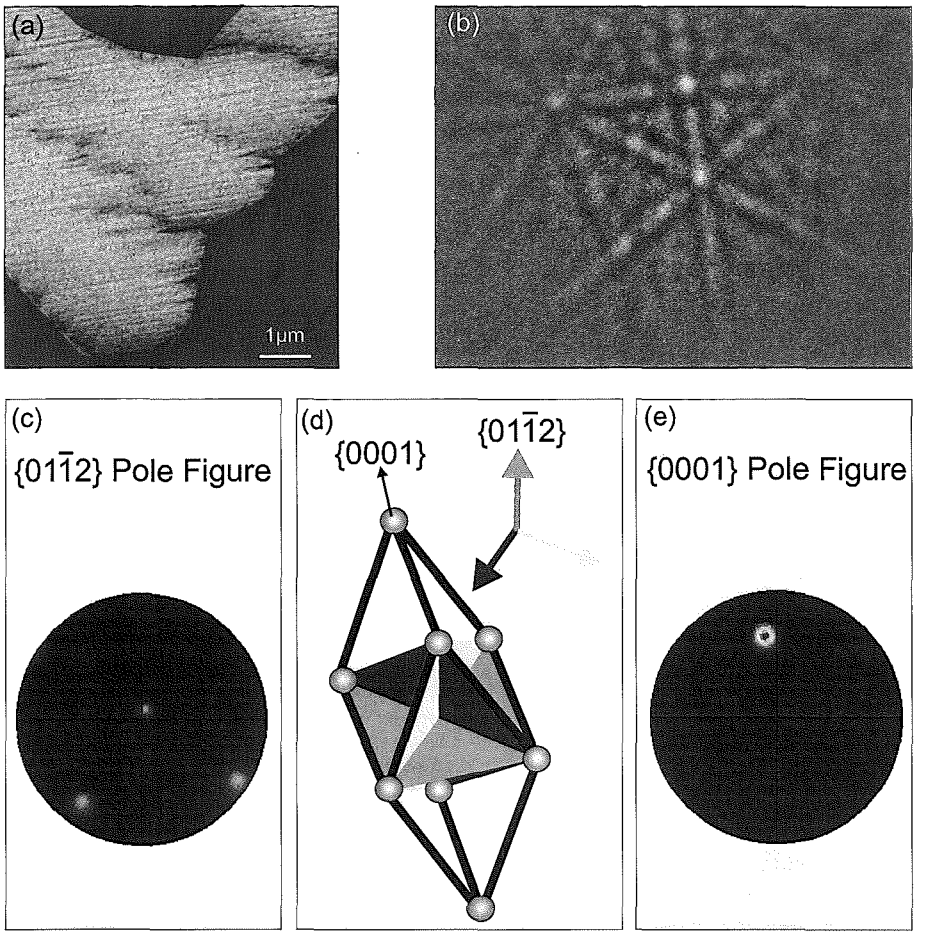

Figure 6.33: (a) FE-SEM image of islands from a θ=12 ML film, the highlighted island area (centre) indicates the region used for local EBSD probing. (b) An EBSP from within the highlighted region. (c) Bi{01$\bar{1}$2} pole figure. (d) Illustration of the three equivalent {01$\bar{1}$2} planes and plane normals in the bismuth structure. Note that a rhombohedral cell is shown for simplicity. (e) Bi{0001} pole figure.

Figure 6.34(a) shows an example of a weak (typical) EBSP pattern from a θ=12 ML sample (left). For such relatively thin films, the EBSPs are often comprised of a convolution of Kikuchi bands from the substrate and the bismuth film, which prohibited automated indexing (the software can not index two superimposed patterns). However, the Kikuchi bands for graphite are significantly wider than those of bismuth (compare for example Figures 6.31(a) and 6.33(b)), which enabled manual detection of both types of bands independently, thus allowing solutions for the orientation of the film and substrate (shown at centre and right respectively in Figure 6.34(a)) to be determined from the same location on the sample. For EBSPs where the graphite bands could not be resolved, the substrate was indexed through the gaps in the film which surround the islands. Figure 6.34(b) shows an FE-SEM image of two striped islands (labeled 1 and 2), and an island which does not exhibit the striped features (labeled 3). Island 3 is representative of the taller morphology shown in the circled regions of the

θ=12 ML SEM image in Figure 6.29. Pole figures for these three islands are shown at right; the individual poles have been labeled according to the island of origin. Figure 6.34(b) illustrates that islands 1 and 2 have the Bi{01-12} plane parallel to the HOPG basal plane ({01$\bar{1}$2}Bi||{0001}HOPG), and island 3 has {0001}Bi||{0001}HOPG (referred to as the trigonal orientation). These were the only two orientation variants observed for all indexed islands (several hundred), and also for a range of fluxes. We now consider the in-plane orientations of the islands, and their orientation relationship to the substrate.

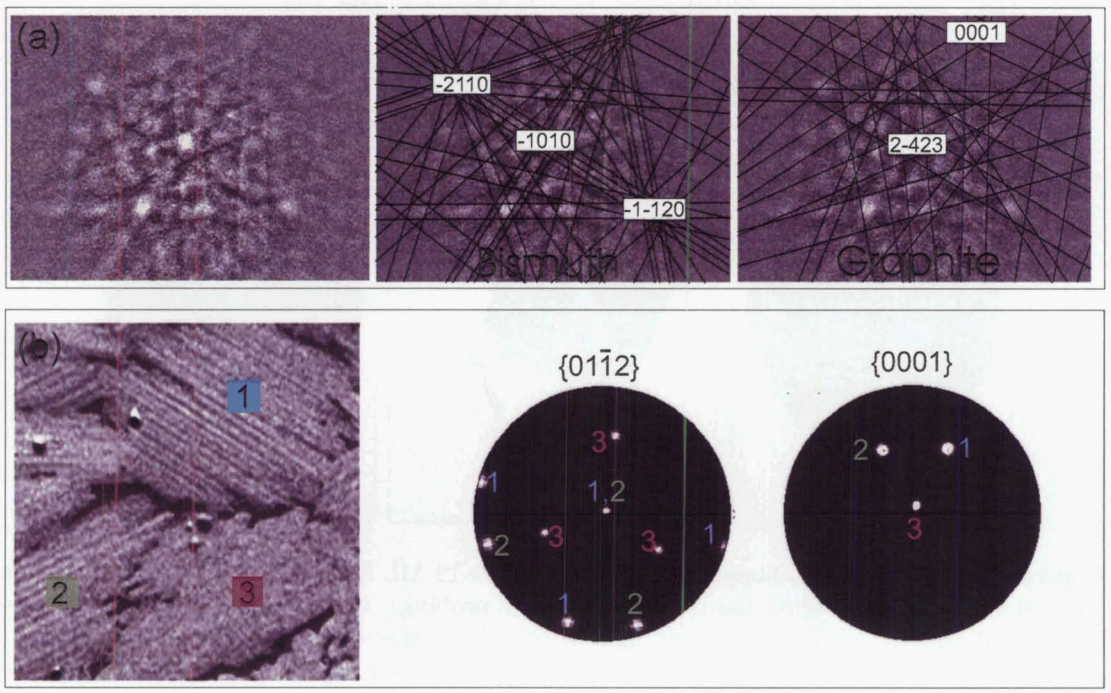

Figure 6.34: (a) An EBSP recorded from a θ=12 ML sample showing Kikuchi bands for both bismuth and graphite (left), the orientation solutions are shown for bismuth (centre) and graphite (right). (b) FE-SEM image of the θ=12 ML film showing both the striped islands (labeled 1 and 2) and the trigonal islands (labeled 3). The pole figures show the orientation solutions for all three islands, each pole has been numbered according to which island it represents.

Figure 6.35 demonstrates the the in-plane orientation of the {01$\bar{1}$2} striped islands (islands 1 and 2), with respect to both the bismuth and graphite crystallography. Figure 6.35(a) shows the rhombohedral bismuth structure, with a {01$\bar{1}$2} plane inscribed (left), and the {01$\bar{1}$2} unit cell (right). Note that the unit cell has a two atom basis (second atom shaded dark), with the second basis atom slightly off center. The solid lines represent the strong intralayer (covalent) bonds and solid lines show the weaker interlayer bonds referred to in Chapter 3.1. Note that the third covalent bond associated with each atom extends either into or out of the plane of the page, resulting in 50% of atoms on the {01$\bar{1}$2} surface

revealing an unsaturated covalent bond. The $\langle 11\bar{2}0\rangle$ direction [5] is also shown with respect to the unit cell. Figure 6.35(b) shows the FE-SEM image from Figure 6.34(b), with arrows drawn in the stripe direction on the two labeled islands. These direction indicators have been superimposed on the $\langle 11\bar{2}0\rangle$ bismuth pole figures in Figure 6.35(c), from which we observe that the island stripes are parallel to the indexed Bi$\langle 11\bar{2}0\rangle$ directions. The same direction indicators have also been placed over the HOPG $\langle 10\bar{1}0\rangle$ pole figure in (d), and show an alignment with the stripes parallel to the HOPG$\langle 10\bar{1}0\rangle$ directions.

For the striped islands, the orientation relationship between the film and substrate is therefore defined by $\{01\bar{1}2\}$Bi$||\{0001\}$HOPG, with the preferred in-plane orientation given by $\langle 11\bar{2}0\rangle$Bi$||\langle 10\bar{1}0\rangle$HOPG. The vast majority (approximately 90%) of Bi$\{01\bar{1}2\}$ island indexing produced the orientation relationship described above.

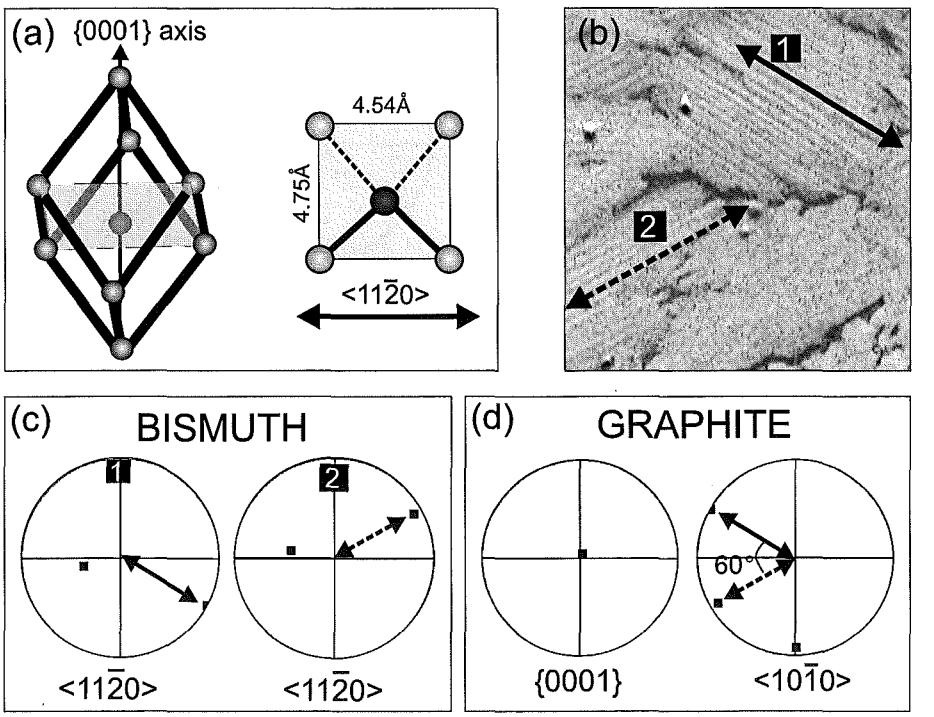

Figure 6.35: (a) Rhombohedral bismuth structure, shown with a $\{01\bar{1}2\}$ plane inscribed (left). The $\{01\bar{1}2\}$ unit cell is shown with the $\langle 11\bar{2}0\rangle$ direction indicated (right). (b) FE-SEM image of the θ=12 ML film showing two striped islands (reproduced from Figure 6.34(b)). The arrows indicate the stripe directions (solid line represents island 1, dashed line represents island 2). (c) Bismuth $\langle 11\bar{2}0\rangle$ pole figures for island 1 (left) and island 2 (right). The island stripe directions from the FE-SEM image are superimposed, showing stripe alignment with a Bi$\langle 11\bar{2}0\rangle$ direction. (d) Graphite pole figures, with the stripe directions again superimposed, showing alignment with HOPG $\langle 10\bar{1}0\rangle$ directions.

[5]Note that in the non-orthogonal hexagonal co-ordinate system a $\langle 11\bar{2}0\rangle$ direction is equivalent to a $\{11\bar{2}0\}$ plane normal since the last Miller index is zero. However, a $\{01\bar{1}2\}$ plane normal is not equivalent to a $\langle 01\bar{1}2\rangle$ direction [102].

Figure 6.36 demonstrates the in-plane orientation of the trigonal {0001} islands. The data is taken from island 3 in Figure 6.34(b), however the triangular surface features which characterize this island type can not be resolved in the FE-SEM image. The pole figures for island 3 and for the substrate are shown in Figure 6.36(a) and (b) respectively. A comparison of the bismuth and graphite pole figures reveals that the trigonal islands do not seem to have a good in-plane orientation match to the substrate. In this example, the bismuth lattice is rotated by 8° from the graphite lattice. Difficulties with indexing, and the relatively small number of these island types prevented a comprehensive study on this orientation. Therefore, the island/substrate orientation relationship is defined by {0001}Bi||{0001}HOPG. From the limited in-plane orientation data, it seems that the the two lattice planes are rotated by several degrees from a $\langle 10\bar{1}0\rangle$Bi||$\langle 10\bar{1}0\rangle$HOPG orientation.

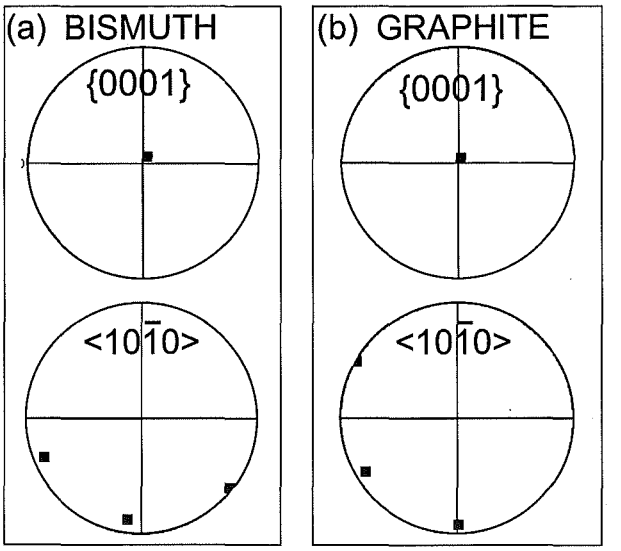

Figure 6.36: (a) Bismuth pole figures for island 3 (in Figure 6.34(b)). (b) Graphite pole figures.

15 ML Film

Figure 6.37(a) shows an EBSP from a sample with 15 ML coverage. Note the improvement in pattern quality compared to the EBSPs from the θ=12 ML sample in Figures 6.33(b) and 6.34(a). This results because as the island thickness increases, the interaction depth of electron beam is better accommodated by the islands, hence minimizing interference from the substrate crystallography. Figure 6.37(b) shows a {0001} pole figure for 45 indexed islands. The centre pole has the maximum intensity, demonstrating that the majority (77% in this example) of islands now adopt the Bi{0001} orientation. The outer clusters of {0001} poles are from a few remaining $\{01\bar{1}2\}$ oriented islands. It was no longer

possible to reliably index the substrate, since the graphite Kikuchi bands are absent from all the EBSPs, and there is not sufficient substrate area between islands to index the graphite locally.

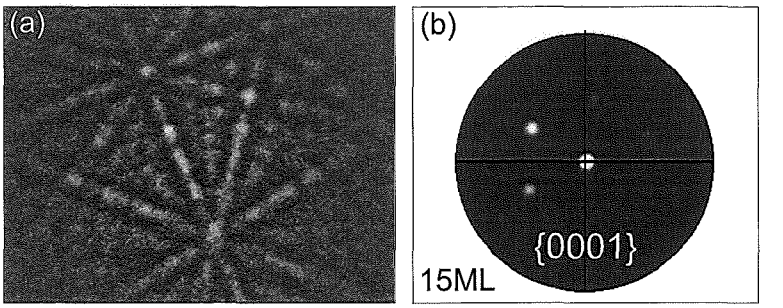

Figure 6.37: (a) EBSP from a θ=15 ML film. (b) Pole figure for 45 indexed islands from a 15 ML film.

100 ML Film

Figure 6.38(a) shows pole figures from an automated indexing scan of a 374μm^2 region of a sample with 100 ML coverage, revealing that the film is now exclusively trigonally oriented. The $\{10\bar{1}0\}$ pole figure shows clusters of poles at 30° in-plane rotations, however the smearing out of the pole densities indicates a degree of disorder in the in-plane orientation. Orientation maps for the θ=100 ML film are shown in Figure 6.38(b) and (c) (left images), with different colored regions representing different in plane orientations of the Bi{0001} lattice. The map in Figure 6.38(b) reveals many large single crystal Bi grains, some of which exceed 25 μm^2. The accompanying plot (right) shows the change in misorientation angle (which represents the difference in crystallographic orientation between adjacent index points) along the line drawn between three grains on the orientation map. The peaks labeled 1 and 2 correspond to the grain boundaries labeled on the map, and show an approximately 60° and 30° in-plane misorientation between the three grains, consistent with the pole figures. The orientation map in Figure 6.38(c) shows a higher resolution scan of two large grains. The misorientation angle plot shown in the accompanying plot (right) is for the line drawn through a single grain on the map, and shows that there is typically less than a 2° angular spread in the orientations within a grain.

Summary and Discussion of Orientation Transition

It is therefore clear that the film undergoes a crystallographic orientation transition from $\{01\bar{1}2\}$Bi||{0001}HOPG to {0001}Bi||{0001}HOPG with increasing thickness. This is illustrated in Figure 6.39 in terms of the rhombohedral unit cell, inside a hexagonal basis. Note however that the rhombohedral atoms are only shown for one cell within the hexagonal basis for simplicity (refer to Figure 3.2

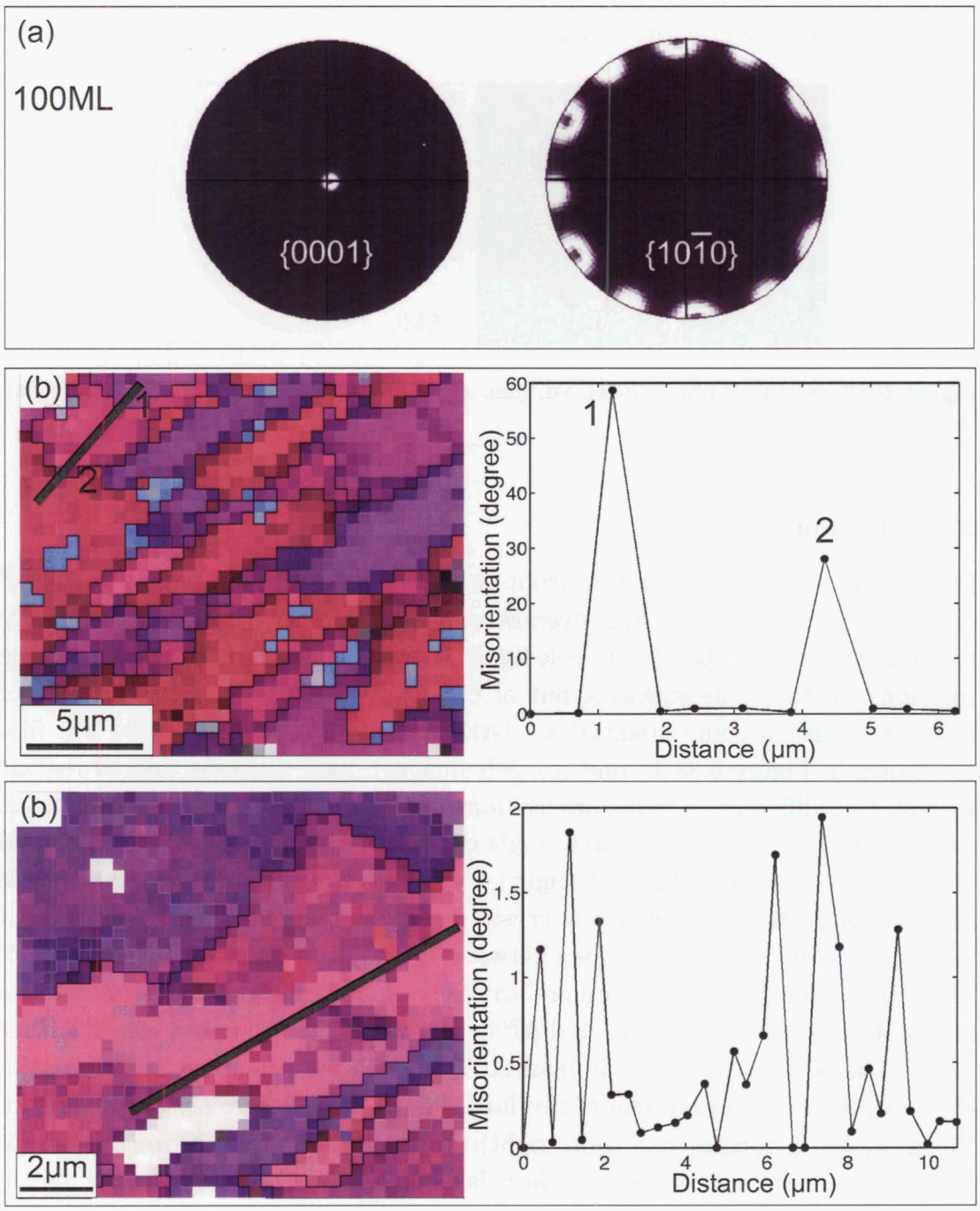

Figure 6.38: (a) EBSD pole figures for 1500 index points from a θ=100 ML film. (b) Left: Orientation map (0.5 μm step size) from a 100 ML film. Misorientation angles between neighboring index points along the line drawn between three grains on the orientation map are shown in the accompanying plot. (c) Orientation map (0.3 μm step size) from a 100 ML sample, featuring two large grains. The accompanying plot shows the misorientation angles between index points on the line drawn through a single grain on the map.

to see this representation along side a diagram with all the atoms included). The $\{01\bar{1}2\}$ striped islands have in-plane orientations matched to the high symmetry directions of the hexagonal substrate, while the $\{0001\}$ islands seem more disordered. This orientation transition explains the introduction of the taller triangular morphology, with increasing coverage observed in the SEM and AFM images, since the inter-planar distance for the $\{0001\}$ orientation (3.9 Å) is greater than for the $\{01\bar{1}2\}$ orientation (3.28 Å).

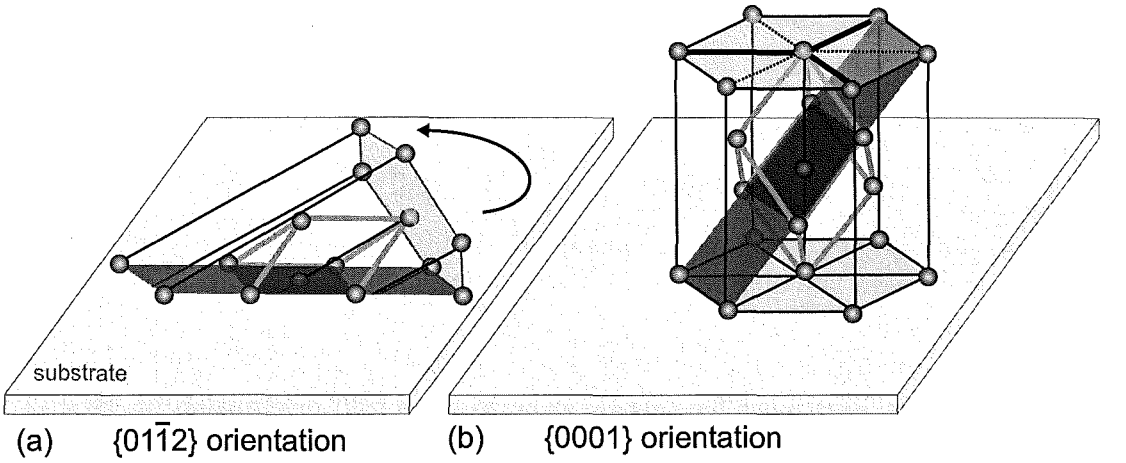

Figure 6.39: Crystallographic representation of the orientation of Bi islands on the substrate. The diagrams show both the rhombohedral structure and the hexagonal basis, with a $\{01\bar{1}2\}$ plane shaded dark grey, and the hexagonal $\{0001\}$ planes shaded light grey. (a) $\{01\bar{1}2\}$ orientation (b) $\{0001\}$ orientation.

Nagao *et al* have recently reported a similar orientation transition in an STM study of the Bi/Si(111)-7 × 7 system [158], but in that case the structure of the thin film form of Bi was reported to be that of a new allotropic form of bismuth (analogous to the puckered layer structure of black phosphorous), which reverts to the bulk Bi$\{0001\}$ phase beyond a critical island thickness of 1.3 nm. The presence of both striped and trigonal island types in the same region in the AFM image from the 12 ML film in Figure 6.29, indicates that the striped island is probably approaching the thickness required for transition to the trigonal orientation. In the height cross-section (same Figure) we can see that the striped island is approximately 5.3 nm (10% uncertainty) tall. Clearly, for Bi/HOPG the transition from a Bi$\{01\bar{1}2\}$ to a Bi$\{0001\}$ film occurs at significantly greater film thicknesses than in the Bi/Si(111) system.

The Nagao paper argues that layer pairing of the Bi$\{01\bar{1}2\}$ planes is required to saturate the dangling covalent bonds exposed on this surface. They subsequently use their STM observations that only bilayer island heights are stable, as experimental evidence for their calculated allotropic phase [6]. However, their low energy electron diffraction (LEED) experiments are consistent with the

[6]More detailed information on the geometry of the new structure is given in ref.[172]

bulk bismuth structure, indicating that these electron diffraction patterns can not discriminate between the bulk rhombohedral and the allotropic phase. Also, another very recent LEED study of the Bi/Si(111)-7 × 7 system [173] showed the same transition, but with no mention of a new allotropic-type phase. EBSD data for the Bi$\{01\bar{1}2\}$ islands is consistent with the bulk rhombohedral bismuth structure, but based on the above discussion, it is unlikely that this technique could discriminate between the two phases. The height data in Section 6.1.4 was not of sufficient resolution to distinguish precise multiples of atomic layer island thicknesses. Additionally, *in situ* measurements for both height and diffraction measurements would likely be required to further investigate the possibility of the new allotropic phase existing in the Bi/HOPG system.

6.4.3 Bismuth/Graphite Lattice Interactions

HOPG is traditionally selected as a substrate due to its weakly interacting properties, which makes the observed orientation transition in the Bi/HOPG system somewhat surprising, particularly since bismuth films usually grow in the trigonal orientation on a variety of substrates (such as CdTe(111) [23], mica [174], and BaF_2(111) [175]), and most fcc metals grow in the (111) orientation on HOPG (for example Au [54], Pd [176], and Ni [94]). It is however worth pointing out that Kaiser *et al* have shown a coverage dependent transition from large branched islands to small faceted crystals with trigonal symmetry in the Sb/HOPG system [20], and this transition is also indicated in our study presented in Chapter 5.

When adsorbates are deposited on foreign substrates, mismatch between the lattice parameters of the two materials at the island/substrate interface can modify the inter-atomic spacing of the island at the interface. For a given lattice mismatch, there are two competing forces: the adatom-adatom interaction, which favors the inter-atomic spacing of a free adatom layer, and the adatom-substrate interaction which attempts to force the adatoms to align with the substrate lattice. The misfit is defined as $M = (a_a - a_s)/a_s$ (standard text book definition [160]), where a_a and a_s are the lattice constants of the adsorbate and substrate respectively. In general, island orientations which produce a minimum misfit are favored, since large misfits increase the total energy of the system [177] .

The Bi$\{01\bar{1}2\}$ orientation has been reported on W(110) [104], where this orientation preference was attributed to a small lattice mismatch with the substrate (3.6%). In the previous study by Wang *et al* [87] of low coverage islands in the Bi/HOPG system, the growth mode was attributed to {0001}Bi||{0001}HOPG, based on arguments relating to minimizing lattice mismatch (experimental verification was not possible in that study). The current EBSD study shows that is clearly not the case, with the orientation relationship $\{01\bar{1}2\}$Bi||{0001}HOPG experimentally observed.

A trigonal orientation for bismuth on the graphite basal plane would produce a minimum lattice misfit of +6.6%, when the in-plane orientation is defined

by $\langle 10\bar{1}0\rangle$Bi$||\langle 10\bar{1}0\rangle$HOPG, as shown in Figure 6.40(a). The Bi and HOPG lattice meshes are shown superimposed for the experimentally preferred orientation $\{01\bar{1}2\}$Bi$||\{0001\}$HOPG and $\langle 11\bar{2}0\rangle$Bi$||\langle 10\bar{1}0\rangle$HOPG in Figure 6.40(b) (note that the positions of the Bi atoms with respect to the substrate carbon atoms are defined arbitrarily with regard to surface translation). This orientation relationship results in an anisotropic lattice mismatch of -7.7% and +11.5% along the short edge (Bi$\langle 11\bar{2}0\rangle$ direction) and long edge respectively of the $\{01\bar{1}2\}$ unit cell (based on bulk values).

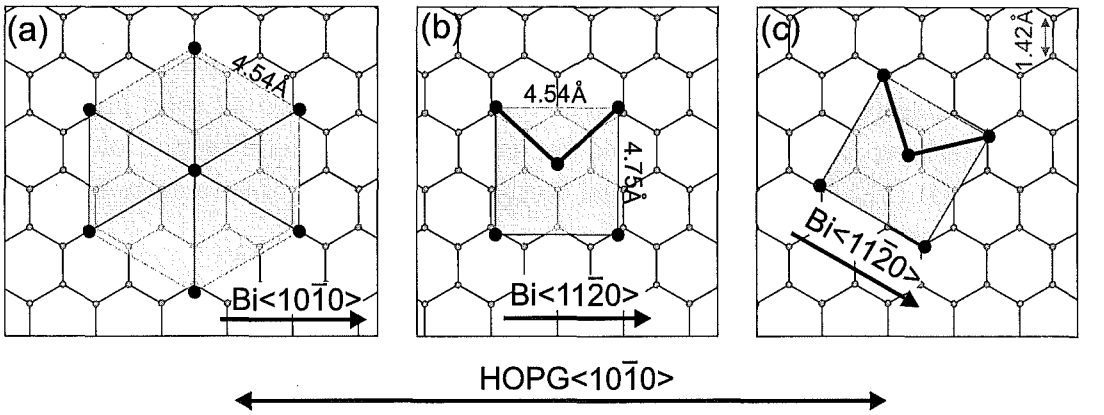

Figure 6.40: Superposition of the bismuth lattice (for various island orientations) on the HOPG basal plane. Cell dimensions are given in the illustrations. (a) Bi{0001} orientation with $\langle 10\bar{1}0\rangle$Bi$||\langle 10\bar{1}0\rangle$HOPG. (b) Bi$\{01\bar{1}2\}$ orientation with $\langle 11\bar{2}0\rangle$Bi$||\langle 10\bar{1}0\rangle$HOPG (experimentally preferred orientation at low coverage). (c) Bi$\{01\bar{1}2\}$ orientation with $\langle 11\bar{2}0\rangle$Bi$||\langle 11\bar{2}0\rangle$HOPG. An HOPG$\langle 10\bar{1}0\rangle$ direction is indicated at the bottom of the Figure.

It may be possible that the experimentally observed orientation is actually more energetically favorable at low coverages due to the anisotropy in the misfit (expansion coupled with contraction of the lattice). However, the alignment $\langle 11\bar{2}0\rangle$Bi$||\langle 11\bar{2}0\rangle$HOPG (Figure 6.40(c)) would produce a smaller mismatch in both directions (+6.6% and -3.5% along the short and long edges respectively of the $\{01\bar{1}2\}$ unit cell), which renders an explanation of the preferred orientation in terms of lattice matching problematic. It should however be noted that in-plane orientations which do not favor a minimum misfit have been observed in the Pd(111)/graphite system [93], due to a slight preference for adsorption sites located above carbon atoms. However, the site bonding preferences for bismuth on the graphite lattice are not known. The adsorbate/substrate relationship of the $\{01\bar{1}2\}$ orientation is also further complicated by the second basis atom, which is slightly off centre in the $\{01\bar{1}2\}$ unit cell. With these considerations in mind, it is likely that a complete understanding of the observed Bi$\{01\bar{1}2\}$ orientation, and transition to a Bi{0001} oriented film, would require rather complex *ab initio* calculations.

6.4.4 Influence of Crystallography on Island Morphologies

In the previous Section, the stripes on the Bi$\{01\bar{1}2\}$ islands were determined to be parallel to a Bi$\langle 11\bar{2}0\rangle$ crystallographic direction, and aligned with the $\langle 10\bar{1}0\rangle$ directions of the substrate. This enables the stripes to be used as an indicator for the crystallographic orientation of low coverage islands which are too thin for direct EBSD indexing.

The AFM images in earlier Sections of this Chapter have shown that the island stripes are always parallel to the direction of island elongation. Therefore the elongation direction, with respect to the adsorbate/substrate crystallography, is also defined by $\langle 11\bar{2}0\rangle$Bi$||\langle 10\bar{1}0\rangle$HOPG. Figure 6.41 shows the Bi$\{01\bar{1}2\}$ lattice mesh, drawn to show the long zigzag chains of covalent bonds which characterize this orientation (the covalent intralayer bonds are represented by solid lines, the weaker interlayer bonds are indicated by dashed lines). The direction of island elongation (Bi$\langle 11\bar{2}0\rangle$) is hence parallel to the zigzag chains of covalently bonded atoms, as illustrated.

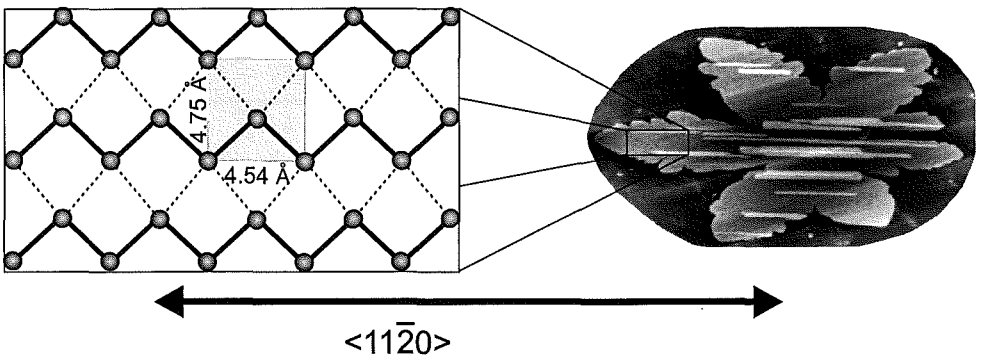

Figure 6.41: Illustration of the Bi$\{01\bar{1}2\}$ lattice mesh (unit cell shaded), showing the zigzag chains of covalent bonds (solid lines) along a Bi$\langle 11\bar{2}0\rangle$ direction. An elongated island is shown, to emphasize that the direction of elongation is parallel to the covalent bond chains.

Island elongation, resulting from the more efficient diffusion of adatoms along the Bi$\langle 11\bar{2}0\rangle$ direction, is likely a result of adatoms having a higher probability of being incorporated at the end of a covalent bond chain, rather than parallel to the chains where bonding is weaker, hence extending the island in a Bi$\langle 11\bar{2}0\rangle$ direction. Needle growth (i.e. extremely elongated growth) has been observed for electrodeposition in the Bi/Au(111) system, and attributed to faster diffusion along the close packed edges of a rectangular Bi unit cell [178], where the 2 sides of the were of very dissimilar length. This may also play a roll in the Bi/HOPG system, since the zigzag covalent bond chains are also parallel to the short edge of the $\{01\bar{1}2\}$ unit cell. It is also worth pointing out that the adsorbate/substrate lattice mismatch is smaller along the Bi$\langle 11\bar{2}0\rangle$ direction (-7.7%) than along the long edge of the $\{01\bar{1}2\}$ unit cell in Figure 6.40(b).

The in-plane orientation with the HOPG$\langle 10\bar{1}0\rangle$ directions (high symmetry

directions) of the substrate accounts for the 60° azimuthal island orientations shown in Figure 6.6(a) (Section 6.1.3). In the previous study of the Bi/HOPG system [87] (with a high substrate defect density), one of the orientations for island elongation was also observed to be parallel to the HOPG $\langle 10\bar{1}0\rangle$ directions via atomic resolution imaging of the substrate, in agreement with the current study. The departure from 60° of the angles between the secondary arms of the star shaped islands shown in Figure 6.6(c), and the flux dependence of the angle, demonstrates that the island morphologies are controlled by an interplay of both crystallography and edge diffusion.

6.4.5 Summary of Crystal Structure and Orientation Transition

This Section has shown that island growth begins with $\{01\bar{1}2\}$ oriented islands, which have the preferential in-plane orientations $\langle 11\bar{2}0\rangle$Bi$||\langle 10\bar{1}0\rangle$HOPG, with the island stripes oriented parallel to a Bi$\langle 11\bar{2}0\rangle$ direction. With increasing film thickness, the islands undergo an orientation transition to $\{0001\}$Bi$||\{0001\}$HOPG beyond θ=12 ML.

The direction of island elongation was shown to be parallel to a Bi$\langle 11\bar{2}0\rangle$ direction, which is characterized by long zigzag chains of covalently bonded atoms. The island morphologies were then discussed in terms of the crystallographic influence.

6.5 Nucleation of Aggregates at HOPG Step Edges

Discussions thus far have focused on islands nucleated on the large defect-free terraces of the substrate. We now turn our attention to the structures that nucleate at step edges on the graphite surface. This section begins with a general overview from SEM images, with varying coverage and flux, from which we note the existence of a rod-like morphology. We then explore this morphology in greater detail with the aid of AFM scans. The growth is discussed in terms of the crystallography of the rods and and established models of DLA.

6.5.1 Elongated Step Edge Aggregates: Variation With Flux and Coverage

Representative SEM images showing the evolution of film morphology with increasing coverage are presented in Figure 6.42, for a fixed flux of 0.005 Å/s. The θ=0.2 ML image shows small rod-like structures protruding from the step edges. The θ=0.7 ML SEM image shows an increased prominence of the rods, and it is also clear that they are well oriented, producing ordered arrays of Bi nanorods at the step edges (the orientation will be discussed further in Section 6.5.3). The θ=1.5 ML image shows a general increase in the size of the rods. It is also interesting to note that the step edges feature continuous lines of coalesced bismuth

along their length, in contrast to antimony, which clearly exhibited denuded zones between the branches that extended from step edges.

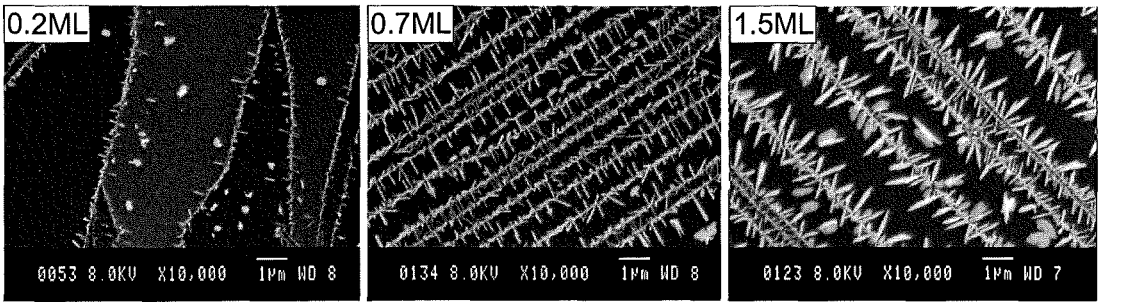

Figure 6.42: Representative SEM images of the evolution of step edge morphology with increasing coverage in the low flux environment. The coverage is indicated on the images, the flux is held constant at 0.005 Å/s.

The evolution of the rod morphology as a function of increasing flux (coverage fixed at 1.5 ML) is shown in Figure 6.43. The F=7×10^{-4} Å/s image shows extremely elongated rod shaped islands extending from the step edges. A high degree of order in their orientation is again evident. When the flux is increased to 0.03 Å/s, the rods generally become shorter and broader. A further increase to F=0.2 Å/s produces markedly more compact step edge decoration, with little evidence of the rod structures. Increasing the flux results in a morphology transition from rod-like to compact structures aggregated along the step edges.

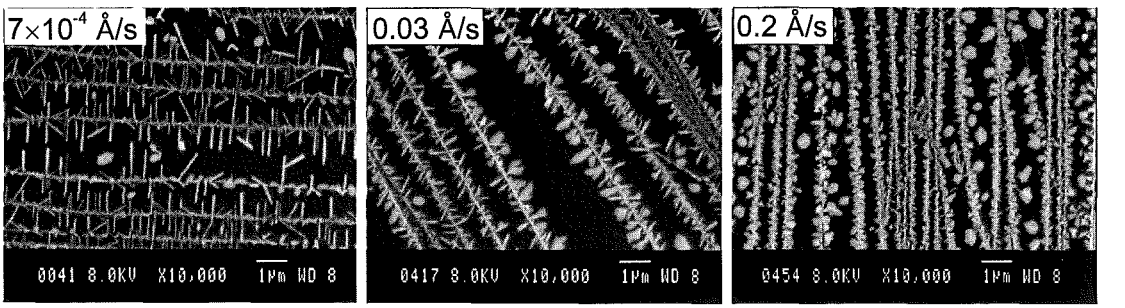

Figure 6.43: Representative SEM images of the evolution of step edge morphology with increasing flux. The flux is indicated on the images, the coverage is held constant at 1.5 ML.

Step edge decoration is well known on graphite substrates, and has been utilized to enable self assembly of nanowire-type structures *parallel* to the step edges, from a range of materials, using a variety of deposition techniques [179], [180]. Typically, decoration of HOPG step edges is characterized by the nucleation of relatively compact clusters, which bear a resemblance to those aggregated on the flat terraces between the step edges [91], [176], [92]. The large scale networks of ordered bismuth nanorods extending *outwards* from the HOPG step edges are clearly different from the terrace nucleated islands.

Quantitative data on the dimensions of the step edge aggregates were obtained from AFM scans, which provide better resolution than SEM imaging for small scan areas. Figure 6.44 shows an SEM scan (left) and an AFM scan with the same magnification (right), to demonstrate the difference in resolution.

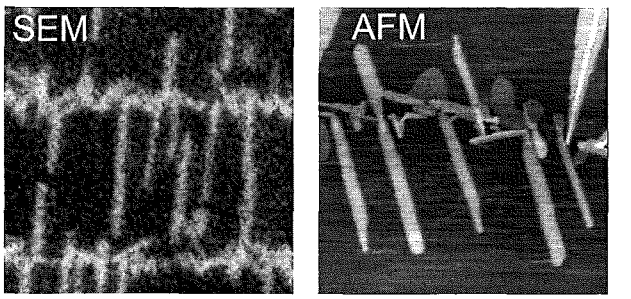

Figure 6.44: Comparison of image resolution from a F=0.005 Å/s, θ=0.7 ML sample: SEM image (left) and AFM image (right), both images have the same scan size (1.75 μm).

Figure 6.45(a) and (b) show histograms of the distribution of rod lengths and widths for coverages of 0.2 ML, 0.7 ML, and 1.5 ML, for high flux (0.2 Å/s) and low flux (0.005 Å/s) conditions. These plots show that the low flux aggregates tend to be both longer and narrower than their high flux counterparts. We also note that many of the histograms for both the length and width data feature a tail on the distributions, showing that occasional elongated islands are significantly longer and wider than the general population. The longest rod-like structures are of order 2.5 μm long in the θ=1.5 ML, F=0.005 Å/s growth environment.

The degree of aggregate elongation is defined here by the aspect ratio (length/width). Histograms of the aspect ratio are shown in Figure 6.45(c) for both the high flux and low flux environments. It is clear that the aspect ratio is higher for the low flux aggregates, and that some structures are again significantly more elongated than the general population.

Figures 6.46(a) and (b) show plots of the step edge aggregates' mean length and width as a function of increasing coverage, for low (0.005 Å/s, open symbols) and high (0.2 Å/s, closed symbols) fluxes. Each plotted point is comprised of measurements taken from multiple regions of the sample, and in some cases multiple samples, to ensure a representative data set. Figure 6.46(a) shows that the mean rod length increases with increasing coverage for both fluxes. From this plot it is evident that, for a given coverage, the mean length of rods grown in a low flux environment is greater than for aggregates grown under high flux conditions. From the slopes of the linear fits to the data in Figure 6.46(a) (and converting coverage into the deposition time domain), the mean growth rate for the low flux rod lengths is 1.2±0.5 nm/s, considerably less than that of high flux aggregates which grow at 26±5 nm/s. Figure 6.46(b) shows that the mean aggregate width also increases with increasing coverage for both fluxes, with a growth rate of 0.2±0.1 nm/s and 17±5 nm/s for the low and high flux

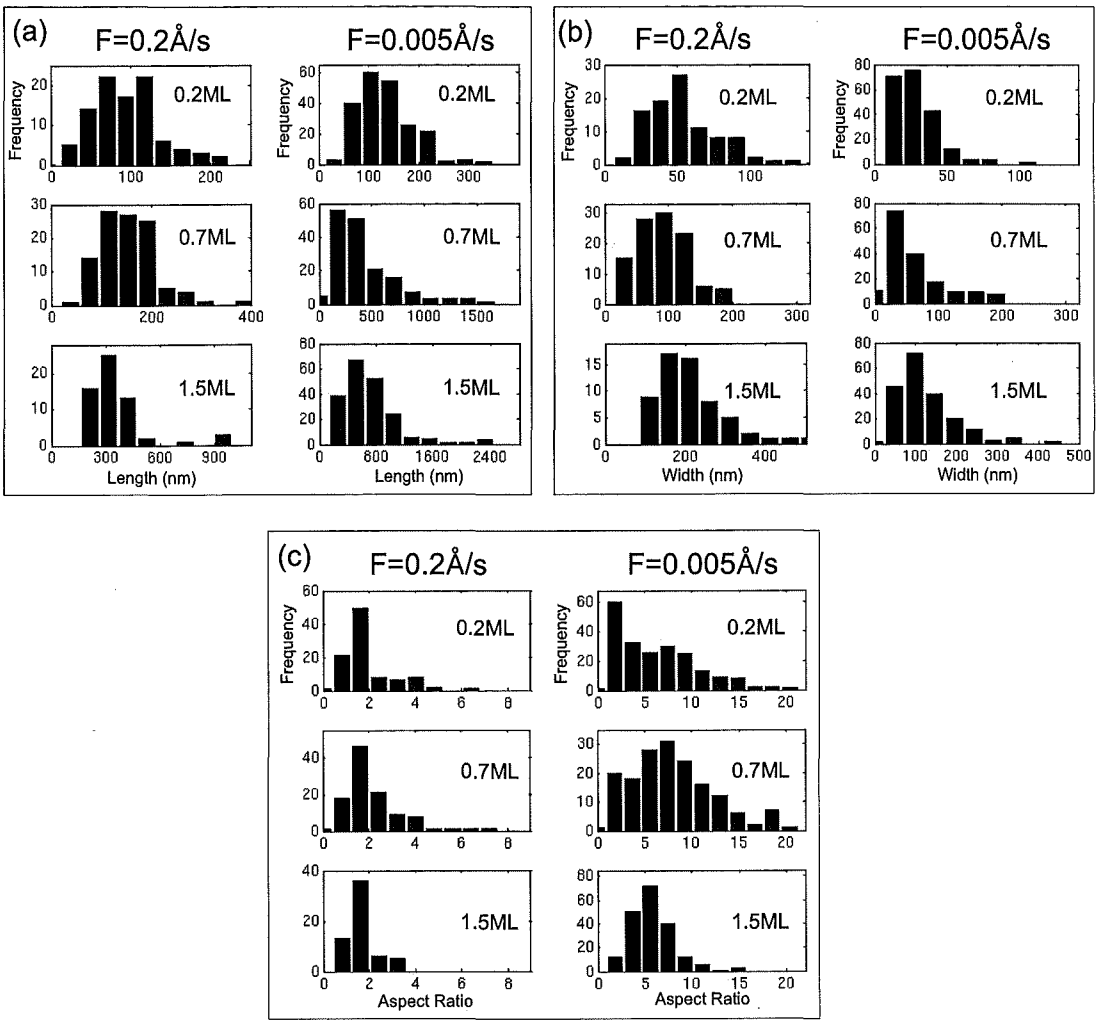

Figure 6.45: Histograms of step edge aggregate lengths, (a) widths, (b) and aspect ratios, (c) for both high flux (0.2 Å/s) and low flux (0.005 Å/s) conditions. The coverage is indicated on each histogram.

environments respectively. It is therefore clear that rod-type structures develop only under low flux conditions, where the aggregates' growth rate is significantly less than in a high flux environment.

Figure 6.46(c) shows the mean aspect ratio as a function of increasing coverage for both high fluxes and low fluxes, and indicates that there is no distinguishable dependence of the degree of elongation on coverage, for both fluxes. It is also obvious from this plot that the mean aspect ratio is significantly greater for step edge structures grown in a low flux environment (7 ± 1) compared to their high flux counterparts (2.0 ± 0.3). These two observations lead to the conclusion that the degree of elongation is approximately independent of the amount of material deposited, and depends only on the particle flux.

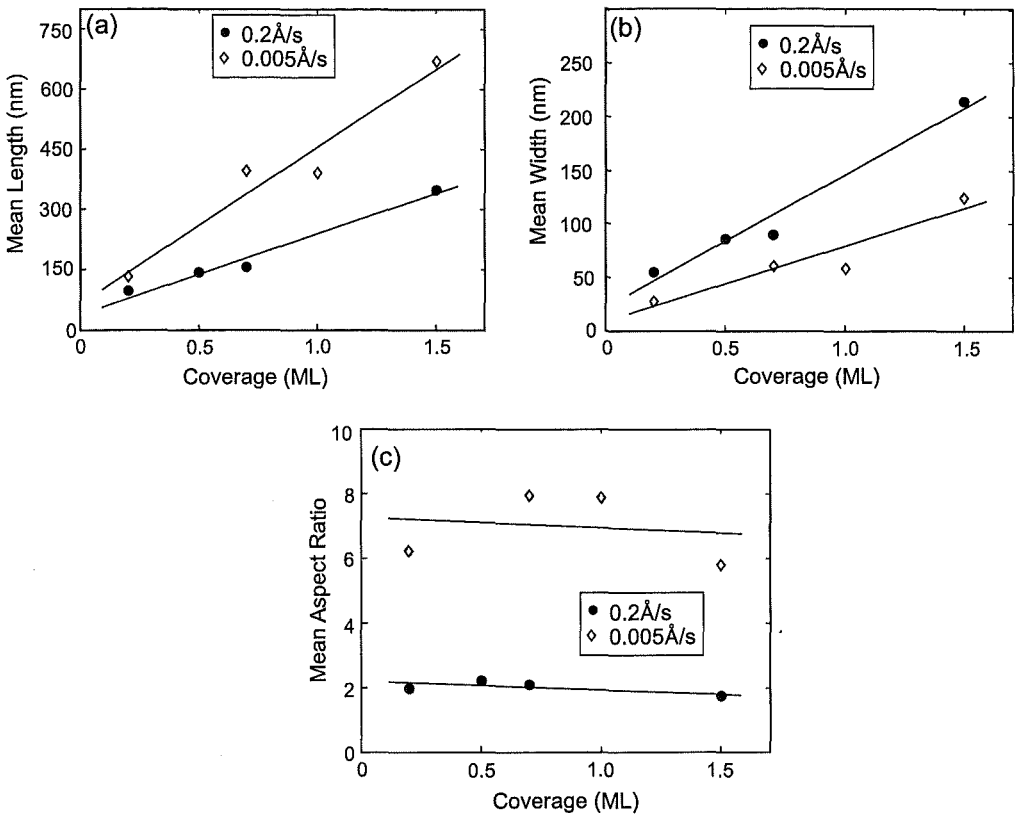

Figure 6.46: Plots of the mean step edge aggregate length (a), width (b), and aspect ratio (length/width) (c), data as a function of increasing coverage, for the coverage range 0.2 ML - 1.5 ML. High flux and low flux examples are plotted (indicated by the legends). The solid lines are least squares fits to the data.

6.5.2 Rod Heights

Figures 6.47(a)-(c) show AFM images and height histograms for step edge aggregates grown in the low flux environment (since this is where the rod shapes are most pronounced), for a range of coverages. The AFM images show that the step edge decoration is comprised of both rod-like structures, and occasional more compact morphologies (indicated with arrows in the AFM images). The black bars in the histogram represent height data taken from the rods, and the grey bars show heights for the smaller broader (arrowed) structures. Figure 6.47(a)-(c) shows that the rod height is of order 2 nm, and the smaller aggregates are of order 1 nm tall. On average, at least 90% of the aggregated material contributes to the growth of rod structures (rather than the smaller broader aggregates) The heights (for both rods and broader structures) remain approximately constant with increasing coverage, within the range 0.2 ML - 1.5 ML, indicating a 2D growth mode. The AFM height cross-section through a rod in Figure 6.47(d) demonstrates the uniform height of the aggregates. Therefore, with increasing coverage, the rods grow in both length and width while keeping a relatively constant aspect ratio, but maintain a constant height of $\sim$2 nm.

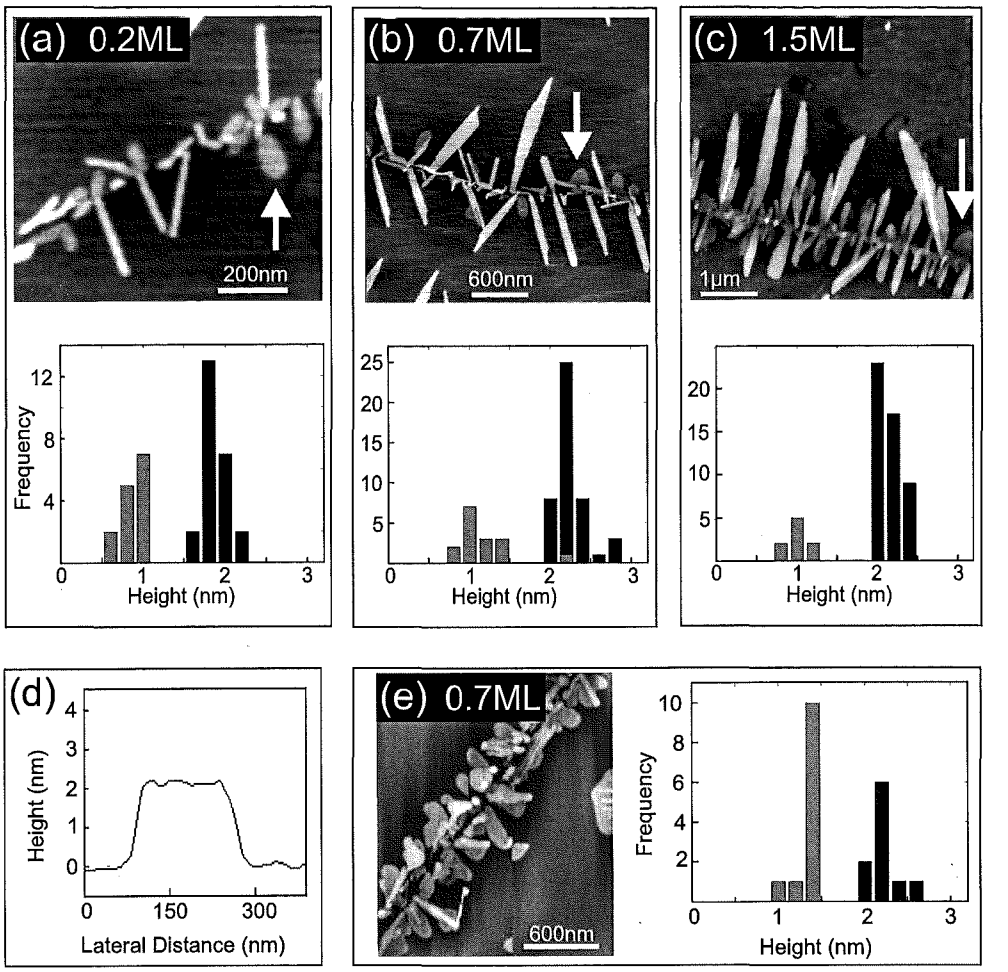

Figure 6.47: Representative AFM images of step edge structures, and histograms of the aggregate heights, the black bars in the histogram represent the rod morphologies, while the grey bars represent the smaller broader aggregates which are indicated with an arrow in the AFM images. (a)-(c) increasing coverage at a constant flux of 0.005 Å/s (d) AFM height cross-section through the largest rod in (b) (center of image, above the step edge). (e) AFM image and histogram for a 0.7 ML coverage sample, F=0.2 Å/s.

An AFM image and height histogram are shown in Figure 6.47(e) for a high flux sample at a coverage of 0.7 ML. The AFM image reveals mainly compact structures, which are again of order 1 nm in height, as shown in the accompanying histogram. The histogram shows a population of taller structures, which are typically small rod-like structures which form part of broader aggregates (as can be seen in the AFM image), rather than the well-defined, isolated rods found in the low flux environment. It is therefore clear that well defined rod growth is only achieved in the low flux environment.

6.5.3 Orientation

Crystallographic orientation of the rods was determined using the EBSD technique, following the method used for the terrace nucleated islands in Section 6.4.

Figure 6.48(a) shows a representative FE-SEM image of step edge decoration from a θ=12 ML film. A higher resolution AFM image of the same sample is shown in Figure 6.48(b), in which the elongated step edge structures can be clearly observed in the center of the image, with stripes running parallel to the direction of elongation. The arrowed line in Figure 6.48(a) serves to represent the stripe direction in this image. The black dots indicate sites where the structure was probed with the electron beam.

The index solutions for bismuth and the HOPG substrate are presented in the pole figures in Figure 6.48(c) and (d) respectively. These pole figures reveal the same adsorbate/substrate orientation relationship that was found for the terrace nucleated islands in Section 6.4, namely $\{01\bar{1}2\}$Bi||$\{0001\}$HOPG, with the preferred in-plane orientation given by $\langle 11\bar{2}0\rangle$Bi||$\langle 10\bar{1}0\rangle$HOPG. As with the terrace nucleated islands, the stripes (and therefore aggregate elongation) are parallel to a Bi$\langle 11\bar{2}0\rangle$ direction.

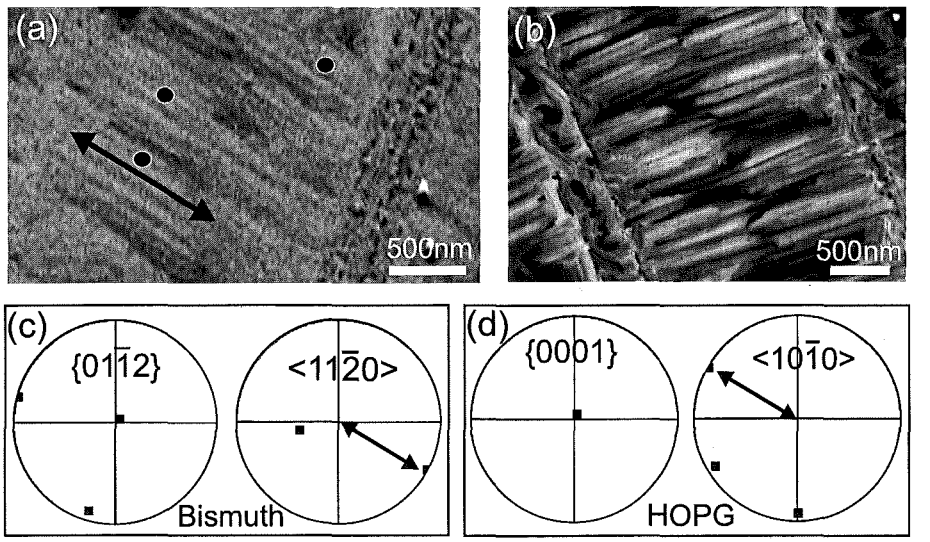

Figure 6.48: EBSD determination of the crystallographic orientation of step edge aggregates. (a) FE-SEM image of a 12 ML (F=0.03 Å/s) coverage film showing structures protruding from a step edge, the black circles indicate sites where local EBSD probing of the films orientation was performed, the arrowed line shows the direction of the stripes. (b) AFM image showing higher resolution of the θ=12 ML step edge structures. (c) Bismuth EBSD pole figures, the arrowed line is a superposition of the stripe direction from (a). (d) Graphite EBSP pole figures, with the stripe direction from (a) superimposed.

The alignment of the rods with a high symmetry direction of the substrate, accounts for the ordering at the step edges observed in the SEM images of Figures 6.42. In the 0.7 ML image the majority of rods protrude perpendicularly from the step edge, while in the 1.5 ML image the dominant rod orientation is at 60° to the step edge. This indicates that the HOPG step edges in these two images are oriented in different crystallographic directions (HOPG$\langle 11\bar{2}0\rangle$ and HOPG$\langle 10\bar{1}0\rangle$ respectively). It is also interesting to note that a 30° rotation is the

most common misorientation of the rods with respect to the preferred orientation (as can be seen in the SEM and AFM images, where an array of rods perpendicular to the step edge has occasional rods oriented at 60°), which corresponds to $\langle 11\bar{2}0\rangle$Bi$||\langle 11\bar{2}0\rangle$HOPG. In Section 6.4.3 this orientation relationship was shown to have a smaller lattice misfit than the preferred orientation.

6.5.4 Growth Mechanism

Edge Diffusion

To maintain a compact morphology, the rate of transport of material around the perimeter of a structure (by edge diffusion) must exceed the arrival rate of new adatoms to the perimeter via random migration on the substrate. The generally smooth perimeter of the rods in the Bi/HOPG system implies very effective adatom transport down the sides (Bi$\langle 11\bar{2}0\rangle$ directions), although it should be noted that very large structures (for example in Figure 6.47(c)) do demonstrate a susceptibility to Mullins-Sekerka [75] type tip instabilities. Nonetheless, the step edge aggregates' morphology is quite different to the case of terrace nucleated islands, which featured varying degrees of star-shaped growth.

The efficient transport of adatoms from the sides to the tips of the rods is evident also from the existence of rods at neighboring step edges which have grown together to form a continuous structure. Figure 6.49(a) shows two rods from adjacent step edges that are almost touching tip-to-tip in the bottom right of the image. Competitive adatom capture rapidly depletes the diffusion field in the region between the two tips, which would normally impose a self-avoiding growth mechanism. The rods can only continue growing towards each other and eventually touch (like the structure in the top right of the same image), if adatoms arriving at the sides of the rods can be transported to the tips. This morphology is frequently observed, and another example is shown in Figure 6.49(b).

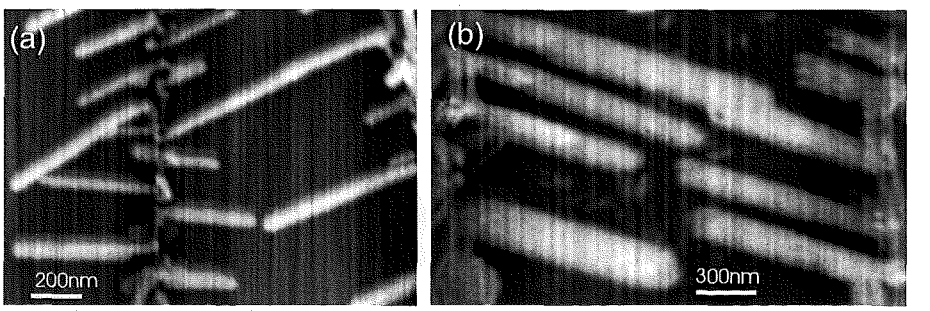

Figure 6.49: AFM images showing examples of rods from adjacent step edges which have grown together to form continuous structures (this morphology is frequently observed).

Anisotropic Diffusion Field

For the terrace nucleated islands, we assumed an approximately isotropic diffusion field around the island perimeter. However, this is certainly not the case for step edge aggregates, where a high linear density of aggregates nucleate along the steps (defect decoration). The resulting distorted diffusion field is illustrated in Figure 6.50. The left illustration shows small structures nucleated along two step edges, with rectangles which surround them representing the adatom capture zones. The drawing to the right depicts the reduced diffusion field between neighboring aggregates, which results from competitive adatom capture. Adatoms within the dark shaded region (in the bottom capture zone) are more likely to arrive at the sides of the rod, while those within the light shaded region will probably impinge near the tip. It is clear that significantly fewer adatoms reach the sides of the rod compared to the tip.

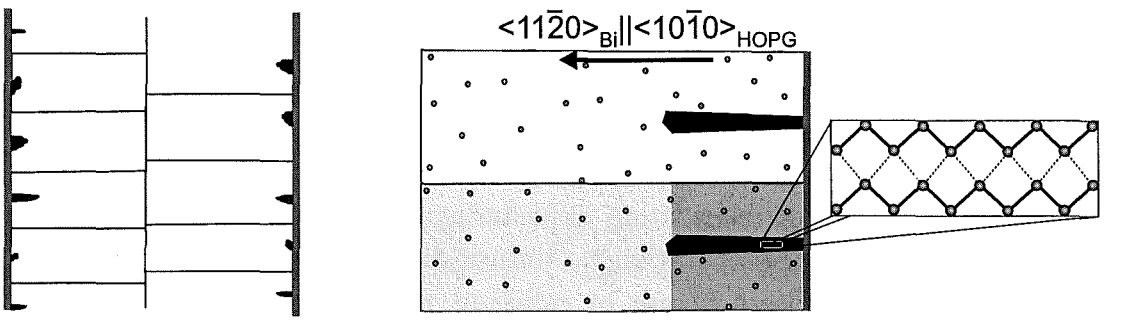

Figure 6.50: Illustration of the capture zones surrounding aggregates nucleated on step edges. The left diagram shows a large scale perspective. The right illustration shows two adjacent capture zones. The light shaded region depicts adatoms that are most likely to arrive at the tips of the rods, while those within the dark shaded regions will likely arrive to the sides of the rods. The crystal structure of the rods is shown in the inset, illustrating the zigzag covalent bond chains which are oriented along their length.

The natural tendency for faster diffusion along Bi$\langle 11\bar{2}0\rangle$ directions in a low flux environment (as observed in the elongation of the terrace nucleated islands in Section 6.1), coupled with a further reduction in local flux arriving to the edges due to competitive adatom capture, results in an exaggeration of the preference for growth in Bi$\langle 11\bar{2}0\rangle$ directions, producing rod-like morphologies at step edges in the low flux environment.

Although the rod heights are significantly taller than the majority of the terrace nucleated islands, they are however consistent with those of the large elongated hexagonal islands, which are only observed in the low flux limit (Section 6.1.4). It seems that the reduction in local flux to the rod sides, imposed by the anisotropic diffusion field, allows more time for upward adatom migration resulting in taller structures.

6.5.5 Step Edge Spacing

The local diffusion field, and hence the aggregate morphology is also affected by the spacing between step edges. Closely spaced steps result in fewer adatoms available per aggregate (competitive capture), and consequently slower growth rates. This tends to enhance any elongation, but limits the length of the rods. Widely spaced steps result in an increased rate of adatom impingement to the rod tips (higher local flux), which has a two-fold effect. Firstly, the increased number of adatoms allows the growth of longer rods (for example, compare the center step edges with those at the bottom in the F=7 $\times$ 10^{-4} Å/s image in Figure 6.43). Secondly, the increased local flux may dominate the growth and cause tip instabilities, hindering elongation. This can be observed in the F=0.03 Å/s image in Figure 6.43, where the widely spaced center steps show branched growth, while the closely spaced steps in the bottom of the image feature compact rod shapes. Note however that the effect of the step edge spacing is much smaller than that of the experimental particle flux (compare images in Figure 6.43).

Figure 6.51 shows SEM images of step edge aggregates grown under 7 $\times$ 10^{-4} Å/s, (a) and 0.2 Å/s, (b) flux conditions. In this example the two step edges have the same separation in both images, demonstrating the dramatic difference in morphology between the two fluxes. It is also clear that the high flux image features island nucleation between the step edges, whereas the low flux case has undecorated terraces. If the adatom diffusion length, L (from Section 6.1.5) is greater than the step edge separation, d_s, diffusing adatoms are more likely to find step edges than to nucleate islands by collisions with other migrating adatoms. Conversely, if $L < d_s$, island nucleation will occur both on the terraces and step edges. Recall from Section 6.1.5 that L ~1.7 μm for F=0.2 Å/s. In Figure 6.51(b) we note that $d_s > 1.7$ μm, so terrace decoration is probable. Although L was not determined for the 7 $\times$ 10^{-4} Å/s flux, it will be at least as large as for F=0.005Å/s, for which $L \sim 3.4$ μm. In Figure 6.51(a), $d_s \lesssim 3.4$ μm, and hence terrace decoration is unlikely.

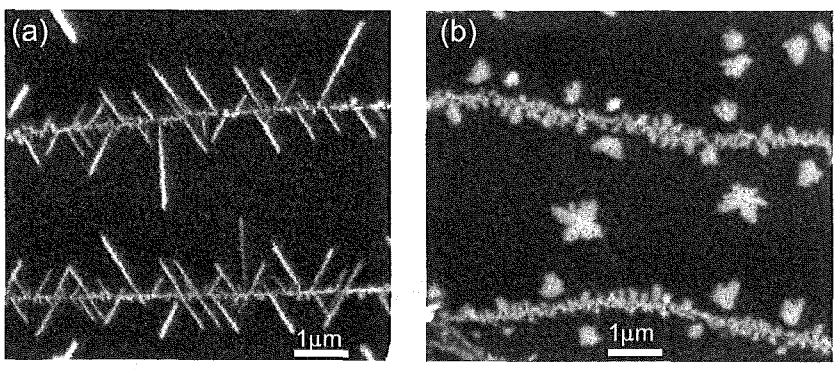

Figure 6.51: Step edge aggregates from different fluxes, featuring similar step edge separations. (a) F= 7 $\times$ 10^{-4} Å/s. (b) F=0.2 Å/s. The coverage is fixed at 0.5 ML.

6.5.6 Summary of Rod Growth

Our SEM, AFM, and EBSD analysis of step edge decoration in the Bi/HOPG system has revealed the formation of large arrays of oriented nanorods in the low flux growth environment. With increasing coverage, the rods grow in both length and width with a constant length/width ratio, but maintain a uniform height of $\sim$ 2 nm within the coverage range 0.2 ML - 1.5 ML. The preferred orientation relationship is defined by $\{01\bar{1}2\}$Bi$||\{0001\}$HOPG and $\langle 11\bar{2}0\rangle$Bi$||\langle 10\bar{1}0\rangle$HOPG, with this alignment of the rods with the high symmetry directions of the substrate producing the ordering at the step edges.

Despite enormous differences in the shapes of the terrace nucleated and step edge nucleated aggregates, the similarities in behavior (2D growth, crystallographic orientation, and rod heights matching those of the F= 7×10^{-4} Å/s hexagonal islands) imply a similar growth mechanism. A tendency for more efficient mass transport along Bi$\langle 11\bar{2}0\rangle$ directions, coupled with an anisotropic diffusion field surrounding the step edge aggregates, results in exaggerated island elongation, and subsequent rod growth in a low flux environment.

6.6 Stability and Degradation: Post-Deposition Effects

This Section briefly examines the effect of post-deposition vacuum time on the island morphology. The deterioration of aggregates under ambient storage conditions is also summarized.

The effect of post-deposition vacuum time on the island morphology must be considered to determine if significant diffusion and aggregation occurs beyond the time scale of deposition. We therefore performed a series of experiments where films with identical coverage and flux (θ=1.0 ML, F=0.03 Å/s) were exposed to varying post-deposition vacuum time. Figure 6.52(a) shows an SEM image of a film that was vented to atmosphere immediately after deposition. An SEM image of a sample that was allowed a 1 hour time delay between the end of deposition and venting the chamber is shown in (b). The film morphology after 2 weeks post-deposition UHV time is shown in (c). A comparison of these three images reveals no detectable change in morphology with varying the post-deposition vacuum time, indicating that adatom diffusion and island aggregation is completed within the time frame of deposition. For this reason, an arbitrary time of 1 hour was selected before the chamber was vented after deposition, as described in Chapter 3.

Note that the particular flux and coverage conditions for the study of post-deposition effects was selected as a representative case. It is possible that very small islands may show more variation. However, small islands would likely require AFM imaging to obtain the necessary resolution, which is particularly problematic as they tend to crumble and move under the cantilever tip, prohibiting their inclusion in this study.

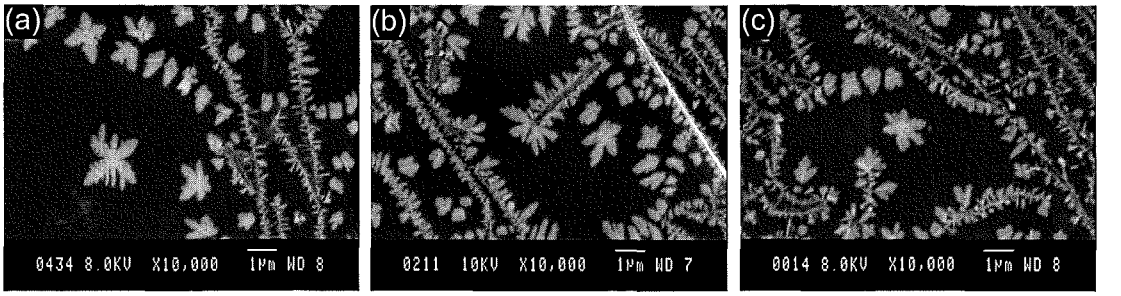

Figure 6.52: Images of aggregates taken with various post-deposition vacuum time. (a) Sample was immediately vented to atmosphere after deposition. (b) Sample remained under UHV for 1 hour after deposition. (c) 2 weeks post-deposition vacuum time. Note that grade ZYB HOPG was used for these deposits. All images are deposited with F=0.03 Å/s and θ=1.0 ML.

Under ambient conditions the samples are exposed to atmospheric gasses and other contaminants. Knowledge of the effect this has on the morphology, and how quickly the films degrade, is important since it allows confidence that images are representative of the actual aggregate morphology, and not some post-deposition effect. Figure 6.53 shows images of islands both before and after prolonged exposure to atmospheric conditions. Figure 6.53(a) presents images of a sample with F=0.03 Å/s and θ=1.0 ML. The left SEM image was taken 2 days after deposition. This is a typical image of a film deposited with this flux and coverage, and represents a 'clean' sample. The centre SEM image shows the same sample after 3 months in ambient conditions, revealing a large amount of background contamination. The right image shows an AFM scan taken after 3 months, demonstrating that the morphology of individual aggregates also begins to deteriorate, with a build up of material around the perimeter of the aggregate, and a generally ragged island appearance. Figure 6.53(b) presents AFM images from the F=0.03 Å/s, θ=0.7 ML environment. The left image was scanned 4 days after deposition and represents a 'clean' sample with well defined island edges. The right AFM image was obtained after 3 months, and shows material attached to the island perimeters.

It is therefore clear that the film morphologies become contaminated after long periods of exposure to atmosphere. For this reason all imaging was performed within one week of deposition.

6.7 Low Temperature Substrate Cleaning

This Section presents a selection of film morphologies that were obtained during the early stages of construction of the UHV system. Primarily we focus on films which were deposited on substrates that were subjected to lower cleaning temperatures. Section 6.7.1 concerns reproduction issues. Section 6.7.2 presents films deposited with a significantly different system configuration.

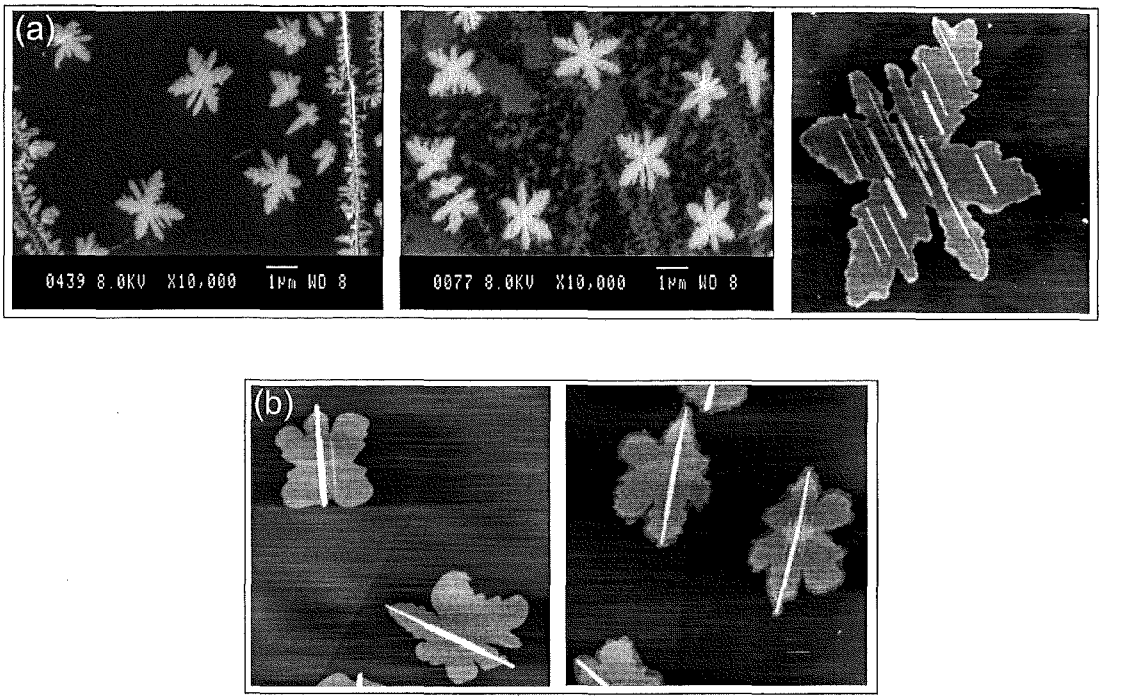

Figure 6.53: Images of aggregates taken both before and after extensive exposure to atmospheric conditions (F=0.03 Å/s). (a) θ=1.0 ML, Left: SEM image scanned 2 days after deposition. Centre: 3 months post-deposition time. Right: AFM scan 3 months after deposition. (b) θ=0.7 ML, Left: AFM scan 4 days after deposition. Right: 3 months post-deposition time (AFM images all have a 3 μm scan size).

6.7.1 Dependence of Film Morphology on Coverage

Figure 6.54 shows the evolution of film morphology with increasing coverage (F=0.2 Å/s) for substrates that were prepared with a cleaning temperature of T$\sim$ 260°C (recall T$\sim$ 420°C in the previous Sections of this Chapter). SEM images are shown in Figure 6.54(a), and higher resolution FE-SEM images are featured in Figure 6.54(b).

It is immediately obvious that there is a much higher density of smaller and irregular island morphologies, compared to the island morphologies found on the clean substrates in Section 6.1 (Figures 6.1 and 6.2). Note that the coverage range of 0.2 ML - 2.0 ML reported in Section 6.1 was not reproduced here, since initial studies found few features of interest within this range. The SEM images in Figure 6.54(a) reveal that some regions of the substrate seem to have relatively uniformly dispersed material, while others have fairly isolated cluster-like islands. The FE-SEM images show the morphology from both these regions in more detail. The θ=1.0 ML FE-SEM image shows two islands (arrowed) which are representative of the isolated cluster-like morphology. The top right of the image features a region of the more densely packed morphology, showing a higher density of small islands. The 5.5 ML FE-SEM image shows a high magnification region of the more densely packed material. Irregular and disordered islands are

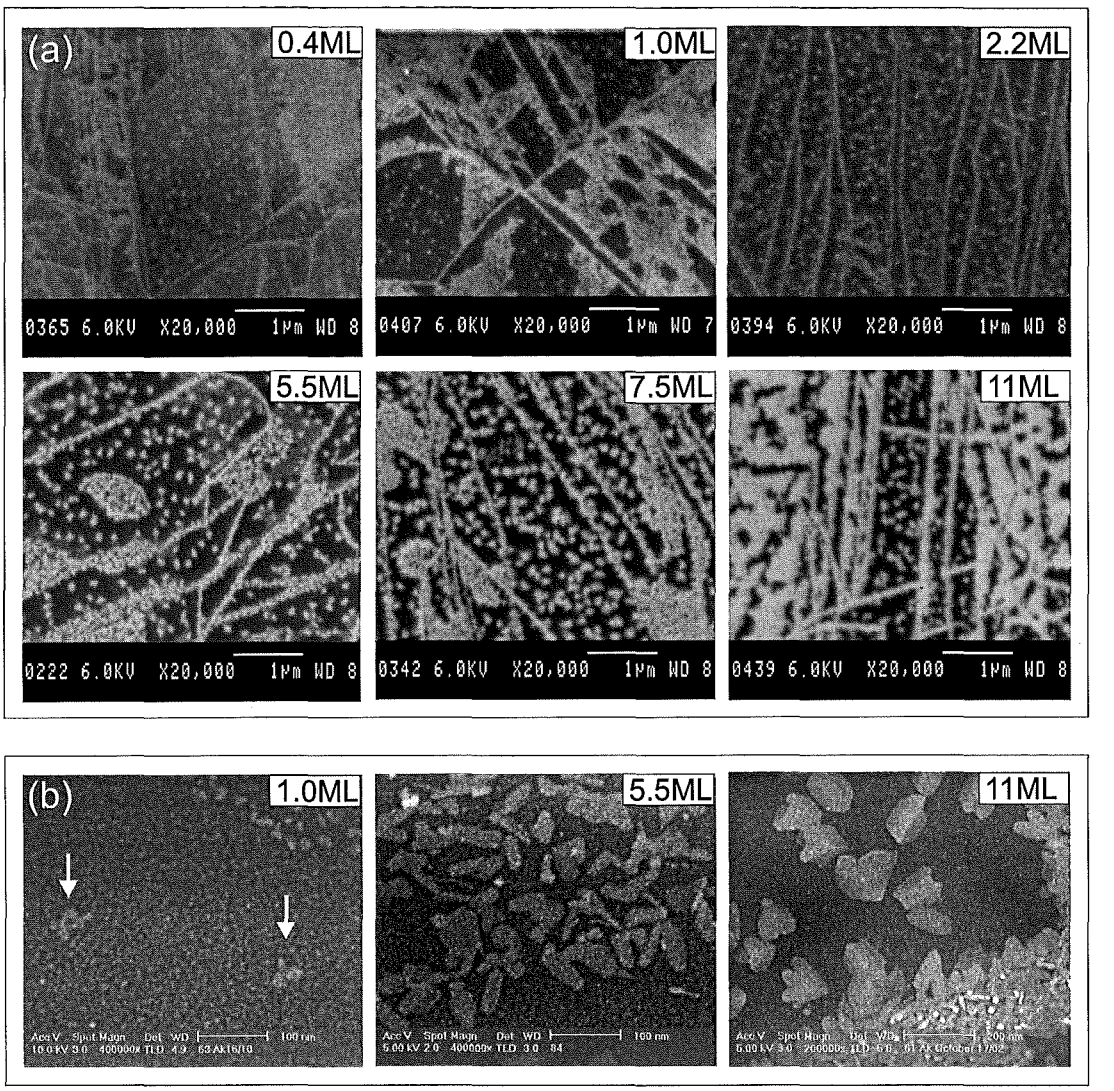

Figure 6.54: SEM micrographs,(a) and FE-SEM micrographs, (b) of the evolution in film morphology with increasing coverage for a low substrate cleaning temperature (T$\sim$ 260°C). The arrowed islands in the θ=1.0 ML FE-SEM image are representative of the isolated clusters shown in the SEM images. The flux is held constant at 0.2 Å/s.

observed. The 11 ML FE-SEM image shows both isolated clusters, with non-uniform shapes, and the more densely packed material (bottom right in image).

From Figure 6.54 it is difficult to discern trends in morphology with coverage. It appears that the amount of material on the substrate increases with increasing coverage. However, the presence of two different types of regions often obscures this, since a higher density of smaller islands can appear as continuous surface coverage (and hence more aggregated material) at the resolution of the SEM images.

Figure 6.55 shows SEM images from 5 different samples, which were deposited under identical conditions (F=0.02 Å/s, θ=5 ML). A comparison of these images reveals that the film morphologies are not reproducible across runs. It

is therefore clear that the defects[7] present on the graphite surface when the substrate is insufficiently heated, have an unpredictable effect on the morphology. Consequently, island morphologies from the low temperature substrate cleaning regime are not considered further.

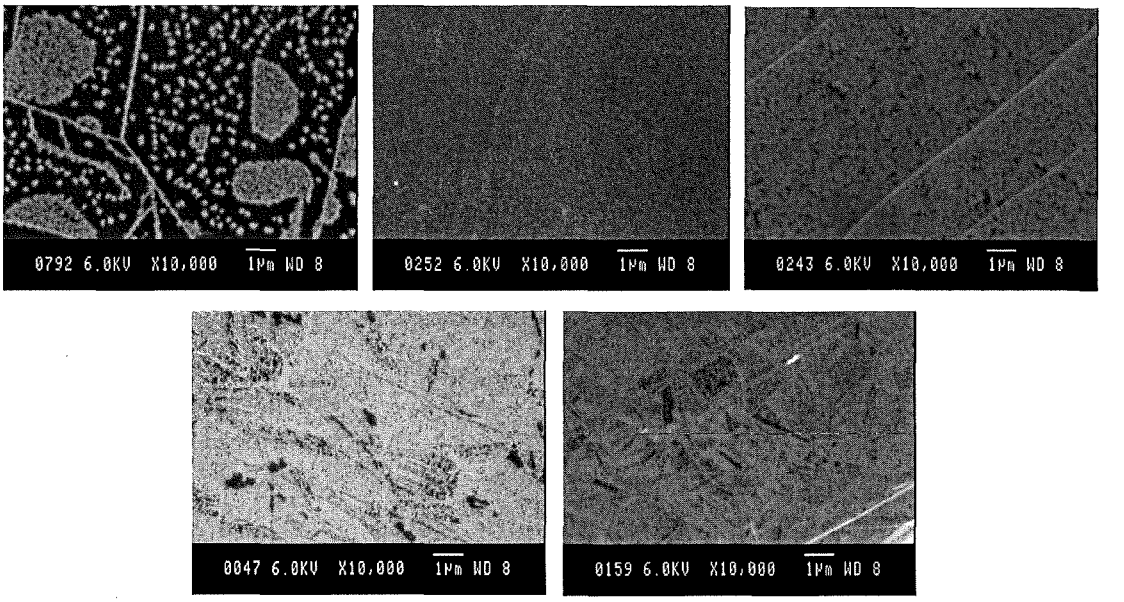

Figure 6.55: SEM images of 5 different films deposited under identical conditions, with a low substrate cleaning temperature (T$\sim$ 260°C). F=0.02 Å/s, θ=5 ML.

6.7.2 Formation of Long Rods

At one of the first stages of deposition system design, the crucible was $\sim$2 cm from the substrates, with minimal heat shielding (substrate cleaning temperature $\sim$ 260°C). Under this configuration, the substrates are likely to experience significant heating from the crucible. Figure 6.56 presents an unusual morphology which is characterized by occasional long rods. These films were grown in a high flux, high coverage environment of F$\sim$5 Å/s and $\theta\sim$50 ML, and could not be reproduced under any other system configuration. The image on the left clearly shows a rod-like structure sitting on top of a film of small crystallites, indicating that it has formed by a mechanism different to the surface diffusion processes observed for other deposition conditions. The image on the right shows that the rods can be several microns in length. Often these rods have a mound of material attached near their centre, which may be associated with their formation. However there are exceptions where no protruding material is observed.

[7]We use the term defect to mean anything that stops diffusion. In this case it is surface adsorbates.

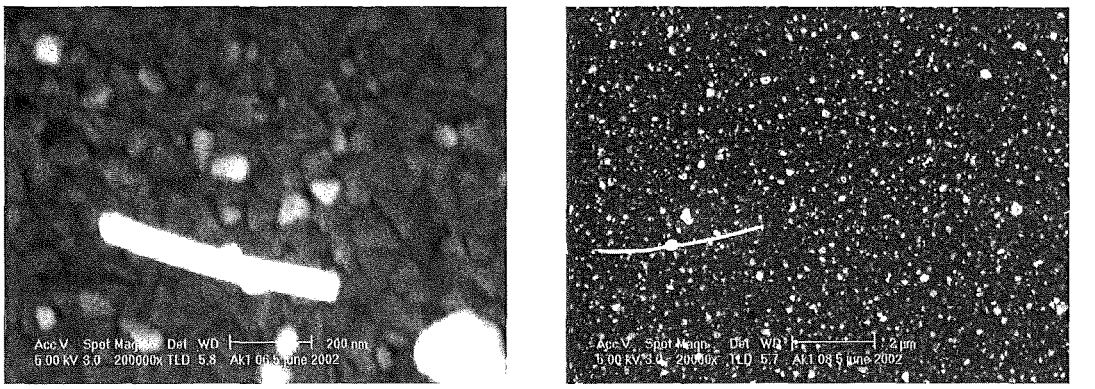

Figure 6.56: Bi thin films grown during an early stage of system development (see text), featuring rods on top of crystallites. F~5 Å/s and $\theta \sim 50$ ML.

6.8 Summary of Bi/HOPG

This Chapter has examined the morphology and growth characteristics of bismuth aggregates on HOPG substrates. The deposition parameters of particle flux and coverage (deposited dose) were varied to study the effect of growth kinetics on the island morphology. Island nucleation and growth were investigated both on the large defect-free terraces and at the natural step edges on the graphite surface. A brief overview of film morphologies obtained during the early stages of UHV system design was also presented.

Using AFM, SEM, and EBSD, we have observed the growth of elongated star shaped islands, with a well defined stripe morphology, on the graphite terraces. When the particle flux is increased, the morphologies become less elongated and more disordered. The growth mode for the island bases is approximately 2D, at a height $\sim$ 1 nm, independent of coverage and flux (within the reproducible range of this study). However, it has also been demonstrated that the stars crossover to a taller elongated hexagonal morphology in the low flux limit.

A power law relation was found for the flux scaling of the island density, showing homogeneous nucleation, with a critical island size of $i = 1$, according to mean field nucleation theory. Also, the island areas were found to have a predictable linear dependence on coverage, and were inversely proportional to the island density. The stripes featured on the island bases were found to arise from direct impingement of the particle flux onto the growing island bases, and were also characterized with varying flux and coverage.

The evolution of island morphology to a continuous film was also investigated, and a different trigonal morphology was found to coexist with the striped islands beyond 12 ML. Eventually a continuous film formed, with trigonal symmetry. The striped islands were shown to have a preferred film/substrate orientation relationship defined by $\{01\bar{1}2\}$Bi$||\{0001\}$HOPG and $\langle 11\bar{2}0\rangle$Bi$||\langle 10\bar{1}0\rangle$HOPG, but undergo a crystallographic orientation transition to a $\{0001\}$ oriented (trigonal) film.

HOPG step edge decoration was found to comprise expansive arrays of oriented rod-type structures, whose preferred orientation was also defined by $\langle 11\bar{2}0\rangle$Bi$||\langle 10\bar{1}0\rangle$HOPG. Their growth mechanism was described in terms of edge diffusion, which results in an exaggeration of island elongation along Bi$\langle 11\bar{2}0\rangle$ (parallel to zigzag chains of covalently bonded bismuth atoms) directions, and subsequent rod growth.

The morphology of films deposited on very high defect density HOPG (resulting from a lower substrate cleaning temperature) was also briefly considered. In general the morphologies were not reproducible, but an interesting rod-type growth was identified on top a film of crystallites for one set of conditions.

Chapter 7

Conclusions and Outlook

In thin film growth, the non-equilibrium conditions generated by a particle diffusion field provide a rich environment for spontaneous pattern formation on the nanoscale. Particles deposited on weakly interacting substrates undergo simultaneous processes of diffusion, nucleation, and aggregation. The balance between these processes governs the prevailing film morphology, and is strongly dependent on experimental conditions. Compact island shapes are energetically favorable, yet dendritic and irregular morphologies are often observed, where diffusion kinetics dominate the growth.

This thesis utilized atomic force microscopy, scanning electron microscopy, and electron backscatter diffraction to investigate the early stages of thin film growth in the Sb/HOPG and Bi/HOPG systems. The films' morphology and structure where characterized with the varying experimental parameters of coverage (deposited dose) and flux (deposition rate).

In the case of Sb/HOPG, increasing the coverage results in a morphology transition from compact to branched islands on the graphite substrates, demonstrating the manifestation of Mullins-Sekerka type instabilities. When the flux is increased, flatter islands form, with a significantly more branched morphology for any given coverage. The proximity of neighboring islands also effects the morphology. Longer and flatter branches extend towards regions where there is an absence of other islands, a result of the increased concentration of the diffusion field in these areas. The aggregation of antimony islands on graphite represents a classic system where the interplay between thermodynamics and kinetics determines the 3D morphology. Lowering the flux shifts the balance towards more energetically favorable compact and taller shapes. Increasing the flux produces more branched and flatter shapes, where diffusion kinetics increasingly dominate the morphology.

The Bi/HOPG system was the main focus of this thesis work. Elongated star shaped islands, with a well defined stripe morphology, were observed on the graphite terraces. The islands were determined to have their crystallographic Bi$\{01\bar{1}2\}$ planes parallel to the graphite basal plane. In-plane orientations were aligned with the high symmetry directions of the substrate, with the islands elongated along a Bi$\langle 11\bar{2}0\rangle$ direction. With increasing flux, there is an evolution

to a higher density of smaller and more disordered island shapes. The growth mode for these islands was found to be approximately 2D, at a fixed base height (height of the islands excluding the stripes) of ~1 nm. In the low flux limit, there is a cross-over to a taller more compact elongated hexagonal morphology. From a comparison with mean field nucleation theory, the islands were determined to nucleate via adatom-adatom collisions, rather than on defect sites.

The size of the bismuth island bases were found to have a predictable linear dependence on the coverage. The stripes featured on the island bases were determined to arise from the direct impingement of the particle flux onto the islands, and were characterized with flux and coverage. With increasing coverage, the striped Bi$\{01\bar{1}2\}$ oriented islands were observed to undergo a crystallographic orientation transition, to a Bi$\{0001\}$ oriented film with trigonal symmetry.

Decoration of the graphite step edges in the Bi/HOPG system, was comprised of arrays of well oriented rod-like structures in a low flux growth environment. The rods' growth mechanism was described in terms of the crystallography of the aggregates, and diffusion processes at the structures' perimeter.

It is clear that island aggregation in the Sb/HOPG and Bi/HOPG systems provides some striking examples of self-organized pattern formation. A high degree of control over the morphologies was obtainable by varying the flux and coverage. Other experimental factors are also known to influence island morphologies. Experiments with varying temperature are particularly useful, as correlation of the island density with the system temperature allows the energy barrier for lattice diffusion to be determined [33]. Plans are currently underway to install a sample heater in the UHV system, which will allow the present study to be expanded to the elevated temperature regime.

Several studies have been performed on the influence of the deposited particle (cluster) size on the morphology of antimony islands on graphite substrates [181], [135], [86], where it is shown that the cluster size introduces another controllable variable into the mechanism of pattern formation. No such study has been performed in the Bi/HOPG system. However, deposition of bismuth clusters on HOPG which had not been subjected to thermal cleaning, in our high vacuum cluster apparatus, showed a high degree of cluster mobility [182]. Certainly, a study of the cluster size dependence of the bismuth island morphologies would be interesting, particularly to note the effect on the star shaped islands.

Intentionally introducing substrate defects, allows control of defect decoration in thin film growth. We attempted to pattern the graphite substrates, but were unable to sufficiently remove contaminants prior to deposition. Clean etching techniques such as focused ion beam nano-engraving, have enabled the growth of the regular arrays of gold islands on graphite substrates [183]. A similar technique would be useful for application to the Bi/HOPG system.

Many opportunities clearly exist to extend the current study of Bi/HOPG, to enhance both the understanding and control of island growth in this system.

Studies of diffusion mediated island growth on surfaces are important both from a fundamental and applied point of view, since the next generation of electronic, optical, and catalytic devices will undoubtedly depend on the ability to manipulate and control the properties of nanostructures via self-assembly techniques.

References

[1] J. R. Hook and H. E. Hall, *Solid State Physics*, John Wiley and Sons, West Sussex, England, 2nd edition, 1999.

[2] L. J. Challis, Contemp. Phys. **33**, 111 (1992).

[3] C. Z. Li, H. X. He, A. Bogozi, J. S. Bunch, and N. J. Tao, Appl. Phys. Lett. **76**, 1333 (2000).

[4] M. Boudart, Nature **372**, 320 (1994).

[5] S. Tans, A. Verschueren, and C. Dekker, Nature **393**, 49 (1998).

[6] H. Weller, Agnew. Chem. Int. Ed. **37**, 1658 (1998).

[7] S. M. Sze, *Semiconductor Devices: Physics and Technology*, chapter 8, John Wiley and Sons, New York, 1985.

[8] K.- H. Meiwes-Broer (Ed.), *Metal Clusters at Surfaces*, Springer, Berlin, 2000.

[9] P. Milani and S. Iannotta, *Cluster Beam Synthesis of Nanostructured Materials*, Springer, Berlin, 1999.

[10] A. Tseng and A. Notargiacomo, J. Nanosci. Nanotech. **5**, 683 (2005).

[11] M. Lagally, Phys. Today , 24 (1993).

[12] Z. Zhang and M. Lagally, Science **276**, 377 (1997).

[13] J. Jacobsen, K. Jacobsen, and J. Nørskov, Surf. Sci. **359**, 37 (1996).

[14] B. Stegemann, C. Ritter, B. Kaiser, and K. Rademann, J. Phys. Chem. B **108**, 14292 (2004).

[15] L. Bardotti et al., Surf. Sci. **367**, 276 (1996).

[16] R. Anton and I. Schneidereit, Phys. Rev. B **58**, 13874 (1998).

[17] J. Arthur and A. Cho, Surf. Sci. **36**, 641 (1973).

[18] A. Koma, K. Sunouchi, and T. Miyajima, J. Vac. Sci. Technol. B **3**, 724 (1985).

[19] B. Kaiser, B. Stegemann, H. Kaukel, and K. Rademann, Surf. Sci. **496**, L18 (2002).

[20] B. Kaiser and B. Stegemann, Chem. Phys. Chem. **5**, 37 (2004).

[21] Z. Zhang, X. Sun, M. Dresselhaus, J. Ying, and J. Heremans, Phys. Rev. B **61**, 4850 (2000).

[22] B. Weitzel and H. Micklitz, Phys. Rev. Lett. **66**, 385 (1991).

[23] S. Cho et al., Appl. Phys. Lett. **79**, 3651 (2001).

[24] L. Hicks, T. Harman, and M. Dresselhaus, Appl. Phys. Lett. **63**, 3230 (1993).

[25] E. Bauer, Z. Krist. **110**, 372 (1958).

[26] M. Volmer and A. Weber, Z. Phys. Chem **119**, 277 (1926).

[27] R. Koch, D. Winau, A. Fuhrmann, and K. Rieder, Vacuum **43**, 521 (1992).

[28] F. C. Frank and J. H. van de Merwe, Proc. Roy. Soc. London, Ser. A **198**, 205 (1949).

[29] J. Kolaczkiewicz and E. Bauer, Surf. Sci. **450**, 106 (2000).

[30] I. Ubogyi and J. Kolaczkiewicz, Vacuum **49**, 145 (1998).

[31] H. M. Kramer, J. Cryst. Growth **33**, 65 (1976).

[32] I. N. Stranski and Von. L. Krastanow, Akad. Wiss. Lit. Mainz Abh. Math. Naturwiss. Kl. **146**, 797 (1939).

[33] H. Brune, H. Roder, C. Borango, and K. Kern, Phys. Rev. B **49**, 2997 (1994).

[34] W. Cho et al., Surf. Sci. **439**, L792 (1990).

[35] P. Jensen, Rev. Mod. Phys. **71**, 1695 (1999).

[36] R. Gomer, Rep. Prog. Phys. **53**, 917 (1990).

[37] J. Perrin, *Atoms*, Constable and Company Ltd, Leicester Square WC, 4th edition, 1920.

[38] F. Reif, *Statistical and Thermal Physics*, McGraw-Hill, New York, 1965.

[39] F. Watanabe and G. Ehrlich, J. Chem. Phys. **96**, 3191 (1992).

[40] G. Ehrlich and F. Watanabe, Langmuir **7**, 2555 (1991).

[41] M. A. Anisimor, V. A. Rabinovich, and V. V. Sychev, *Thermodynamics of The Critical State of Individual Substances*, CRC Press, Florida, 1995.

[42] S. Chang and P. Thiel, Crit. Rev. Surf. Chem. **3**, 239 (1994).

[43] R. Kern, G. Leglay, and J. Métois, *Current topics in Materials Science*, volume 3, North-Holland, Amsterdam, 1979.

[44] J. A. Venables and G. L. Price, Epitaxial growth: Part b, in *Materials Science Series*, edited by J. Matthews, chapter 4, Academic Press, New York, 1975.

[45] A. Donohoe and J. Robins, J. Vac. Sci. Technol. B **17**, 70 (1972).

[46] H. Brune, S. Bales, C. Borango, J. Jacobsen, and K. Kern, Phys. Rev. B **60**, 5991 (1999).

[47] B. Müller, L. Nedelmann, B. Fischer, H. Brune, and K. Kern, Phys. Rev. B **54**, 17858 (1996).

[48] J. A. Venables, G. D. Spiller, and M. Hanbucken, Rep. Prog. Phys. **47**, 399 (1984).

[49] H. Brune, H. Röder, C. Borango, and K. Kern, Phys. Rev. Lett. **73**, 1955 (1994).

[50] H. Lüth, *Solid Surfaces, Interfaces and Thin Films*, Springer, 4th edition, 2001.

[51] C. Herring, Phys. Rev. **82**, 87 (1951).

[52] H. Bonzel, Interface Sci. **9**, 21 (2001).

[53] J. Bermond and J. Venables, J. Cryst. Growth **64**, 239 (1983).

[54] T. Darby and C. Wayman, J. Cryst. Growth **29**, 98 (1975).

[55] J. Metois and J. Heyraud, Thin Solid Films **75**, 1 (1981).

[56] R. Nishitani, A. Kasuya, S. Kubota, and Y. Nishina, J. Vac. Sci. Technol. B **9**, 806 (1991).

[57] B. Blum, R. Salvarezza, and A. Arvia, J. Vac. Sci. Technol. B **17**, 2431 (1999).

[58] J. Heyraud and J. Métois, Acta. Met. **28**, 1789 (1980).

[59] E. Ben-Jacob, Philos. Tr. R. Soc. S-A **361**, 1807 (2003).

[60] E. Ben-Jacob, I. Cohen, and H. Levine, Adv. Phys. **49**, 395 (2000).

[61] D. Grier, E. Ben-Jacob, R. Clarke, and L. Sander, Phys. Rev. Lett. **56**, 1264 (1986).

[62] E. Ben-Jacob et al., Phys. Rev. Lett. **55**, 1315 (1985).

[63] R. Segev and E. Ben-Jacob, Neural Networks **13**, 185 (2000).

[64] J. S. Langer, Rev. Mod. Phys. **52**, 1 (1980).

[65] I. Golding, Y. Kozlovsky, I. Cohen, and E. Ben-Jacob, Physica A **260**, 510 (1998).

[66] E. Yokoyama and T. Kuroda, Phys. Rev. A **41**, 2038 (1990).

[67] T. A. Witten and L. M. Sander, Phys. Rev. Lett. **47**, 1400 (1981).

[68] M. Eden in, *Proceedings of the Forth Berkeley Symposium on Mathematical Statistics and Probability*, volume IV, University of California Press, 1961.

[69] S. K. Friedlander, *Smoke, Dust and Haze*, John Wiley and Sons, New York, 1977.

[70] S. R. Forrest and T. A. Witten, J. Phys. A **12**, L109 (1979).

[71] T. A. Witten and L. M. Sander, Phys. Rev. B **27**, 5686 (1983).

[72] M. James and P. Prusinkiewicz, World Wide Web, `www.algorithmicbotany.org/vmm-delux/Section-04.html#eden`.

[73] P. Meakin, Phys. Rev. A **27**, 1495 (1983).

[74] J. S. Langer and H. Muller-Krumbhaar, Acta Metall. **26**, 1681 (1978).

[75] W. Mullins and R. Sekerka, J. Appl. Phys. **34**, 323 (1963).

[76] T. Irisawa, M. Uwaha, and Y. Saito, Europhys. Lett. **30**, 139 (1995).

[77] R. Hwang, J. Schroder, C. Gunther, and R. Behm, Phys. Rev. Lett. **67**, 3279 (1991).

[78] J. Zhong, T. Zhang, Z. Zhang, and M. Lagally, Phys. Rev. B **63**, 113403 (2001).

[79] G. S. Bales and D. C. Chrzan, Phys. Rev. B **50**, 6057 (1994).

[80] Y. Xu, B. Liu, E. Wang, and D. Wang, J. Phys. D: Appl. Phys. **34**, 1137 (2001).

[81] H. Röder, K. Bromann, H. Brune, and K. Kern, Phys. Rev. Lett. **74**, 3217 (1995).

[82] T. Michely, M. Hohage, M. Bott, and G. Cosma, Phys. Rev. Lett. **70**, 3943 (1993).

[83] S. Liu, Z. Zhang, G. Cosma, and H. Metiu, Phys. Rev. Lett. **71**, 2967 (1993).

[84] H. Brune et al., Surf. Sci. Lett. **349**, L115 (1996).

[85] C. Brechignac et al., Eur. Phys. J. D **16**, 265 (2001).

[86] B. Yoon et al., Surf. Sci. **443**, 76 (1999).

[87] H. Wang, J. Jing, and P. Henriksen, J. Vac. Sci. Technol. A **11**, 1987 (1993).

[88] H. Velfe, H. Stenzel, and M. Krohn, Thin Solid Films **98**, 115 (1982).

[89] T. Darby and C. Wayman, J. Cryst. Growth **28**, 41 (1975).

[90] C. Wayman and T. Darby, J. Cryst. Growth **28**, 53 (1975).

[91] R. Anton and P. Kreutzer, Phys. Rev. B **61**, 16077 (2000).

[92] G. Francis, L. Kuipers, J. Cleaver, and R. Palmer, J. Appl. Phys. **79**, 2942 (1996).

[93] C. Chapon, S. Granjeaud, A. Humbert, and C. Henry, Eur. Phys. J. AP **13**, 23 (2001).

[94] M. Baumer, J. Libuda, and H. Freund, Surf. Sci. **327**, 321 (1995).

[95] G. Wu and K. Chan, Surf. Rev. Lett. **4**, 855 (1997).

[96] H. Xu and K. Ng, J. Vac. Sci. Technol. B **13**, 2160 (1995).

[97] Z. Rakocevic, S. Strbac, N. Bibic, D. Perusko, and T. Nenadovic, Thin Solid Films **257**, 83 (1995).

[98] E. Ganz, K. Sattler, and J. Clarke, Surf. Sci. **219**, 33 (1989).

[99] C. Binns, S. H. Baker, C. Demangeat, and J. C. Parlebas, Surf. Sci. Rep. **34**, 105 (1999).

[100] P. J. Brown and J. B. Forsyth, *The Crystal Structure of Solids*, Edward Arnold Limited, 25 Hill Street, London, 1973.

[101] J. Donohue, *The Structures of the Elements*, John Wiley and Sons, New York, 1974.

[102] E. A. Wood, *Crystal Orientation Manual*, chapter 22, Columbia University Press, 1963.

[103] B. Stegemann, C. Ritter, B. Kaiser, and K. Rademann, Phys. Rev. B **5**, 37 (2004).

[104] C. Koitzsch et al., Surf. Sci. **527**, 51 (2003).

[105] F. Jona, Surf. Sci. **8**, 57 (1967).

[106] S. Agergaard et al., New J. Phys. **3**, 15.1 (2001).

[107] J. F. O'Hanlon, *A Users Guide to Vacuum Technology*, John Wiley and Sons Inc, Canada, 1989.

[108] J. Metois, J. Heyraud, and Y. Takeda, Thin Solid Films **51**, 105 (1978).

[109] P. Simonis et al., Surf. Sci. **511**, 319 (2002).

[110] Z. Klusek, Appl. Surf. Sci. **125**, 339 (1998).

[111] X. Chu and L. D. Schmidt, Surf. Sci. **268**, 325 (1992).

[112] P. Melinon et al., J. Cryst. Growth. **275**, 317 (2005).

[113] D. Halliday, R. Resnick, and J. Walker, *Fundamentals of Physics*, chapter 21, John Wiley and Sons, New York, 5th edition, 1993.

[114] J. Mühlbach, P. Pfau, E. Recknagel, and K. Sattler, Surf. Sci. **106**, 18 (1981).

[115] A. Fischer, J. Chem. Phys. **45**, 375 (1966).

[116] Sycon Instruments Inc., New York, *Sycon Instruments users manual*, 1997.

[117] Group Scientific, Australia, *Digital Instruments Scanning Probe Microscopy Training Notebook*, 2001.

[118] G. Binnig, C. Quate, and C. Gerber, Phys. Rev. Lett. **56**, 930 (1986).

[119] E. Chung, Nano gallery, Toronto Star, 22 November, 2004.

[120] November image, Veeco calender, World Wide Web, `www.veeco.com/calendarcontest05/default.asp`, 2005.

[121] Electron, ion, and photo beam technology and nanofabrication conference, World Wide Web, `www.zyvex.com/EIPBNuG/2004MicroGraph.html#SPM`, 2004.

[122] L. Reimer, *Scanning Electron Microscopy: The Physics of Image Formation and Microanalysis*, Springer, Berlin, 4 edition, 1998.

[123] P. Perkes, image downloaded from, World Wide Web, `http://acept.la/asu.edu/PiN/rdg/elmicr/elmicr.shtml`, 2005.

[124] S. Kikuchi, Jap. J. Phys. **5**, 83 (1928).

[125] A. Schwartz, M. Kumar, and B. Adams, *Electron Back Scatter Diffraction in Materials Science*, Plenum, 2000.

[126] M. Alam, M. Blackman, and D. Pashley, Proc. Roy. Soc. Lond. A **221**, 224 (1954).

[127] J. Venables and C. Harland, Phi. Mag. **27**, 1193 (1973).

[128] M. V. Kral, H. R. McIntyre, and M. J. Smillie, Scripta Mater. **51**, 215 (2004).

[129] M. V. Kral and G. Spanos, Acta. Mater. **51**, 301 (2003).

[130] D. Bera, S. Kuiry, and S. Seal, J. Phys. Chem. B **108**, 556 (2004).

[131] C. Trager-Cowan et al., Mat. Sci. Eng. B **82**, 19 (2001).

[132] HKL technology, *Channel5 users manual.*

[133] D. Reinhard, B. Hall, P. Bertould, S. Valkealahti, and R. Monot, Phys. Rev. Lett. **79**, 1459 (1997).

[134] M. Hyslop, *Electron Diffraction Studies of Unsupported Clusters*, PhD thesis, University of Canterbury, 2002.

[135] J. Le Roux, *Nanostructures Formees Par Depot D'Afregats: Croissance, Morphologie Et Stabilite*, PhD thesis, Universite de Paris-Sud, 2002.

[136] E. Ben-Jacob and P. Garik, Nature **343**, 523 (1990).

[137] H. S. Hele-Shaw, Nature **56**, 34 (1898).

[138] E. Ben-Jacob, G. Deutscher, P. Garik, N. Goldenfeld, and Y. Lareah, Phys. Rev. Lett. **57**, 1903 (1986).

[139] J. V. Mayher, Phys. Rev. Lett. **54**, 1498 (1985).

[140] Images from University of Pittsburg, World Wide Web, `www.phyast.pitt.edu/groups/cond_mat/research/pattern_formation.html`, 2005.

[141] P. G. Saffman and G. I. Taylor, Proc. Roy. Soc. London, Ser. A **245**, 312 (1958).

[142] E. Sharon, M. Moore, W. McCormick, and H. Swinney, Phys. Rev. Lett. **91**, 205504 (2003).

[143] M. Conti, B. Meerson, and P. Sasorov, Phys. Rev. Lett. **80**, 4693 (1998).

[144] P. Mulheran and J. Blackman, Philos. Mag. Lett. **72**, 55 (1995).

[145] M. Nezadal and O. Zmeskal, Demonstration version of HarFA program used for fractal analysis, World Wide Web, `www.fch.vutbr.cz/lectures/imagesci/harfa.html`, 2003.

[146] L. Knüfing, H. Schollmeyer, H. Riegler, and K. Mecke, Langmuir **21**, 992 (2005).

[147] J. Rogowska, Vacuum **74**, 153 (2004).

[148] K. Reshöft, C. Jensen, and U. Köhler, Surf. Sci. **421**, 320 (1999).

[149] B. Kaiser, private communication.

[150] R. Schwoebel and E. Shipsey, J. Appl. Phys. **37**, 3682 (1966).

[151] R. Pfanderzelter, G. Steierl, and C. Rau, Phys. Rev. Lett. **74**, 3467 (1995).

[152] S. Gwo et al., Phys. Rev. Lett. **90**, 185506 (2003).

[153] M. Batzill, J. Kim, D. Beck, and B. Koel, Phys. Rev. B **69**, 165403 (2004).

[154] G. Potschke, J. Schroder, C. Gunther, R. Hwang, and R. Behm, Surf. Sci. **251-252**, 592 (1991).

[155] R. Otero, A. Vázquez de Parga, and R. Miranda, Phys. Rev. B **66**, 115401 (2002).

[156] W. Su et al., Phys. Rev. B. **68**, 033405 (2003).

[157] Z. Zhang, Q. Niu, and C. Shih, Phys. Rev. Lett. **80**, 5381 (1998).

[158] T. Nagao et al., Phys. Rev. Lett. **93**, 105501 (2004).

[159] L. Tan, J. Phys. I France **3**, 935 (1993).

[160] A. Pimpinelli and J. Villain, *Physics of Crystal Growth*, Cambridge University Press, Trumping Street, Cambridge, UK, 1998.

[161] J. Villain, A. Pimpinelli, L. Tang, and D. Wolf, J. Phys. I France **2**, 2107 (1992).

[162] A. Pimpinelli, J. Villain, and D. Wolf, Phys. Rev. Lett. **69**, 985 (1992).

[163] M. Bartelt, S. Gunther, E. Kopatzki, R. Behm, and J. Evans, Phys. Rev. B **53**, 4099 (1996).

[164] C. Chen and T. Song, Phys. Rev. B **41**, 12403 (1990).

[165] I. Beszeda, I. Szabo, and E. Gontier-Moya, Appl. Surf. Sci. **212-213**, 787 (2003).

[166] L. Bardotti, P. Jensen, A. Hoareau, M. Treilluex, and B. Cabaud, Phys. Rev. Lett. **74**, 4694 (1995).

[167] P. Deltour, J. Barrat, and P. Jensen, Phys. Rev. Lett. **78**, 4597 (1997).

[168] L. Lewis, P. Jensen, N. Combe, and J. Barrat, Phys. Rev. B **61**, 16084 (2000).

[169] J. Carrey, L. Maurice, F. Petroff, and A. Vaures, Phys. Rev. Lett. **86**, 4600 (2001).

[170] C. Henry, Surf. Sci. Rep. **31**, 235 (1998).

[171] G. W. Clark and L. L. Kesmodel, J. Vac. Sci. Technol. B **11**, 131 (1993).

[172] M. Saito, T. Ohno, and T. Miyazaki, Appl. Surf. Sci. **237**, 80 (2004).

[173] M. Kammler and M. Horn-von Hoegen, Surf. Sci. **576**, 56 (2005).

[174] J. Jing, P. Henriksen, H. Chu, and H. Wang, Appl. Surf. Sci. **62**, 105 (1992).

[175] D. Partin, C. Thrush, J. Heremans, D. Morelli, and C. Olk, J. Vac. Sci. Technol. B **7**, 348 (1989).

[176] S. Granjeaud et al., Microsc. Microanal. Microstruct. **4**, 409 (1993).

[177] J. H. van der Merwe and C. A. B. Ball, Epitaxial growth: Part b, in *Materials Science Series*, edited by J. Matthews, chapter 6, Academic Press, New York, 1975.

[178] C. Jeffrey, D. Harrington, and S. Morin, Surf. Sci. **512**, L367 (2002).

[179] M. Atashbar, D. Banerji, S. Singamaneni, and V. Bliznyuk, Nanotechnology **15**, 374 (2004).

[180] E. Walter et al., J. Phys. Chem. B **106**, 11407 (2002).

[181] R. Palmer, S. Pratontep, and H. Boyen, Nat. Mater. **2**, 443 (2003).

[182] M. Schulze et al., Eur. J. Phys. D **24**, 291 (2003).

[183] A. Perez et al., New J. Phys. **4**, 76.1 (2002).

List of Figures

List of Tables

List of Acronyms

AFM	-	Atomic force microscope
DLA	-	Diffusion limited aggregation
DRM	-	Deposition rate monitor
EBSD	-	Electron backscatter diffraction
EBSP	-	Electron backscatter pattern
FE-SEM	-	Field-emission scanning electron microscope
KMC	-	Kinetic Monte Carlo
MBE	-	Molecular beam epitaxy
RGA	-	Residual gas analyzer
TEM	-	Transmission electron microscope
UHV	-	Ultra high vacuum

Acknowledgments

There are many people who contributed to this thesis. First I would like to thank my supervisor Assoc. Prof. Simon Brown, both for his constant encouragement and support over the duration of this work, and for his guidance and input into the project.

This thesis has also benefited greatly from the input of my Mentor Dr. Milo Kral, who made his electron microscopy lab available for use, and introduced EBSD to the project. The many stimulating discussions, and technical guidance are also greatly appreciated. The technical assistance from Mike Flaws with SEM imaging, and Helen Devereux with AFM imaging is also appreciated.

The FE-SEM based EBSD was made available by Dr. Richard Tilley at Victoria University in Wellington, NZ. This contribution significantly enhanced the project.

I would also like to thank Dr. Bernhard Kaiser from Humboldt University in Berlin, whose help with the early stages of establishing this project was invaluable. Also, the many useful discussions throughout the course of this work are very much appreciated.

The Department of Physics and Astronomy is fortunate to have excellent workshop technicians, whose skill and advice contributed enormously to the successful construction of the UHV system. In particular Owen Caughley's efforts on the mechanical construction were invaluable. The assistance of Ross Ritchie, Wayne Smith, and Graeme Kershaw is also acknowledged.

I would also like to acknowledge the funding provided by The MacDiarmid Institute for Advanced Materials and Nanotechnology, and by the University of Canterbury.

Thanks must also go to my family for their encouragement, and to Sam for his support throughout the years of study which finally led to the completion of this thesis.